



## City Research Online

### City, University of London Institutional Repository

---

**Citation:** Soltanahmadi, Abbasali (1988). Dynamics of Flexible Riser Systems.  
(Unpublished Doctoral thesis, City, University of London)

This is the accepted version of the paper.

This version of the publication may differ from the final published version.

---

**Permanent repository link:** <https://openaccess.city.ac.uk/id/eprint/20155/>

**Link to published version:**

**Copyright:** City Research Online aims to make research outputs of City, University of London available to a wider audience. Copyright and Moral Rights remain with the author(s) and/or copyright holders. URLs from City Research Online may be freely distributed and linked to.

**Reuse:** Copies of full items can be used for personal research or study, educational, or not-for-profit purposes without prior permission or charge. Provided that the authors, title and full bibliographic details are credited, a hyperlink and/or URL is given for the original metadata page and the content is not changed in any way.

**DYNAMICS OF FLEXIBLE RISER SYSTEMS**

**By**

**ABBASALI SOLTANAHMADI**

**B.Sc. (Hons), M.Sc. (Structures)**

**A Thesis Submitted for the degree  
of Doctor of Philosophy**

**The City University  
Department of Civil Engineering**

**November 1988**

**To My Brother, Ali**

## ACKNOWLEDGEMENTS

I would sincerely like to thank Dr M R Barnes for his generous encouragement and supervision throughout the duration of this work. I wish also to express my gratitude to Professor J Chaplin for his advice and guidance towards the experimental work of the project. I would like to thank the technical staff of the Department of Civil Engineering in the City University for their assistance in the laboratory.

I wish also to express my sincere appreciation to Zentech Consultants for most generously giving me the opportunity to contribute the numerical validation for this work.

I would like to thank Mrs Pat Walker who typed this manuscript.

I wish to express my deep appreciation to my wife's patience and my brother's moral and financial support, without which this project would not have been possible.

Last, but not least, I would like to acknowledge the financial support given by Robert Kitchin (Saddlers) through the City University.

## SYNOPSIS

This thesis is concerned with the static and dynamic analyses and the model testing of deep sea flexible riser systems which are the key components associated with semi-submersible oil platforms. A numerical method based on explicit integration of Newton's second law is developed to predict the 3-dimensional dynamic behaviour of the riser due to the hydrodynamic loadings induced by wave and current motion. In this analysis the effects of waves and currents from separate directions, vessel movements, vortex-shedding and structural damping are included. The material damping for the riser is modelled by a single Kelvin system and the hydrodynamic loadings are assessed from the modified Morison equation. The effect of vortex-shedding on the riser is modelled by considering the interaction of drag-inertia and lift forces due to wave and current motion. The drag coefficient being modified by the vortex-shedding effects which are predicted by calculating the maximum response of the flexible riser in the lift force direction.

The formfinding and static analysis of the riser when subject to structural self-weight and other static loadings is carried out by the method of Dynamic Relaxation using kinetic damping. The method is well suited to computer aided design procedures in which various shapes for the riser catenary have to be investigated together with the effects of boundary support conditions and alternative arrangements of mooring buoys.

The theories described above are implemented into three computer programs. The first program deals with the formfinding of the riser and the second investigates the dynamic behaviour of the riser due to non-linear current and wave loadings. The third program is concerned with the static solution of the riser due to current loading. The latter is employed when the hydrodynamic force consists of current loading only and therefore the dynamic solution is not desired. The iterative use of the first and third programs allows potential designs to be quickly investigated.

The results predicted by the numerical analyses are compared with those obtained from two series of model tests in wave flumes. The tests were scaled from prototype situations using Froude number criteria. The first set of tests used a small scale flexible chain model with negligible material damping and structural bending stiffness and no induced vortex shedding; the aim of these tests being only to validate the assessment of the hydrodynamic forces on the riser. The second set investigated the response of a larger scale model which induced vortex-shedding and in which the riser system had significant structural damping. The comparison of experimental and computed results showed close agreement.

The developed computer programs were also validated numerically by comparing the predicted results with those obtained from the well known riser program "FLEXRISER".

CONTENTS

	<u>Page</u>
LIST OF FIGURES	xiii
LIST OF TABLES	xxiii
LIST OF PLATES	xxvi
LIST OF SYMBOLS	xxvii
CHAPTER 1	
GENERAL INTRODUCTION	1
1.1	1
Introduction	
1.2	2
Outline of Thesis	
CHAPTER 2	
LITERATURE REVIEW OF HYDRODYNAMIC LOADINGS ON	4
FLEXIBLE RISERS	
2.1	4
Introduction	
2.2	4
Fluid Hydrodynamics	
2.2.1	4
Wave Hydrodynamics	
2.2.2	8
Interaction of Wave and	
Current Motion	
2.3	10
Drag-Inertia Hydrodynamic Forces on	
Cylinders	
2.3.1	10
Hydrodynamic Forces on a	
Vertical Rigid Cylinder	
2.3.2	17
Hydrodynamic Forces on a Rough	
Cylinder	
2.3.3	21
Hydrodynamic Forces on an	
Inclined Cylinder	

	<u>Page</u>
2.3.4	Hydrodynamic Forces on a Flexible Cylinder 23
2.3.5	Hydrodynamic Forces on Cylinder Groups 25
2.3.6	Hydrodynamic Forces along a Cylinder 32
2.4	Hydrodynamic Loadings Induced by Vortex-Shedding on Cylinders Placed in the Plane of the Wave and Current Motion 33
2.4.1	Forces on a rigid Cylinder Induced by Vortex-Shedding in Steady Flow (No Vibration) 34
2.4.2	Vortex-Excited Vibration of Cylinders in Steady Flow 35
2.4.3	Forces on Rigid Cylinders due to Vortex-Shedding in Waves 38
2.4.4	Vortex-Excited Vibration of Flexible Cylinders in Waves 40
2.5	Forces Induced by Vortex-Shedding on Randomly Oriented Cylinders 42
CHAPTER 3	FLEXIBLE RISERS 44
3.1	Introduction 44
3.2	Flexible Pipe Cross-Section 45
3.3	Background to the Analysis of Flexible Risers 49

	<u>Page</u>
CHAPTER 4 THEORETICAL COMPUTATION AND ASSESSMENT OF HYDRODYNAMIC LOADINGS ON FLEXIBLE RISERS	54
4.1 Introduction	54
4.2 Fluid Mechanics	55
4.2.1 Derivation of Basic Relationships for Incompressible, Irrotational and Inviscid Fluid Flow	55
4.3 Wave Theory	60
4.3.1. Linear (Airy) Wave Theory	62
4.3.2 Stokes Finite Amplitude Wave Theory	69
4.3.3 Numerical Solution of Equations (4.42) and (4.43)	73
4.4 Hydrodynamic Loading	77
4.4.1 Developing the Theory to Estimate the Drag-Inertia Hydrodynamic Loading on a Flexible Catenary Riser	77
4.4.2 Forces Induced by Vortex-Shedding on a Randomly Oriented Flexible Catenary Riser	83
4.4.3 Modification of Drag-Inertia Force Equation due to Vortex-Shedding	92

		<u>Page</u>
4.5	Assessment of Drag-Inertia Hydrodynamic Forces of Flexible Risers	93
4.5.1	Region 1 - Hydrodynamic Loadings Induced by Wave and Current Flows	94
4.5.2	Region 2 - Hydrodynamic Loading Induced by Current Motion Only	99
4.6	Assessment of Hydrodynamic Forces Induced by Vortex-Shedding on Flexible Risers	100
4.7	Simulation of Splash Zone	101
4.8	Modelling of Platform Motion	105
CHAPTER 5	THEORETICAL DEVELOPMENTS FOR THE ANALYSIS OF FLEXIBLE RISERS	109
5.1	Introduction	109
5.2	Dynamic Analysis of Flexible Risers	110
5.2.1	Numerical Schemes for Structural Dynamics	110
5.2.2	Dynamic Solution	111
5.2.3	Stability of the Numerical Integration	119
5.2.4	Optimization of the Numerical Integration	121

		<u>Page</u>
5.3	Formfinding and Static Solution of Flexible Risers	123
5.4	Calculation of Visco-Elastic Material Damping Constants	128
5.5	Determination of Structural Natural Frequencies	129
5.6	Dimensional Analysis and Model Scaling	136
	5.6.1 Dimensional Analysis	136
	5.6.2 Model Scaling of a Riser in Wave Flow	137
	5.6.3 Model Scaling of a Riser in Current Flow	140
CHAPTER 6	NUMERICAL IMPLEMENTATION	141
6.1	Introduction	141
6.2	Implementation of Static Solution for Formfinding	142
	6.2.1 Program FLEXSTATIC (Program 1)	142
	6.2.2 Critical Criteria in Designing Flexible Riser Catenary Shapes	143
	6.2.3 Optimization of Program FLEXSTATIC	143
	6.2.4 Validation of Program FLEXSTATIC	145
	6.2.5 Parameter Study on the Number of Elements Used to Compute the Riser Equilibrium Shape	146

	<u>Page</u>
6.3	Implementation of Dynamic Solution 147
6.3.1	Program STOKWAVE 147
6.3.2	Program FLEXDYNAMIC 148 (Program 2)
6.3.3	Optimization of Program 149 FLEXDYNAMIC
6.4	Program FLEXCURRENT (Program 3) 151
6.5	Validation of Program FLEXSTATIC, 152 FLEXCURRENT and FLEXDYNAMIC Computations by Hand Calculations
6.6	Implementation and Numerical Validation 152 of the Method Used to Determine Structural Natural Frequencies
CHAPTER 7	EXPERIMENTAL WORK TO VALIDATE NUMERICALLY COMPUTED 198 RESULTS
7.1	Introduction 198
7.2	Objectives of the Experiments 198
7.3	Model Scaling and Description of Test 199 Models, Regular Waves and Current Flows
7.3.1	First Series of Experiments 199
7.3.2	Second Series of Experiments 201
7.4	Experimental Apparatus 207
7.4.1	Current Channel 207
7.4.2	Small Wave Flume 209
7.4.3	Large Wave Flume 209
7.5	Description of Measuring Instrumentation 210
7.5.1	Current Meter 210

		<u>Page</u>	
	7.5.2	Wave Probe	210
	7.5.3	Horizontal Top Tension Measuring Strain Gauges	211
	7.5.4	Ultra Violet Recorder	211
	7.5.5	High Speed Camera	212
	7.5.6	The Modular Film Analysis System (Digitizer System)	212
7.6		Calibration of Measuring Instruments	213
	7.6.1	Wave Probe	213
	7.6.2	Strain Gauges	213
	7.6.3	Displacement Transducer	213
7.7		Experimental Procedure	214
	7.7.1	The First Series of Tests	214
		7.7.1.1 Current Channel Ex- periments	214
		7.7.1.2 Wave Flume Experi- ments	216
	7.7.2	The Second Series of Tests	217
		7.7.2.1 Current Channel Ex- periments	217
		7.7.2.2 Wave Flume Experi- ments	218
		7.7.2.3 Material Damping Test	219
CHAPTER 8		RESULTS	221
	8.1	Introduction	221
	8.2	Results for the Chain Model	221

		<u>Page</u>
8.2.1	Determination of Young's Modulus, $E$ , for the Chain	221
8.2.2	Determination of the Drag Coefficient, $C_d$ , for the Model in Steady Current Flow and Validation of Static Program 3	221
8.2.3	Determination of Drag Coefficient, $C_d$ , and Inertia Coefficient, $C_m$	222
8.2.4	Results of the Generated Wave in the Small Flume	226
8.2.5	Results of the Tests in the Small Wave Flume	227
8.3	Results for the Tube Model	229
8.3.1	Results of the Material Damping Tests	229
8.3.2	Determination of the Drag Coefficient, $C_d$ , for the Model in Steady Current Flow	229
8.3.3	Determination of Drag Coefficient, $C_d$ , and Inertia Coefficient, $C_m$	230
8.3.4	Results for the Generated Wave in the Large Wave Flume	230
8.3.5	Calculation of the Buoyancy Force Induced by the Sub-Buoy and the Cradle	231

		<u>Page</u>
	8.3.6 Results of Tests in the Large Wave Flume	231
8.4	Results for the Vibrating Tube Model due to Vortex-Shedding	250
	8.4.1 Results for High Amplitude Wave Generated in the Large Wave Flume	250
	8.4.2 Determination of Drag Coefficient, $C_d$ , and Inertia Coefficient, $C_m$	250
	8.4.3 Evaluation of the Model Natural Frequencies	251
	8.4.4 Determination of the Model Response due to Vortex- Shedding	252
	8.4.5 Comparison of the Model Response to the Wave with and without taking account of Vortex-Shedding Effects	254
CHAPTER 9	NUMERICAL VALIDATION	279
	9.1 Introduction	279
	9.2 Static Test Cases without Current Loadings	281
	9.3 Static Test Cases with Current Loadings	282
	9.4 Dynamic Test Cases	282

	<u>Page</u>	
CHAPTER 10	CONCLUSIONS AND RECOMMENDATIONS	296
	10.1 Conclusions	296
	10.2 Recommendations	302
APPENDIX A	Coefficients $A_{ij}$ , $B_{ij}$ and $C_i$ of Stokes Wave Theory	305
APPENDIX B	Derivation of Formulae for Determining the Hydrodynamic Forces on a Riser Element	307
APPENDIX C	Calculation of Nodal Twisting Forces due to Torsion of Flexible Risers	309
APPENDIX D	Static Solution for the Riser Structure Using Dynamic Relaxation with Viscous Damping	312
APPENDIX E	Input Data of the Test Cases in Chapter 9	314
References		325

LIST OF FIGURES

Page

Figure

3.1	Different shapes of flexible risers	47
3.2	Cradle system	48
3.3	Flexible riser cross-section	48
3.4	Type of elements used in finite difference scheme	49
3.5	Type of elements used in finite element scheme	50
4.1	Fluid element	55
4.2	Components of fluid element motion	56
4.3	Ranges of wave theories giving the best fit to the dynamic free surface boundary condition (Dean 1970)	61
4.4	Ranges of suitability for various wave theories (Méhauté (1976))	61
4.5	Specifications for a wave train	62
4.6	Modification of the linear wave theory	68
4.7	Orientation of a riser element in space	81
4.8	Variation of lift coefficient with the Reynolds and the Keulegan-Carpenter numbers for rigid cylinders	86
4.9	The frequency of vortex-shedding in waves (two-dimensional results from Sarpkaya (1976a), wave results from Isaacson (1974)).	88
4.10	Prediction of "lock-in" frequency from Rajabi et. al. (1984)	89
4.11	Lift amplification correction	90
4.12	$CL_0$ against $Re$ for current flows	91
4.13	An idealized flexible riser	93
4.14	Hydrodynamic loading on member AB	96

		<u>Page</u>
4.15	The first two force segments on member AB	97
4.16	Trapezoidal rule	99
4.17	Iteration procedure to obtain the conjunction point of the piercing member and wave profile	102
4.18	Nodal hydrodynamic forces on the piercing member	103
4.19	Adjustment of current induced velocity with wave profile	103
4.20	Platform motion	105
4.21	Pitch induced translational motions of the riser top connector	107
5.1	Single Kelvin model	112
5.2	Definition sketch for flexure of adjacent members in the x-y plane	115
5.3	Flow chart of dynamic solution algorithm	118
5.4	Damping of kinetic energy peaks with time	125
5.5	Flow chart of static solution algorithm	127
5.6	Strain against time for visco-elastic materials	128
5.7	Dynamic response of a structure and its reflected image	132
5.8	Time history of nodal displacements	135
5.9	Values of coefficients A and B against r	135
6.1	Computed static equilibrium shape of a free hanging riser	164
6.2	Computed static equilibrium shape of a single catenary riser	165
6.3	Computed static equilibrium shape of a double catenary riser	166

		<u>Page</u>
6.4	Computation of static equilibrium shape of a double catenary riser from the initial input shape	167
6.5	Critical configurations of a single catenary riser corresponding to far and near movements of the platform	168
6.6	Key configurartion to estimate the length of a single catenary riser	169
6.7	Optimization of static solution with reduced axial stiffness	170
6.8	Optimization of static solution with number of kinetic energy peaks at which the riser length is corrected	171
6.9	Comparison of the digitized and computed static configurations of the catenary snake chain representing the upper part of a single or double catenary riser	172
6.10	Comparison of the digitized and computed static configurations of the catenary snake chain representing a free hanging riser	173
6.11	Reaction forces of a single catenary riser with different number of elements	174
6.12	Definition sketch of platform motion	175
6.13	Comparison of the computed dynamic responses of a single catenary riser with calculating the wave and current induced hydrodynamic forces at every 1, 5, 10 or 15 integration time intervals	176
6.14	Snap-shots of the dynamic response of a single catenary riser subjected to wave and current induced hydrodynamic loadings	177

		<u>Page</u>
6.15	Time histories of horizontal nodal displacements of a single catenary riser subjected to wave and current induced hydrodynamic loadings	178-179
6.16	Time histories of vertical nodal displacements of a single catenary riser subjected to wave and current induced hydrodynamic loadings	180-181
6.17	Snap-shots of the dynamic response of a single catenary riser subjected to wave and current induced hydrodynamic forces and platform motion	182
6.18	Time histories of horizontal nodal displacements of a single catenary riser subjected to wave and current induced hydrodynamic loadings and platform motions	183-184
6.19	Time histories of vertical nodal displacements of a single catenary riser subjected to wave and current induced hydrodynamic forces and platform motion	185-186
6.20	Flow chart for static solution algorithm for program FLEXCURRENT	187
6.21	Computed static equilibrium shapes of a single catenary riser with and without current induced hydrodynamic loadings	188
6.22	Computed static equilibrium shapes of a single catenary riser with and without current induced hydrodynamic loadings and vertical platform movement	189
6.23	Computed static equilibrium shapes of a single catenary riser with and without current induced hydrodynamic loadings and horizontal platform movement	190
6.24	Hand calculation test case 1	191

	<u>Page</u>	
6.25	Hand calculation test case 2	192
6.26	Specifications of a catenary cable used by Triantafyllou et. al. (1983) to calculate the structural natural frequencies	193
6.27	The first four natural frequencies of a catenary for $WL/H = 1.5$ as a function of the static angle at the top after Triantafyllou et. al. (1983)	194
6.28	Static equilibrium shape of the natural frequency validation test case	195
6.29	Time history of the "poked" natural frequency validation test case	196
6.30	Values of coefficients A and B against $r$ for the natural frequency validation test case	197
7.1	Arrangement of the snake chain in catenary shape at $0^\circ$ to wave flow	202
7.2	Arrangement of the tube model in catenary shape at $0^\circ$ to wave flow	205
7.3	Experimental cradle system	206
7.4	Arrangement of the tube model in single catenary riser shape	208
7.5	Model chain and current channel	215
7.6	Geometry of nodal displacement	215
7.7	Material damping test arrangement	220
8.1	Equivalent current velocity variation with water depth	224
8.2	Comparison of the measured and computed nodal displacements along the chain due to current induced hydrodynamic loadings	234

		<u>Page</u>
8.3	Drag coefficient ( $C_d$ ) against Keulegan-Carpenter number (KC) in subcritical Reynolds number region after Sarpakya et. al. (1974)	235
8.4	Inertia coefficient ( $C_m$ ) against Keulegan-Carpenter number (KC) in subcritical Reynolds number region after Sarpakya et. al. (1974)	235
8.5a	Height and period of the wave generated in the small wave flume from X-Y plotter	236
8.5b	The wave train generated in the small wave flume	236
8.6	Comparison of the computed and digitized wave profile for the wave generated in the small wave flume	237
8.7	Computed static equilibrium shape of the chain model at $0^\circ$ to the wave direction	238
8.8	Computed and measured envelopes for the dynamic response of the chain model at $0^\circ$ to the wave direction	239
8.9	Comparison of the computed and measured horizontal nodal displacements along the chain model at $0^\circ$ to the wave direction	240
8.10	Computed static equilibrium shape of the chain model at $30^\circ$ to the wave direction	241
8.11	Computed and measured envelopes in the wave direction for the dynamic response of the chain model at $30^\circ$ to the wave direction	242
8.12	Comparison of the computed and measured horizontal nodal displacements in the wave direction along the chain model at $30^\circ$ to the wave direction	243

	<u>Page</u>	
8.13	Computed static equilibrium shape of the chain model in U-Shape at 30° to the wave direction	244
8.14	Computed and measured envelopes in the wave direction for the dynamic response of the chain in the U-Shape at 30° to the wave direction	245
8.15	Comparison of the computed and measured horizontal nodal displacements in the wave direction along the chain model in the U-Shape at 30° to the wave direction	246
8.16	Computed static equilibrium shape of the chain model in disconnected shape	247
8.17	Computed and measured envelopes for the dynamic response of the chain model in disconnected shape	248
8.18	Comparison of the computed and measured horizontal nodal displacements along the chain model in disconnected shape	249
8.19	Curve-fitting for material damping constants: $E = 8.3 \times 10^6 \text{ N/m}^2$ , $a = 4.9 \times 10^{-6} \text{ m}^2/\text{N. sec}$ and $b = 30 \text{ sec}^{-1}$	256
8.20	Comparison of the measured and computed nodal displacements along the tube model due to current induced hydrodynamic loadings	257
8.21a	Height and period of the first wave generated in the large wave flume	258
8.21b	The first wave train generated in the large wave flume	258
8.22	Comparison of the computed and digitized wave profile for the first wave generated in the large wave flume	259

	<u>Page</u>	
8.23	Computed static equilibrium shape of the tube model in catenary shape at $0^{\circ}$ to the wave direction	260
8.24	Computed and measured envelopes for the dynamic response of the tube model in catenary shape at $0^{\circ}$ to the wave direction	261
8.25	Comparison of the computed and measured horizontal top tension and nodal displacements along the tube model in catenary shape at $0^{\circ}$ to the wave direction	262
8.26	A typical graph output from the U. V. recorder for the horizontal top tension of the tube model in the large wave flume	263
8.27	Computed static equilibrium shape of the tube model at $0^{\circ}$ to the wave direction	264
8.28	Computed and measured envelopes for the dynamic response of the tube model at $0^{\circ}$ to the wave direction	265
8.29	Comparison of the computed and measured horizontal top tension and nodal displacements along the tube model at $0^{\circ}$ to the wave direction	266
8.30	Computed static equilibrium shape of the tube model at $45^{\circ}$ to the wave direction	267
8.31	Computed and measured envelopes in the wave direction for the dynamic response of the tube model at $45^{\circ}$ to the wave direction	268
8.32	Comparison of the computed and measured horizontal top tension and nodal displacements in the wave direction along the tube model at $45^{\circ}$	269

	<u>Page</u>
8.33a	Height and period of the larger wave generated in the large wave flume from (X-Y plotter) <span style="float: right;">270</span>
8.33b	The wave train of the larger wave generated in the large wave flume <span style="float: right;">270</span>
8.34	Comparison of the computed and digitized wave profile for the larger wave generated in the large wave flume <span style="float: right;">271</span>
8.35	Time history of the nodal displacements of node 7 induced by "poking" <span style="float: right;">272</span>
8.36	Values of coefficients A and B against r for the tube model <span style="float: right;">273</span>
8.37	Determination of the dominant vortex-shedding frequency and corresponding structural natural frequency for the tube model <span style="float: right;">274</span>
8.38	Lift coefficient ( $C_{L0}$ ) against Keulegan-Carpenter number (KC) in subcritical Reynolds number region for a rigid cylinder (after Sarpakya et. al. (1974)) <span style="float: right;">275</span>
8.39	Computed static equilibrium shape of the tube model at $0^\circ$ to the wave direction <span style="float: right;">276</span>
8.40	Comparison of the measured and computed envelopes of the dynamic response of the tube model (with and without account of the effects of vortex-shedding) <span style="float: right;">277</span>
8.41	Comparison of the measured and computed horizontal top tension and nodal displacements along the tube model (with and without account of the effects of vortex-shedding) <span style="float: right;">278</span>

		<u>Page</u>
9.1	Comparison of static configuration (Free Hanging riser)	284
9.2	Comparison of static configuration (Double Free Hanging riser)	285
9.3	Comparison of static configuration (Steep S riser)	286
9.4	Comparison of static configuration (Steep Wave riser)	287
9.5	Comparison of static configuration (Lazy S riser)	288
9.6	Comparison of static configuration (Lazy Wave riser)	289
9.7	Comparison of static configuration with current (Double Free Hanging riser)	290
9.8	Comparison of static configuration with current (Steep S riser)	291
9.9	Comparison of the Double Free Hanging riser dynamic response without platform motion	292
9.10	Comparison of the Double Free Hanging riser dynamic response with platform motion	293
9.11	Comparison of the Steep S riser dynamic response without platform motion	294
9.12	Comparison of the Steep S riser dynamic response with platform motion	295
10.1	Spectral density graph	304
C.1	Three adjacent members in space	309
D.1	Definition of different damping states	313

LIST OF TABLES

<u>Table</u>		<u>Page</u>
6.1	Input data for the free hanging riser	155
6.2	Input data for the single catenary riser	155
6.3	Input data for the double catenary riser	156
6.4	Reaction forces of the single catenary riser with different number of elements	156
6.5	Horizontal and vertical co-ordinates of the single catenary riser with different number of elements	157
6.6	Results of the example given by Skjelberia and Hendrickson	147
6.7	Predicted wave parameters for Stokes 5th order	158
6.8a	Data for dynamic run with no platform motion	159
6.8b	Predicted wave parameters of Stokes 5th order wave theory for the dynamic test case	160
6.9	Data for dynamic run of the single catenary riser with platform motion	161
6.10	Data for static run with current loadings	162
6.11	Comparison of structural natural frequencies predicted by Triantfyllou et. al. (1983) and the present work	163
8.1	Computation of the experimental nodal displacements induced by the current	223
8.2	Variation of the current velocity with water depth	224
8.3	Comparison of the computed and experimental horizontal nodal displacements	225
8.4	Wave parameters of the wave generated in the small flume	227

	<u>Page</u>
8.5	Comparison of the computed and experimental horizontal nodal displacements 230
8.6	Wave parameters of the first wave generated in the large flume 231
8.7	Wave parameters of the second wave generated in the large flume 250
8.8	Natural frequencies of the single catenary model 252
8.9	Possible vortex-shedding frequencies along the model from figure (4.9) 253
8.10	Computed results from the vortex-shedding model 254
E.1	Input data for the static run of the free hanging riser 314
E.2	Input data for the static run of the free hanging riser (simple catenary) 314
E.3	Input data for the static run of the steep-S riser 315
E.4	Input data for the static run of the steep wave riser 316
E.5	Input data for the static run of the lazy-S riser 317
E.6	Input data for the static run of the lazy wave riser 318
E.7	Data for the simple catenary riser subjected to current induced hydrodynamic loadings 319
E.8	Data for the steep-S riser subjected to current induced hydrodynamic loadings 320
E.9	Data for the dynamic run of the simple catenary riser subjected to wave and current induced hydrodynamic loadings with no platform motion 321
E.10	Data for the dynamic run of the simple catenary riser subjected to wave and current induced hydrodynamic loadings with platform motion 322

	<u>Page</u>
E.11	Data for the dynamic run of the Steep-S riser subjected to wave and current induced hydrodynamic loadings with no platform motion 323
E.12	Data for the dynamic run of the steep-S riser subjected to wave and current induced hydrodynamic loadings with platform motion 324

LIST OF PLATES

Page

Plates

1	View of snake chain hung in a catenary shape as the upper part of a single or double catenary riser	146a
2	View of snake chain hung in a catenary shape as a free hanging riser	146a
3	General view of experimental arrangements in current channel	220a
4	View of snake chain in small wave flume at $0^{\circ}$ to wave flow	220b
5	View of snake chain in small wave flume at $30^{\circ}$ to wave flow	220b
6	View of base plate in small wave flume	220c
7	View of snake chain in U shape in small wave flume at $30^{\circ}$ to wave flow	220d
8	View of snake chain in disconnected shape in small wave flume	220d
9	View of plastic tube model in current channel	220e
10	View of sub-buoy and cradle system	220e
11	View of tube model arranged in catenary shape in large wave flume at $0^{\circ}$ to wave flow	220f
12	View of tube model arranged in single catenary riser shape in large wave flume at $0^{\circ}$ to wave flow	220g
13	View of tube model arranged in single catenary riser shape in large wave flume at $45^{\circ}$ to wave flow	220h
14	General view of experimental arrangement for material damping calibration test	220i
15	Detailed view of the calibration test arrangement	220i

SYMBOLS

a	Material damping coefficient; Wave amplitude
A	Cross-sectional area of a cylinder
$A_i$	Amplitude of platform motion
$A_{ij}$	Wave parameters used in the Stokes wave theory
$A_p$	Projected frontal area
$A_r$	Coefficient used in the Fourier analysis
b	Interaction parameter between fluid and a cylinder; Material damping constant
$B_{ij}$	Wave parameters used in the Stokes wave theory
$B_r$	Coefficient used in the Fourier analysis
C	Speed of a transverse wave, Wave celerity
$C_o$	Linear wave celerity
$C_d$	Drag coefficient
$C_d/C_{do}$	Magnification of drag coefficient in the Morison equation
$C_l$	Wave parameters used in the Stokes Wave theory
$C_m$	Inertia coefficient
$C_{td}$	Tangential drag coefficient
$CL_o$	Lift coefficient for a rigid cylinder
$CL/CL_o$	Magnification of lift coefficient for a flexible riser
dx	Projection length of an element in the x-axis direction
D	Diameter of a cylinder
$DX_1, DX_2, DX_3$	Distance of the riser top position from the centre of motion in the surge, heave and sway directions
EI	Bending stiffness of an element
f(x)	Function of x used in the derivation of Simpson's rule
$f_i$	Variable used in Newton's iteration scheme
$f_L$	Lift frequency

$f_n$	Structural natural frequency
$f_{ni}$	Harmonics of structural natural frequency
$f_v$	Vortex-shedding frequency
$f_w$	Wave frequency
$F_r$	Froud number
$F_x$	Nodal tension force in the x axis direction
$g$	Gravitational acceleration
$h$	Step length used in Simpson's rule; Water depth
$h^*$	Distance from mean water level (positive upwards)
$HF$	Hydrodynamic loadings per unit length of a riser
$HF_l$	Total hydrodynamic loading on a riser due to wave motion
$HF_n$	Hydrodynamic loading per unit length normal to a riser axis
$HF_{nxy}$	Component of $HF_n$ on the vector lying on the xy plane
$HF_{nz}$	Component of $HF_n$ on the z axis direction
$HF_t$	Tangential hydrodynamic loading per unit length on a riser
$i, j, k$	Cartesian axes
$\bar{I}$	Constant alternating current
$K$	Wave number
$KC$	Keulegan-Carpenter number
$K_L, K_T, K_V$	Scale factors for length, time and velocity respectively
$K.E.$	Nodal kinetic energy
$l$	Riser length
$l_{crit}$	Length of the critical member regarding the travelling of a transverse wave
$l_h$	Horizontal distance of the theodolite from the chain model
$L$	Cylinder length; Wave length
$L_o$	Original length of a riser member

$m$	Mass of a cylinder and its contents also including added mass per unit length of the cylinder
$M$	Structural mass at the node
$M_i, M_j$	Bending moments at nodes $i$ and $j$
$N$	Number of elements
$P$	Fluid pressure; Structural self weight at the node
$r$	The number representing the harmonics of the Fourier expansion
$r_{ix}, r_{jx}$	Mean radii of curvature of node $i$ and $j$ in the $xy$ plane
$\bar{R}$	Resistance of the prob wire
$R(t)$	Time varying nodal forces
$R_p$	Response parameter
$R_e$	Reynolds number
$S$	Nodal axial stiffness $\sum_{i=1}^i (EA/L_0)$ ; Distance from sea bed all links at $i$
$SF_{bi}, SF_{bj}$	Shear force at node $i$ and $j$ of member $b$
$St$	Strouhal number
$t$	Time
$T$	Tension force; Wave period
$T_i$	Initial specified tension in an element
$T_n$	Smallest natural period of a structure
$TC$	Tension coefficient
$TF_L$	Lift force
$TF_{vor}$	Force on a cylinder induced by vortex-shedding
$TF_r$	Resisting force to riser movement due to lift force
$U$	Horizontal fluid velocity; Unit vector along a cylinder
$\dot{U}$	Horizontal fluid acceleration

$U_x, U_y, U_z$	x, y and z components of a unit vector along a cylinder
$\bar{V}$	D.C. voltage
$V, \dot{V}$	Vertical fluid velocity and acceleration
$V_c$	Current induced velocity
$V_{crit}$	Critical fluid velocity at which resonance of a cylinder will occur
$V_{nc}$	Current induced velocity normal to riser axis
$V_{nmax}$	Amplitude of wave induced fluid velocity normal to riser axis in the drag-inertia force direction
$V_{nx}, V_{ny}, V_{nz}$	x, y and z components of fluid velocity normal to riser axis
$\dot{V}_{nx}, \dot{V}_{ny}, \dot{V}_{nz}$	x, y and z components of fluid acceleration normal to riser axis
$V_{nxy}$	Component of fluid velocity normal to riser axis on a vector lying in the xy plane
$V_{nz}$	Component of fluid velocity normal to riser axis in the z direction
$V_r$	Reduced velocity
$V_r^*$	Reduced velocity at lock-in condition
$V_t$	Fluid velocity tangential to riser axis
$V_{tc}$	Current induced fluid velocity tangential to riser axis
$V_{tw}$	Wave induced fluid velocity tangential to riser axis
$V, \dot{V}_w$	Wave induced fluid velocity and acceleration
$\dot{V}_x, \dot{V}_y, \dot{V}_z$	x, y and z components of fluid velocity
$V_x, V_y, V_z$	x, y and z components of fluid acceleration
$W_r$	$(1+2 X_{Lmax}/D)/(V_r St)$

$x_i$	Variable used in Newton's iteration scheme
$x, \dot{x}, \ddot{x}$	Structural displacement, velocity and acceleration
$x_1, \dot{x}_2, \ddot{x}_3$	Surge, heave and sway motions of a platform
$x_L, \dot{x}_L, \ddot{x}_L$	Structural displacement, velocity and acceleration in the lift force direction
$x_{Lmax}$	Maximum structural displacement in the lift force direction
$x_{Lx}, x_{Ly}, x_{Lz}$	x, y and z components of $x_L$
$x_{Lxy}, \dot{x}_{Lxy}, \ddot{x}_{Lxy}$	Component of structural displacement, velocity and acceleration in the lift force direction on a vector lying on the xy plane
$x_n$	Duration of riser response used in the Fourier analysis to determine the structural natural frequencies
$\alpha, \beta$	Van der Pol coefficient; Horizontal and vertical angles of the nodes along the chain model measured by the theodolite
$\alpha_1, \alpha_2, \alpha_3$	Pitch, yaw and roll motions of a platform
$\beta$	Frequency parameter ( $R_e/KC$ ); Wave constant related to the total pressure head
$\beta_1, \beta_2, \beta_3$	Phase angles associated with pitch, yaw and roll motions of a platform respectively
$\delta$	Logarithmic decrement of cylinder damping
$\delta_r$	Reduced damping
$\delta\phi_i, \delta\phi_j$	Rotations of adjacent elements at nodes i and j
$\Delta L$	Total extension of an element
$\Delta L_e$	Elastic extension of an element
$\Delta t$	Integration time step

$\Delta t_{\text{cri}}$	Maximum integration time step for the central difference numerical scheme
$\epsilon_c$	Accumulated creep strain
$\epsilon_p$	Primary creep strain
$\dot{\epsilon}_c$	Rate of creep strain
$\xi$	Structural damping ratio
$\eta$	Wave free surface
$\theta$	$KX - \omega t$ ; Phase angle
$\theta_1, \theta_2, \theta_3$	Phase angles associated with surge, heave and sway motions of a platform respectively
$\lambda$	Perturbation parameter
$\nu$	Kinematic viscosity
$\rho$	Water density
$\rho_c$	Riser density
$\sigma$	Stress level
$\psi$	Stream function
$\psi, \phi$	Polar co-ordinate of a riser element
$\psi'_n$	Constant containing wave coefficients $A_{ij}$
$\omega$	Wave circular frequency
$\omega_v$	Lift circular frequency
$\phi$	Velocity potential

## CHAPTER 1

### GENERAL INTRODUCTION

#### 1.1 - Introduction

In recent years, offshore technology has experienced a remarkable growth and it promises efficient development of oil fields at greater depths. Important components for such deep operations are flexible risers. Considering the large financial losses consequent on a riser failure in deep water, it is essential to perform a comprehensive analysis of such structures in relation to the actual environmental conditions.

A number of non-linear computer programs have been developed in recent years to analyse flexible risers and they are usually very expensive to run. The American Petroleum Institute Committee on the standardization of offshore structures, API (1977) compared eight existing computer programs for a simple standard set of riser problems. The results for the computed dynamic structural stresses were so different that no valid comparison could be made. Discrepancies in computed results were due to the differences in assessing hydrodynamic forces on the riser and in the structural modelling of the risers.

The foregoing reveals that more research work is required to understand the response of flexible risers to hydrodynamic loadings.

In order to advance the study of loading and response mechanisms, it is useful to resort to laboratory experiments with idealized conditions. Once a reliable model of the loading and

response is established, it is possible to extend the model towards the prototype situation by considering the effect of additional parameters on the idealization and empiricism of the adopted model. The ultimate objectives of the model are:

- 1) Every aspect of hydrodynamic loading (such as vortex shedding) should be included.
- 2) The formulation should be reasonably economical to incorporate in numerical integration methods for the non-linear dynamic response.

## 1.2 - Outline of Thesis

The aim of this work was to develop a numerical analysis for flexible risers and to validate this theory by experimental work.

A comprehensive knowledge of hydrodynamics and hydrodynamic loading on small cylinders is required in order to understand and assess the hydrodynamic loading due to wave and current motion on a flexible catenary riser. An introduction and background to this is presented in chapter 2.

Chapter 3 describes the structure of flexible risers. It also reviews the methods adopted to idealize the riser structure and different numerical solution procedures for the governing equations of motion.

Chapter 4 outlines hydrodynamic theory and presents the necessary theory for this work which is used to assess the hydrodynamic loading on a flexible riser.

Chapter 5 is concerned with the development of an explicit vector method of analysis for the non-linear dynamic response of a flexible riser. It also describes the modification of this theory to cater for the formfinding and static analysis of the riser. The technique applied for these static analyses is known as Dynamic Relaxation with kinetic damping.

Chapter 6 concerns the implementation of the above theories in computer programs and the optimization of control parameters in these programs.

Chapter 7 describes the two sets of experimental tests used to validate the theory. The model for the first experiment was a snake chain which had negligible material damping. The aim was to validate the assessment of the hydrodynamic forces on the riser. The second experimental model was a polythene tube filled with mercury and had significant material damping. The models for both series of tests were positioned at various angles in the wave flumes, and the latter series of tests modelled a single catenary riser arrangement incorporating an intermediate mooring buoy. Chapter 8 presents the results and a comparison with the numerical predictions.

Chapter 9 presents the comparison of the results predicted by the numerical analyses with those obtained from the riser program "FLEXRISER" which was developed by Zentech Consultants and has been validated by other well known flexible riser programs.

Chapter 10 is concerned with conclusions and recommendations.

## CHAPTER 2

### LITERATURE REVIEW OF HYDRODYNAMIC LOADINGS ON FLEXIBLE RISERS

#### 2.1- Introduction

This chapter covers the background study of fluid hydrodynamics in section 2.2, and considers hydrodynamic loadings on cylinders in sections 2.3, 2.4 and 2.5. Hydrodynamic loadings on a cylinder can be divided into two distinct components: one consisting of drag and inertia forces and the other of a lift force associated with vortex-shedding. Section 2.3 is concerned with drag-inertia forces on smooth or rough, inclined, flexible, and bundled cylinders which are the practical cases encountered for catenary flexible risers. Sections 2.4 and 2.5 consider respectively the lift forces on cylinders placed in the plane of wave and current motion and on randomly orientated cylinders.

#### 2.2- Fluid Hydrodynamics

##### 2.2.1- Wave Hydrodynamics

A comprehensive description of wave hydrodynamics was presented by Stokes (1847). He assumed that the fluid was incompressible and inviscid and the flow was irrotational. The incompressibility assumption for the fluid yields the continuity equation. The irrotationality of the flow indicates that there exists a scalar function, the velocity potential  $\phi$ , which describes information

about kinematics of the motion. The continuity equation was expressed in term of  $\phi$  which gave the Laplace equation.

A solution for  $\phi$  was obtained by solving Laplace's equation subject to a number of boundary conditions; these conditions being as follows:

- a) bottom boundary condition - there is no flow through the rigid bottom on which the fluid rests. Thus, the velocity of water particles normal to the bottom surface is zero.
- b) free surface boundary conditions :
  - 1) kinematic condition - the fluid particle velocity normal to the surface is equal to the velocity of the free surface in that direction.
  - 2) dynamic condition - the pressure at the free surface is zero. So the unsteady bernouilli equation can be used with a zero pressure term.

The Stokes first order theory which was identical to the linear wave theory was obtained by solving Laplace's equation with linearized boundary conditions. In addition, the free surface boundary conditions were applied at the still water level rather than the unknown free surface.

The linear wave theory predicts the following flow behaviours:

- a) the fluid particles move in close orbits. The orbits are circular in deep waters and elliptical in shallow waters.
- b) the amplitudes of vertical and horizontal velocities

of the particles decrease exponentially with the depth of the particles below the surface.

Stokes introduced a second order solution in which the wave profile and  $\phi$  had second harmonic terms, but the celerity remained as for first order theory. This resulted in sharpening the wave crest and flattening the wave trough. The particle orbits were no longer closed and there was a net velocity in the wave propagation direction, called drift or mass transport velocity.

The higher orders of the Stokes wave theory (3rd and 5th orders) were obtained using perturbation method by Skjelbreia (1958) and Skjelbreia and Hendrickson (1960) respectively.

Since then other wave theories have been formulated. Dean (1970) developed a non-linear wave theory which was based on a stream function rather than a potential velocity concept. This theory was extended up to the 5th order.

The cnoidal wave theory which is used for shallow water waves was introduced by Korteweg and Vries (1895). The wave characteristics were expressed in terms of the Jacobian elliptic function, cn. The solitary wave theory reported by Russell in 1844 can be considered as a limiting case of the cnoidal wave theory in which the crests are so far apart that they can be assumed to be separate from one another.

There are some complex modern wave theories such as Schwartz (1974) and Cokelet (1977) which can predict the flow behaviour more accurately than other theories for all types of waves but the use of the simpler wave theories, which give acceptable

results for engineering requirements, may be preferable from the viewpoint of economic computing of dynamic structural response (Sarpakaya and Isaacson (1981)).

Dean (1970) made a theoretical comparison of several wave theories. The criterion for the comparison was the closeness of fit of the predicted motion to the complete problem formulation. Therefore, he used the error of fit to the free surface boundary conditions in assessing the validity of the wave theories (all theories satisfied the bottom boundary condition). He produced a graphical representation of the suitability of the various wave theories for different water conditions (see fig. 4.3). He recommended the first order cnoidal, the linear, the Stokes fifth order, and the stream function wave theories over the ranges shown in fig. 4.3.

Le Mehaute (1976) presented a graphical representation to illustrate the suitability of various wave theories (fig. 4.4). His graphs include the different orders of the Stokes wave theory which is well suited for use in validating experimental wave flume work. He stated, however, that his graph was not based on any quantitative investigation.

A summary of the works on the comparison of various wave theories on both theoretical and experimental bases was given by Sarpkaya and Isaacson (1981). They concluded that the cnoidal and Stokes fifth order wave theories were most suitable for shallow and deep waters respectively because they are relatively simple compared with modern theories and yet produce sufficient accuracy for most engineering purposes.

Fenton (1979) recommended the use of the conidal wave theory for wave lengths smaller than eight times the water depth, and the use of Stokes fifth order wave theory for other situations.

From the foregoing discussion, it can be concluded that the Stokes fifth order wave theory is ideal for offshore applications. It produces the most realistic wave surface profile which is a crucial factor in designing oil production platforms.

In the computer program which was developed in the present work, the Stokes theories of any order (1-5) and linear wave theory can be adopted.

#### **2.2.2- Interaction of Wave and Current Motion**

In real sea conditions, a body is usually situated in a flow and subjected to currents as well as waves. If the current is in the same direction as the wave propagation, the wave length increases and its amplitude decreases. If the current opposes the wave, the wave gets shorter and steeper. Combinations of waves and currents may be treated in two ways: a) their interaction is ignored and the current is simply superimposed on the wave, or b) the interaction is considered and the problem is treated as a complex fluid-mechanics phenomenon.

There are a few experimental studies on wave and current interaction and a review of these works has been given by Sarpkaya and Isaacson (1981). A summary of the mathematical formulations of these interactions was presented by Peregrine (1976).

Method (a) is usually adopted in offshore engineering to take care of the presence of current action together with waves. The water particle possess an acceleration due to wave motion which has two convective components as well as the local one. The first convective component is a multiple of the horizontal particle velocity due to the wave action and the other component is a multiple of the velocity due to the current. For bodies with drag dominant loading, the inertia force due to convective acceleration components becomes very small, so the convective components of the acceleration are usually ignored.

There are different opinions concerning the estimation of the particle velocities due to wave and current motions above still water level for calculating the forces on offshore structures such as risers. It is well known that the wave theories overpredict the velocities above the still water level but this is considered as an extra margin of safety in practice. The current velocity is usually measured up to the still water level and to adjust this velocity with wave profile, the following different arbitrary techniques are used in industry:

- a) by appropriate mathematical techniques the current velocity profile is either fattened and considered just down to the wave trough, or made thinner and considered up to the wave crest.
- b) the current velocity is considered up to the wave profile. In the case of the wave profile being above the still water level, the current velocity is considered to be constant and has a value equal to that at the still water level.

Method (b) was adopted for this study.

## 2.3 - Drag-Inertia Hydrodynamic Forces on Cylinders

### 2.3.1 - Hydrodynamic Forces on a Vertical Rigid Cylinder

In uniform steady flow the hydrodynamic force on a cylinder is caused by drag action. This force which is called drag force, is a combination of viscous and pressure drag. The viscous or skin friction is caused by the shear stress of the water on the body. The pressure drag which is also termed form drag is the result of a pressure differential caused by boundary layer growth around the surface of the cylinder and its eventual separation from the body.

There would be an analytical solution for the drag force if the momentum equation of fluid mechanics could be solved in the boundary layer, but there are no such solutions available so far. Therefore an empirical drag coefficient " $C_d$ " is introduced to define the drag force. Delany and Sorensey (1953) performed experimental work on a smooth cylinder in uniform steady flow. They showed that  $C_d$  had a value of 1.2 in subcritical flow and had a minimum value of 0.25 in critical flow.

In evaluating hydrodynamic forces on a body in waves, the size of the body compared with the wave length is very important. When the ratio of the cylinder diameter to the wave length is smaller than 0.2, the body is categorized as a small body. The term small body implies that the wave flow remains unaffected by the presence of the body, that is, the cylinder does not diffract the wave flow. To calculate the wave forces on large bodies which

disturb the incident wave, a diffraction theory such as that due to MacCamy and Fuchs (1954) is used. The estimation of the forces on large bodies is outside the scope of the present study, and is not significant for the design of practical riser systems.

Wave loading on small bodies is calculated by using the well known Morison equation. Morison et. al. (1950) proposed that the total force per unit length on a vertical cylinder is the linear sum of two components. The first component is a drag force proportional to the square of the horizontal fluid velocity. The drag force is represented by an empirical drag coefficient,  $C_d$ , having substantially the same value as for steady flow situations. The second component is an inertia force proportional to the horizontal component of the fluid acceleration and having an empirical inertia coefficient,  $C_m$ . The inertia force itself is made up of two parts; one is the pressure of the undisturbed incident wave in the absence of the body which is usually known as the Froude-Krylov force and the other is the pressure disturbance due to the presence of the body which accounts for the added mass effect due to the flow of the water around the cylinder. Therefore the inertia coefficient was defined as "1+added mass coefficient". The force coefficients were obtained experimentally.

The Morison equation has been criticised for representing the force on a body in time-dependent separated flow by a linear-quadratic sum. Numerous attempts have been made either to improve the equation or to present a new equation but so far no success has been achieved. In spite of its theoretical drawbacks, the Morison equation has been used satisfactorily in the offshore

industry, perhaps with due regard to the various uncertainties and safety factors that are incorporated in design. Moreover, considerable amounts of experimental work have been carried out to evaluate the force coefficients,  $C_d$  and  $C_m$ , since the formulation of the Morison equation.

The Morison equation force coefficients are fluid velocity and body geometry dependent. The reason for this is that their values must take care of the complex interaction between fluid and structure and also between drag and inertia forces. Generally, three experimental methods are used to evaluate  $C_d$  and  $C_m$  values as follows:

- 1 - placing body in a controlled wave flume
- 2 - placing body in a harmonic oscillating flow
- 3 - oscillating body in still water.

Schemes 2 and 3 provide a flow with simple harmonic velocity. Since in waves the velocity is depth dependent, the horizontal flow simulated by schemes 2 and 3 can be considered as the wave motion around a particular section of a vertical cylinder, while bearing in mind that the Morison equation expresses the sectional force on the cylinder in terms of the horizontal fluid velocity and acceleration at that section. The advantage of the second and third methods over the first method is that the high Reynolds numbers (Re) which exist in practice can be simulated.

It is common practice to use constant average values of  $C_d$  and  $C_m$  for the whole cycle of the wave rather than local values. There are several analytical methods to calculate the average values of  $C_d$  and  $C_m$  for the experimentally measured forces of the whole cycle as follows:

- 1 - Fourier-averaging technique - the force is expressed in fourier series form and compared with the actual measured force to obtain the average values of  $C_d$  and  $C_m$ .
- 2 - Least squares method - the equations for  $C_d$  and  $C_m$  are obtained by using the least squares method to minimize the errors between the measured and the calculated forces.
- 3 - The values of the coefficients obtained by considering the measured and the calculated forces at the points corresponding to the maximum velocity and the maximum acceleration.
- 4 - Writing the Morison equation once for the maximum force and once for the zero force with the corresponding velocities and accelerations.
- 5 - Calculating  $C_d$  over a short wave segment in which the drag force is dominant, and  $C_m$  over a short segment in which the inertia force is dominant.

Morison et. al. used the 3rd averaging scheme to calculate the average values of  $C_d$  and  $C_m$  for a pile in small amplitude waves. The first and second averaging schemes are the most commonly used experimental methods to evaluate  $C_d$  and  $C_m$ .

A comprehensive summary of data on force coefficients has been presented by the British Ship Research Association (1976) and also by Hogben et. al. (1977). A few of the important papers will be discussed here.

Keulegan and Carpenter (1958) performed experiments with cylinders held horizontally at the node of a standing wave. They correlated the fourier average values of the coefficients with their period number. Their period number, which is known as the Keulegan Carpenter number,  $KC$ , expresses the ratio of the particle motion amplitude to the cylinder diameter. The authors produced graphs for the variation of  $C_d$  and  $C_m$  with  $KC$ . They found a critical range at which  $C_d$  and  $C_m$  reached their maximum and minimum values respectively at  $KC$  values around 15. In this range the correlation between the measured force and that predicted by the Morison equation was poor. The Fourier-averaging technique was used to obtain the values of  $C_d$  and  $C_m$ . A residual force function which contained the higher harmonics of  $C_d$  and  $C_m$  was introduced. This residual force was larger for the critical range of  $KC$  numbers. These higher harmonics of  $C_d$  and  $C_m$  were ignored in the evaluation of the  $C_d$  and  $C_m$  values. The authors also did not find any variation of  $C_d$  and  $C_m$  with Reynolds number,  $Re$ , and thus concluded that the coefficients were independent of  $Re$ .

The Keulegan-Carpenter number is an important factor in assessing the relative magnitudes of the drag and inertia forces. At low values of  $KC$ , 95 percent of the forces exerted on the body are inertial, whilst for intermediate values of  $KC$  (i.e. in the critical region), the inertia and drag forces are equally

important. Finally at high values of KC, 95 percent of the forces are of drag type.

Sarpkaya (1976a) performed a series of experiments on horizontal cylinders in uniform oscillatory flow by means of a 'U' tube water tunnel. He introduced another nondimensional variable, known as the frequency parameter,  $\beta$ , which is the ratio of Re to KC. He showed the dependence of the force coefficients on KC as well as Re. However, the coefficients were found to be independent of Re for values below about 20,000, and this may explain the conclusion reached by Keulegan and Carpenter (1958). The results for the coefficients were the same as the Keulegan and Carpenter values.

Sarpkaya and Isaacson (1981) presented the third harmonic of the residual force function, which was introduced by Keulegan and Carpenter, as the third term in the Morison equation. They expressed the coefficient of the new term in terms of  $(2 - C_m)$ . The authors demonstrated that by using the new modified Morison equation, the r.m.s. value of the residual forces, which was presented previously by Sarpkaya (1976a), reduced by 60 percent in the critical range of KC numbers. They suggested that additional work along these lines may lead to a substantial improvement of the Morison equation in the critical region of KC numbers.

Garrison et. al. (1977) performed a series of tests in which a cylinder was oscillated through still water. After making allowance for the lack of the Froude-Krylov force in the inertia term for this type of flow, the variations of  $C_d$  and  $C_m$  with Re were found to be almost the same as Sarpkaya's results (1976a).

Susbielles et. al. (1971) carried out some experimental work on a vertical cylinder in a wave tank. They used the harmonic flow results of Keulegan and Carpenter to calculate the local wave forces on the cylinder and obtained agreement with measured forces to within 10 percent.

Chakrabarti (1980a), performed a series of tests on a small section of fixed vertical cylinder in a wave flume. The wave kinematics were calculated using the fifth order stream-function wave theory and the least squares averaging technique was used to calculate the average values of  $C_d$  and  $C_m$ . The values of the force coefficients were in good agreement with those obtained from the simple harmonic flow by Sarpkaya (1976a) for values of  $KC < 40$ , except that for values of  $KC < 15$  the values of  $C_m$  were higher. Since low and limited values of  $Re$  were used in the experiment, the authors could not establish the variation of the force coefficients with  $Re$ . The total force on the cylinder was measured and compared with the calculated one. In calculating the total force along the cylinder, the force coefficients were taken as functions of  $KC$  numbers and allowed to vary over the length of the cylinder. In each case the values for the coefficients were obtained from the mean  $C_d$  and  $C_m$  curves produced in the experiment.

Sarpkaya (1976a and 1976b) presented comprehensive values of  $C_d$  and  $C_m$  for a wide range of  $Re$  and  $KC$  numbers for both smooth and rough cylinders. Several experiments were carried out on prototype cylinder models in the following sea environments: Davenport on The Pacific coast, the Gulf of Mexico, Bass Straits in Australia, Christchurch Bay, and the B.P. Forties Field

production platform in the North Sea. The different methods used to analyse the measured random forces were comprehensively discussed by Pearcey and Bishop (1979) and will not be discussed here. The data obtained from these experiments for the force coefficients showed a very wide scatter.

Water particle movements in waves are orbital and their velocities decay exponentially with distance away from the free-surface. This means that the values of  $Re$  and  $KC$ , and hence also  $C_d$  and  $C_m$ , are continuously changing along a vertical cylinder in waves. Bearing in mind that in moving away from the free surface the hydrodynamic forces on a cylinder reduce almost in proportion to the square of the velocity decay, the change in the values of the force coefficients will not be very important. In natural flows there are current flows as well as wave flows so the Reynolds numbers for such flows are very high. Hence the variation of the force coefficients at high  $Re$  numbers are very small, and the changes in the coefficients with depth can be neglected. For this reason, in most riser programs constant values for the force coefficients, which are obtained from available tables corresponding to the maximum values of  $Re$  and  $KC$  along the riser, are used. The maximum values of  $Re$  and  $KC$  along the riser usually occur near the free surface.

### **2.3.2- Hydrodynamic Forces on a Rough Cylinder**

In a marine environment, growths such as barnacles, shell fish, and seaweeds can quickly build up on most surfaces, causing change in the roughness of the riser as well as its diameter, which should be taken into consideration in design. Heaf (1979)

presented a comprehensive discussion of the effect of marine growth on the performance of fixed offshore platforms in The North Sea.

Several researchers such as Fage and Worsap (1929), Roshko (1961), Achenbach (1971), Szechengi (1975), and Miller (1977) studied drag force on a rough cylinder in steady flow at high Re numbers. Achenbach (1971) demonstrated that increasing roughness of a cylinder in steady uniform flow reduced the critical Re at which flow separation occurs. The graph of  $C_d$  versus Re was presented. The results showed that at the subcritical region, the roughness of the cylinder didn't effect the values of  $C_d$ . For higher values of Re, the values of  $C_d$  remained constant and greater than the value of  $C_d$  corresponding to the postcritical region for a smooth cylinder.

Sarpkaya (1976b) carried out experiments to observe the effects of roughness of cylinders in an oscillating flow. The results for  $C_d$  showed a great increase in value compared with those obtained for a smooth cylinder.

Sarpkaya and Isaacson (1981) presented graphs of  $C_d$  and  $C_m$  versus roughness Reynolds number for constant values of KC and several different roughness heights. The Roughness Reynolds number was defined as having the same formulation as Re except that the cylinder diameter term was replaced by the roughness height. They suggested that these graphs accounting for the effective diameter of rough cylinders might be used to calculate the forces on the cylinders.

Matten (1977) performed tests on cylinders in small amplitude waves at the National Maritime Institute in order to observe the effect of roughness by comparing the ratio of the total force acting on a rough and a smooth cylinder situated some distance apart. He worked mainly in the critical region for KC but his results for  $C_D$  were so scattered that he was unable to present any drag or inertia coefficient data. Matten did, however, show that for a rough vertical cylinder in waves, the transition occurred at relatively very low Re whilst this was not the situation in uniform steady flow. He stated that the reason for early transition was the existence of axial flow along the cylinder which was caused by the orbital movement of water particles. His evidence for this statement was the unpublished results of an experiment cited by Miller (1977) for a horizontal cylinder, identical to his own, placed parallel to the wave crest but just beneath the water surface so that it always remained submerged. The results of the experiment showed that transition did not occur at low values of Re, as it did for a vertical cylinder. This observation indicated that the reason for the early transition on the vertical cylinder could only be the existence of the axial flow.

Gaston and Ohmart (1979) placed a smooth and a roughened cylinder, one at a time, in a big wave tank under conditions of regular and random waves. The in-line moment was measured and the water particle kinematics were predicted from stream function wave theory. Then by using the least-squares averaging method, the force coefficients were determined. Comparison of the results showed that the drag coefficient was significantly affected by the roughness. In fact, the change from the smooth to the rough

surface approximately doubled the drag coefficient. Further increase in the roughness had a lesser effect than the initial change from a smooth to the first rough cylinder. They suggested some values for  $C_d$  and  $C_m$  for a smooth cylinder and for three cylinders each having a different roughness height.

Garrison (1980) criticized the results obtained by Sarpkaya (1976b) for  $C_d$  at high Re numbers for rough cylinders. He contradicted Sarpkaya's statement that  $C_d$  became constant and independent of Re for  $Re > 1.5 \times 10^5$ . Garrison oscillated rough cylinders in still water and the results of the experiment showed a sharp decrease in  $C_d$  values for  $Re > 2 \times 10^5$ . Similar results were obtained from ocean tests on a structure which were presented by Dean and Aagaard (1970), and Kim and Hibbard (1975).

Garrison suggested that the reason Sarpkaya obtained high values of  $C_d$  for rough cylinders in flows with high Re, (which were not revealed in real sea tests), might be caused by wake blockage in the test U-tube. That is, when the cylinder passed back through its own wake the drag force on the cylinder was affected by the presence of the wake, and the stronger the wake, the greater was the drag force generated. The water tunnel walls tended to limit the inflow of the surrounding fluid into the wake, so causing a reduced rate of wake dissipation. Thus at successive cycles the wake was pronounced more than it would have been if the fluid was of an infinite extent.

### 2.3.3- Hydrodynamic Forces on an Inclined Cylinder

There are inclined members as well as vertical members in offshore structures, such as inclined bracing members in a jacket-type platform and catenary flexible risers in a semi-submersible platform, etc. Little experimental work has been carried out in this area and more research work is required in order to understand the consequence of cylinder orientation. However, four methods have been established to modify the terms in the Morison equation to calculate the forces exerted on inclined cylinders. An appraisal of these schemes, reported in detail by Wade and Dwyer (1976), is given in the following section.

In the Morison equation, the horizontal components of velocity and acceleration of water particles due to waves which are normal to the axis of a vertical cylinder, are used to calculate the forces on the cylinder. Thus the force on the cylinder is considered to be solely a function of the normal component of the hydrodynamic force. The tangential component which is proportional to the vertical velocity of the water particles is ignored. Borgman (1958) used the same analogy and showed how the Morison equation for a vertical cylinder in waves could be extended to the case of a generally oriented cylinder. He derived expressions for velocity and acceleration normal to the axis of the inclined cylinder in terms of the horizontal and vertical velocities and accelerations of water particles.

The above assumption was partially verified by Pote (1950). He performed a series of experiments at The David Model Basin to

determine hydrodynamic forces on an inclined cable under steady flow condition. The normal and tangential forces on the cable were measured. The results showed that the measured normal force could be represented by the usual drag force equation using the velocity component normal to the cable axis. It was also shown that the measured tangential force which was created by the skin friction action had a magnitude less than two percent of the measured normal force, so it could be ignored. This normal velocity concept was confirmed by Watson (1953) when carrying out a series of towing tests on submerged wooden dowls. Glenn (1966) also confirmed this concept by placing an inclined cylinder in a steady flow.

Chakrabarti et. al. (1975,1977) carried out a series of experiments with a small inclined tube in a wave flume and calculated the force coefficients by using Borgman's extended Morison equation. They presented graphs of force coefficients versus Keulegan-carpenter number which were calculated by using the maximum normal velocity. The above mentioned graphs were produced for different orientation angles of the cylinder. The authors also presented a second set of graphs for the ratio of the normal force over the in-line force versus KC. They suggested that the in-line force on an inclined cylinder may be calculated using the first set of graphs which gives the force coefficients. Then the normal force on the cylinder may be calculated by multiplying the in-line force by the ratio obtained from the second set of graphs. The values of Re used by the authors were limited to the subcritical range so they could not establish the dependence of the force coefficients on Re values.

A comparison of the results for the force coefficients obtained by Chakrabarti et al. (1977) for an inclined cylinder with those obtained by Sarpkaya (1976) for a vertical cylinder in harmonically oscillating flow was presented by Sarpkaya and Isaccson (1981). The comparison showed that the values of the force coefficients at the corresponding KC and frequency parameter, for both cases, were nearly identical. The authors thus suggested that the forces on an inclined cylinder might be calculated using Borgman's extended Morison equation with the force coefficients obtained from the graphs presented by Sarpkaya (1976a) or the available tables for a vertical cylinder. In obtaining the force coefficients, the maximum Re and KC values were calculated using the maximum normal velocity of the water particles. Hogben et. al. (1977), and a publication by the British Ship Research Association (1976), also suggested the same procedure.

#### **2.3.4- Hydrodynamic Forces on a Flexible Cylinder**

When a cylinder is flexible, its motion will not be negligible. Therefore a complex fluid-structure interaction effect needs to be considered in the analysis. Very little work has been carried out in this area and research is required in order to understand the effect of the cylinder flexibility on its response in currents and waves.

Two schemes have been suggested to calculate the forces on flexible risers. The first one is the "Relative Velocity" method which uses a modified form of the Morison equation. This is

constructed by replacing the kinematics in the original Morison equation by the vectorial difference between the kinematics of the incident fluid flow and the resulting kinematics of the cylinder. The force coefficients  $C_d$  and  $C_m$  may be found from the data available for rigid cylinders provided that the values of the corresponding Reynolds number and Keulegan-Carpenter number are calculated using the maximum relative velocity rather than purely the velocity of the water particles. This procedure was introduced by Mathotra and Penzien (1970) and Berge and Penzien (1974).

The second method is the "independent flow field" model which is based on the superposition of two independent flow fields, a far field which is unaffected by the cylinder motion and a near field resulting from the cylinder motion. The force equation for each flow field is expressed in the same form as the Morison equation with each of them having its own individual force coefficients. The force coefficients for the first flow have the same values as for a rigid cylinder in the same flow, and for the second flow they have the same value as a rigid cylinder vibrated in still water. This scheme was originally postulated and investigated for a steady flow condition by Moe and Verley (1978, 1980) and subsequently extended to a wave flow situation by Laya and Connor (1981).

Laya and Connor (1981) carried out a numerical comparison between the "relative velocity" model and the "independent flow field" model using a vertical flexible pile as the test case. They concluded that the independent flow field model always predicted a lower hydrodynamic drag damping than the relative velocity

model. The difference in the damping value increased with the wave height. Therefore in extreme sea conditions which are assumed in the design of members of an offshore structure, the applicability of the independent flow field model diminishes. The results obtained from both models in the inertia dominant region, in which the drag forces were negligible, were in close agreement. Finally for intermediate sea conditions which must be considered for fatigue life design, the response predicted by the two models was significantly different. The authors believed that the relative velocity model predicted a higher hydrodynamic damping than the actual one. They therefore suggested that the applicability of the two models needed to be established by further experimental work. The relative velocity method, which is also known as the modified Morison equation, is usually used in industry.

### **2.3.5- Hydrodynamic Forces on Cylinder Groups**

Numerous studies have been carried out to evaluate the hydrodynamic forces on a group of cylinders in order to understand the real response of offshore structures such as production risers, piles, etc. due to fluid loading. This complex problem was looked at initially by observing the flow interference between only two cylinders in various arrangements.

Zdravkovich (1977) presented a careful review of flow interference between two identical cylinders in various arrangements in steady flow. The arrangement of the cylinders was categorized into three types:

- a) tandem arrangement - one cylinder behind the other
- b) side-by-side arrangement - two cylinders placed beside each other so that the line joining the axes of the cylinders was normal to the flow direction
- c) staggered arrangement - The staggered angle was defined as the angle between the flow and the line joining the centres of the two cylinders.

In tandem arrangement, it was shown experimentally that there was a critical spacing ratio for the two cylinders of 3.5. The spacing ratio was defined as the ratio of the distance between the centres of the cylinders to the diameter of the cylinder. Drag forces on the cylinders were affected strongly by the tandem arrangement and were sensitive to the spacing of the cylinders. Below the critical spacing, there was strong interference between the cylinders. The upstream cylinder contributed most of the drag force; with the drag force on the downstream cylinder being reduced partly by shielding and partly by the occurrence of earlier transition in the boundary layers due to turbulence. At the critical spacing ratio, the flow became discontinuous and, for the upstream cylinder, this caused a jump in the drag coefficient, commencement of vortex shedding, and a drop in the base pressure. For the downstream cylinder, the base and the side pressure coefficients dropped, the vortex shedding frequency jumped, and the gap pressure and drag coefficient increased suddenly. Beyond the critical spacing, the downstream cylinder had a negligible effect on the upstream cylinder. But, even for large spacing, the downstream cylinder was affected by the presence of the upstream cylinder and had a smaller drag

coefficient than that for a single cylinder. In general, for any spacing, the total drag force on the group was smaller than the sum of the drag forces on the two isolated cylinders.

In the side-by-side arrangement, the interference between the two cylinders was negligible for a spacing ratio greater than 5. As the spacing ratio was decreased from 5 to 2.2, the drag coefficient was slightly increased. Below the spacing ratio of 2.2, the flow became bistable and this bistable nature of the flow between the cylinders resulted in two values of drag coefficient rather than a single one. This phenomenon was caused by mutual interference of the vortices on the adjacent sides of the vortex streets. The sum of the bistable high and low drag coefficients was often less than twice the drag coefficient for an isolated cylinder.

In the staggered arrangements, the drag force on the upstream or downstream cylinders was smaller than that on an isolated cylinder, except when the orientation of the cylinders approached the side-by-side arrangement.

It is important to note that in the above cases resonance of the cylinders was avoided.

Horner (1965) stated that in steady subcritical flow, the interaction between two cylinders in the side-by-side and tandem arrangements could be neglected if the spacing ratios were respectively more than three or four.

The interaction effects among three cylinders in an array were reported by Dalton and Szabo (1976). They observed a strong mutual interference between the middle and downstream cylinders

but only a partial interaction between the upstream and downstream cylinders. The drag forces on the middle and downstream cylinders were smaller and more sensitive to orientation of the flow direction than the drag on the upstream cylinder.

Mair and Maull (1971) measured the forces on a cylinder in a group of similar cylinders as a function of the flow direction. They showed that over a small range of flow angle relative to the array, the force acting on the cylinder could change by nearly 100 percent.

Løken et. al. (1979) performed a series of tests on a group of cylinders which had a core cylinder surrounded by smaller cylinders in a ring arrangement. They towed the cylinders in a uniform steady flow at the Danish Hydraulic Institute (DHI). The results showed that the upstream cylinders experienced more drag than the downstream cylinders. The most shielded cylinders induced the smallest drag forces. A graphical representation of the relative distributions of the maximum drag force on the cylinders was presented.

It is worthwhile to mention that methods such as the method of images which was used by Dalton et al. (1971) and Yamamoto (1976), and the linear potential theory (including wave diffraction theory) which was used by Spring et al. (1974) and Chakrabarti (1978) to calculate the inertia coefficient for a group of cylinders, are only applicable to cylinders in unseparated flows. These methods are therefore irrelevant to a separated flow condition which is the one that exists around

cylinders in natural sea conditions.

Relatively few studies have been carried out on a group of cylinders in oscillating flow. In this type of flow, the interaction between cylinders depends on; a) the spacing ratio (as in the case of steady flow) and b) the amplitude of the oscillating flow which is proportional to the Keulegan-Carpenter number. If the amplitude of the oscillating flow is very large, the flow condition will be similar to the steady flow and so dependence of the interaction between the cylinders on the Keulegan-Carpenter number can be ignored. At the other extreme, when the amplitude of the flow is very small the interaction of the cylinders can be completely neglected (Heideman and Sarpkaya (1985) ).

Sarpkaya (1980) placed two cylinders in various arrangements and spacings in his u-shaped water tunnel to observe the effects of interaction between the cylinders in oscillating flow. He concluded that in the side-by-side arrangement, for a spacing ratio greater than 2.5, the cylinders responded as if they were independent. The results for the drag coefficient in tandem arrangement were in conformity with those reported by Zdravkovich (1977) for cylinders in steady flow.

Bushnell (1977) carried out a series of tests on two cylinders as well as arrays of 3x3 cylinders in oscillating flow. In both cases the spacing ratio for the cylinders was 3, and the observed drag forces decreased substantially on the shielded cylinders. The oscillating flow was applied at 0, 20, and 40 degrees to the centre line of the array, and it was found that interaction between the cylinders increased with increasing obliqueness of

the flow. Bushnell suggested that if a high Reynolds number single cylinder drag coefficient was applied throughout in design, the array would have a margin of safety against maximum drag loading due to interference effects.

Sarpkaya (1979) performed experiments on two groups of 15 outer and one central cylinders in oscillating flow. He introduced expressions for the mass and drag coefficients of the tube-bundle using the Fourier averaging method. The expressions were found to be functions of the Keulegan-Carpenter number, KC. He also showed that the force coefficients were independent of the Reynolds number. In general, the total drag on the group was 10 percent less than the sum of the drag forces on the individual cylinders. The inertia coefficient was considerably larger than that predicted by the potential theory and this indicated that some fluid mass was entrapped within the bundle as a consequence of "solidification" induced by the group configuration.

Ross (1959) placed one cylinder on each side of a test cylinder in a large wave tank. The results indicated that the wave force increased significantly only when the spacing ratio between two cylinders was less than 2.

Chakrabarti (1979) placed an array of 2,3,and 5 cylinders in a separate series of tests in a wave tank. All the cylinders were equally spaced in an array, and various spacing ratios and flow directions were used in the experiments. The total force on the cylinders plus the forces on 1-foot sections of two adjacent cylinders were measured. The maximum non-dimensional forces as functions of KC, relative spacing, and the flow angle were

presented. It was stated that interaction among the cylinders virtually disappeared at a spacing ratio above 5.

Verley and Every (1977) conducted a series of tests on flexible cylinders in a wave tank to observe the effect of flexibility on the cylinder responses. They measured the additional response of a flexible cylinder compared with that of a similar rigid cylinder. This was achieved by subtracting the measured response of the rigid cylinder from that measured for the flexible cylinder (placed next to the rigid cylinder in the tank). Experiments were also carried out on two flexible cylinders in both side-by-side and tandem arrangements, and on a group of 12 flexible cylinders in a 3x4 matrix with a spacing ratio of 2. The results indicated that the type of interaction effects for the flexible cylinder groups was the same as that for similarly arranged rigid cylinders.

Beynet and Frase (1982) carried out large scale wave loading experiments on four catenary risers which were used as the production risers in the Cadlao field. The most important observation was that the parallel risers did not tangle or impact with each other even under the severest test conditions and large surface buoy motions.

In common platform design practice, the flow interference in a group of cylinders is usually ignored and each cylinder is modelled as an isolated cylinder. The total force on a group is obtained by adding the forces on each isolated cylinder of the group (as suggested by Bushnell (1977)). This isolated modelling was verified in an ocean test conducted by Beckmann and Merwin (1979) on a 3x7 rectangular matrix of cylinders with spacing

ratios of 3.6 in one direction and 5.4 in the other direction. The validity of the modelling was also confirmed in laboratory tests by Hansen and Knudson (1980) using a group of roughened cylinders in an oscillatory flow. Heideman and Sarpkaya (1985) carried out experiments on rough cylinders in oscillatory flow and concluded that the isolated model was good for arrays with spacing ratios greater than 5. Sea test observations made by Beckmann and Merwin (1979) suggested a reduction of this ratio to 3.6. When the spacing ratio of the cylinders in a group is smaller than this limit, the interaction between cylinders is found to be very strong and neglect of the interference effects would therefore be unrealistic; the interaction between closely spaced cylinders causing a significant decrement in the total force on the group. Conversely, it is possible that vortices in the wake of upstream cylinders may excite a dynamic response of the downstream cylinders, leading to an effective increase in the forces computed from the Morison equation. In this case only reliable experiments can guide the designer (Sarpkaya and Isaacson (1981) ).

### **2.3.6. - Hydrodynamic Forces along a Cylinder**

The Morison equation gives only the forces normal to the longitudinal axis of a cylinder and assumes that the forces along the member are negligible. This is valid if the body has only a small skin friction value, which is true for most offshore structures with clean surfaces. The accumulation of marine growth on cylinders in real sea conditions may, however, invalidate this assumption. In such cases the forces along a cylinder should be

evaluated either by experimental means or by assuming values for the skin friction coefficient which are usually approximately one tenth of the drag coefficient (Hallam et al. (1978) ). The skin friction coefficient depends on the Reynolds number and the relative roughness height of the cylinder. For given values of  $Re$  and relative roughness height of a cylinder the skin friction coefficient can be obtained from the Moody's diagram (see Massey (1979)). The forces along the cylinder are included in the present work.

#### **2.4- Hydrodynamic Loadings Induced by Vortex-Shedding on Cylinders Placed in the Plane of the Wave and Current Motion**

When a fluid flows around a stationary cylinder, it forms a boundary layer around the cylinder surface. This boundary layer is laminar in the upstream portion of the cylinder surface but it becomes turbulent at some point on the downstream surface. At this point, the turbulent boundary layer breaks away from the surface and forms two separate shear layers which, eventually, roll into vortices and form the cylinder wake. Each time a vortex is shed, it alters the pressure distribution around the cylinder surface. Therefore, the cylinder experiences a time varying force due to vortex-shedding in addition to that calculated by the Morison equation. The forces induced by this vortex-shedding effect act in a direction normal to the plane of the cylinder in contrast to those calculated from the Morison equation.

#### 2.4.1- Forces on a Rigid Cylinder Induced by Vortex-Shedding in Steady Flow (No Vibration)

A great deal of research has been carried out to understand the phenomenon of vortex shedding from a stiffly mounted cylinder in steady flow. Strouhal (1878) discovered the relation between the vortex shedding frequency and the flow velocity. He made the frequency dimensionless by dividing it by the flow velocity and multiplying by the diameter of the cylinder. This dimensionless frequency is known as the Strouhal number.

Although the Strouhal number was considered to be a constant for a wide range of velocities, Rayleigh (1896) showed that it is a function of the Reynolds number. Since then, various studies have been carried out to define the relationship between the Strouhal number and various Reynolds number regions and this has been reviewed by Narris (1964) and Sarpkaya and Isaacson (1981).

Bishop and Hassan (1964) measured the forces caused by vortex-shedding on a vertical rigid cylinder in steady flow. They concluded that the vortex-shedding caused two types of forces as follows:

- 1) Lift force (transverse force) - this force was produced in a direction normal to the flow direction and it had a frequency equal to the vortex-shedding frequency ( $f_v$ ).
- 2) In-line force - this force was in the flow direction and had a frequency of twice  $f_v$ . It was, however, one order of magnitude smaller than the lift force.

The fact that the magnitude of the in-line force is relatively small was also substantiated by Mcgrego (1957), and Fung (1960).

#### 2.4.2- Vortex-Excited Vibration of Cylinders in Steady Flow

When a cylinder is flexible or flexibly mounted, the force due to vortex shedding can cause the cylinder to vibrate at or near to one of its natural frequencies. This phenomenon is called lock-on or synchronization and it occurs when the frequency of the exciting force coincides with one of the natural frequencies of the cylinder. The oscillation of the cylinder at lock-on situations strengthens the vortices, by extracting energy from the fluid, and increases the correlation length of the vibration along the cylinder.

Work in this field was given great impetus as a result of the vibration observed during construction of the Immingham Jetty in 1968-1969 (see Sainsbury and King (1971) ). Tidal currents caused the supporting piles to vibrate in the direction of the fluid flow. As a result, Wooton (1972) carried out full scale tests at the Immingham site, and King (1974) performed model tests in a laboratory.

King used two parameters, reduced velocity ( $V_r = V / f_n \cdot D$ ) and reduced damping ( $\delta_r = 2m\delta / \rho D^2$ ) to describe the vibration of the cylinder due to vortex shedding.

Where  $V$  = Velocity of water particles in the in-line direction

$f_n$  = natural frequency of cylinder

$D$  = diameter of cylinder

$m$  = mass of cylinder and its contents also including  
added mass per unit length of cylinder

$\delta$  = logarithmic decrement of cylinder damping

$\rho$  = density of fluid

Oscillation in the in-line direction occurred for  $V_r < 3.8$ . This happened within two regions. The first one was in the range of  $1.25 < V_r < 2.5$ , with maximum amplitude occurring at  $V_r \approx 2.1$ . The second region was in the range  $2.7 < V_r < 3.8$  with maximum amplitude at  $V_r \approx 3.2$ . The first instability region was accompanied by symmetric vortex shedding and the second region by alternate vortex shedding. It was shown that the in-line excitation was suppressed for  $\delta_r > 1.8$ . Transverse excitation occurred for  $V_r > 4.5$  by alternate vortex shedding with maximum amplitude falling within the range of  $6.5 < V_r < 8$ . No excitation in the transverse direction was observed when  $\delta_r > 10$ .

A great amount of work has been carried out to study the oscillations of flexible cylinders in steady flow. A review of this work was given by King (1977) and Sarpkaya (1979).

Skop et. al. (1977) presented a design chart to calculate the inline steady drag amplification due to resonant vortex-excited oscillation.

Hallam et. al. (1978) also presented a design chart to calculate the response of a single cylinder or array of nearly rigid cylinders due to vortex shedding. They gave the condition for suppressing the vortex-excited oscillation of the group as equivalent to  $\delta_r > 30$ .

In general, the step-by-step procedure of these design charts was: a) compute/measure vibration properties of the cylinder (natural frequency, normal modes, modal scaling factor etc.) ; b) compute strouhal frequencies and test for critical velocities at which the resonances occur,  $V_{crit.}$ , (in-line and cross-flow) ; c) test for reduced damping,  $\delta_r$ . If the flow velocity is greater than  $V_{crit.}$  and the reduced damping is smaller than the limiting value given above, then oscillation is predicted to occur. Subsequent operations are: 1- compute the maximum amplitude of the oscillation, 2- calculate the increment of the steady drag force in the in-line direction due to vortex shedding using the given relationship with previously computed amplitude, 3- compute the new stresses and check for the critical stresses and the fatigue life. For great detail with some practical examples, refer to the paper presented by Griffin (1981).

The correlation lengths of a vortex along a cylinder depends on  $Re$ , turbulence, aspect ratio (L/D), and surface roughness. Typical values for a stationary cylinder were summarised by King (1977). As was mentioned before, in the lock-on condition the correlation length increases. This increment was measured by Toebe (1969) and Ramberg and Griffin (1976).

Several mathematical oscillatory models have been presented to simulate the results obtained from experiments. These models do not include the analysis of the flow field and the fluid-mechanics justification arguments but they have the ability to produce results which are qualitatively similar to those obtained experimentally. A general review of existing mathematical models is given by Parkinson (1974) and Sarpkaya and Isaacson (1981).

The idea that vortex shedding vibration might be modelled by a simple non-linear oscillator equation was suggested by Birkhoff and Zapantonello (1957), and reinforced by Bishop and Hassan (1964) through their observation of an oscillating cylinder in a uniform flow. This idea was pursued by Hartlen and Currie (1970). They used a Van der Pol-type non-linear oscillator for the lift force, coupled to the cylinder motion by a linear dependence on cylinder velocity. The model had three dimensionless parameters;  $\alpha$ ,  $\beta$ , and  $b$ .  $\alpha$  and  $\beta$  were Van der Pol coefficients and  $b$  was the interaction parameter between the fluid and the cylinder. These coefficients were obtained experimentally and they varied from one experiment to another.

Other models were given by Skop and Griffin (1973) and Iwan and Blevins (1974). Initial studies were conducted using Iwan and Blevins model for vortex shedding by Nordgren (1982). But, in general, the wake oscillator models have not been developed to the stage where they can represent a practical design procedure (Griffin and Ramberg (1982)).

#### 2.4.3- Forces on Rigid Cylinders due to Vortex-Shedding in Waves

Many investigations have been carried out in order to understand the characteristics of the forces induced by vortex shedding in oscillatory flows (simple harmonic oscillating flows or waves). A summary of these studies was given by Sarpkaya and Isaacson (1981). The studies indicated that the induced forces are dependent on three parameters, a) Keulegan carpenter number, b)

Reynolds number, c) wave depth parameter ( $kh$ ), where  $k$  = wave number, and  $h$  = water depth. The fluctuating transverse force (lift force) can be of similar magnitude to the flow induced in-line force. The predominant frequency of the lift force is usually a multiple of the wave frequency and mainly depends on KC number.

Bidde (1971) measured extensively the lift forces on a vertical cylinder in waves. He concluded that the lift forces were dependent on KC and that the lift frequency was twice the wave frequency for KC values up to 20. Bidde's work was extended to higher values of KC by Wiegel and Delmonte (1972), who found that the lift force frequency was three times the wave frequency for these higher KC numbers.

Isaacson and Maul (1976) performed experiments on rigid vertical cylinders in waves. They presented a relationship between lift force coefficient and surface KC as a function of wave depth parameter ( $Kh$ ).

Sarpkaya (1976a) measured the lift forces acting on smooth and rough cylinders for a wide range of  $Re$  and KC and relative roughness. He presented a relationship between the lift coefficient and KC as a function of his frequency parameter ( $\beta = Re/KC$ ).

Lift force on a rigid inclined cylinder was measured by Chakrabarti et. al. (1977), who used the velocity component normal to the cylinder to derive the relationship between lift coefficient and KC.

There have been few studies concerning the effect of surface roughness of a cylinder on vortex-excited oscillation. Sarpkaya (1979c) measured the total transverse force on a sand-roughened oscillating cylinder and compared it with a similar smooth cylinder. A Substantial increase in the total force coefficient was observed due to the roughness. Additional study, however, is required to determine which components of the total transverse force are amplified due to the roughness. The components of the transverse force are: a) the exciting force component, by which energy is transferred to the cylinder, b) the reaction, or damping force, which is exactly out-of-phase with the velocity, c) the added mass force, which is exactly out-of-phase with the acceleration of the cylinder, and d) the flow-induced inertia force ( Griffin (1981) ).

#### 2.4.4- Vortex-Excited Vibration of Flexible Cylinders in Waves

The dynamic responses of flexible or flexibly mounted cylinders in oscillating flows are not sufficiently understood. This is mainly due to the complexity of the phenomena, because of a) the oscillatory nature of the incident flow, b) variation of the incident flow with depth in waves (possessing a vertical velocity component).

Sarpkaya and Rajabi (1979) studied the transverse response of an elastically-mounted cylinder in harmonic flow. They attempted to analyse their experimental results in the same manner as for a steady flow but encountered too much scatter in these results. Their main observation was that the response of an oscillating

cylinder was necessarily dependent on the dynamics of the same flow past a similar fixed cylinder.

They introduced a response parameter as  $R_p (= m \xi / \rho D^2 CL_0)$ , where  $m$  = actual mass of cylinder per unit length,  $\xi$  = damping ratio,  $CL_0$  = lift coefficient for the similar fixed cylinder,  $\rho$  = fluid density, and  $D$  = diameter of the cylinder. Their results indicated the following:

- a) lock-on occurred when the reduced velocity,  $V_r (= V_m / f_n D)$  was about 5.5, where  $V_m$  = maximum water particle velocity in the drag-inertia force direction, and  $f_n$  = natural frequency of cylinder. In this condition the lift force was nearly double that for a fixed cylinder.
- b) the relative amplitude of oscillation was a unique function of  $R_p$ .

Zedan et. al. (1980) studied experimentally the transverse oscillation of a cantilevered cylinder in waves. The results showed that the lock-on occurred at a reduced velocity,  $V_r$ , somewhere between 5.5 and 7.5 depending on wave depth parameter,  $Kh$ . Zedan and Rajabi (1981) used the results of Zedan et. al. (1980) and established the characteristics of the lift force in that experiment. They compared the results with those obtained by Sarpkaya and Rajabi (1979) in harmonic flow. Their results showed the following:

- a) the maximum response was in good agreement with those obtained from the harmonic flow

- b) the amplitude of the lift coefficient at lock-on condition was magnified by a factor of 1.6 to 1.9 (for different tests) compared with those of a stiffly mounted cylinder in harmonic flow with the same KC and Re numbers
- c) the correlation of the lift coefficient with only KC was poor because it also depended strongly on  $V_r$ .

The lift amplification parameter,  $CL/CL_0$  was shown in harmonic flow by Sarpkaya (1981b) and Rajabi (1979), and in waves by Zedan and Rajabi (1981), to be a function of  $KC / KC^*$  which is obviously equal to  $V_r / V_r^*$ . Where  $KC^*$  and  $V_r^*$  were respectively equal to KC and  $V_r$  at perfect lock-on conditions.

Rajabi et. al. (1984) presented a vortex-shedding model for a vertical flexible riser in waves and currents based on the above discussion. They obtained the lift amplifications along a riser by calculating the values of  $V_r/V_r^*$  and using the graphs of  $CL/CL_0$ . Then the transverse oscillation amplitude was computed. From this amplitude, and using the available relationships from steady flow, the amplification of the drag coefficient in the in-line direction due to the vortex-shedding was calculated.

## 2.5 Forces Induced by Vortex-Shedding on Randomly Oriented Cylinders

If the cylinder is not in the plane of the wave and current motion, the lift force on the cylinder does not lie in the transverse direction but acts in a direction normal to the plane constructed by the cylinder and drag-inertia force on the

cylinder. The response of the cylinder in this direction is purely associated with the vortex-shedding. The vortex-shedding forces on the cylinder are applied and the maximum response of the cylinder is obtained in this direction. This response is then used to evaluate the magnification factor for drag coefficient in the drag-inertia force.

The recent vortex-shedding model suggested by Rajabi et. al. (1984) is extended in the present study to the case of a flexible riser oriented in a random manner.

## CHAPTER 3

### FLEXIBLE RISERS

#### 3.1 - Introduction

Floating drilling and production in deep waters has become increasingly important in recent years. Marine risers are considered key components for such operations. The importance of production risers occurs because output is reduced or curtailed when malfunctions of these risers occur. Loss of integrity of the riser system may also mean fouling of the environment.

In general there are two alternative riser structural systems. One is a rigid type, the other is the flexible type. The two concepts are quite different in both structural behaviour and configuration.

The rigid riser consists of a central export line with the individual risers clamped externally around this line. This type of riser will not be discussed in this thesis.

There are three basic types of flexible riser, as shown in figure

3.1:

- a - free hanging - this system consists simply of a free hanging pipe running to the bottom in a catenary shape.

- b - single catenary - this system consists of two parts. The lower part is nearly vertical when connecting to a base plate on the bottom and is tensioned by a floating sub-buoy. The upper part hangs in a catenary curve with one side connected to the sub-buoy and the other connected to the floating platform deck. The sub-buoy system consists of a cylindrical tank (buoy) and an interconnected framework forming a cradle, figure 3.2. Alternatively the sub-buoy system can be replaced by a series of buoyant collars which are installed along a certain length of a riser, figure 9.4.
  
- c - double catenary shape - this system consists of a flexible pipe suspended from the deck of the platform and running in a catenary curve to the sub-buoy, from which it also runs in a catenary curve to the bottom. The sub-buoy is anchored to a base plate on the sea-bed by means of a chain. Alternatively the sub-buoy system can be replaced by buoyant collars, figure 9.6.

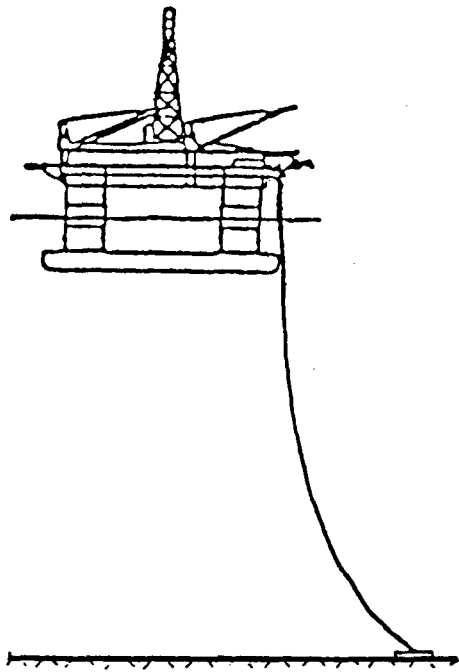
In this chapter a typical flexible riser cross-section is described, and the practical implications for the analysis of flexible risers is subsequently presented.

### **3.2- Flexible Pipe Cross Section**

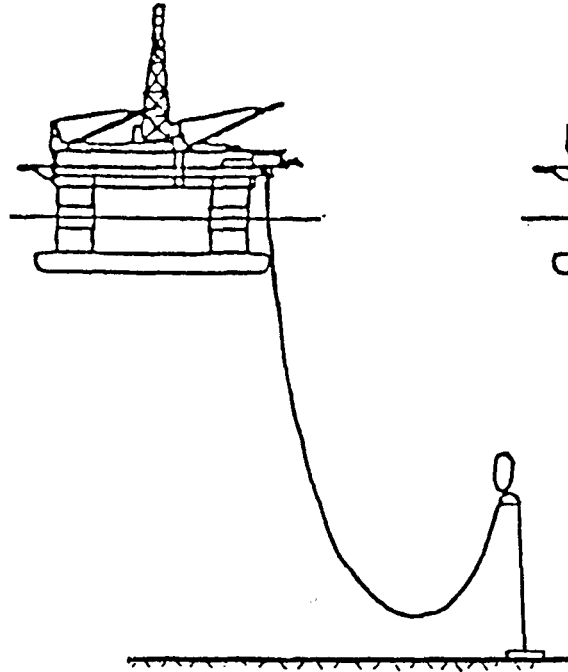
The pipe cross-section is basically composed of steel and plastic. Steel components ensure the mechanical performance and plastic components render the flexible pipe leak proof. The typical riser cross-section used for deep water applications includes five principal layers, the characteristics and

dimensions of which are determined according to the requirements of the service involved. From the inside to the outside the flexible line is composed of, (fig 3.3):

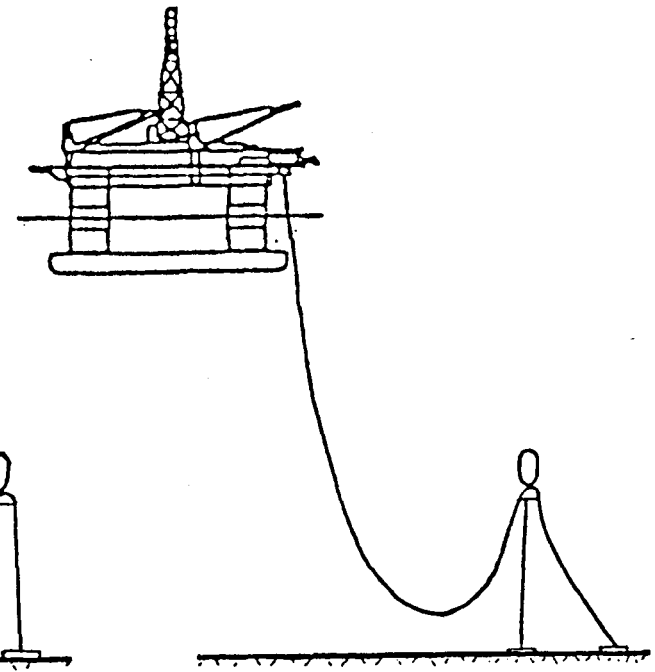
- An interlocked stainless steel carcass (layer) which provides resistance to crushing and prevents deformation of the pipe even when subjected to a fairly short bending radius or various inside or outside pressure and tensile stresses.
- An internal thermoplastic sheath (layer 2) and external thermoplastic sheath (layer 5) which render the riser leak proof (internally and externally) and corrosion resistant. The major qualities required for these sheaths are : a) Their flexibility to allow the spooling of the line, b) Their physico chemical resistance to the fluid transported in the temperature operating range.
- An interlocked zeta spiral (layer 3), called the pressure armour, which ensures binding of the inner sheaths and the integrity of the internal pressure, while reclining and unreclining the pipe. It is made of shaped steel which allows the interlocking of each spiral with its neighbour.
- Two cross-armoured steel wire layers (layer 4) which provide resistance to pulling and longitudinal stresses induced by internal pressure. In order to achieve the flexibility of the line, they are installed in an helicoidal pattern and to avoid any torsion effects, the two layers are wound in opposite directions.



a) free hanging



b) single catenary



c) double catenary

Fig 3.1 - Different shapes of flexible risers

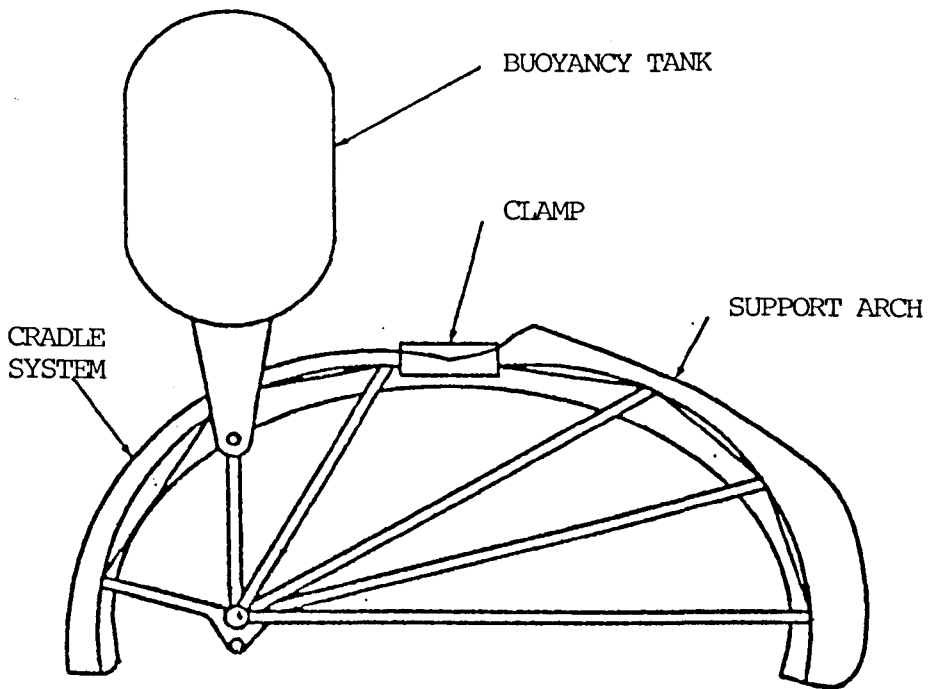


Fig 3.2 - Cradle system

1. INTERLOCKED CARCASS
2. POLYAMIDE SHEATH
3. PRESSURE ARMOR
4. TENSILE ARMOR
5. POLYAMIDE SHEATH

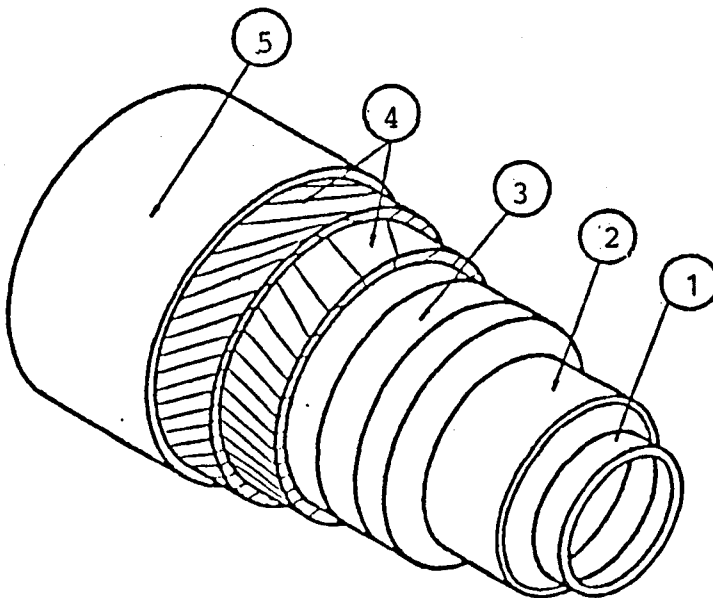
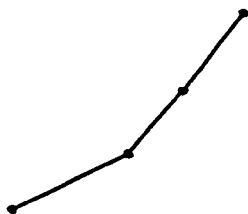


Fig 3.3 - Flexible riser cross-section

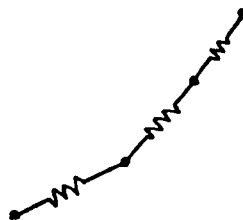
### 3.3- Background to the Analysis of Flexible Risers

The analysis of a riser is usually achieved by subdividing the riser into sets of discrete elements and the system of partial differential equations, describing the variables along the pipe, are replaced by equations of motion of the discrete nodal points in each global co-ordinate direction. The most successful discrete element techniques are the lumped mass (finite difference) scheme and the Finite Element Scheme.

The lumped Mass Scheme involves lumping all the effects of mass, external forces and internal reactions at a finite number of points ("nodes") along the pipe. By applying the equations of dynamic equilibrium and continuity to each mass, a set of discrete equations of motion is derived. The sections of inextensible pipe between nodes are considered to be either straight lines without mass (figure 3.4a/ Walton and Polachek 1959,1960), Dominguez (1971), and Dominguez and Smith (1972)), or Springs without mass (figure 3.4b/ Paquette and Henderson (1965), Liu and Drelicharz (1969), Crist (1970), and Hicks and Clark (1972)).



(a) - Straight line element



(b) - Spring element

Figure - 3.4 - Type of elements used in Finite difference scheme

The finite Element Scheme utilises interpolation functions to describe the behaviour of a given variable internal to the element in terms of the displacement of the nodes defining the element. The equations of motion for a single element are obtained by applying the interpolation functions to kinematic relations (stress/strain) and the equations of dynamic equilibrium. Various models based on the Finite Element Scheme have been presented using either linear or higher order shape functions (figure 3.5a,b/Strandhagen and Thomas (1963), Paul and Soler(1972), Morgan (1970), Leonard and Recker (1972), Fyllina and Wold (1979), Larsen and Fylling (1982), and Lindahl and Sjoberg (1983)).



(a) - Linear Shape function      (b) - Higher order Shape function

Figure 3.5 - Type of elements used in finite element scheme

H.J.J. Van den Boom (1985) compared the results of a developed computer algorithm based on the lumped mass method with results of harmonic oscillation tests for various cables. He concluded that the lumped mass method provides economic predictions of dynamic line motions and tensions which are sufficiently accurate for engineering applications.

The three most common numerical methods used to solve the equations of motion of riser elements subjected to time varying hydrodynamic forces are:

1 - Frequency domain scheme

2 - A deterministic time domain scheme

3 - A nondeterministic random vibration analysis

In the frequency domain method, (Burke (1973), Young et. al. (1977), and Lawrence et.al. (1980)), the total motion of the riser is expanded as the sum of components. By linearizing the differential equations, and expanding the forcing function in a Fourier Series, a closed form algebraic solution is achieved. The frequency domain computations are much faster than the time domain equations but the disadvantage of this method is that the non-linear drag force (the relative velocity square term in Morison's equation) must be linearized. If this approximation is not chosen carefully, large inaccuracies result. The unknown effect of drag linearization is the major drawback of this method (Sarpkaya (1981c)).

In the time domain dynamic method (Gardner and Kotch (1976), and Macnamara et. al. (1981)), discrete time steps are used to integrate the equations of motion which leads to the time history solution. This method allows calculation of the nonlinear drag on the riser and accounts for relative riser motion and dynamics. The disadvantage of the time domain method, however, is that it usually requires a lot of computer time. Time integration is carried out by either explicit or implicit algorithms. A comparison between explicit and implicit algorithms has been given by Soltanahmadi (1985).

In implicit schemes, the displacements at time  $t + \Delta t$  are obtained using the equilibrium equations at time  $t + \Delta t$ . Hydrodynamic forces on flexible risers are riser displacement dependent, and therefore iteration is required at each time increment. The method may be termed a mixed method since it employs incrementation with equilibrium iterations to correct the riser displacements to some specified level of convergence.

Implicit schemes have the advantage that, for linear systems, they are unconditionally stable for large time steps. But they have the major disadvantage of requiring iteration and assembly of the overall structural stiffness at each time step.

In Explicit schemes, the displacement at time  $t + \Delta t$  is obtained using the equilibrium equation at time,  $t$ . Therefore no iteration is required within each time step for the solution. The main disadvantage of such schemes is that they are only conditionally stable, so that small time steps must be adopted to prevent instability in the solution.

The analysis of risers is carried out either by using a Finite Element structural idealization with an implicit or explicit algorithm, or by using a Lumped Mass Scheme with an explicit algorithm (finite difference).

Finally, the third numerical method, nondeterministic random vibration scheme (Tucker and Mutha (1973)) can use either frequency domain or time domain solutions but instead of regular waves, random waves are used. In this method, the random wave spectrum is input to the riser model, and the riser response is output in the form of a spectrum.

A number of non-linear computer codes using the numerical methods discussed above have been developed in recent years to analyse flexible risers. In spite of this, however, the issue is far from resolved (Sarpkaya (1981c) ).

API (1977) compared existing computer programs for a standard set of riser problems. The comparison showed that different computer programs gave a considerable scatter in the resulting stresses. It was not certain why the different programs gave such a variation in results, but the mechanisms of riser behaviour are such that there is ample room for different interpretations of how the physical effects should be formulated and how the hydrodynamic loading on the riser should be assessed. Therefore, comparing one particular program with other available programs is not necessarily a measure of how accurate it is. However, it may give a general guide as to whether any significant deviation from other programs is due to programming errors or due to a more refined formulation of certain important effects (Natvig and Torset (1985) ). The only objective way to validate riser analysis programs is to compare computed results with experimental measurements.

From the foregoing, it can be concluded that more research work is required to develop a riser analysis computer program which produces reliable results with reasonable economy. It is essential that every aspect of the computed results including the assesment of hydrodynamic loading on the riser and the physical performance of the riser should be validated experimentally. This was the aim of this project.

## CHAPTER 4

### THEORETICAL COMPUTATION AND ASSESSMENT OF HYDRODYNAMIC LOADINGS ON FLEXIBLE RISERS

#### 4.1 - Introduction

This chapter describes the theory of basic fluid hydrodynamics and presents the derivation of the Linear and Stokes wave theories. It then considers the theories used to evaluate the drag-inertia and Vortex-Shedding induced hydrodynamic forces on a flexible riser due to wave and current motions. Finally, it deals with the assessment of these forces on the riser.

## 4.2 - Fluid Mechanics

### 4.2.1. - Derivation of Basic Relationships for Incompressible, Irrotational and Inviscid Fluid Flow

The object is to obtain relationships between parameters such as velocities, accelerations and pressures in a moving fluid.

Consider a small rectangular element of real fluid ABCD in 2-dimensional flow, with particle velocity components of  $U$  and  $V$  in the  $x$  and  $y$  directions at position  $A$ , and pressure,  $p$ , at the centre of the element:

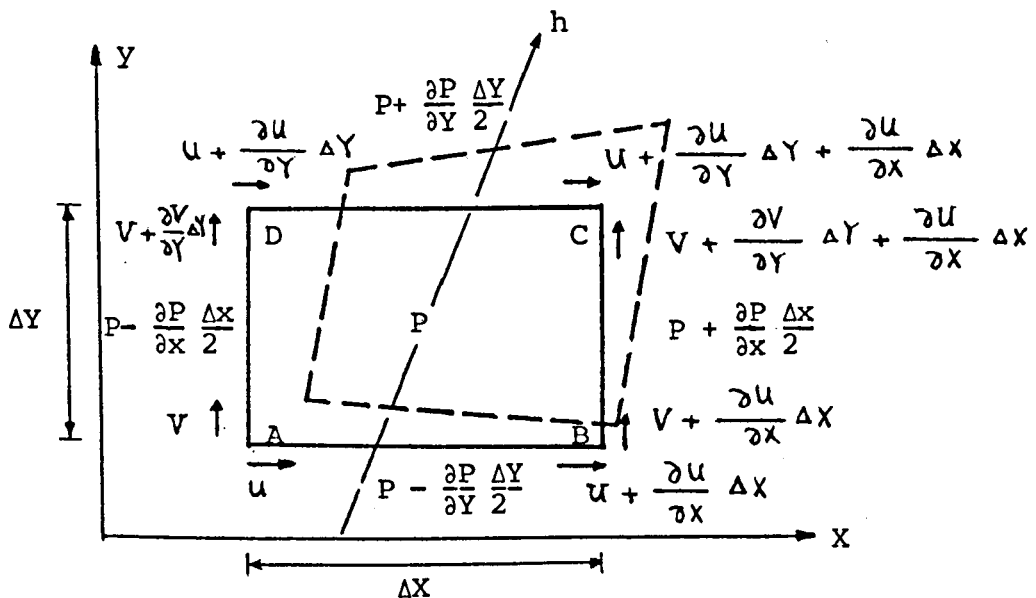
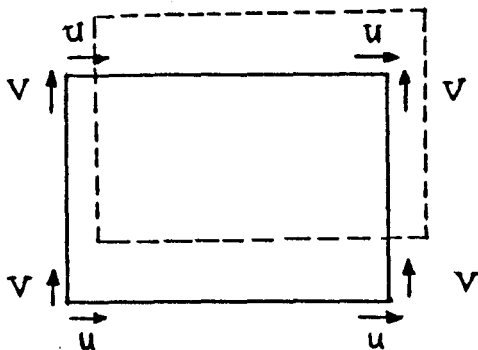


Figure 4.1. - Fluid element

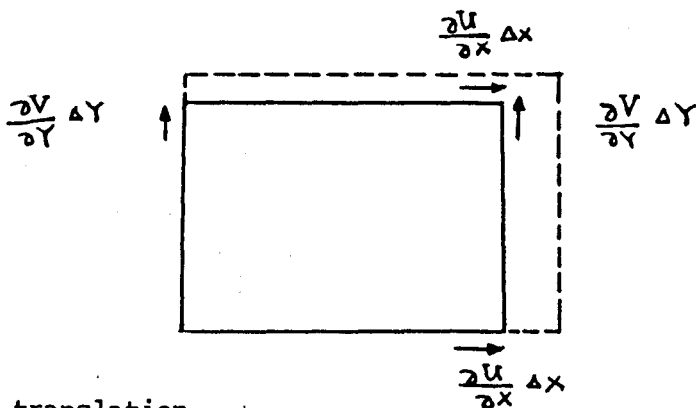
### Kinematics

As far as the velocities are concerned, Figure 4.1 can be considered as the sum of four distinct types of motions. These are:

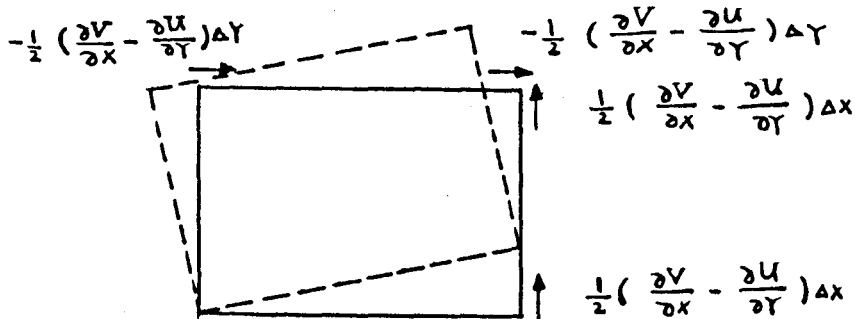
1 - Linear translation



2 - Linear deformation



3 - Angular translation



4 - Angular deformation

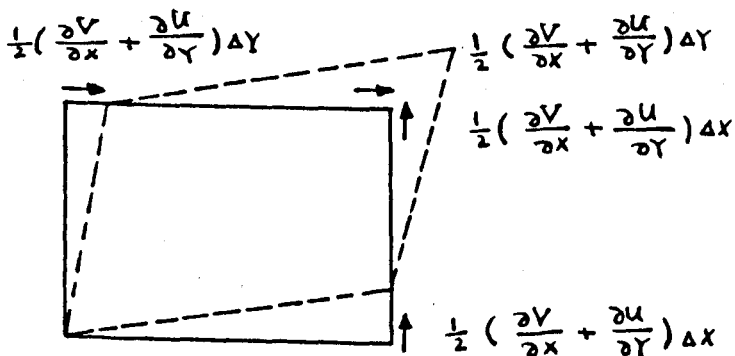


Figure 4.2. - Components of fluid element motion

Note : the sum of the velocities at each corner of figure 4.2 is the same as that in figure 4.1.

The change of area (or volume) of the element ABCD can only result from the linear deformation component. But the incompressible fluid assumption (i.e, no volume change) requires that this component is zero.

$$\text{Thus, } \frac{\partial U}{\partial X} + \frac{\partial V}{\partial Y} = 0 \quad (4.1)$$

This is the continuity equation.

The vorticity is generated by shear stress and is defined as:

$$\omega = \frac{\partial V}{\partial X} - \frac{\partial U}{\partial Y}$$

which is twice the angular velocity. The irrotationality assumption of the fluid requires the vorticity to be zero.

$$\text{Thus, } \frac{\partial V}{\partial X} - \frac{\partial U}{\partial Y} = 0 \quad (4.2)$$

For irrotational flows, there is a scalar function, the velocity potential  $\phi(X, Y, t)$ , which contains all the information about the kinematics of the motion. particle velocities are derived from it as follows:

$$U = \frac{\partial \phi}{\partial X}, \quad V = \frac{\partial \phi}{\partial Y} \quad (4.3)$$

Substituting (4.3) into equation (4.1), the Laplace equation is obtained:

$$\frac{\partial^2 \phi}{\partial X^2} + \frac{\partial^2 \phi}{\partial Y^2} = 0 \quad (4.4)$$

For incompressible flows, there is a second rather similar Scalar function, the stream function  $\psi (X, Y, t)$ , from which the particle velocities can be derived as follows:

$$U = \frac{\partial \psi}{\partial Y}, \quad V = - \frac{\partial \psi}{\partial X} \quad (4.5)$$

Substituting equation (4.5) into equation (4.9) gives:

$$\frac{\partial^2 \psi}{\partial X^2} + \frac{\partial^2 \psi}{\partial Y^2} = 0$$

### Dynamics

Newton's second law is used to obtain the dynamic relationship. With reference to Figure 4.1 and resolving the net force on the element per unit area (or volume) due to the pressure gradients and gravity in the x and y directions:

$$\begin{aligned} x : & - \frac{\partial P}{\partial X} - \rho g \frac{\partial h^*}{\partial X} \\ Y : & - \frac{\partial P}{\partial Y} - \rho g \frac{\partial h^*}{\partial Y} \end{aligned} \quad (4.6)$$

where  $\rho$  is the fluid density and  $h^*$  is a co-ordinate measured vertically upwards.

The acceleration in each direction has local and convective components. Using Newton's second law:

$$\begin{aligned} \text{x} : \rho \left( \frac{\partial U}{\partial t} + U \frac{\partial U}{\partial X} + V \frac{\partial U}{\partial Y} \right) &= - \frac{\partial P}{\partial X} - \rho g \frac{\partial h^*}{\partial X} \\ \text{y} : \rho \left( \frac{\partial V}{\partial t} + U \frac{\partial V}{\partial X} + V \frac{\partial V}{\partial Y} \right) &= - \frac{\partial P}{\partial Y} - \rho g \frac{\partial h^*}{\partial Y} \end{aligned} \quad (4.7)$$

dividing equation (4.7) by  $\rho$ , Euler's equation is obtained:

$$\text{x} : \frac{\partial U}{\partial t} + U \frac{\partial U}{\partial X} + V \frac{\partial U}{\partial Y} = - \frac{1}{\rho} \frac{\partial P}{\partial X} - g \frac{\partial h^*}{\partial X} \quad (4.8a)$$

$$\text{y} : \frac{\partial V}{\partial t} + U \frac{\partial V}{\partial X} + V \frac{\partial V}{\partial Y} = - \frac{1}{\rho} \frac{\partial P}{\partial Y} - g \frac{\partial h^*}{\partial Y} \quad (4.8b)$$

Note: if the fluid were not assumed as inviscid, an extra viscous force would have been added to the force terms in equation (4.8) which would have given the Navier-Stokes equation.

Substituting  $U = \frac{\partial \phi}{\partial X}$ ,  $U \frac{\partial U}{\partial X} = \frac{1}{2} \frac{\partial U^2}{\partial X}$  and

$$V \frac{\partial U}{\partial Y} = V \frac{\partial V}{\partial X} = \frac{1}{2} \frac{\partial V^2}{\partial X} \quad \text{into equation (4.8a)}$$

all terms become derivatives with respect to X. Integration with respect to X introduces an arbitrary function of Y and t. Operating similarly on equation (4.8b) and comparing the results leads to Bernoulli's equation which expresses the requirement of conservation of energy for irrotational unsteady flow:

$$\frac{\partial \phi}{\partial t} + \frac{1}{2} (U^2 + V^2) + g h^* + \frac{P}{\rho} = f(t) \quad (4.9)$$

In equation (4.9)  $f(t)$  is an unknown function of time. Since any  $\int_0^t f(t) dt$  can be incorporated into  $\phi(X, Y, t)$  without modifying the derived velocities, the right hand side of equation (4.9) can normally be set to zero without loss of generality.

$$\text{Thus, } \frac{\partial \phi}{\partial t} + \frac{1}{2} (U^2 + V^2) + g h^* + \frac{P}{\rho} = 0 \quad (4.10)$$

### 4.3 - Wave Theory

The range of suitability of the different wave theories for different situations was given by Dean (1970) as Figure 4.3, and by Le Mehante (1976) as figure 4.4. The latter includes the different orders of Stokes wave theory, and is particularly useful for experimental work in a wave flume.

In off-shore situations which usually involve deep water waves, Stokes 5th order or alternatively linear wave theories are generally adopted. One reason for preferring the use of Stokes 5th order wave theory is its prediction of the most realistic wave crest height which is a critical factor in the design of semi-submersible platforms.

The definition of deep or shallow water waves is indicated by the range of  $Kh$  values, where  $K$  = wave number and  $h$  = depth of still water, as follows:

$Kh > \pi$  for deep water waves

$Kh < \frac{\pi}{10}$  for shallow water waves

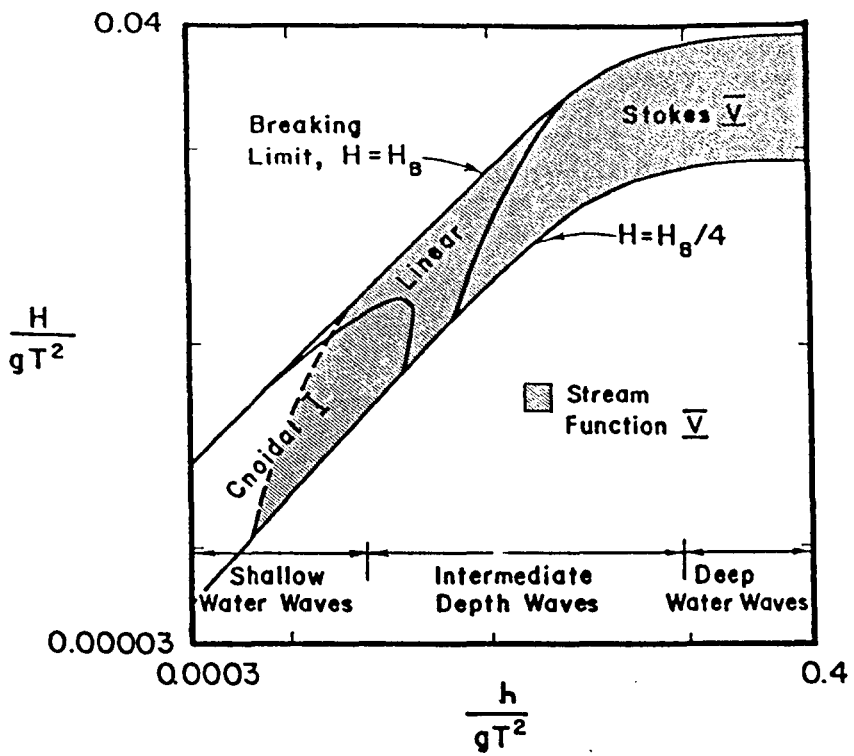


Figure 4.3 - Ranges of wave theories giving the best fit to the dynamic free surface boundary condition (Dean 1970)

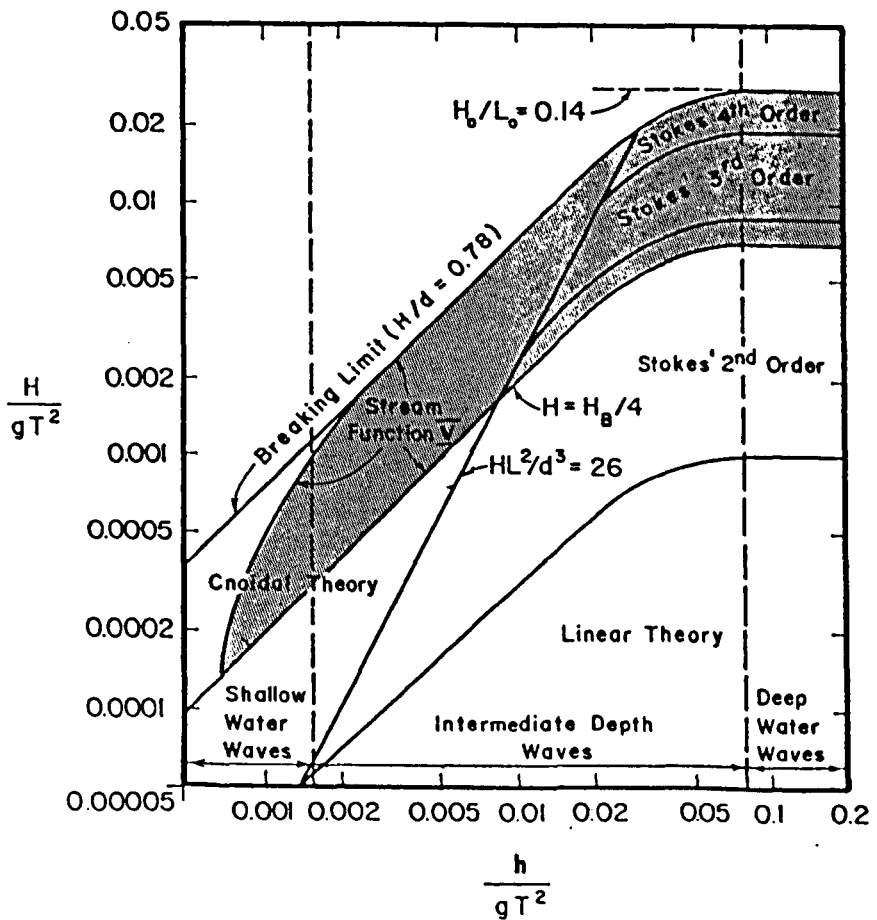


Figure 4.4 - Ranges of suitability for various wave theories (Méhauté (1976))

4.3.1 - Linear (Airy) Wave Theory

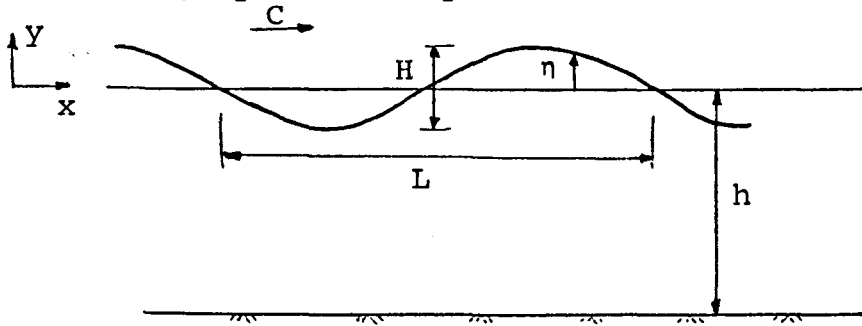


Figure 4.5  
Specifications for a wave train

A particular wave train is generally described by the quantities  $H$ ,  $T$  and  $h$  (Figure 4.5), and the objective of any wave theory is to determine celerity (wave speed) and hence the wave length ( $L$ ) and a description of water particle kinematics through the velocity potential  $\phi$  (or stream function  $\psi$  in the case of stream function wave theory).

To determine the velocity potential ( $\phi$ ), a solution of Laplace's equation of continuity (equation (4.4)), subject to a number of boundary conditions, is required. The boundary conditions are:

- (1) The bottom boundary condition - it is assumed that the bottom surface is impermeable. This means that the vertical velocity must be zero at the bottom ( $Y=-h$ ), thus:

$$\frac{\partial \phi}{\partial Y} = 0 \quad \text{at} \quad Y = -h \quad (4.11)$$

- (2) The free surface boundary conditions ( $Y=\eta$ );

- (a) Kinematic condition - the surface moves with the fluid, and thus the vertical velocity of the particles on the surface is equal to that of the surface.

The vertical velocity of the water particles at the free surface

$$(Y=\eta) = \frac{\partial \phi}{\partial Y}.$$

The surface vertical velocity  $\left( \frac{d\eta}{dt} \right) = \frac{\partial \eta}{\partial t} + \frac{\partial \eta}{\partial X} \frac{\partial X}{\partial t}$

Thus, 
$$\frac{\partial \phi}{\partial Y} = \frac{\partial \eta}{\partial t} + \frac{\partial \eta}{\partial X} \frac{\partial X}{\partial t} \quad \text{at } Y = \eta(X,t) \quad (4.12)$$

But  $\frac{\partial X}{\partial t} = U = \frac{\partial \phi}{\partial X}$ , and substituting this into equation (4.12):

$$\frac{\partial \phi}{\partial Y} = \frac{\partial \eta}{\partial t} + \frac{\partial \eta}{\partial X} \frac{\partial \phi}{\partial X} \quad \text{at } Y = \eta(X,t) \quad (4.13)$$

(b) Dynamic condition - it is assumed that the pressure at the surface is atmospheric so the term P in equation (4.10) (which is the unsteady-state Bernoulli equation) can be neglected. Thus equation (4.10) at the free surface becomes:

$$\frac{\partial \phi}{\partial t} + \frac{1}{2} (U^2 + V^2) + g \eta = 0 \quad \text{at } Y = \eta(X, t)$$

or

$$\frac{1}{g} \frac{\partial \phi}{\partial t} + \frac{1}{2g} \left( \left( \frac{\partial \phi}{\partial X} \right)^2 + \left( \frac{\partial \phi}{\partial Y} \right)^2 \right) + \eta = 0 \quad \text{at } Y = \eta(X, t) \quad (4.14)$$

In linear (small amplitude) wave theory, the free surface boundary conditions are simplified. The slope of the free surface,  $\frac{\partial \eta}{\partial X}$ , is assumed to be negligible for all values of X. It is also assumed that the water particle velocities,  $\frac{\partial \phi}{\partial X}$  and  $\frac{\partial \phi}{\partial Y}$ , are small and hence their squares are negligible. The boundary conditions are further simplified by applying them at the still water level,  $Y=0$ , rather than at  $Y=\eta$  which is the (unknown) free surface. Thus the linearised free surface boundary conditions can be written as:

$$\frac{\partial \phi}{\partial Y} = \frac{\partial \eta}{\partial t} \quad \text{at } Y = 0 \quad (4.15)$$

$$\frac{1}{g} \frac{\partial \phi}{\partial t} + \eta = 0 \quad \text{at } Y = 0 \quad (4.16)$$

A solution for the velocity potential can be obtained as follows:

$$\phi (X, Y, t) = f (X) \cdot f (Y) \cdot f (t) \quad (4.17)$$

Differentiating equation (4.17) twice with respect to both X and Y and substituting into the continuity equation (equation (4.4)), we obtain:

$$f'' (X) \cdot f (Y) \cdot f (t) + f (X) \cdot f'' (Y) \cdot f (t) = 0$$

or

$$\frac{f'' (X)}{f (X)} = - \frac{f'' (Y)}{f (Y)} \quad (4.18)$$

Equation (4.18) is only possible if we have:

$$\frac{f'' (X)}{f (X)} = - \frac{f'' (Y)}{f (Y)} = \text{constant} = - K^2$$

Thus

$$f'' (X) + K^2 f (X) = 0 \quad (4.19)$$

$$f'' (Y) - K^2 f (Y) = 0 \quad (4.20)$$

The solutions for equations (4.19) and (4.20) can be written as:

$$f (X) = A \sin K X + B \cos K X \quad (4.21)$$

$$f (Y) = C e^{K Y} + D e^{-K Y} \quad (4.22)$$

From the periodic nature of the wave train, we have:

$$f (t) = F \sin \omega t + E \cos \omega t \quad (4.23)$$

Considering equations (4.21) and (4.23), we may write:

$$f(X) \cdot f(t) = A \sin(KX - \omega t) \quad (4.24)$$

Substituting equations (4.22) and (4.24) into equation (4.17) gives:

$$\phi = (C e^{KY} + D e^{-KY}) A \sin(KX - \omega t) \quad (4.25)$$

A solution for equation (4.25) can be obtained by considering the boundary equations. From the bottom boundary equation (4.11), we have:

$$\frac{\partial \phi}{\partial Y} = 0 \quad \text{at } Y = -h$$

and substituting for  $\phi$  from equation (4.25);

$$C e^{-Kh} - D e^{Kh} = 0$$

Thus,  $C = D e^{2Kh}$

Substituting equation (4.26) into equation (4.25) and simplifying yields:

$$\phi = (e^{K(Y+h)} + e^{-K(Y+h)}) D e^{Kh} A \sin(KX - \omega t)$$

$$\text{thus, } \phi = 2D e^{Kh} A \cdot \text{Cosh } K(h+Y) \cdot \text{Sin } (KX - \omega t) \quad (4.26)$$

Considering now the dynamic free surface boundary condition, equation (4.16);

$$\frac{1}{g} \frac{\partial \phi}{\partial t} + \eta = 0 \quad \text{at } Y = 0$$

and substituting for  $\phi$  from equation (4.26);

$$\eta = \frac{1}{g} 2AD\omega e^{Kh} \cosh Kh \cdot \cos(KX - \omega t) \quad (4.27)$$

But the free surface in linear wave theory is given by

$$\eta = \frac{H}{2} \cos(KX - \omega t) \quad (4.28)$$

Comparing equations (4.27) and (4.28) gives:

$$\frac{H}{2} = \frac{1}{g} 2AD\omega e^{Kh} \cosh Kh$$

$$\text{thus, } 2ADe^{Kh} = \left( \frac{H}{2} \cdot \frac{g}{\omega} \right) / \cosh(Kh) \quad (4.29)$$

Substituting equation (4.29) into equation (4.26), the equation for the velocity potential is obtained:

$$\phi = g \frac{H}{2\omega} \frac{\cosh K(h+y)}{\cosh Kh} \sin(KX - \omega t) \quad (4.30)$$

The celerity of the wave can be obtained by considering the kinematic free surface boundary condition (equation (4.15)),

$$\frac{\partial \phi}{\partial Y} = \frac{\partial \eta}{\partial t} \quad \text{at } Y = 0 \quad (4.15)$$

From equation (4.28):

$$\frac{\partial \eta}{\partial t} = \frac{H\omega}{2} \sin(KX - \omega t)$$

and from equation (4.30),  $\frac{\partial \phi}{\partial Y}$  at  $Y=0$  is:

$$\frac{\partial \phi}{\partial Y} = g \frac{HK}{2\omega} \tanh Kh \sin(KX - \omega t)$$

therefore,  $\frac{\partial \phi}{\partial Y} = \frac{\partial \eta}{\partial t}$  at  $Y = 0$  gives:

$$g \frac{HK}{2\omega} \tanh Kh = \frac{H\omega}{2}$$

Thus,  $\omega^2 = gK \tanh Kh$

$$\text{but } \omega = \frac{2\pi}{T} = \frac{L}{T} \cdot \frac{2\pi}{L} = CK$$

$$\text{Then, } C^2 K^2 = (gK) \tanh Kh \quad (4.31)$$

and thus,  $C^2 = (g/K) \tanh Kh$

Equation (4.31) is called the dispersion equation.

The particle velocity and acceleration can be obtained by differentiation of equation (4.30).

The horizontal particle velocity and acceleration are respectively:

$$U = \frac{\partial \phi}{\partial X} = \frac{\pi H}{T} \frac{\cosh(KS)}{\sinh(Kh)} \cos \theta \quad (4.32)$$

$$\dot{U} = \frac{\partial U}{\partial t} = \frac{2\pi^2 H}{T^2} \frac{\cosh(KS)}{\sinh(Kh)} \sin \theta \quad (4.33)$$

The vertical particle velocity and acceleration are respectively:

$$V = \frac{\partial \phi}{\partial Y} = \frac{\pi H}{T} \frac{\text{Sinh}(KS)}{\text{Sinh}(Kh)} \sin \theta \quad (4.34)$$

$$\dot{V} = \frac{\partial V}{\partial t} = -\frac{2\pi^2 H}{T^2} \frac{\text{Sinh}(KS)}{\text{Sinh}(Kh)} \cos \theta \quad (4.35)$$

where  $s = h+Y$  and  $\theta = KX - \omega t$

This wave theory gives the particle motion under a constant still water plane and it does not include any surface movements of the waves. This may be corrected by setting the particle motion in the wave crest equal to that at the still water plane, Figure 4.6:

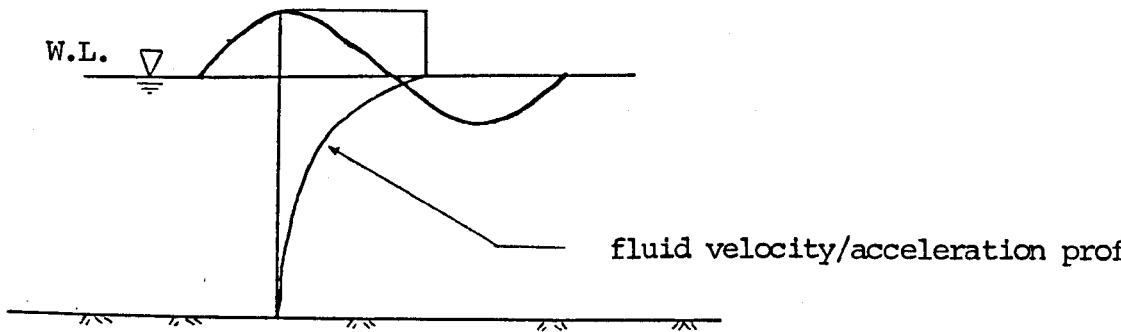


Figure 4.6. - Modification of the linear wave theory

### 4.3.2. - Stokes Finite Amplitude Wave Theory

Derivation of the Stokes 5th order wave theory is presented and it is used to obtain any lower order (1 - 4) theory by eliminating the higher order coefficients.

Recalling the boundary equations (4.11), (4.13) and (4.14):

bottom boundary condition is: 
$$\frac{\partial \phi}{\partial Y} = 0 \quad \text{at } Y = -h \quad (4.11)$$

free surface conditions:

$$\frac{\partial \phi}{\partial Y} = \frac{\partial \eta}{\partial t} + \frac{\partial \eta}{\partial X} \cdot \frac{\partial \phi}{\partial X} \quad \text{at } Y = \eta(X,t) \quad (4.13)$$

$$\frac{1}{g} \frac{\partial \phi}{\partial t} + \frac{1}{2g} \left( \left( \frac{\partial \phi}{\partial X} \right)^2 + \left( \frac{\partial \phi}{\partial Y} \right)^2 \right) + (\beta + Y) = 0$$

$$\text{at } Y = \eta(X,t) \quad (4.14)$$

where  $\beta$  is a constant for a given wave, related to the total head.

It is convenient to carry out the derivation with respect to a frame of reference moving with the waves, so that if the wave-induced flow is  $(U,V)$ , the particle velocities seen on the moving reference frame are  $(U-C,V)$ . By introducing the reference frame the dependence of  $Y$  with  $t$  disappears so that equations (4.13) and (4.14) become as equations (4.36) and (4.37) respectively):

$$V = \frac{\partial \eta}{\partial X} (U - C) \quad \text{at } Y = \eta(X)$$

thus,

$$\frac{\partial \eta}{\partial X} = \frac{V}{U-C} \quad \text{at } Y = \eta(X) \quad (4.36)$$

$$-\frac{1}{g} \frac{\partial \phi}{\partial X} \frac{\partial X}{\partial t} + \frac{1}{g} (U^2 + V^2) + (\beta + \eta) = 0 \quad \text{at } Y = \eta(X)$$

thus,  $-2UC + (U^2 + V^2) = -2g(\beta + \eta) \quad \text{at } Y = \eta(X)$

$$(U-C)^2 + V^2 = C^2 - 2g(\beta + \eta) \quad \text{at } Y = \eta(X) \quad (4.37)$$

The series form for  $\phi$ , which satisfies the Laplace's equation bottom boundary equation (4.11), and symmetry requirements can be assumed as follows:

$$\begin{aligned} \phi = & \frac{C}{K} [ (\lambda A_{11} + \lambda^3 A_{13} + \lambda^5 A_{15}) \cosh KS \sin \theta \\ & + (\lambda^2 A_{22} + \lambda^4 A_{24}) \cosh 2KS \sin 2 \theta \\ & + (\lambda^3 A_{33} + \lambda^5 A_{35}) \cosh 3KS \sin 3 \theta \\ & + (\lambda^4 A_{44} \cosh 4KS \sin 4 \theta \\ & + (\lambda^5 A_{55} \cosh 5KS \sin 5 \theta ) \end{aligned} \quad (4.38)$$

where  $\lambda = Ka$ ,  $a =$  wave amplitude,  $S = h+Y$  and  $\theta = KX - \omega t$ . The equation for  $\eta$  which satisfies the symmetry requirement can be assumed as:

$$\begin{aligned} \eta = & \frac{1}{K} [ \lambda \cos \theta + (\lambda^2 B_{22} + \lambda^4 B_{24}) \cos 2 \theta \\ & + (\lambda^3 B_{33} + \lambda^5 B_{35}) \cos 3 \theta \\ & + \lambda^4 B_{44} \cos 4 \theta + \lambda^5 B_{55} \cos 5 \theta \end{aligned} \quad (4.39)$$

Further, the following equations can be assumed for the wave celerity and the constant  $\beta$  ;

$$C^2 = \frac{C_0^2}{K} (1 + \lambda^2 C_1 + \lambda^4 C_2) \quad (4.40)$$

$$\beta = \frac{1}{K} (\lambda^2 C_3 + \lambda^4 C_4) \quad (4.41)$$

Where  $C_0$  is the linear wave celerity as calculated in the linear

$$\text{wave theory } (C_0^2 = \frac{g}{K} \tanh Kh)$$

Any lower order of Stokes wave theory is obtained by setting the corresponding  $A_{ij}$  and  $B_{ij}$  coefficients to  $\lambda$  with powers higher than the considered order equal to zero. For example for the 3rd order wave theory,  $A_{ij}$  and  $B_{ij}$  coefficients corresponding to  $\lambda^4$  and  $\lambda^5$  are set to zero. In addition  $C_2$  and  $C_4$  coefficients are set equal to zero except for the 5th order theory, and  $C_1$  and  $C_3$  are set equal to zero only for the 1st and the 2nd order theories.

In order to obtain  $A_{ij}$ ,  $B_{ij}$  and  $C_i$  coefficients, equations (4.38), (4.39), (4.40) and (4.41) should satisfy the free surface boundary conditions, equations (4.36) and (4.37). This is achieved by solving equations (4.36) and (4.37) for the values of

$$\frac{K}{C} U \text{ and } \frac{K}{C} V, \text{ and setting these values equal to } \frac{K \partial \phi}{C \partial X} \text{ and } \frac{K \partial \phi}{C \partial X}$$

respectively at  $S = h + Y$ . Such a procedure results in two equations involving the unknown constants, powers of  $\cos \phi$  and powers of  $\lambda$ . These equations are grouped according to powers of  $\lambda$  and sub-grouped according to powers of  $\cos \phi$ . Since the equations must hold for any value of  $\phi$ , terms in each equation involving the same order of approximation (i.e. the same power of  $\lambda$ ) and the same power of  $\cos \phi$  are set equal, this results in 20 equations. These equations are solved to obtain the 20 constants  $A_{ij}$ ,  $B_{ij}$  and  $C_i$ . The solution of these equations which is taken from the paper presented by Skjelberia and Hendrickson (1960) is presented in appendix A.

The values of  $K$  and  $\lambda$ , which still have not been determined, can be obtained by using the given wave data (i.e.  $H$ ,  $h$ , and  $T$ ). The wave height ( $H$ ) is equal to the difference between the crest and the trough heights, that is:

$$H = \eta (\theta = 0) - \eta (\theta = \pi)$$

Thus, using equation (4.39) and rearranging, we get:

$$H = \frac{2}{K} [\lambda + \lambda^3 B_{33} + \lambda^5 (B_{35} + B_{55})] \quad (4.42)$$

Also, using equation (4.40) and the expression for  $C_0^2$ , it can readily be shown that:

$$\frac{2\pi}{L_0} = K (1 + \lambda^2 C_1 + \lambda^4 C_2) \tanh Kh \quad (4.43)$$

$$\text{where } L_0 = \frac{gT^2}{2\pi}$$

Equations (4.42) and (4.43) are solved numerically to obtain  $\lambda$  and  $K$ .

The horizontal particle velocity and acceleration can be obtained from the velocity potential equation, (4.38):

$$U = \frac{\partial \phi}{\partial X} = C \left( \sum_{n=1}^5 n \psi'_n \text{Cosh}(nKS) \text{Cos}(n\theta) \right) \quad (4.44)$$

$$\dot{U} = \frac{\partial U}{\partial t} = \omega C \left( \sum_{n=1}^5 n^2 \psi'_n \text{Cosh}(nKS) \text{Sin}(n\theta) \right) \quad (4.45)$$

The vertical particle velocity and acceleration are respectively:

$$V = \frac{\partial \phi}{\partial Y} = C \left( \sum_{n=1}^5 n \psi'_n \text{Sinh}(nKS) \text{Sin}(n\theta) \right) \quad (4.46)$$

$$\dot{V} = \frac{\partial V}{\partial t} = -\omega C \left( \sum_{n=1}^5 n^2 \psi_n' \text{Sinh}(nKS) \text{Cos}(n\theta) \right) \quad (4.47)$$

where  $\omega = \frac{2\pi}{T}$

$$\begin{aligned} \psi_1' &= \lambda A_{11} + \lambda^3 A_{13} + \lambda^5 A_{15} \\ \psi_2' &= \lambda^2 A_{22} + \lambda^4 A_{24} \\ \psi_3' &= \lambda^3 A_{33} + \lambda^5 A_{35} \\ \psi_4' &= \lambda^4 A_{44}, \quad \psi_5' = \lambda^5 A_{55} \end{aligned} \quad (4.48)$$

4.3.3- Numerical Solution of Equations (4.42) and (4.43)

$$\begin{aligned} \frac{2}{K} [ \lambda + \lambda^3 B_{33} + \lambda^5 (B_{35} + B_{55}) - H ] &= 0 \\ (K \tanh Kh) (1 + \lambda^2 C_1 + \lambda^4 C_2) - \frac{4\pi^2}{gT^2} &= 0 \end{aligned} \quad (4.49)$$

To solve the simultaneous equations (4.49), Newton's iteration method is used. The method is commonly used for the solution of systems of non-linear algebraic equations. Its popularity is due to the fact that it has better convergence properties than does the method of direct iteration.

The basis for Newton's iteration method is a Taylor expansion for each of the n equations:

$$\begin{aligned} f_1(x_1 + \Delta x_1, \dots, x_n + \Delta x_n) &= f_1(x_1, \dots, x_n) + \Delta x_1 \frac{\partial f_1}{\partial x_1} + \dots + \Delta x_n \frac{\partial f_1}{\partial x_n} + \text{higher orders} \\ &\vdots \\ &\vdots \\ &\vdots \\ &\vdots \\ f_n(x_1 + \Delta x_1, \dots, x_n + \Delta x_n) &= f_n(x_1, \dots, x_n) + \Delta x_1 \frac{\partial f_n}{\partial x_1} + \dots + \Delta x_n \frac{\partial f_n}{\partial x_n} + \text{higher orders} \end{aligned} \quad (4.50)$$

If changes  $\Delta x_i$  in the variable values bring the function  $f_i$  close to a root, it will be assumed that the left sides of these equations are zero. Thus the problem reduces to that of finding the changes  $\Delta x_i$  that achieve the goal. If all higher order terms are dropped, the problem becomes one of finding the roots of the linear system:

$$\begin{bmatrix} \frac{\partial f_1}{\partial x_1} & \frac{\partial f_1}{\partial x_2} & \dots & \dots & \frac{\partial f_1}{\partial x_n} \\ \vdots & \vdots & \vdots & \vdots & \vdots \\ \frac{\partial f_n}{\partial x_1} & \dots & \dots & \dots & \frac{\partial f_n}{\partial x_n} \end{bmatrix} \begin{bmatrix} \Delta x_1 \\ \Delta x_2 \\ \vdots \\ \vdots \\ \Delta x_n \end{bmatrix} = \begin{bmatrix} -f_1 \\ -f_2 \\ \vdots \\ \vdots \\ -f_n \end{bmatrix} \quad (4.51)$$

In this system the partial derivative matrix and the vector on the right side can each be evaluated at any approximate set of solution waves. Once the  $\Delta x_i$  values are known, they may be applied as corrections to the initial approximations:

$$\begin{aligned} x_1 &= x_1 + \Delta x_1 \\ &\vdots \\ &\vdots \\ x_n &= x_n + \Delta x_n \end{aligned} \quad (4.52)$$

If all correction factors are sufficiently small, the process is terminated. If not, the new values are used as root approximation, and the process is repeated until a solution is found.

The above iteration scheme is used to solve equations (4.49). The variables in (4.49) are  $\lambda$  and  $K$ . But  $\lambda$  is a function of  $K$  (i.e.  $\lambda = Ka$ ). Thus substituting this into (4.49) and simplifying:

$$2 [ a + K^2 a^3 B_{33} + K^4 a^5 (B_{35} + B_{55}) ] - H = 0 \quad (4.53)$$

$$(K \tanh Kh) (1 + K^2 a^2 C_1 + K^4 a^4 C_2) - \frac{4\pi^2}{gT^2} = 0$$

Comparing equations (4.50) and (4.53), we have:

$$f_1 = 2 [ a + K^2 a^3 B_{33} + K^4 a^5 (B_{35} + B_{55}) ] - H \quad (4.54)$$

$$f_2 = (K \tanh Kh) (1 + K^2 a^2 C_1 + K^4 a^4 C_2) - \frac{4\pi^2}{gT^2}$$

It is important to note that  $B_{33}$ ,  $B_{35}$ ,  $B_{55}$ ,  $C_1$  and  $C_2$  are functions of "K".

Equation (4.51) for this case becomes:

$$\begin{bmatrix} \frac{\partial f_1}{\partial a} & \frac{\partial f_1}{\partial K} \\ \frac{\partial f_2}{\partial a} & \frac{\partial f_2}{\partial K} \end{bmatrix} \begin{bmatrix} \Delta a \\ \Delta K \end{bmatrix} = \begin{bmatrix} -f_1 \\ -f_2 \end{bmatrix} \quad (4.55)$$

But:

$$\frac{\partial f_1}{\partial a} = 2 [ 1 + 3 K^2 a^2 B_{33} + 5 K^4 a^4 (B_{35} + B_{55}) ]$$

$$\frac{\partial f_1}{\partial K} = [ 2 K a^3 B_{33} + 4 K^3 a^5 (B_{35} + B_{55}) + K^2 a^3 B'_{33} + K^4 a^5 (B'_{35} + B'_{55}) ]$$

$$\frac{\partial f_2}{\partial a} = (K \tanh Kh) (2 K^2 a C_1 + 4 K^4 a^3 C_2)$$

$$\frac{\partial f_2}{\partial K} = (\tanh Kh) (1 + K^2 a^2 C_1 + K^4 a^4 C_2) +$$

$$\left( \frac{h}{\cosh^2 Kh} \right) K (1 + K^2 a^2 C_1 + K^4 a^4 C_2) +$$

$$(K \tanh Kh) (2 K a^2 C_1 + 4 K^3 a^4 C_2 + K^2 a^2 C'_1 +$$

$$K^4 a^4 C'_2) \quad (4.56)$$

Equations for  $B_{33}$ ,  $B_{35}$ ,  $B_{55}$ ,  $C_1$ , and  $C_2$  are given in appendix A. Prime (') denotes differentiation with respect to  $K$ .

The above relations are substituted into equation (4.55) which is then solved for  $\Delta a$  and  $\Delta K$ . The values obtained for  $\Delta a$  and  $\Delta K$  are then added to the previous values of  $a$  and  $K$  and the whole procedure is repeated. The iteration is terminated when the values of  $f_1$  and  $f_2$  are less than 0.01. Initial values for  $a$  and  $K$  are set equal to those obtained from linear wave theory which, for deep water, are:

$$\begin{aligned} K &= 4 \pi^2 / gT^2 \\ a &= H/2 \end{aligned} \tag{4.57}$$

#### 4.4- Hydrodynamic Loading

##### 4.4.1.- Developing the Theory to Estimate the Drag-Inertia Hydrodynamic Loading on a Flexible Catenary Riser

The following theory is obtained by combining the theories for estimating the hydrodynamic loading on a rigid cylinder with those for a flexible cylinder and an inclined cylinder. Equation (4.58) which is known as the Morison equation is used to calculate the wave loading on a rigid cylinder with a ratio of diameter to wave length of less than 0.2 (i.e. small body).

$$HF_1 = 0.5 \rho C_d A_p V_w |V_w| + \rho C_m \forall \frac{dV_w}{dt} \quad (4.58)$$

where

$\rho$  = fluid density

$C_d$  = drag Coefficient

$A_p$  = projected frontal area

$V_w$  = velocity of ambient flow

$C_m$  = inertia Coefficient

$\forall$  = displaced volume of cylinder

$\frac{dV_w}{dt}$  = total acceleration

Total acceleration is the sum of local acceleration and convective acceleration. But since the nature of the hydrodynamic forces on risers is drag dominant the convective acceleration term is ignored.

For a vertical rigid circular cylinder, equation (4.58) can be expressed as:

$$HF_1 = 0.5 \rho C_d D l V_w |V_w| + \rho C_m \left( \frac{\pi D^2}{4} \right) l \dot{V}_w \quad (4.59)$$

or, wave loading per meter length is:

$$HF = 0.5 \rho C_d D V_w |V_w| + 0.25 \rho C_m (\pi D^2) \dot{V}_w \quad (4.60)$$

The Morison equation has been modified (as discussed in the review) to calculate wave loading on a flexible cylinder as follows:

$$HF = 0.5 \rho C_d D (V_w - \dot{X}) |V_w - \dot{X}| + 0.25 \rho C_m \pi D^2 \dot{V}_w - 0.25 \rho (C_m - 1) \pi D^2 \ddot{X} \quad (4.61)$$

where

$\dot{X}$  = velocity of cylinder

$\ddot{X}$  = acceleration of cylinder

In the presence of current flow as well as waves, the current velocity must be added to the velocity component in equation (4.61). So the general form of equation (4.61) becomes:

$$HF = 0.5 \rho C_d D (V_w + V_c - \dot{X}) |V_w + V_c - \dot{X}| + 0.25 \rho C_m \pi D^2 \dot{V}_w - 0.25 \rho (C_m - 1) \pi D^2 \ddot{X} \quad (4.62)$$

In the absence of wave, current or structural movements, the corresponding Kinematic Components in equation (4.62) must be set to zero.

Drag and inertia coefficients are obtained from experiments. They depend on Reynolds number, Re, Keulegan-Carpenter number, KC, and the roughness of the riser.

where

$$Re = \frac{VD}{\nu} \quad \text{and} \quad KC = \frac{VT}{D}$$

with V = velocity term in equation (4.62)

D = cylinder diameter

T = wave period

$\nu$  = kinematic viscosity

There are three types of experimental procedures to determine these coefficients:

1. placing the cylinder in a wave flume which has the disadvantage of not producing high Reynolds numbers
2. placing the cylinder in a one dimensional oscillating flow which is usually performed in a u-tube water tunnel. Its disadvantage is the lack of orbital movement of the water particles (i.e. there is no vertical component of particle movement). Hence, for a particular section along the cylinder only  $C_D$  and  $C_M$  can be determined
3. oscillating the cylinder in still water which gives the same results for  $C_D$  and  $C_M$  as the above methods after correcting for the lack of the Froude-Krylov force,  $0.25 \rho \cdot \pi D^2 \dot{V}_w$ , in the inertia term.

Four theories have been suggested to estimate hydrodynamic loading on inclined rigid cylinders. The most popular theory, suggested by Borgman (1958), is adopted in the current work. He used the same analogy as in the Morison equation for rigid vertical cylinders to derive a formula to calculate the hydrodynamic forces on inclined rigid cylinders. Morison et.al. (1958) assumed that the forces caused by waves on a vertical cylinder are dependent only on the velocity and acceleration of water particles normal to the cylinder longitudinal axis in the wave direction. Thus, applying an analogous assumption to an

inclined cylinder, the relevant water particle velocity and acceleration components are those normal to the cylinder axis in the direction defined by equation (4.69).

It is important to note that the vertical Kinematics of water particles due to wave motion were ignored by Morison and et. al. This is reasonable if the cylinder is smooth so that tangential forces due to friction will be a magnitude smaller than normal forces. But if the cylinder is a rough cylinder, this assumption will not be true. Considering that in a marine environment, a riser is usually covered with growth such as barnacles, shell fish and seaweeds which create a rough surface, it is desirable to include tangential hydrodynamic forces in the analysis.

Thus, equation (4.62) for an inclined flexible riser is:

$$\begin{aligned} HF_n = & 0.5 \rho C_d D (V_{nw} + V_{nc} - \dot{X}_n) |V_{nw} + V_{nc} - \dot{X}_n| + \\ & + 0.25 \rho C_m \pi D^2 \dot{V}_n - 0.25 \rho (C_m - 1) \pi D^2 \ddot{X}_n \end{aligned} \quad (4.63)$$

$$HF_t = 0.5 \rho C_{td} (V_{tw} + V_{tc} - \dot{X}_t) |V_{tw} + V_{tc} - \dot{X}_t| \quad (4.64)$$

where  $HF_n$  = normal hydrodynamic force per length

$HF_t$  = tangential hydrodynamic force per length

Subscript (n) denotes the component normal to the riser axis

Subscript (t) denotes the component tangential to the riser axis.

The normal and tangential components of the water particles and the structural velocities and accelerations are determined by considering a small element of riser in space, figure 4.7.

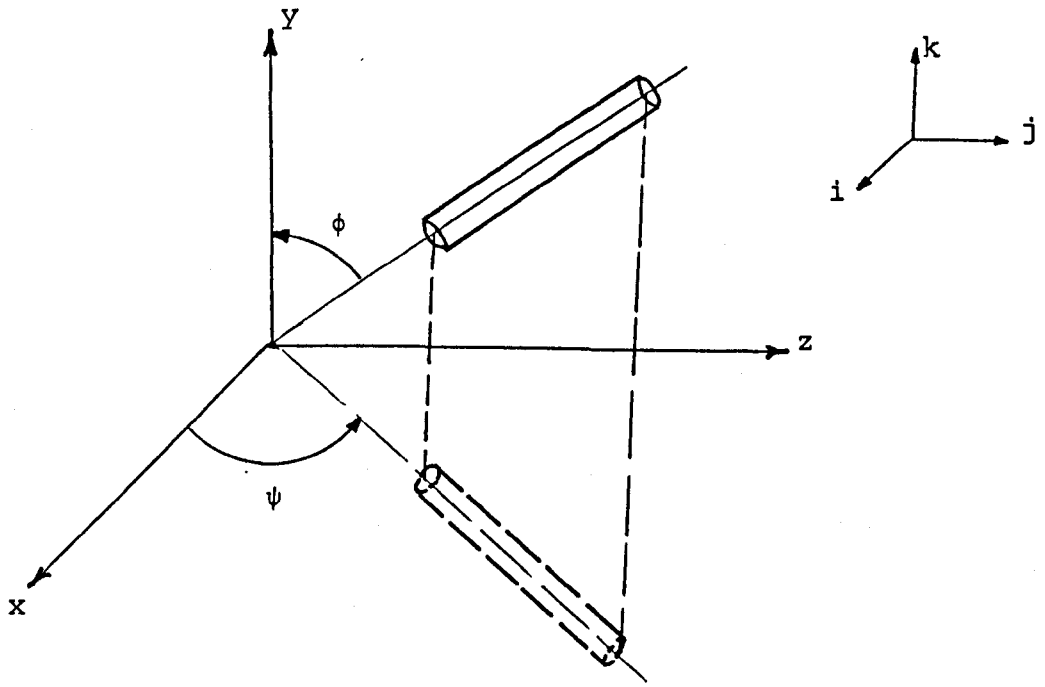


Figure 4.7  
Orientation of a riser element in space

The velocity and acceleration of the water particle or riser can be written as:

$$V = V_x i + V_z j + V_y k \text{ or } V = (V_x \ V_z \ V_y) \quad (4.65)$$

$$\dot{V} = \dot{V}_x i + \dot{V}_z j + \dot{V}_y k \text{ or } \dot{V} = (\dot{V}_x \ \dot{V}_z \ \dot{V}_y) \quad (4.66)$$

Let  $U$  be the unit vector along the cylinder. Then from figure 4.7:

$$U = U_x i + U_z j + U_y k = \sin \phi \cos \psi i + \sin \phi \sin \psi j + \cos \phi k \quad (4.67)$$

Where  $i$ ,  $j$  and  $k$  are unit vectors parallel to the  $x$ ,  $z$  and  $y$  axis respectively.

Thus,

$$\begin{aligned} U_x &= \sin \phi \cos \psi \\ U_z &= \sin \phi \sin \psi \\ U_y &= \cos \phi \end{aligned} \quad (4.68)$$

The velocity component normal to the cylinder axis can be obtained from elementary vector algebra and the direction cosine relation,  $U_x^2 + U_z^2 + U_y^2 = 1$  :

$$\begin{aligned}
 V_n &= U \times (V \times U) = \\
 & [V_x - U_x (U_x V_x + U_y V_y + U_z V_z)] i + \\
 & + [V_z - U_z (U_x V_x + U_y V_y + U_z V_z)] j + \quad (4.69) \\
 & + [V_y - U_y (U_x V_x + U_y V_y + U_z V_z)] k
 \end{aligned}$$

Equation (4.69) in matrix form is:

$$V_n = \begin{bmatrix} V_{nx} \\ V_{ny} \\ V_{nz} \end{bmatrix} = \begin{bmatrix} V_x & V_y & V_z \end{bmatrix} \cdot \begin{bmatrix} 1 - U_x^2 & -U_x U_y & -U_x U_z \\ -U_x U_y & 1 - U_y^2 & -U_y U_z \\ -U_x U_z & -U_y U_z & 1 - U_z^2 \end{bmatrix} \quad (4.70)$$

Thus:

$$\begin{aligned}
 V_{nx} &= V_x (1 - U_x^2) + V_y (-U_x U_y) + V_z (-U_x U_z) \\
 V_{ny} &= V_x (-U_x U_y) + V_y (1 - U_y^2) + V_z (-U_y U_z) \\
 V_{nz} &= V_x (-U_x U_z) + V_y (-U_y U_z) + V_z (1 - U_z^2)
 \end{aligned}$$

On simplifying:

$$\begin{aligned}
 V_{nx} &= V_x - U_x (U_x V_x + U_y V_y + U_z V_z) \\
 V_{ny} &= V_y - U_y (U_x V_x + U_y V_y + U_z V_z) \quad (4.71) \\
 V_{nz} &= V_z - U_z (U_x V_x + U_y V_y + U_z V_z)
 \end{aligned}$$

And

$$V_n = \sqrt{V_{nx}^2 + V_{ny}^2 + V_{nz}^2} \quad (4.72)$$

The component of the normal velocity in the xy plane which is the plane of wave motion can be written as:

$$V_{nxy} = \sqrt{V_{nx}^2 + V_{ny}^2} \quad (4.73)$$

Equations similar to (4.71), (4.72) and (4.73) can be derived for water particle or structural accelerations. And, since almost all wave theories are two-dimensional, the term  $V_z$  is set to zero.

The velocity component tangential to the cylinder axis can be obtained simply as follows:

$$V_t = V \cdot U = V_x U_x + V_y U_y + V_z U_z \quad (4.74)$$

Similarly a relation like (4.74) can be written for the accelerations.

#### 4.4.2 - Forces Induced by Vortex-Shedding on a Randomly Oriented Flexible Catenary Riser

Vortex shedding induced by wave and current motion around a riser produces two types of oscillations in the riser: one in the drag-inertia force and the other in the lift force directions. The former oscillation is a magnitude smaller than the latter and is also negligible compared with the response induced by the drag-inertia forces calculated from the Morison equation, so is usually ignored.

The response of flexible cylinders due to vortex-shedding in waves has not been extensively researched and almost all of the available riser programs lack the capacity to predict such responses of risers.

On the basis of recent studies of vortex-shedding induced from a cantilever cylinder, as outlined in Chapter 2, Rajabi et. al. (1984) suggested a method to deal with vortex-shedding induced response of a vertical flexible riser due to wave and current flows. This model is extended in the present work, and verified experimentally, for a riser oriented in a random manner.

The force induced by vortex-shedding per unit length,  $TF_{vor}$  on a riser, is split into two parts; namely, a lift force,  $TF_L$ , and a resisting force  $TF_r$ .

Thus,

$$TF_{VOR}(X, t) = TF_L(X, t) - TF_R(X, t) \quad (4.75)$$

The lift force is the sum of the components induced by wave and current motion.

Initially the lift force due solely to wave motion is discussed. The lift force per unit length on a flexible cylinder due to wave motion is:

$$TF_L(X, t) = 0.5 \rho D V_{nmax}^2 CL_0 (CL/CL_0) \cos(\omega_v t - \theta) \quad (4.76)$$

where

$CL/CL_0$ , the lift amplification parameter, =

the ratio of the actual lift coefficient of the oscillating cylinder to that of a stationary cylinder in a hydrodynamically similar flow

$\omega_v$  = predominant circular lift frequency

$\theta$  = a phase angle

$t$  = time

$V_{nmax}$  = amplitude of water particle velocity induced by wave motion normal to the riser axis in the direction of the drag-inertia force.

The resisting force generated as a result of the cylinder oscillation in the direction of the lift force is presented as a Morison type equation:

$$TF_R(X, t) = 0.5 \rho C_d D (\dot{X}_L) | \dot{X}_L | + \frac{\rho \pi D^2}{4} (C_m - 1) \ddot{X}_L \quad (4.77)$$

Where  $X_L(X, t)$  is the structural displacement in the direction of the lift and  $\dot{X}_L$  and  $\ddot{X}_L$  are the corresponding velocity and acceleration respectively.

The direction of the lift force is normal to the plane containing the cylinder axis and the drag-inertia force vector. The structural displacement in the direction of the drag-inertia force vector is defined as follows:

$$X_n = U \times (X \times U)$$

where U is the unit vector along the riser axis, figure 4.7. This relation suggests that the three vectors,  $X_n$ , U, and  $(X \times U)$  are orthogonal vectors. Therefore, the structural displacement in the direction of the lift force is:

$$X_L = X \times U = \begin{vmatrix} i & j & k \\ X_x & X_z & X_y \\ U_x & U_z & U_y \end{vmatrix} = (X_z U_y - X_y U_z) i \\ - (X_x U_y - X_y U_x) j + (X_x U_z - X_z U_x) k$$

Thus

$$X_{Lx} = X_z U_y - X_y U_z \\ X_{Lz} = -X_x U_y + X_y U_x \quad (4.78a) \\ X_{Ly} = X_x U_z - X_z U_x$$

And

$$X_L = \sqrt{X_{Lx}^2 + X_{Ly}^2 + X_{Lz}^2} \quad (4.78b)$$

The component of  $X_L$  in the xy plane can be written as:

$$X_{Lxy} = \sqrt{X_{Lx}^2 + X_{Ly}^2} \quad (4.78c)$$

In equation (4.76), the values of  $C_{Lo}$ ,  $\omega_v$ ,  $\theta$  and  $(C_L/C_{Lo})$  must be determined in order to calculate the lift force,  $TF_L$ .

$C_{Lo}$  which is a function of both the Reynolds and the Keulegan-Carpenter numbers, is obtained from a graph such as that presented by Sarpkaya (1976d) and reproduced in figure 4.8.

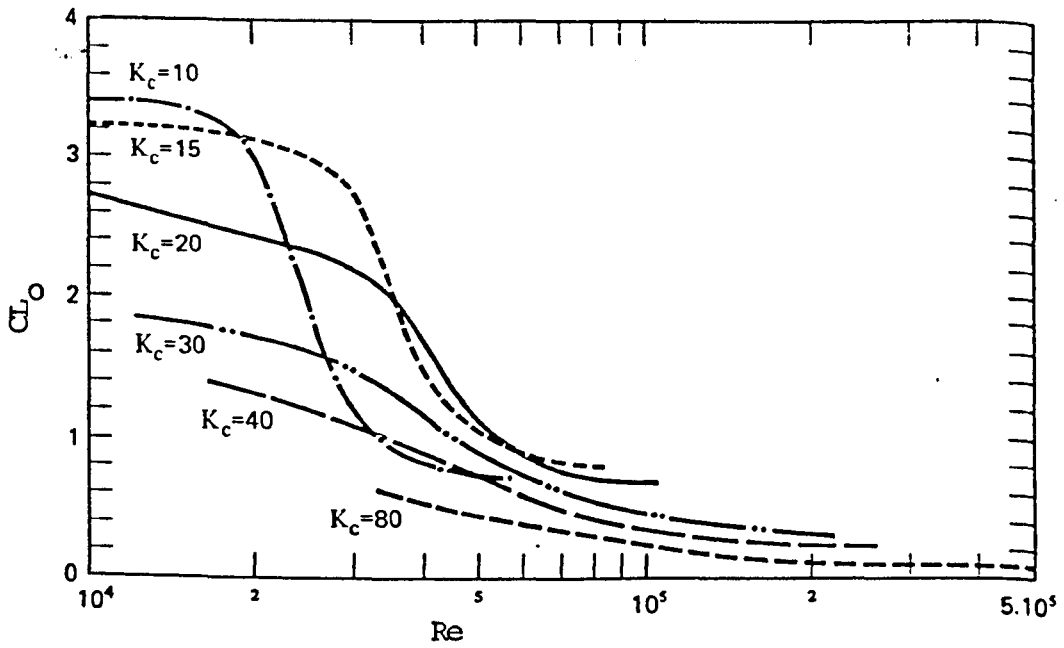


Figure 4.8 - Variation of lift coefficient with the Reynolds  
and the Keulegan-Carpenter numbers for rigid cylinders

where

$$Re = \frac{V_{nmax} \cdot D}{\nu} \quad (4.79)$$

$$KC = \frac{V_{nmax} \cdot T}{D}$$

$V_{nmax}$  = amplitude of water particle velocity normal to riser axis in the direction of the drag-inertia force.

$\nu$  = kinematic viscosity ( $10^{-6}$  for water)

D = diameter of cylinder

T = wave period

The lift frequency,  $f_L$ , is assumed to be equal to the dominant vortex-shedding frequency,  $f_v$ . The ratio of  $f_v/f_w$ , where  $f_w$  is the wave frequency, is obtained from the following graph produced by Hallam et. al. (1978), figure (4.9)

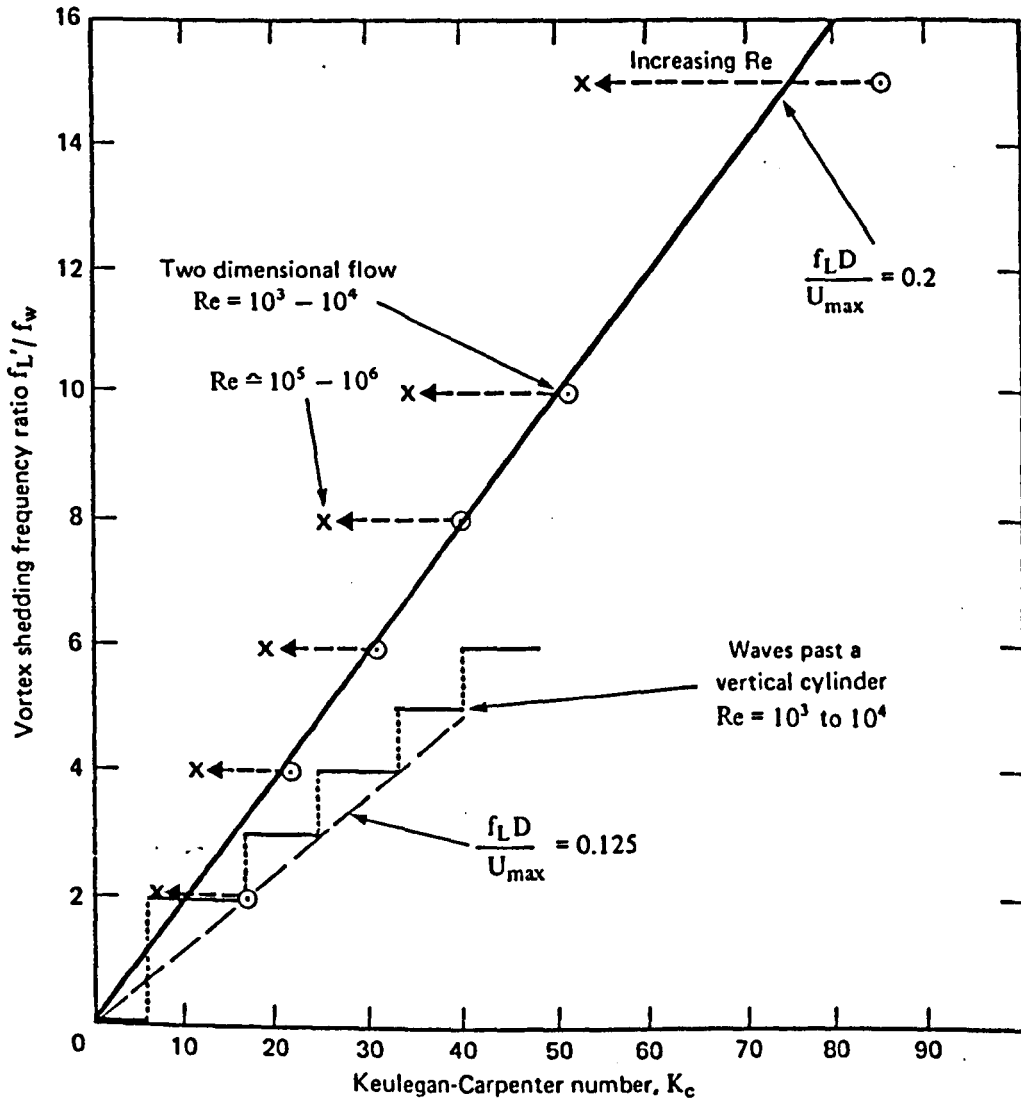


Figure 4.9 - The frequency of vortex-shedding in waves (two-dimensional results from Sarpkaya(1976a), wave results from Isaacson (1974))

For a given wave, the KC values along the riser can be calculated and hence all possible values of  $f_v$  along the riser are determined from figure (4.9). Different natural frequencies,  $f_n$ , of the riser structure are evaluated by the method explained in Chapter 5. The dominant value of  $f_v$  can then be chosen as that corresponding most closely with one of the natural frequencies  $f_n$  (see figure 4.10)

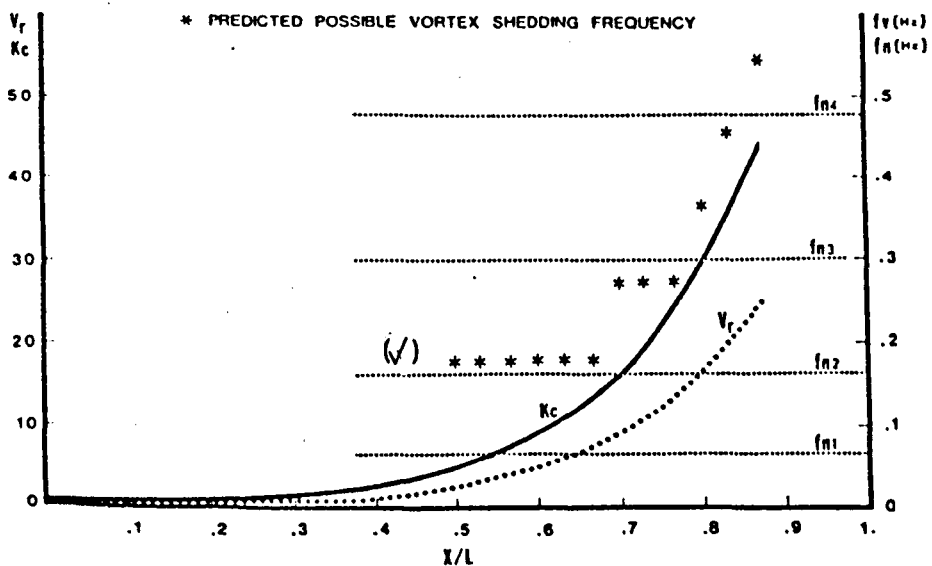


Figure 4.10 - Prediction of "lock-in" frequency from Rajabi et al (1984), the dominant  $f_v$  and  $f_n$  are shown by (✓)

Having obtained the "lock-in" values of  $f_v$  with  $f_n$ , the reduced velocities,  $V_r$ , along the riser are calculated from equation (4.80). The values of the ratio  $V_r/V_r^*$  will then enable  $C_L/C_{Lo}$  (the lift amplification parameter) values to be determined from the graph produced by Sarpkaya (1981d), figure (4.11).

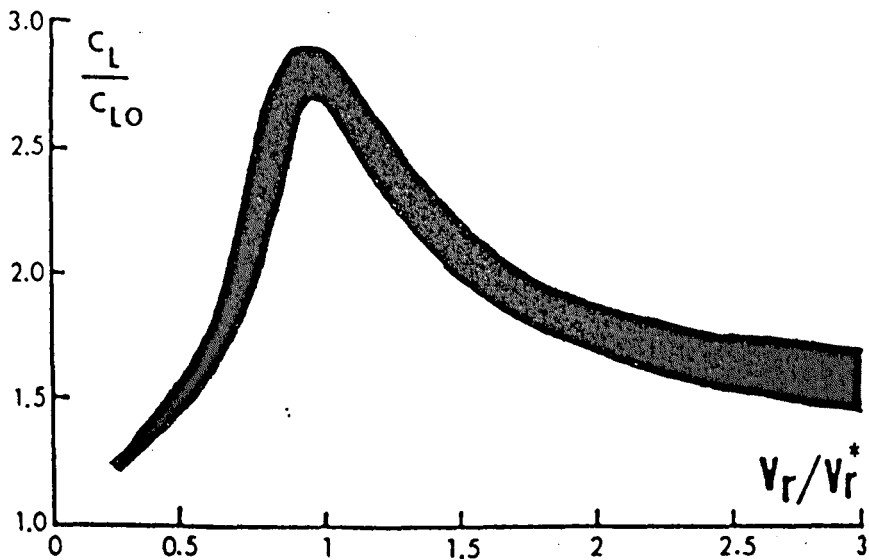


Figure 4.11 - Lift amplification correction

Where

$$V_r = \frac{V_{nmax}}{f_n D} \quad (4.80)$$

$f_n$  = natural frequency of riser

$V_r^*$  =  $V_r$  at perfect resonance. This is defined from available experimental works for different ranges of  $V_r$  values.

Since the values of  $C_{LO}$ ,  $C_L/C_{LO}$ ,  $f_v$  and hence  $\omega_v$  are defined, if it is assumed that  $\theta = 0$ , then equations 4.76 and 4.77 (and hence 4.75) can be evaluated for a whole period of vortex-shedding and the maximum values the displacements in the lift direction,  $X_{Lmax}$ , along the riser can be obtained. The following well known relations are used to obtain the magnification factor of the drag coefficient,  $(C_d/C_{do})$ , along the riser:

$$C_d/C_{do} = 1 \quad \text{for } W_r < 1 \quad (4.81)$$

$$C_d/C_{do} = 1 + 1.16 (W_r - 1)^{0.65}$$

where  $W_r = (1 + 2 X_{Lmax}/D) / (V_r St)$

$$St \text{ (Strouhal number)} = \frac{f_v D}{V_{nmax}} \quad (4.82)$$

A similar lift model can be used for the case of current motion. In equation (4.76),  $V_{nmax}$  is replaced by the local current velocity normal to the riser axis,  $V_{nc}$ , and  $C_{Lo}$  values are obtained from the graph presented by Hallam et. al. (1978), figure (4.12).

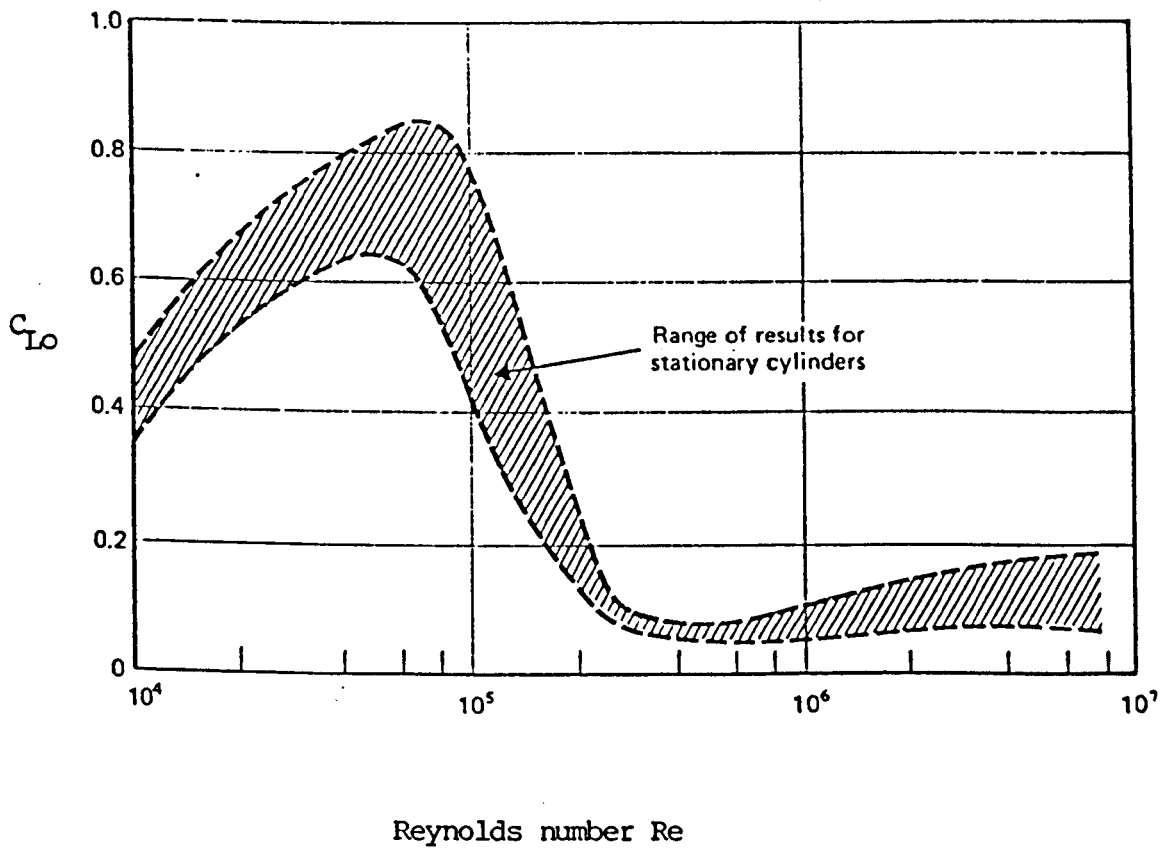


Figure 4.12 -  $C_{Lo}$  against  $Re$  for current flows

The dominant lift frequency,  $f_v$ , is evaluated as in the case of waves except that the Strouhal numbers along the riser are obtained from the Strouhal-Reynolds number correlation and then the  $f_v$  values are calculated from equation (4.82). The value usually assumed for the Strouhal number is 0.2 for a wide range of Reynolds numbers. It does, however, change for higher Reynolds numbers and rough cylinders. Since there is no available data for the ratio  $(C_L/C_{L0})$  for current alone, a value of 1 is assumed.

#### 4.4.3 - Modification of Drag-Inertia Force Equation due to Vortex-Shedding.

Taking the magnification factor of the drag coefficient into account the force equation (4.63) becomes:

$$HF_n = 0.5 \rho D C_d (C_d/C_{d0}) (V_{nw} + V_{nc} - \dot{x}_n) |V_{nw} + V_{nc} - \dot{x}_n| + 0.25 \rho C_m \pi D^2 \dot{V}_{nw} - 0.25 \rho (C_m - 1) \pi D^2 \ddot{x}_n$$

Resolving  $HF_n$  into components in the directions of the vector lying in the xy plane and the vector along the z axis:

$$HF_{nxy} = 0.5 \rho D C_d (C_d/C_{d0}) (V_{nwx} + V_{ncx} - \dot{x}_{nxy}) |V_{nw} + V_{nc} - \dot{x}_n| + 0.25 \rho C_m \pi D^2 \dot{V}_{nwx} - 0.25 \rho (C_m - 1) \pi D^2 \ddot{x}_{nxy} \quad (4.83a)$$

$$HF_{nz} = 0.5 \rho D C_d (C_d/C_{d0}) (V_{nwz} + V_{ncz} - \dot{x}_{nz}) |V_{nw} + V_{nc} - \dot{x}_n| + 0.25 \rho C_m \pi D^2 \dot{V}_{nwz} - 0.25 \rho (C_m - 1) \pi D^2 \ddot{x}_{nz} \quad (4.83b)$$

Equations (4.83a) and (4.83b) are used to calculate the normal hydrodynamic forces on flexible risers.

#### 4.5 - Assessment of Drag-Inertia Hydrodynamic Forces on Flexible Risers

For numerical analysis purposes a riser can be sub-divided into several elements as illustrated in figure 4.13.

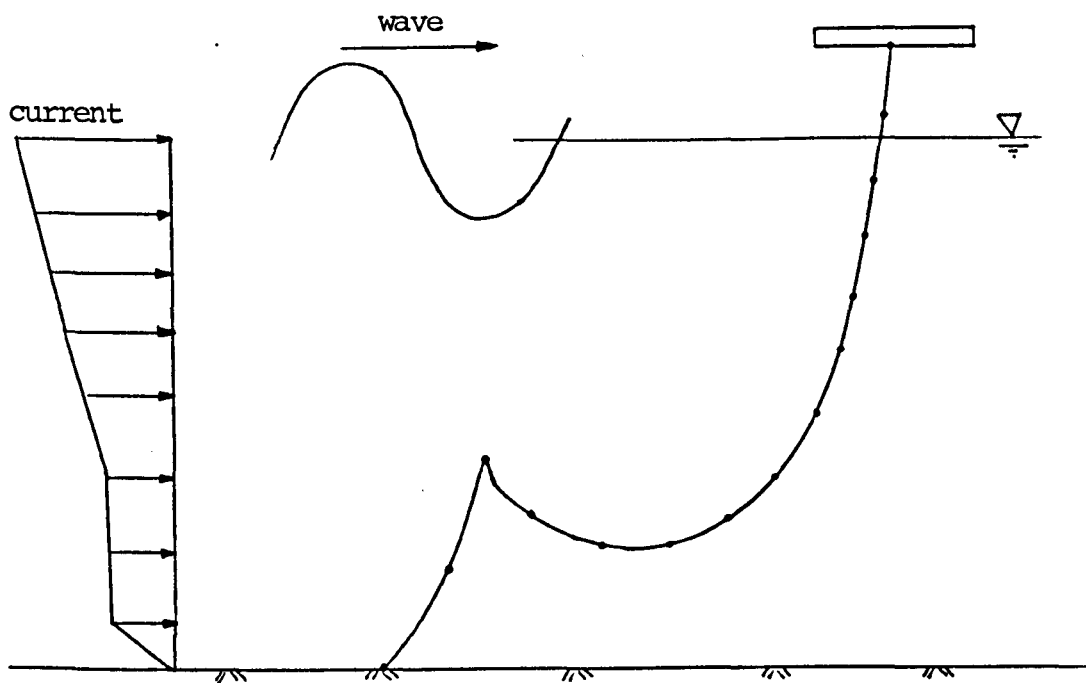


Figure 4.13 - An idealized flexible riser

The hydrodynamic loading on each element is calculated and lumped at its nodes.

The hydrodynamic loadings on the riser are calculated separately for two regions. The first region includes the forces due to waves and current flows in the range extending from the free surface down to the depth at which the horizontal wave velocity is less than 0.01 m/sec. This depth is found to have a value of half the wave length. The second region, extending to the seabed, includes the forces due to current flows only.

#### 4.5.1 - Region 1 - Hydrodynamic Loadings Induced by Wave and Currents flows.

This region includes the calculation of hydrodynamic loadings on those members for which one or both of their nodes are situated inside the effective depth of the region.

To calculate water particle velocities or accelerations induced by a wave at any point along the riser, the phase angle of the point is required. For flexible risers lying in any plane other than that normal to the wave plane, each point on the riser will be subjected to wave motion which is not in phase with that at the top node (which is known). The phase angle at any point is calculated from equation (4.84)

$$\text{Phase angle} = XK + \text{phase angle at the top node} \quad (4.84)$$

where  $X$  = horizontal distance of the point from the top node

$K$  = wave number

Having determined the phase angles, the vertical and horizontal velocities and accelerations of water particles due to a wave at any point can be calculated using Stokes wave theory (equations 4.44 to 4.47) or Linear Wave theory (equations 4.32 to 4.35).

Water particle velocity induced by a current flow is assumed to be in the horizontal plane and to change linearly with water depth; and the rate of this change can vary over the whole depth of the water. The  $x$  and  $z$  components of the velocity at any point along the riser are evaluated by knowing the vertical coordinate of that point.

The normal and its components in the  $xy$  plane and in the  $z$  direction of the water particle and structural kinematics at any

point along the riser are calculated using equations similar to (4.72), (4.73) and (4.71) respectively. Then equations (4.83a) and (4.83b) are used to evaluate the components of the hydrodynamic forces normal to the riser axis : a) in the xy plane and b) in the z axis direction at any point. The hydrodynamic forces in the wave motion plane,  $HF_{nxy}$ , along the riser are non-linear. But on the other hand, the contribution of hydrodynamic forces due to a wave in the z direction,  $HF_{nz}$ , is relatively small, and the variations of these forces along any structural element may be assumed also to be small.

There are two methods to lump the non-linear ( $HF_{nxy}$ ) forces acting on the element at its end nodes:

- 1) The number of elements is increased so that the forces on each element become nearly linear and can be lumped using a simple trapezoidal rule. This method, however, requires a very small time step for numerical stability (i.e.  $\Delta t \propto$  member length).
- 2) The forces on the element are lumped at the nodes by using the Simpson's rule.

The computation time required for a similar accuracy by both methods has been investigated. For method 1, the riser was subdivided into a certain number of elements and the dynamic response of a typical node i for a complete wave period was obtained. The number of elements was then doubled and the response of node i was compared with that obtained from the previous case. This procedure was repeated until the response of node i for the current and previous cases was reasonably close. The computation time was then compared with that taken by method

2 to obtain a similar convergence accuracy. The comparison revealed that method 2 was more efficient than method 1. Method 2 was formulated as follows:

Figure 4.14 shows the distributed hydrodynamic loading on member AB. Simpson's rule is used to calculate the total force on the member (i.e. the area). The area is initially sub-divided into 2 segments and the area is calculated. Then the number of segments is doubled and the area re-calculated and is compared with the previously calculated area. This procedure is repeated until the required precision in the calculated area is met. To minimize the computations in subsequently calculating the nodal forces at A and B, Figure 4.14, the number of segments is limited to that used in the penultimate stage.

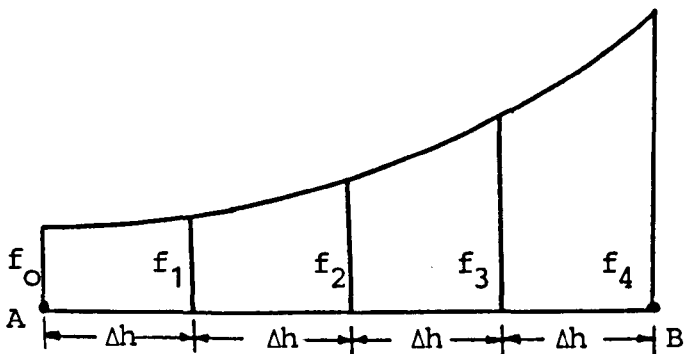


Figure 4.14 - Hydrodynamic loading on member AB

Simpson's rule is:

$$\int_{x_0}^{x_2} f(x) dx \approx \frac{h}{3} (f_0 + 4f_1 + 2f_2 + 4f_3 + \dots + 2f_{2n-2} + 4f_{2n-1} + f_{2n}) \quad (4.85)$$

The nodal forces at nodes A and B are obtained as follows;

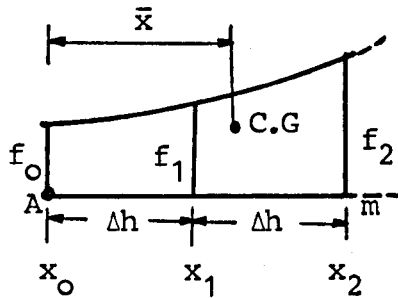


Figure 4.15 - The first two force segments on member AB

To find the centre of gravity of figure 4.15, the first moment of area of figure 4.15 is required. Using the basic formulation of Simpson's rule the following expression can be derived:

$$\int_{x_0}^{x_2} f(x) (x - x_0) dx = \frac{2}{3} (2f_1 + f_2) \Delta h^2 \quad (4.86)$$

Equation 4.86 is the first moment of area of figure 4.15 about node A. Thus the centre of gravity of the figure from node A is:

$$\bar{x} = \frac{\int_{x_0}^{x_2} f(x) (x-x_0) dx}{\int f(x) dx} = \frac{2(2f_1 + f_2) \Delta h}{f_0 + 4f_1 + f_2} \quad (4.87)$$

Equation (4.87) is used for every group of two adjacent segments along member AB (figure 4.14) and the distance of the centre of gravity of the group from its first point ( $\bar{x}$ ) and hence from node A is calculated. All the first moments of area of the groups about node A are summed up to give the total first moment of area, and the centre of gravity for the total area is evaluated by dividing the total first moment of area by the total force area. The nodal force at node B is then obtained by taking moments about point A, and the nodal force at node A by statics. This scheme is shown to be very efficient compared with the alternative of taking a larger number of structural elements. The reason for this is that the hydrodynamic loading varies more rapidly than the tension along the riser. The maximum number of segments required for the calculation of loading on any one structural element was found to be 8 during a complete cycle of wave loading. The number of such segments at any stage in the numerical procedure is varied automatically as outlined in appendix B.

The nodal forces at nodes A and B of member AB due to  $HF_{nz}$ , the z component of the hydrodynamic loads normal to the riser axis, are calculated using the trapezoidal rule, figure 4.16. However, Simpson's rule could also be adopted in the implementation if  $HF_{nz}$  is required to be more accurately represented.

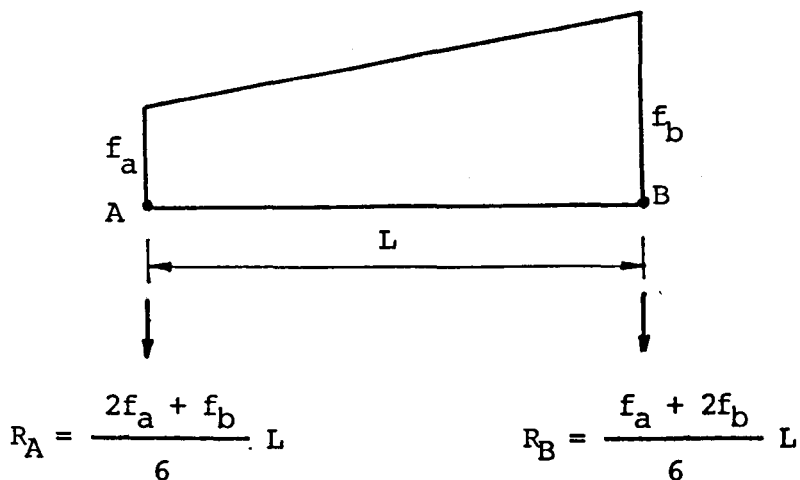


Figure 4.16 - Trapezoidal rule

The components of the water particle and structural velocities and accelerations tangential to the riser axis at both nodes of any member are calculated using an equation such as (4.74). Equation (4.64) is then employed to calculate the tangential forces which are lumped at the nodes by using the trapezoidal rule, figure 4.16.

4.5.2 - Region 2 - Hydrodynamic Loading Induced by  
Current Motion only

This region includes the hydrodynamic loading on those members that lie below the effective wave depth. The same formulations of region 1 are used to calculate the hydrodynamic loadings normal and tangential to the riser axis, but assuming zero water particle velocities and accelerations due to waves. Since the variations in loading along any structural element due to current alone are small, all forces are lumped at nodes using the trapezoidal rule, figure 4.16.

#### 4.6 - Assessment of Hydrodynamic Forces Induced by Vortex-Shedding on Flexible Risers

The forces induced by vortex-shedding on a riser are assessed in the same way as the drag-inertia forces with the following changes:

- a) The lift forces induced by wave and current flows are calculated from an equation such as (4.76). These forces are then resolved into components in the xy plane and in the z direction using relationships such as equations (4.78c) and (4.78a).
- b) The component of the structural velocity and acceleration at any point along a riser in the direction of the lift force are obtained from relations like equations (4.78a, b and c). Hence the components of the resisting forces due to structural movement in the xy plane and in the z direction may be calculated.
- c) The resultant forces due to vortex-shedding are subsequently calculated from equation (4.75).
- d) Both components of the resultant forces in the xy plane and z direction are lumped at nodes using Simpson's rule.

The term  $V_{nmax}$  in equation (4.76) for each member of the riser is obtained by considering the equation for water particle velocity normal to the riser axis,  $V_n$ :

$$V_n = [ V_x^2 + V_y^2 - (U_x V_x + U_y V_y)^2 ]^{1/2} \quad (4.88)$$

Where  $U$  is the unit vector along the riser. From the Linear wave theory for deep water waves:

$$\begin{aligned} V_x &= A f(y) \cos \theta \\ V_y &= A f(y) \sin \theta \end{aligned} \quad (4.89)$$

where  $\theta = KX - \omega t$  and  $A = \text{constant}$

Substituting  $V_x$  and  $V_y$  from equation (4.89) into equation (4.88) and simplifying:

$$V_n = A f(y) [1 - (U_x \cos \theta + U_y \sin \theta)^2]^{1/2}$$

$V_n$  at any position along a riser is a maximum when  $\partial V_n / \partial \theta = 0$ .

Thus,  $V_n$  is maximum when the following relation exists:

$$U_x \cos \theta + U_y \sin \theta = 0$$

$$\text{or } \theta = \tan^{-1} \left( -\frac{U_x}{U_y} \right) \quad (4.90)$$

The values of  $\theta$  for each member are initially calculated and  $V_{n\max}$  is considered to be dependent only on the position along the riser.

#### 4.7 - Simulation of Splash Zone

The area around the free surface of the wave is usually referred to as the splash zone. An iteration procedure is required to obtain the conjunction point of the flexible riser with this free surface for hydrodynamic force calculation purposes. Figure 4.17 shows the wave profile and the position of member AB (piercing member) at time  $t$  and  $t + \Delta t$  and the iteration procedure. The aim is to determine the position of the conjunction point at time  $t + \Delta t$ , (point  $m'$ ).

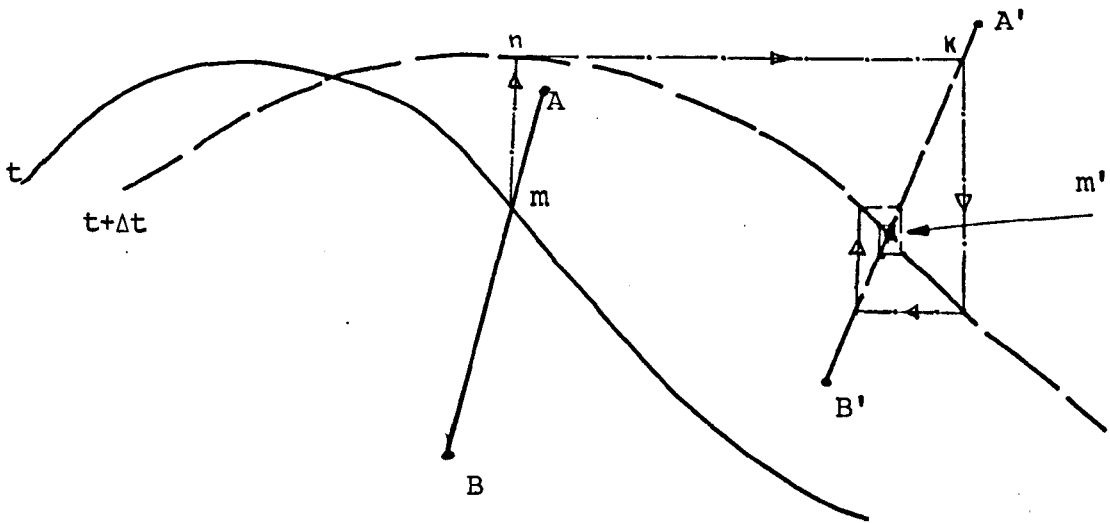


Figure 4.17 - Iteration procedure to obtain the conjunction point of the piercing member and wave profile

The iteration is started by considering point  $m$  (the conjunction point of member  $AB$  with the wave surface at the previous time step) to be the initial trial point. Point  $m$  is projected vertically to the wave surface at time  $t + \Delta t$  to give the intercept, point  $n$ . This point is then projected horizontally onto member  $A'B'$  (the position of member  $AB$  at time  $t + \Delta t$ ) to give point  $k$ . Point  $k$  is subsequently considered as the new initial guess point and the above procedures are repeated. This iteration process is carried out until convergence is obtained. The length of member  $A'B'$  is then temporarily set equal to  $B'm'$ , though only for the purpose of calculating the hydrodynamic loading. When, however, the nodal forces at nodes  $A$  and  $B$  are to be calculated, the whole length of the member must be considered (figure 4.18).

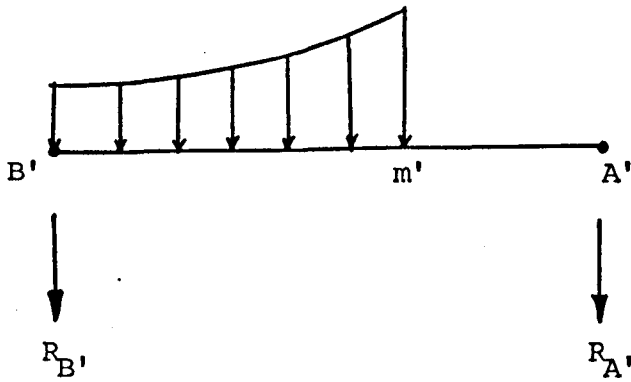


Figure 4.18 - Nodal hydrodynamic forces  
on the piercing member

The current velocity is given up to the still water surface. In order to adjust the current velocity at the wave surface the following modification is carried out:

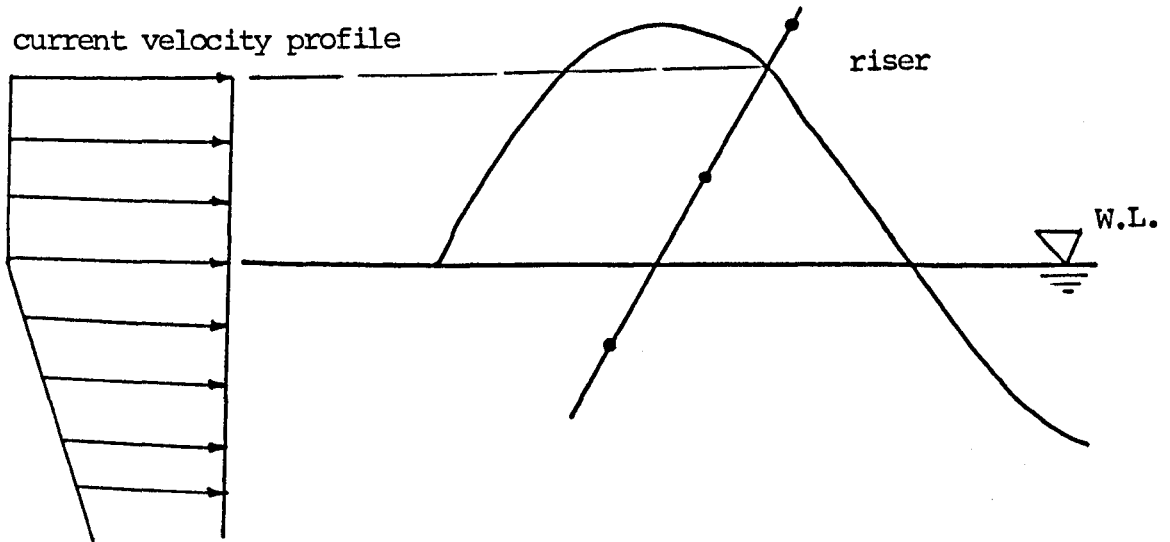


Figure 4.19 - Adjustment of current induced  
velocity with wave profile

- a) When the wave surface is above the still water level, a constant current velocity profile which is extended from the still water level up to the wave surface, and has a value equal to that at the still water level is considered (figure 4.19).
  
- b) When the wave surface is below the still water level, only the standard variation for the current velocity is considered.

#### 4.8 - Modelling of Platform Motion

Platform motion is considered as a motion with six degrees of freedom: three translational and three rotational. The translational motions in the x, y and z directions are referred to respectively as surge, heave and sway; and the rotational motions about the x, y and z directions as respectively the roll, yaw and pitch (figure 4.20).

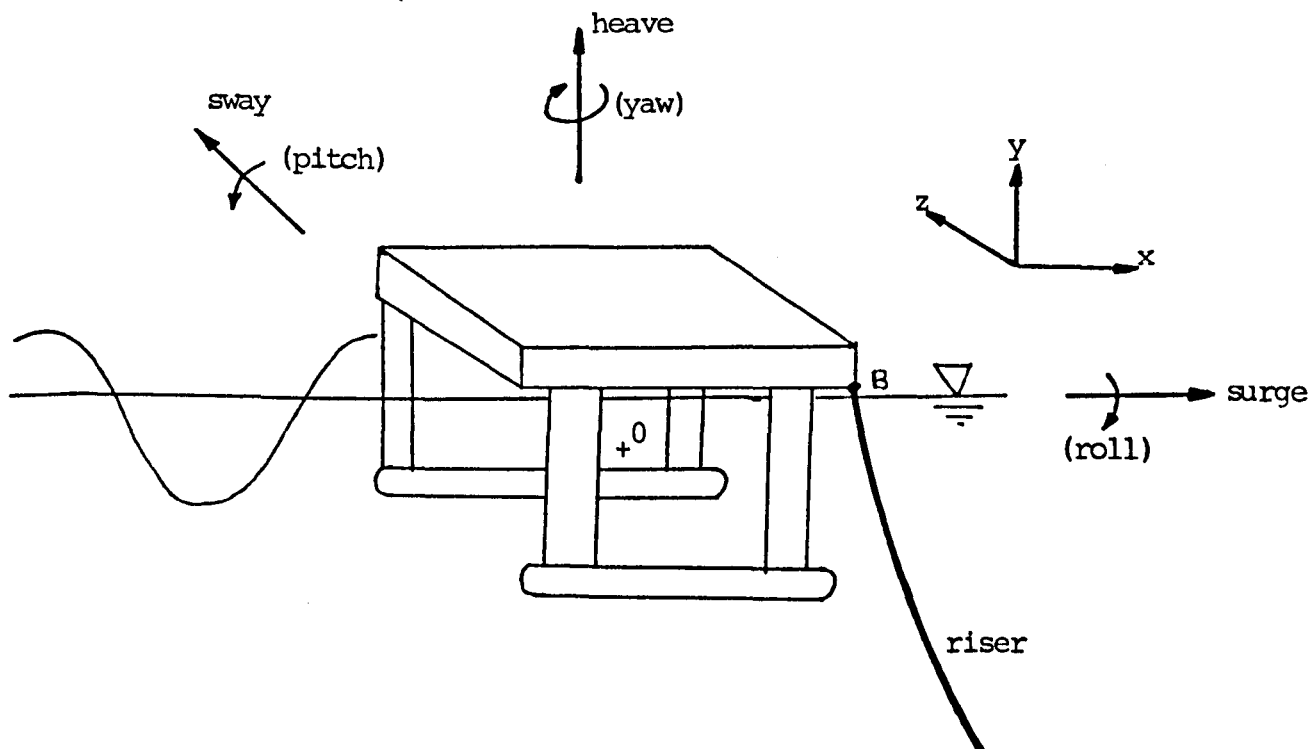


Figure 4.20 - Platform motion

These motions are usually given at the centre of gravity of the platform (point O in figure 4.20) which is referred to as the centre of motion. The motions are then transferred to the connector at which the riser top is attached (point B in figure 4.20) using the given position of the connector on the platform. The translational motions on the riser top are expressed by the following equation:

$$X_i = A_i \cos (K DX_1 - \omega t + \theta_i) \quad (4.88)$$

$i = 1, 3$

where

$X_1$  = surge motion

$X_2$  = heave motion

$X_3$  = sway motion

$A_i$  = amplitude of the motion in the  
direction considered

$K$  = wave number

$DX_1$  = distance of the riser top position  
from the centre of motion in the  
surge direction

$\omega$  = wave circular frequency

$\theta_i$  = phase angle of the platform motion with  
wave motion in the directions considered

The rotational motions, which introduce additional translational motions at the riser top, are described by the following equation:

$$\alpha_j = A_j (-\omega t + \beta_j) \quad (4.89)$$

$j = 1, 3$

where

$\alpha_1$  = pitch motion

$\alpha_2$  = yaw motion

$\alpha_3$  = roll motion

$A_j$  = amplitude of the rotation in the  
direction considered

$\beta_j$  = phase angle of the platform motion with  
wave motion in the direction considered.

These rotational motions cause the following additional translational motions:

- a) Pitch motion causes surge and heave motions.
- b) Yaw motion causes surge and sway motions.
- c) Roll motion causes sway and heave motion.

Let the components of the distance between the riser top and the centre of motion (OB) along the x, y and z axes be  $DX_1$ ,  $DX_2$  and  $DX_3$  respectively. The translational motions caused by pitch are calculated using the projected length of OB in the xy plane (figure 4.21).

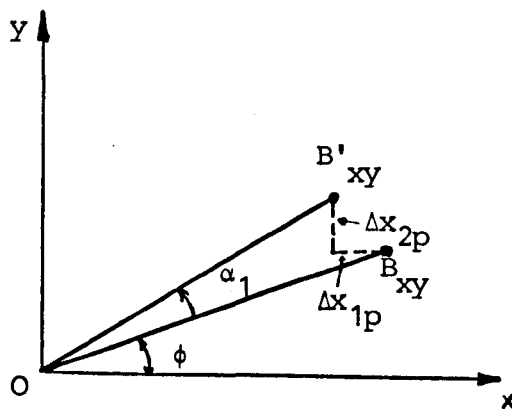


Figure 4.21 - Pitch induced translational motions of the riser top connector

Let  $OB_{xy}$  be the projected length of OB in the xy plane, where  $OB_{xy} = \sqrt{DX_1^2 + DX_2^2}$ , and  $\phi = \tan^{-1} (DX_2/DX_1)$ . Suppose  $OB_{xy}$  is displaced to  $OB'_{xy}$  after pitch motion  $\alpha_1$ , and produces the translational motions,  $\Delta X_{1p}$  and  $\Delta X_{2p}$ , at the riser top.  $\Delta X_{1p}$  and  $\Delta X_{2p}$  can be calculated using the simple geometry in figure 4.21 as follows:

$$\Delta X_{1p} = OB_{xy} [\cos (\phi) - \cos (\alpha_1 + \phi)] \quad (4.90)$$

$$\Delta X_{2p} = OB_{xy} [\sin (\phi + \alpha_1) - \sin (\phi)] \quad (4.91)$$

Similarly for yaw motion, using the projected length of OB in the xz plane:

$$\Delta X_{1y} = OB_{xy} [\cos (\psi) - \cos (\alpha_3 + \psi)] \quad (4.92)$$

$$\Delta X_{2y} = OB_{xz} [\sin (\alpha_3 + \psi) - \sin (\psi)] \quad (4.93)$$

where

$$OB_{xz} = \sqrt{DX_1^2 + DX_3^2}$$

$$\psi = \tan^{-1} (DX_1/DX_3)$$

Similarly for roll motion, using the projected length of OB in the zy plane:

$$\Delta X_{3r} = OB_{zy} [\cos (\theta) - \cos (\alpha_2 + \theta)] \quad (4.94)$$

$$\Delta X_{2r} = OB_{zy} [\sin (\alpha_2 + \theta) - \sin (\theta)] \quad (4.95)$$

where

$$OB_{zy} = \sqrt{DX_2^2 + DX_3^2}$$

$$\theta = \tan^{-1} (DX_2/DX_3)$$

Thus, the total translational motions with the consideration of the conventional directions used in figure 4.20 are:

$$\text{surge} = X_1 - \Delta X_{1p} + \Delta X_{1y} \quad (4.96)$$

$$\text{heave} = X_2 + \Delta X_{2p} + \Delta X_{2r} \quad (4.97)$$

$$\text{sway} = X_3 - \Delta X_{3y} - \Delta X_{3r} \quad (4.98)$$

## CHAPTER 5

### THEORETICAL DEVELOPMENTS FOR THE ANALYSIS OF FLEXIBLE RISERS

#### 5.1 - Introduction

In this chapter various numerical schemes to solve the motion equations are reviewed and the central difference scheme for the time integration of Newton's second law is developed in detail. Methods to optimize this numerical technique are subsequently considered.

Static solutions for flexible risers are obtained using a similar technique to the dynamic analyses but with artificially high damping. This technique corresponds with the method known as Dynamic Relaxation. Natural frequencies for the riser can also be obtained from numerical results using Fourier analysis. As indicated in the previous chapter, these frequencies are required in order to assess the effect of vortex shedding on the hydrodynamic forces.

Finally, the model scaling laws for flexible risers in waves and current flows are outlined as a prelude to the interpretation of experimental results.

## 5.2 - Dynamic Analysis of Flexible Risers

### 5.2.1 - Numerical Schemes for Structural Dynamics

Generally, there are two broad approaches to solving transient structural problems. One is to integrate numerically the motion equations by marching in a series of time steps,  $\Delta t$ , evaluating displacements, accelerations and velocities at each time step (i.e. direct integration). The second approach is the mode-superposition method, which transforms the problem into a set of independent differential equations, one for each degree of freedom. Solution of these equations is followed by superposition of the results. This scheme is much faster than the first method but it can not readily be used for non-linear dynamic problems. When this scheme is used to analyse the flexible riser problem, it is essential to linearise the relative velocity square term in the Morison equation. If this approximation is not chosen carefully, large inaccuracies result.

There are two basic classes of direct integration methods: explicit and implicit methods. In the implicit method the equations for the displacement at time  $t + \Delta t$  involve the velocities and accelerations at time  $t + \Delta t$ . Considering the fact that in the motion equations for a flexible riser the non-linear hydrodynamic forces are a function of the riser displacement, using the implicit technique therefore requires an iteration procedure at each time step to evaluate the displacements. Implicit schemes have the advantage that, for linear systems, they are unconditionally stable. Thus the magnitude of the time step is only restricted in size by accuracy requirements. In explicit methods, the displacement at time  $t + \Delta t$

is obtained by solving the equations of motion at time  $t$ . This means that iteration in each time step is not required. However, such schemes are only conditionally stable which means that the size of the time step is restricted by numerical stability requirements. This will usually result in a time increment much smaller than that needed for the requisite accuracy.

In this study, the dynamic response of the flexible riser is analysed by central difference discretisation (i.e. an explicit scheme) of the motion equations based on Newton's Second law. The theory is subsequently optimized in order to adopt the largest possible integration time step and reduce the computation time.

### 5.2.2 - Dynamic Solution

The riser is subdivided into a number of segments. The external forces due to the hydrodynamic loadings and self weight of the riser are lumped at the nodes. The method for calculating and lumping the hydrodynamic forces were described in Chapter 4 in Sections 4.4 and 4.5 respectively. The self weight of each element is equally distributed on each node of the element.

The equation of motion for each node in any co-ordinate direction is established by considering Newton's Second law:

$$M \ddot{X}_t = R(t)_t \quad (5.1)$$

where  $M$  = Structural mass at the node.

$\ddot{X}$  = Structural acceleration in the direction considered.

$R(t)$  = Time varying force in the direction considered.

The central difference approximation for the acceleration is:

$$\ddot{X}_t = (\dot{X}_{t+\Delta t/2} - \dot{X}_{t-\Delta t/2}) / \Delta t \quad (5.2)$$

Where  $\dot{X}$  = structural velocity in the direction considered. On substituting equation (5.2) into equation (5.1) and rearranging:

$$\dot{X}_{t+\Delta t/2} = (\Delta t/M) R(t) + \dot{X}_{t-\Delta t/2} \quad (5.3)$$

The time varying force  $R(t)$  should include forces due to hydrodynamic loading, structural self weight, structural damping, axial forces in structural segments and shear forces due to the difference in bending moments between adjacent segments.

It is assumed that material properties of the riser are visco-elastic and can be represented by a single Kelvin System coupled with an elastic response (Zienkiewicz et. al. (1968)). Considering uni-axial creep stress-strain relations characterized by a single Kelvin model (fig. 5.1), the 'creep rate' may be written as:

$$\dot{\epsilon}_c = a. \sigma - b. \epsilon_c \quad (5.4)$$

Where  $a, b =$  constants which depend on material damping and are obtained from simple experiments on a riser segment

$\epsilon_c =$  accumulated creep strain

$\dot{\epsilon}_c =$  rate of creep strain

$\sigma =$  current stress level.

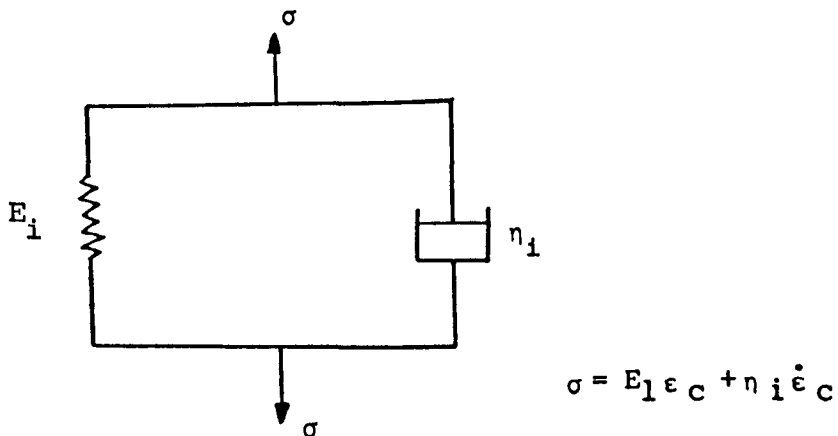


Figure 5.1 - Single Kelvin model

The material properties may be presented more accurately by employing several Kelvin elements placed in series:

$$\dot{\epsilon}_c = \sum_{r=1,n} a_r \cdot \sigma - \sum_{r=1,n} b_r \cdot \epsilon_c \quad (5.5)$$

But since in this study the vibration damping effect of visco-elastic properties is the main concern rather than the long-term creep investigations, a single model is considered to be sufficient. The procedure outlined, however, applies equally well to series models for long-term creep.

Using a central difference scheme:

$$\epsilon_c^t = ( \epsilon_c^{t+\Delta t/2} + \epsilon_c^{t-\Delta t/2} ) / 2 \quad (5.6)$$

$$\dot{\epsilon}_c^t = ( \epsilon_c^{t+\Delta t/2} - \epsilon_c^{t-\Delta t/2} ) / \Delta t \quad (5.7)$$

on substituting equations (5.6) and (5.7) into equation (5.4) and rearranging:

$$\epsilon_c^{t+\Delta t/2} = \frac{a \cdot \Delta t}{1 + b \cdot \Delta t/2} \sigma^t + \frac{1 - b \cdot \Delta t/2}{1 + b \cdot \Delta t/2} \epsilon_c^{t-\Delta t/2} \quad (5.8)$$

where  $\sigma^t = [ (EA/L_0) / A ] ( \Delta L^t - \epsilon_c^{t-\Delta t/2} \cdot L_0 )$

$EA/L_0$  = longitudinal stiffness of the member

$A$  = cross-sectional area of the element

$\Delta L$  = total extension in the element

$L_0$  = original length of the member.

The elastic extension of an element is:

$$\Delta L_e^t = \Delta L^t - \epsilon_c^{t-\Delta t/2} \cdot L_0 \quad (5.9)$$

Where

$\Delta L_e$  = elastic extension in the element

Considering the compatibility equation for the riser, the current tension coefficient (tension/length) in an element is given by:

$$TC_t = [T_i + (EA/L_0) \cdot \Delta L_e^t] / L_t \quad (5.10)$$

Where

TC = tension coefficient

EA/L<sub>0</sub> = longitudinal stiffness of the element

T<sub>i</sub> = initial specified tension in the element

The forces in the x co-ordinate direction contributed by the element at its end nodes are:

$$F_{xt} = TC_t \cdot dX_t \quad \text{at node 1} \quad (5.11)$$

$$F_{xt} = - TC_t \cdot dX_t \quad \text{at node 2} \quad (5.12)$$

where

dX = projection of the element length in the x direction.

Similar relations can be written for the y and z directions.

The changes in the values of the curvatures and hence the moments acting across element sides at any stage from their initial values are determined from the normal nodal displacement of adjacent elements and the moments are then transferred to equivalent nodal shear forces. Considering three elements (a), (b), and (c), figure (5.2), and if the normals to the element mid-point are constructed then for small  $\delta\phi_i$  and  $\delta\phi_j$ :

$$r_{ix} \cdot \delta\phi_i = (L_a + L_b) / 2$$

$$r_{jx} \cdot \delta\phi_j = (L_b + L_c) / 2$$

Then, if it is assumed that  $r_{ix}$  and  $r_{jx}$  are the mean radii of curvature of deformation for the flexural members in the x-y plane at nodes i and j respectively, the bending moments,  $M_i$  and  $M_j$  may be expressed as:

$$M_i = EI \cdot \frac{1}{r_{ix}} = EI \cdot \frac{2 \delta \phi_i}{(L_a + L_b)}$$

$$M_j = EI \cdot \frac{1}{r_{jx}} = EI \cdot \frac{2 \delta \phi_j}{(L_b + L_c)}$$

Where  $EI$  is the bending stiffness of the element.

For  $M_i$  and  $M_j$  taken as a positive hogging moment, with  $\delta\phi_i$  and  $\delta\phi_j$  positive as shown in Figure (5.2), then:

$$M'_{im} = M_i = - M'_{ij} \quad (5.13)$$

$$M'_{ji} = M_j = - M'_{jk} \quad (5.14)$$

The bending action is effectively idealised as a series of constant moments between element mid-points. The resultant nodal shear forces are:

$$SF_{bi}^t = - (M'_{ij} + M'_{ji}) / L_b^t \quad (5.15)$$

$$SF_{bj}^t = (M'_{ij} + M'_{ji}) / L_b^t \quad (5.16)$$

where

$SF_{bi}^t$ ,  $SF_{bj}^t$  = shear force at node  $i$  and  $j$  of member  $b$  at time  $t$  respectively

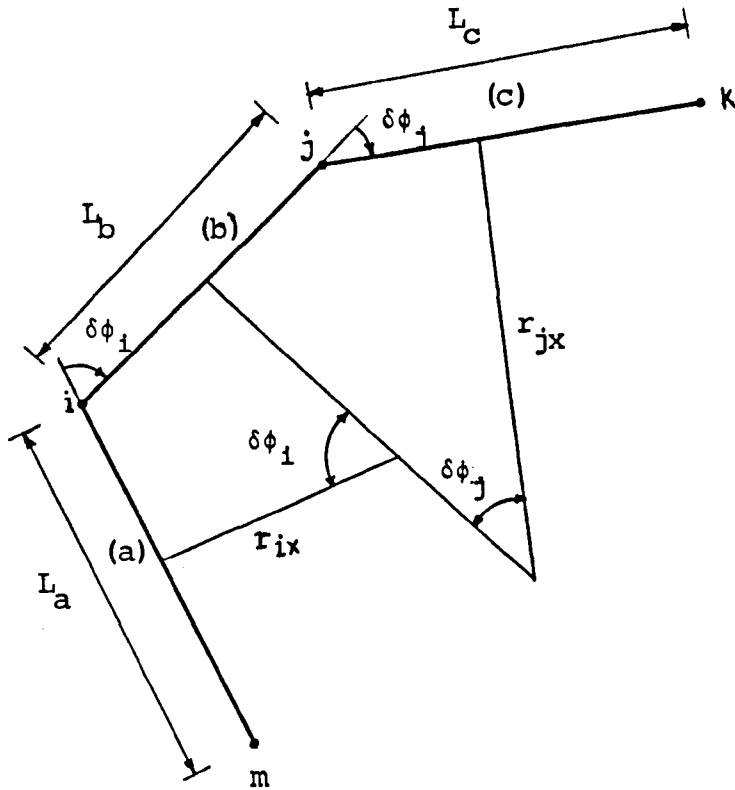


Figure 5.2 - Definition sketch for flexure of adjacent members in the x-y plane

Similarly the above relations for the nodal shear forces can be written for the z-y plane using the mean radii curvature in the z-y plane.

The above shear forces are then resolved in the x, y and z directions.

Since the movements of the riser are in space there are also twisting moments induced by swaying the elements relative to adjacent elements from their initial positions. These moments should be transformed to equivalent twisting nodal forces normal to the members. But the torsional stiffness of flexible risers is very small and hence these nodal twisting forces are ignored in this work. The method of calculating these nodal forces is, however, given in Appendix C.

The time varying nodal forces  $R(t)$  in the x, y and z directions are then:

$$\begin{aligned} R(t)_{xt} &= F_{xt} + SF_{xt} + HF_{xt} \\ R(t)_{zt} &= F_{zt} + SF_{zt} + HF_{zt} \\ R(t)_{yt} &= F_{yt} + SF_{yt} + HF_{yt} + P \end{aligned} \quad (5.17)$$

where

$P$  = nodal force due to self weight of adjacent elements

$HF$  = nodal hydrodynamic loading in the direction considered.

Substituting  $R(t)$  from equation (5.17) into equation (5.3),

$\dot{X}_{t+\Delta t/2}$  may be evaluated. Updating the nodal displacements:

$$X_{t+\Delta t} = X_t + \dot{X}_{t+\Delta t/2} \cdot \Delta t \quad (5.18)$$

The procedures from equations (5.3) to (5.18) represent the complete iteration sequence which is given in figure 5.3.

For the initial conditions (at time = 0),  $\dot{X}_{-\Delta t/2}$  is assumed to be equal and opposite to  $\dot{X}_{\Delta t/2}$  and  $\epsilon_c^{-\Delta t/2}$  is assumed zero.

Calculation of the hydrodynamic forces at time  $t+\Delta t$  requires the structural velocity and acceleration at time  $t+\Delta t$ . But the equation of motion is solved for the velocity at time  $t+\Delta t/2$ . Thus the following central difference approximations are made to obtain the structural velocity and acceleration at time  $t+\Delta t$  and are only used in calculating the hydrodynamic loadings:

$$\dot{X}_t = (\dot{X}_{t+\Delta t/2} + \dot{X}_{t-\Delta t/2}) / 2 \quad (5.19)$$

$$\dot{X}_{t+\Delta t/2} = (\dot{X}_{t+\Delta t} + \dot{X}_t) / 2 \quad (5.20)$$

Substituting for  $\dot{X}_t$  from equation (5.19) into equation (5.20) and rearranging for  $\dot{X}_{t+\Delta t}$  :

$$\dot{X}_{t+\Delta t} = \frac{1}{2} (3 \dot{X}_{t+\Delta t/2} - \dot{X}_{t-\Delta t/2})$$

The structural acceleration at time  $t+\Delta t$  from equation (5.2) is:

$$\ddot{X}_{t+\Delta t} = (\dot{X}_{t+3\Delta t/2} - \dot{X}_{t+\Delta t/2}) / \Delta t \quad (5.21)$$

Writing equation (5.19) for  $\dot{X}_{t+\Delta t}$  and rearranging it for  $\dot{X}_{t+3\Delta t/2}$  :

$$\dot{X}_{t+3\Delta t/2} = 2\dot{X}_{t+\Delta t} - \dot{X}_{t+\Delta t/2} \quad (5.22)$$

Substituting for  $\dot{X}_{t+3\Delta t/2}$  from equation (5.22) into equation (5.21) and simplifying, gives an expression for the structural acceleration at time  $t+\Delta t$ :

$$\ddot{X}_{t+\Delta t} = (2/\Delta t) (\dot{X}_{t+\Delta t} - \dot{X}_{t+\Delta t/2})$$

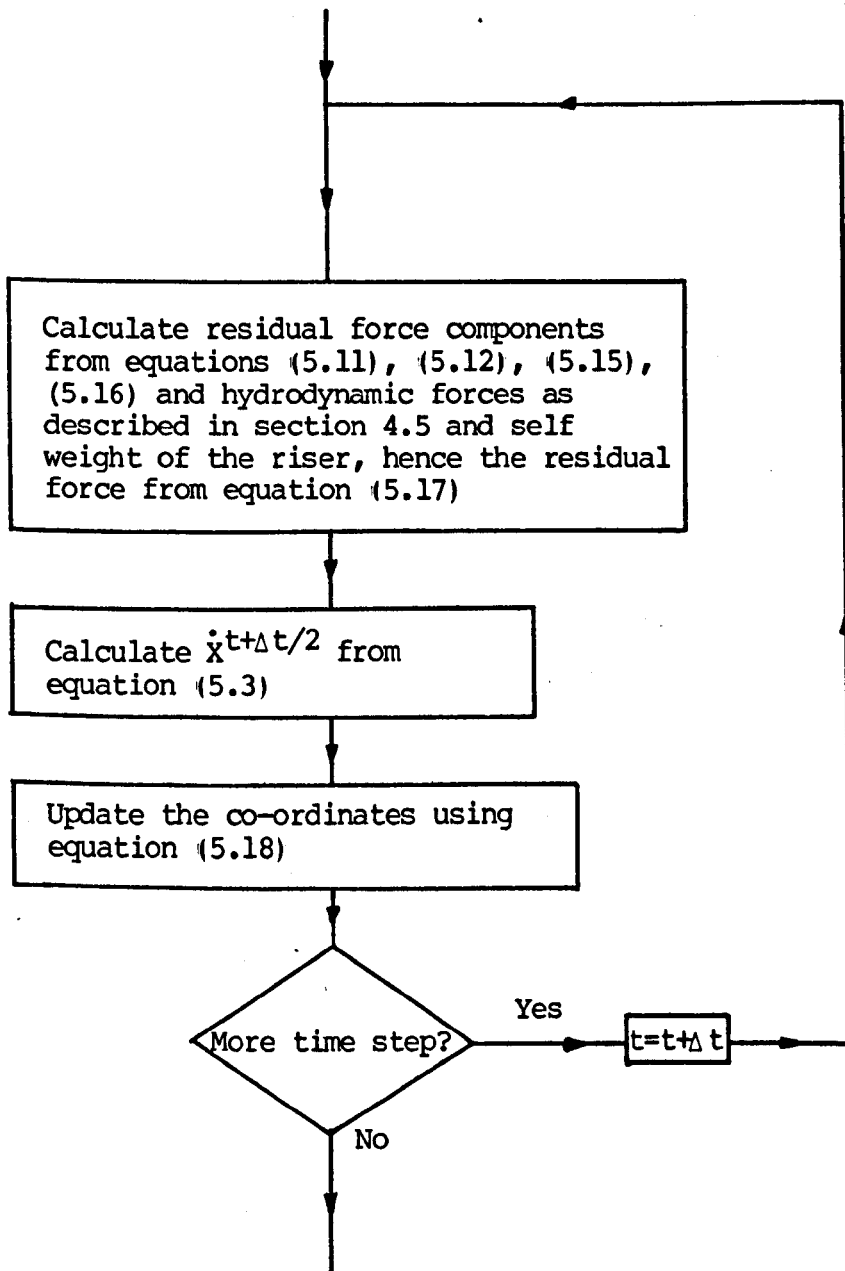


Figure 5.3 - Flow chart of dynamic solution algorithm

### 5.2.3 - Stability of the Numerical Integration

The central difference numerical scheme which is used in this work, is a conditionally stable scheme which means that if the integration time interval,  $\Delta t$ , exceeds a certain critical value then numerical instability may occur. The critical time step is given by Bath et. al. (1976) as:

$$\Delta t_{\text{cri}} = \frac{T_n}{\pi} \quad (5.23)$$

where  $T_n$  is the period of the smallest natural frequency of the riser. This can be found by solving the eigenvalue problem for the structure.

Barnes (1974) has directly derived criteria for stability of the numerical integration by considering the relative motion of adjacent nodes as follows:

Consider the vibration of a node  $i$  in the principle-axis direction. Let node  $i$  have structural connections to adjacent nodes  $k$ . Using equation (5.3):

$$\dot{x}_{t+\Delta t/2}^{ip} = (\Delta t/M) R(t)^{ip} + \dot{x}_{t-\Delta t/2}^{ip} \quad (5.24)$$

For simplicity let  $A = \frac{\Delta t}{M}$ .

Thus,

$$\dot{x}_{t+\Delta t/2}^{ip} = A_i R(t)^{ip} + \dot{x}_{t-\Delta t/2}^{ip} \quad (5.25)$$

For the next time step, assuming that the motions of nodes  $i$  and  $k$  are parallel to the  $p$ -axis:

$$\dot{x}_{t+3\Delta t/2}^{ip} = A_i [ R(t)^{ip} - \sum_{\text{all links at } i} S_{t+\Delta t}^{ikp} \cdot \Delta X_{t+\Delta t}^{ikp} ] + \dot{x}_{t+\Delta t/2}^{ip} \quad (5.26)$$

Where,  $S_{t+\Delta t/2}^{ikp}$  = the p-axis direct stiffness of node i relative to adjacent nodes k due to the structural elements connecting nodes i and k

$\Delta X_{t+\Delta t/2}^{ikp}$  = the increment of p-deflection of node i relative to adjacent node k during the time interval  $t \longrightarrow t+\Delta t$

If the time interval is large when the stiffness/mass ratio ( $S^{ikp}/M$ ) is large, instability in the form of successive reversal and build up in the amplitude of velocities and deflections may occur.

Bounds to  $\Delta t$  may be obtained by considering adjacent nodes I and K of a part of a structure at which the S/M ratio of the nodes, or one of the nodes (in the p-axis direction), is highest. The most critical structural configuration and state of motion will be such that all nodes k adjacent to I are different from all nodes i adjacent to K, with the relative vibrations of node i and k exactly out of phase.

Substituting  $R(t)^{ip}$  from equation (5.25) into equation (5.26), for node I, leads to:

$$X_{t+3\Delta t/2}^{.Ip} - 2 X_{t+\Delta t/2}^{.Ip} + X_{t-\Delta t/2}^{.Ip} = - A_I \sum [S^{Ikp} \cdot (\Delta X^{IP} - \Delta X^{kp})]_{t+\Delta t} \quad (5.27)$$

and similarly for node K

$$X_{t+3\Delta t/2}^{.Kp} - 2 X_{t+\Delta t/2}^{.Kp} + X_{t-\Delta t/2}^{.Kp} = - A_K \sum [S^{Kip} \cdot (\Delta X^{Kp} - \Delta X^{ip})]_{t+\Delta t} \quad (5.28)$$

For the most critical condition assume that the direct stiffness/mass ratios of all nodes i and k are equal, and for oscillations which are just stable: All  $\Delta X^{iP} = \Delta X^{kP}$  and all  $\Delta X^{kP} = \Delta X^{kP}$ .

Thus, subtracting equation (5.28) from equation (5.27):

$$\dot{X}_{t+3\Delta t/2}^{IKp} - 2\dot{X}_{t+\Delta t/2}^{IKp} + \dot{X}_{t-\Delta t/2}^{IKp} = -A_i \left[ S^{IP} \cdot 2 \Delta X^{IKp} \right]_{t+\Delta t} \quad (5.29)$$

Where  $\dot{X}^{IKp}$  = the velocity of I relative to K  
 $S^{IP}$  = the direct stiffness of node I relative to all adjacent nodes (assumed highest in the p - direction,  $\Sigma (EA/L_0)_m$  all links m connecting to node i for line element cable structures).

The limiting case of stability is when  $\dot{X}^{IKp}$  during one time increment produces relative deflection changes  $\Delta X^{IKp}$  such that  $\dot{X}^{IKp}$  in the next time increment is equal and opposite to the previous value. Hence:

$$-4\dot{X}_{t+\Delta t/2}^{IKp} = -A_I \left[ S^{IP} \cdot 2 \Delta X_{t+\Delta t}^{IKp} \right] \quad (5.30)$$

Thus,  $2/A_I = S^{IP} \cdot \Delta t$

$$\Delta t_{cri} = \sqrt{\frac{2M_I}{S^{IP}}} \quad (5.31)$$

#### 5.2.4 - Optimization of the Numerical Integration

The aim of the optimization is to reduce the computation time by means of being able to adopt a bigger integration time step without introducing any numerical instability and intolerable inaccuracies in the dynamic response of the riser.

The critical integration time step,  $\Delta t$ , from equation (5.31) is:

$$\Delta t_{\text{cri}} = \sqrt{\frac{2M}{S}}$$

Where

$$S = \Sigma \frac{EA}{L_0}$$

One way of increasing the critical time step is to reduce EA values. This has been employed suggested by Barnes (1976) and Wang (1979). The results of numerical study (Chapter 6 Section 6.3.3) showed that reducing the EA values by 10 times for a riser with no top platform motion, hardly affected the response and top tension of the riser. Reducing EA values results in ignoring the higher order components of the stress wave which travels along the riser. But for this reason, when a longitudinal motion, such as platform motion is introduced to a riser, an artificial reduction in EA value is not desirable. This optimization is useful for flexible risers connecting two fixed platforms or for idealized experimental work.

Reducing EA values can be compared with the modal analysis of a structure in which only a certain number of eigenvalues are used in the solution, rather than all; that is the remaining higher order eigenvalues are ignored. On the basis of a numerical study, a reduction factor of 10 times in the EA values was found to be generally acceptable in situations involving no platform movement.

Further optimization of the numerical procedure (whether or not there is platform movement) is achieved by calculating the non-linear hydrodynamic forces after every  $n$  time steps, rather than

at every time step. The value of  $n$  is chosen so that  $n \cdot \Delta t$  does not exceed say  $1/2$  of the time taken by a transverse wave to travel along the critical member of the riser.

The speed of a transverse wave travelling along the critical member is given by:

$$C = \sqrt{\frac{T}{\rho_C}}$$

Where,

$C$  = speed of a transverse wave

$T$  = tension in the critical member

$\rho_C$  = density of riser

Thus, the time taken for a transverse wave to travel along the most critical member of a riser of length  $l_{cri}$  is given by:

$$\text{time of travel} = ( l_{cri} \sqrt{\rho_C / T} ) \text{ min} \quad (5.35)$$

Thus,  $n \cdot \Delta t < (1/2) \cdot ( l_{cri} \sqrt{\rho_C / T} ) \text{ min} \quad (5.35)$

Where,  $l_{cri}$  = length of the critical member

$\Delta t$  = time integration step required for numerical stability

The creep strain  $\epsilon_c$  may also be calculated at every  $m \cdot \Delta t$  rather than at every time step (Barnes (1976)). However, the computation time taken to evaluate  $\epsilon_c$  is small compared to the total computation time and in the present work this optimization is ignored.

### 5.3 - Formfinding and Static Solution of Flexible Risers

The same dynamic formulation without structural bending and damping is used to obtain the shape and static solution of the risers. The structure is brought to a steady equilibrium state

by employing a fictitious damping function. This method is usually called Dynamic Relaxation and it was originally proposed by Day (1965).

Two types of fictitious damping can be used to bring the structure to the equilibrium state; a) Viscous damping, b) Kinetic energy damping. In the former case nodal viscous damping is introduced in the equilibrium equation. For the most efficient solution the value of the damping constant  $C$  is required to be  $4 \pi f_n$ , where  $f_n$  is the fundamental frequency of the structure. This value of  $C$  corresponds to the critical damping state for the structure and it is assumed to be constant for the whole structure. Thus, employing this method requires some initial solution to obtain the fundamental frequency of the structure. Formulation for this kind of damping is given in Appendix D.

The alternative damping scheme, Kinetic damping, is an automatic method which does not require any initial trial run. In this method, the structure is brought to a steady equilibrium state by tracing the structural Kinetic energy, and when a peak is reached (i.e.  $KE^{t-\Delta t} > KE^{t+\Delta t}$ ), the nodal velocities are set to zero, figure 5.4. This was originally suggested by Cundall (1976) and has been applied extensively to Compliant Structures (Barnes et. al. (1984)). The restarting co-ordinates after each peak are calculated as follows:

The actual K.E. peak is assumed to occur at co-ordinate

$$X = X_{t-\Delta t}/2.$$

$$\text{Thus, } X = (X_{t-\Delta t} + X_t) / 2 \quad (5.36)$$

Equation (5.36) is a linear approximation, alternatively a quadratic interpolation can be adopted. However, it was found that there is no great advantage in this. For computation purposes equation (5.36) is required to be expressed in terms of

$X_{t+\Delta t}$ ,  $\dot{X}_{t+\Delta t/2}$ , and  $R(t)$ . Recalling equations (5.3) and (5.18):

$$\dot{X}_{t+\Delta t/2} = (\Delta t/M) R(t) + \dot{X}_{t-\Delta t/2} \quad (5.3)$$

$$X_{t+\Delta t} = X_t + \dot{X}_{t+\Delta t/2} \cdot \Delta t \quad (5.18)$$

Writing equation (5.18) for  $X_t$  and rearranging for  $X_{t-\Delta t}$ , then substituting for  $\dot{X}_{t-\Delta t/2}$  from equation (5.3), gives:

$$X_{t-\Delta t} = X_t + [ \dot{X}_{t-\Delta t/2} - \frac{\Delta t}{M} R(t) ] \Delta t \quad (5.37)$$

Substituting equation (5.37) into equation (5.36) and then substituting for  $X_t$  from equation (5.18) in equation (5.36) leads to:

$$X = X_{t+\Delta t} - \left(\frac{\Delta t}{2}\right) \left[ 3 \cdot \dot{X}_{t+\Delta t/2} - \frac{\Delta t}{M} R(t) \right] \quad (5.38)$$

Both damping schemes are implemented in this work but the Kinetic damping was found to be more efficient for formfinding.

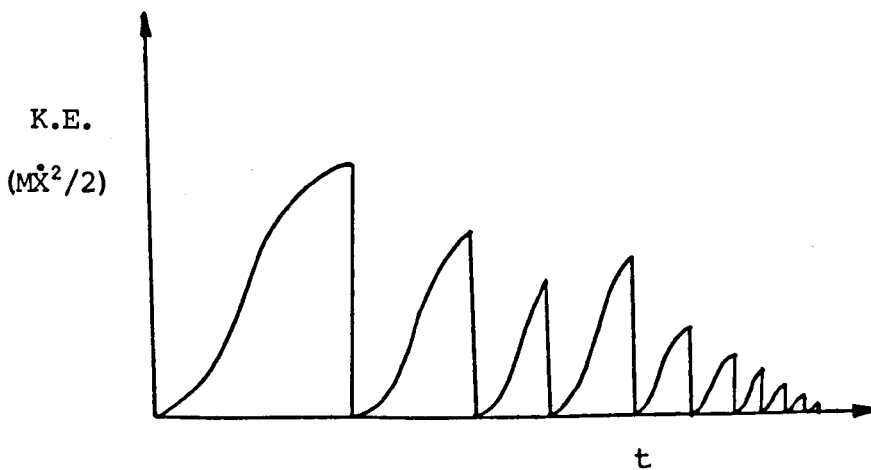


Figure 5.4 - Damping of kinetic energy peaks with time

For efficient use of the static solution optimized fictitious mass components should be employed instead of real masses. This is achieved by using the stability relation (equation 5.31):

$$\Delta t_{\text{cri}} = \sqrt{\frac{2M}{S}} \quad (5.31)$$

where the critical time integration step,  $\Delta t_{\text{cri}}$ , for a static solution is an arbitrary constant. Fictitious nodal mass matrices with directional components  $M_{xx}$ ,  $M_{xy}$ ,  $M_{xz}$ ,  $M_{yy}$  etc., can be used to optimize convergence (Barnes et. al. (1984)). However, for a flexible riser system there is no computational advantage and it is preferable to use either lumped mass components  $M_x$ ,  $M_y$  and  $M_z$  or a single value with  $M = M_x = M_y = M_z$ , in which  $M$  at each node is set according to  $M = \Delta t^2 \cdot S/2$ , where

$$S = \sum \frac{EA}{L} .$$

Time to convergence is additionally dependent on the "condition" number of the system i.e.: the ratio of the highest to the lowest eigenvalues. Hence further optimization for a static solution can be obtained by using a reduced fictitious axial stiffness for the riser which reduces the highest eigenvalue significantly. Since the fundamental mode is governed principally by geometric deformation of the riser as a mechanism the lowest eigenvalue is almost unaltered. Consequently the rate of convergence is increased. The parameter study in chapter 6 section 6.2.3 shows that for riser shape structures, the optimum reduced stiffnesses are obtained when the non-dimensional parameter,  $N \cdot EA/WL$  is approximately 25, where  $N$  is the number of elements and  $W$  is the riser self-weight for unit length.

The flow chart of static solution algorithm for formfinding of a flexible riser is given by figure 5.5.

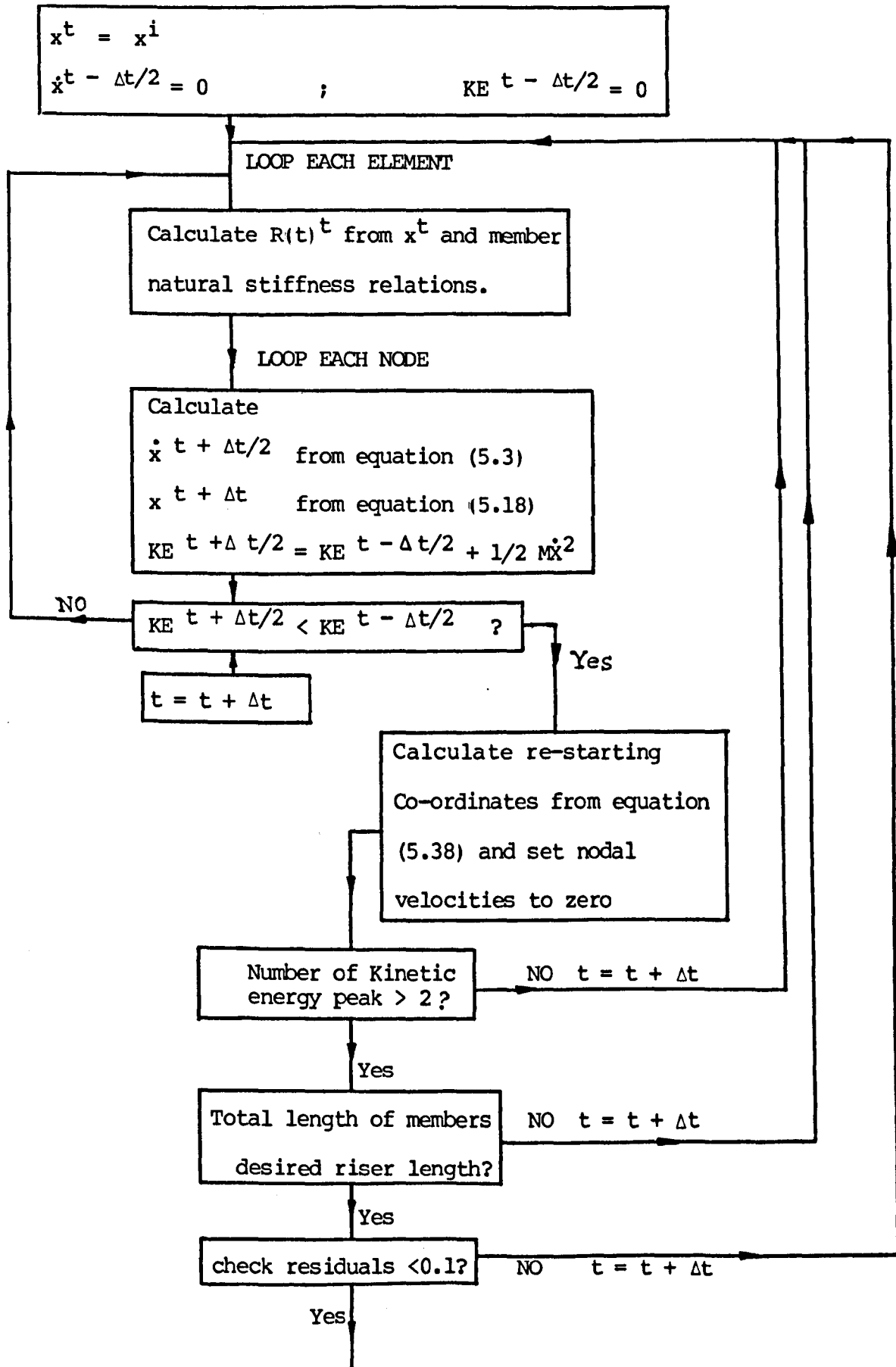


Figure 5.5 - Flow chart of static solution algorithm

### 5.4 Calibration of Visco-Elastic Material Damping Constants

The calibration method proposed by Barnes (1980) is used in this study as follows;

For short time dynamic loading, interest is centred on the immediate elastic response and primary creep. For flexible risers dynamically loaded, this creep is high compared with the secondary quasi-static creep rate. If a segment of the riser is subjected to a suddenly applied constant load and dynamic deflections are recorded in a way which does not induce external friction to the system, a plot of strain against time is obtained such as figure 5.6.

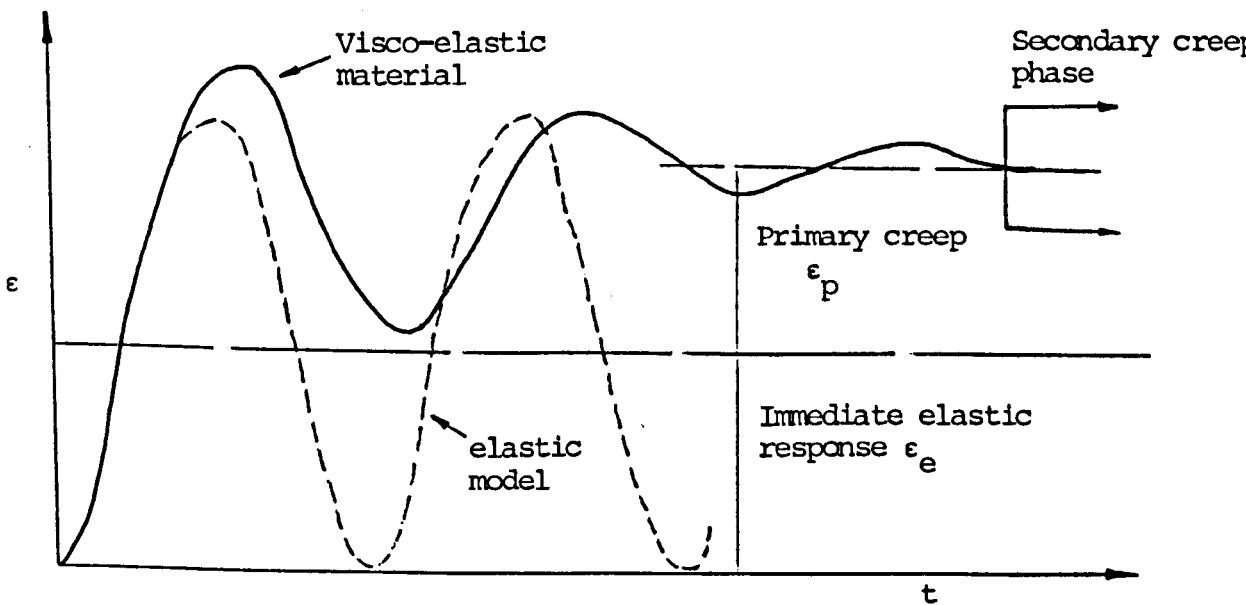


Figure 5.6 - Strain against time for visco-elastic materials

Restricting equation (5.8) to the region termed primary creep stage, during which deflections are damped by the viscous property of the material, at the end of this stage:

$$\epsilon_c \quad \text{at} \quad t + \Delta t/2 \quad \approx \quad \epsilon_c \quad \text{at} \quad t - \Delta t/2 \quad \approx \quad \epsilon_p \quad (5.39)$$

hence since  $\sigma$  is then constant:

$$b \approx \frac{a \sigma t}{\epsilon_p} \tag{5.40}$$

Also the immediate elastic modulus is of the order, but greater than,  $\frac{\sigma}{\epsilon_e}$ .

With these relations as guides, the material constants a, b and E may be evaluated by curve fitting a simple analysis to the experimental data.

Since in general the material constants depend on stress level, calibration should be carried out as a perturbation from the expected initial stress.

### 5.5 - Determination of Structural Natural Frequencies

Barnes (1977) has used Fourier Analysis of the output from a Dynamic Relaxation Scheme to obtain the structural natural frequencies for cable and space structures. In this work the same procedure is carried out. The method is outlined below:

The resultant displacement of any particle in a wave represented by a complex periodic vibration is:

$$y = f(t) = A_0 + a_1 \cdot \cos (\omega t + \theta_1) + a_2 \cos (2\omega t + \theta_2) + \dots + a_n \cdot \cos (n\omega t + \theta_n)$$

$$\text{or } y = A_0 + \sum_{r=1}^{r=n} A_r \cos (r\omega t) + \sum_{r=1}^{r=n} B_r \sin (r\omega t) \tag{5.41}$$

Where  $\theta_1$  etc., are phase angles and  $A_1, B_1$  etc., represent the amplitudes of the various fundamental and harmonic terms; the fundamental frequency being given by  $\omega/2\pi$ .  $A_0$  is a constant

term representing the mean level of the ordinates. Since by integrating both sides of equation (5.41) with respect to  $t$  over a complete vibration period  $T = 2\pi/\omega$ , it follows that all the terms on the right-hand side are zero except  $A_0$ .

$$\text{Thus, } \int_0^T f(t) dt = \int_0^T A_0 dt = A_0 T$$

$$\text{So, } A_0 = \frac{1}{T} \int_0^T f(t) dt = \text{Average value of } f(t) \text{ over one cycle.} \quad (5.42)$$

To determine amplitude coefficients  $A_r$  and  $B_r$ , consider the following trigonometric relations:

$$\int_0^T \sin(m\omega t) \sin(n\omega t) dt = 0 \quad m \neq n$$

$$\int_0^T \cos(m\omega t) \cos(n\omega t) dt = 0 \quad m \neq n$$

$$\int_0^T \sin(m\omega t) \cos(n\omega t) dt = 0 \quad m = n \text{ or } m \neq n$$

But,

$$\int_0^T \sin^2(m\omega t) dt = \int_0^T \cos^2(m\omega t) dt = \frac{T}{2}$$

Hence, the coefficients of the cosine series,  $A_r$ , and the coefficients of the sine series,  $B_r$ , are obtained by multiplying equation (5.41) by  $\cos(r\omega t)$  and  $\sin(r\omega t)$  respectively and taking

account of the above trigonometric relations as follows:

$$\int_0^T f(t) \cos (r\omega t) \cdot dt = A_r \cdot \frac{T}{2}$$

$$\int_0^T f(t) \sin (r\omega t) \cdot dt = B_r \cdot \frac{T}{2}$$

Thus,

$$A_r = \frac{2}{T} \int_0^T f(t) \cos (r\omega t) \cdot dt \quad (5.43)$$

$$B_r = \frac{2}{T} \int_0^T f(t) \sin (r\omega t) \cdot dt \quad (5.44)$$

The above theory applies to periodic vibrations. The output from the dynamic response of the riser may be treated in the following manner:

Consider figure 5.7, the full line represents the dynamic response of a riser and the dashed line represents the reflected image of the trace from  $X$  to  $X + X_n$ , where  $X$  is the last maximum or minimum of the trace and  $X - X_n$  is the first.

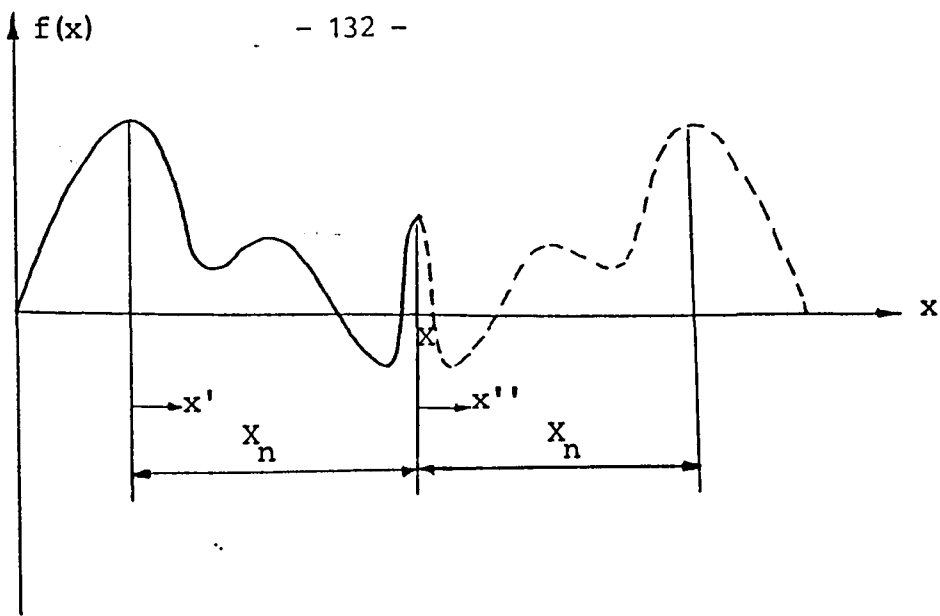


Figure 5.7 - Dynamic response of a structure and its reflected image

Associating  $2X_n$  with the period  $T$ , from equation (5.42):

$$A_0 = \frac{1}{X_n} \int_{X-X_n}^X f(x) dx$$

hence, assuming  $n$  intervals (of length  $\delta x = X_n/n$ ) from  $X - X_n$  to  $X$ , and  $f(x) = \alpha_m$  at the mid-point of interval  $m$ , then by discrete summation:

$$A_0 = \frac{1}{n} \sum_{m=1}^{m=n} \alpha_m \tag{5.45}$$

$$A_T = \frac{2}{2X_n} \int_{X-X_n}^X f(x) \cos(r\omega x) \cdot dx + \frac{2}{2X_n} \int_X^{X+X_n} f(x) \cos(r\omega x) \cdot dx$$

or, redefining origins for  $x'$  and  $x''$ :

$$A_T = \frac{1}{X_n} \int_0^{X_n} f(x') \cos(r\omega x') dx' + \frac{1}{X_n} \int_0^{X_n} f(x'') \cos(r\omega x'') \cdot dx''$$

and, since  $f(x') = f(x'') = \alpha_m$  at  $x' = \left(\frac{2m-1}{2}\right) \delta x = \left(\frac{2m-1}{2}\right) X_n$

$$\text{and, } x'' = X_n - \left(\frac{2m-1}{2}\right) \delta x$$

$$A_r = \sum_{m=1}^{m=n} \frac{\alpha_m}{X_n} (\cos (r\omega x') \delta x + \cos (r\omega X_n - r\omega x') \delta x)$$

hence, since  $\omega = \pi/X_n$  :

$$A_r = \sum_{m=1}^{m=n} \frac{\alpha_m}{n} \cos \left(\frac{r\pi x'}{X_n}\right) (1 + \cos r \pi) = 0 \text{ for all odd integers } r$$

$$(5.46)$$

$$A_r = \frac{2}{n} \sum_{m=1}^{m=n} \alpha_m \cos \left(\frac{r\pi}{2n} (2m-1)\right) \text{ for all even integers } r$$

Similarly for the sine coefficients:

$$B_r = \sum_{m=1}^{m=n} \frac{\alpha_m}{n} (\sin (r\omega x') + \sin (r\omega X_n - r\omega x')) =$$

$$= \sum_{m=1}^{m=n} \frac{\alpha_m}{n} \sin (r\omega x') (1 - \cos r \pi) = 0 \text{ for all even integers } r$$

$$(5.47)$$

$$B_r = \frac{2}{n} \sum_{m=1}^{m=n} \alpha_m \cdot \sin \left(\frac{r\pi}{2n} (2m-1)\right) \text{ for all odd integers } r$$

To evaluate the natural frequencies of a riser, one of its nodes is poked and then released and the dynamic response of the node is traced to obtain a graph such as figure (5.8). A time duration say  $X_n$  corresponding to two maximum nodal displacements is chosen and equations (5.46) and (5.47) are then used to calculate the coefficients  $A_r$  and  $B_r$ ; the values for  $r$  being varied from 1 to some certain value depending on the required

number of structural natural frequencies. A graph such as figure (5.9) is produced. Each  $r$  value corresponding to maximum or minimum values of  $A_r$  and  $B_r$  is recorded and the natural frequency is calculated as follows:

$$f_n = \frac{v\omega}{2\pi} = \frac{1}{2X_n} r \quad (5.48)$$

This theory is also validated in this work by applying it to a simple slack cable. The results are compared with those obtained from an alternative theoretical approach for simple slack cables developed by triantafyllou et. al. (1983).

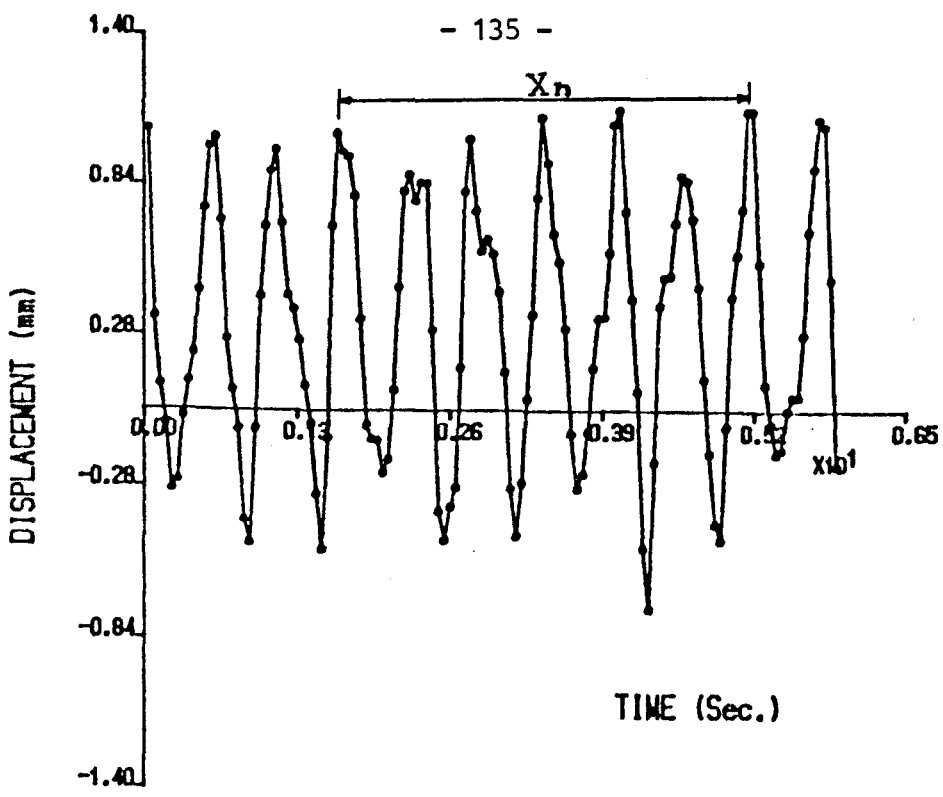


Figure 5.8 - Time history of nodal displacement

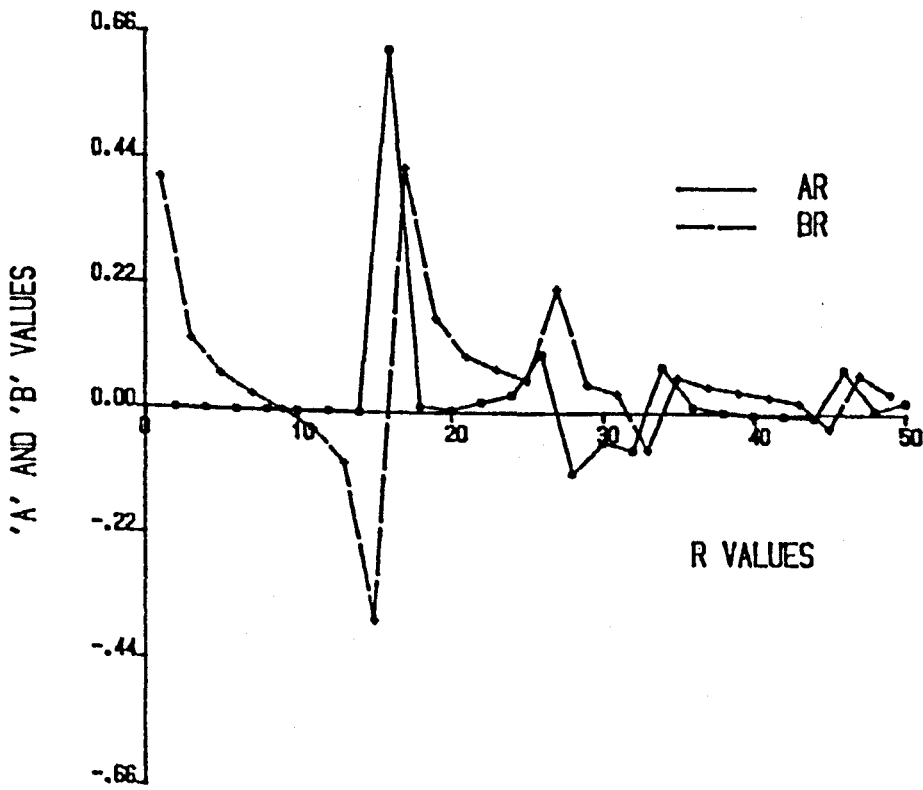


Figure 5.9 - Values of coefficients A and B against r

## 5.6 - Dimensional Analysis and Model Scaling

### 5.6.1 - Dimensional Analysis

The hydrodynamic forces induced by waves on a riser in terms of independent variables can be written as:

$$HF = f(\rho, g, H, L, h, D) \quad (5.49)$$

where

HF = hydrodynamic forces

$\rho$  = fluid density

g = acceleration due to gravity

H = wave height

L = wave length

h = depth of still water

D = diameter of riser

The elements of equation (5.49) in terms of primary elements; length, time and mass (L, T and M respectively) are:

$$HF = MLT^{-2}$$

$$\rho = ML^{-3}$$

$$g = LT^{-2} \quad (5.50)$$

$$H = L$$

$$D = L$$

$$h = L$$

$$L = L$$

equation (5.49) can be expressed as:

$$HF \propto \rho^a g^b H^c L^k h^m D^n \quad (5.51)$$

Substituting equation (5.50) into equation (5.51), one gets:

$$MLT^{-2} \propto (ML^{-3})^a (LT^{-2})^b (L)^c (L)^k (L)^m (L)^n \quad (5.52)$$

Equating the powers of the primary elements in equation (5.52):

$$1 = a$$

$$1 = -3a + b + c + k + m + n \quad (5.53)$$

$$-2 = -2b$$

thus,

$$a = 1, b = 1 \text{ and } c + k + m + n = 3 \quad (5.54)$$

Now it is a matter of choice to give different values to  $c, k, m$  and  $n$  to satisfy equation (5.54). For this reason a wide variety of dimensionless parameters are used in the literature to define the wave motion. One of the most popular relationships is obtained by giving the following values to the variables:

$$c = 2, k = -3, m = 1 \text{ and } n = 3$$

Thus, equation (5.51) becomes:

$$HF \propto g H^2 L^{-3} h D^3 \quad (5.55)$$

Or, in terms of dimensionless variables:

$$\frac{HF}{gHD^2} \propto \frac{h}{L} \cdot \frac{H}{L} \cdot \frac{D}{L}$$

Thus,

$$\frac{HF}{gHD^2} = f\left(\frac{h}{L}, \frac{H}{L}, \frac{D}{L}\right) \quad (5.56)$$

### 5.6.2 - Model Scaling of a Riser in Wave Flow

The aim of model scaling is to construct a small scale physical model of a structure and by using this model to predict full-scale performance. To achieve this, a certain physical similarity should be maintained between the model and prototype. In general the physical similarity involves the geometric, kinematic and dynamic similarities. Geometric similarity exists when the ratio of corresponding lengths is constant, kinematic similarity exists when the ratio of corresponding velocities is constant and dynamic similarity exists when the ratio of corresponding forces is constant. The requirement of model laws is obtained by resort to a scale factor. The scale factor of a quantity  $f$ , denoted  $K_f$ , is the ratio of the value of  $f$  in the

model to that in the prototype, i.e.  $K_p = f_m/f_p$ . The constancy of a particular dimensionless product provides a relationship between various scale factors. So, the condition of geometric similarity implies that a single length scale factor  $K_L$  applies to all lengths pertaining to the problem.

Equation (5.56) is used to model a riser in wave flow. Writing equation (5.56) for the model and prototype respectively:

$$\left(\frac{HF}{gHD^2}\right)_m = f\left(\frac{h}{L}, \frac{H}{L}, \frac{D}{L}\right)_m \quad (5.57)$$

$$\left(\frac{HF}{gHD^2}\right)_p = f\left(\frac{h}{L}, \frac{H}{L}, \frac{D}{L}\right)_p$$

For physical similarity between the model and prototype, the following conditions should be satisfied:

$$\left(\frac{h}{L}\right)_m = \left(\frac{h}{L}\right)_p, \left(\frac{H}{L}\right)_m = \left(\frac{H}{L}\right)_p, \text{ and } \left(\frac{D}{L}\right)_m = \left(\frac{D}{L}\right)_p$$

$$\text{or } \frac{h_m}{h_p} = \frac{H_m}{H_p} = \frac{D_m}{D_p} = \frac{L_m}{L_p} = K_L \quad (5.58)$$

When condition equation (5.58) is met, one has:

$$\left(\frac{HF}{gHD^2}\right)_m = \left(\frac{HF}{gHD^2}\right)_p \quad (5.59)$$

By calculating forces on the model and using equation (5.59), the forces on the prototype can be calculated.

A wave motion is usually identified by H and T, where T is the

wave period, so the condition  $\left(\frac{L_m}{L_p}\right)$  in equation (5.58) is

satisfied if  $\left(\frac{T_m}{T_p}\right) = K_T$ . The time scale factor is calculated by

considering the dynamic similarity between the model and prototype. The corresponding force ratio for dynamic similarity of risers in waves is the ratio of inertia force to gravitational force. This condition can be met if the Froude dimensionless number,  $F_r = V\sqrt{gL}$ , where  $V$  is the water particle velocity induced by wave motion, is kept constant for the model and prototype. Considering the Froude number and assuming  $K_g = 1$ :

$$K_V = \frac{V_m}{V_p} = \sqrt{\frac{L_m}{L_p}} = K_L^{1/2} \quad (5.60)$$

Thus,

$$K_T = \frac{K_L}{K_V} = K_L^{1/2} \quad (5.61)$$

But in flow around the riser, flow separation occurs and this adds another condition for dynamic similarity which is Reynolds number (inertia force/viscous force).  $V_m D/\nu$ , where  $V_m$  is the maximum water particle velocity and  $\nu$  is the kinematic viscosity of the fluid. In small scale modelling it is very difficult to satisfy the constancy of Reynolds number as well as the Froude number. From constancy of the Froude number one has  $K_V K_L = K_L^{3/2}$ , so to ensure the constancy of Reynolds number, one has to hold  $K_\nu = K_V K_L = K_L^{3/2}$ . And it is impossible to find a fluid with such a small kinematic viscosity. This is one of the reasons that the results of wave flume experiments do not correlate well with those obtained from the prototype in sea.

In modelling the riser it is also desirable to model its elastic properties. This is achieved by ensuring the constancy between

model and prototype of  $\frac{\rho_r}{\rho}$ ,  $\xi$ , and  $EA/A_p V^2$ ; where  $\rho_r$  is the riser

density,  $\xi$  is the structural damping ratio, A is the riser cross-sectional area, and EA is the axial stiffness of the unit length of the riser. It is again difficult to maintain the constancy of  $EA/A\rho V^2$  between the small model and prototype together with the constancy of the Froude number. However, the Primary Structural Stiffness is geometric and associated with deformation as a mechanism rather than elastic deformation. The value of EA may thus not be critical in the majority of cases.

### 5.6.3 - Model Scaling of a Riser in Current Flow

From geometric similarity one has:

$$\frac{D_m}{D_p} = K_L \quad (5.62)$$

The dynamic similarity is satisfied by considering the ratio of inertia force to gravitational force:

$$\frac{\text{inertia force}}{\text{gravitational force}} = \frac{0.5 \rho D C_d V^2}{\rho_r D^2 \pi g/4} \propto \frac{\rho V^2}{\rho_r Dg} \quad (5.63)$$

Assuming  $K_g = 1$  and  $K_\rho = 1$ , and ensuring  $K_{\rho_r} = 1$ , from equation (5.63) one has:

$$K_V^2 = \left(\frac{V_m}{V_p}\right)^2 = \frac{D_m}{D_p} = K_L$$

thus, 
$$K_V = K_L^{1/2} \quad (5.64)$$

The constancy of  $\xi$  (and perhaps  $EA/A\rho V^2$ ) for modelling the riser in both current flow and wave conditions is desirable.

## CHAPTER 6

### NUMERICAL IMPLEMENTATION

#### 6.1 - Introduction

The theories which were presented in Chapters 4 and 5, for the static and dynamic analyses of flexible risers, are implemented in the following computer programs:

- a) Program FLEXSTATIC (Program 1) - computes the static configuration of the riser which is subsequently used in program FLEXDYNAMIC or FLEXCURRENT.
- b) Program FLEXDYNAMIC (Program 2) - evaluates the dynamic response of the riser induced by wave and current motion.
- c) Program FLEXCURRENT (Program 3) - determines the riser response due solely to current motion and static offsets of the platform.
- d) Program STOKWAVE - is used to calculate the wave parameters using any order (1-5) of Stokes Wave Theory. These parameters are used as input to the program FLEXDYNAMIC.

This chapter describes each of the above programs and presents a detailed parameter study for Program 1 and optimization of Program 2. Consideration is also given to the method of finding structural natural frequencies and a comparison of results for a simple test case with previously published results.

## 6.2 - Implementation of Static Solution for Formfinding

### 6.2.1 - Program FLEXSTATIC (Program 1) -

The theory and flow chart for the program have been presented in chapter 5, section 5.3 and figure 5.5 respectively. The program is well suited to computer aided design procedures in which various shapes for the riser catenary can be investigated together with the effects of boundary support conditions and alternative arrangements of mooring buoys. The input data and computed equilibrium shapes of the three well known riser configurations; free hanging, single catenary and double catenary are given in tables 6.1 to 6.3 and figures 6.1 to 6.3 respectively. The program has been optimized by employing fictitious nodal masses and reduced axial stiffnesses. The CPU computing time on a Gould 9005 computer system for each of the above test cases was 5 to 10 seconds.

The initial input configuration of a riser is considered to be a vertical straight line which is subdivided into the desired number of elements with the loads due to structural self-weight applied at the nodes. The nodal motion equations are iterated until an equilibrium shape with required length is achieved. Figure 6.4 shows the convergence shape of a double catenary riser from its initial input shape. In computing the equilibrium shape of a double catenary riser, the anchoring chain which tethers the sub-buoy to the sea bed is considered as an element with high axial stiffness.

The program is incorporated with a user interface which gives the list of the required input data associated with the considered riser type. The results of the riser equilibrium shape are output both in tabular and in graphical forms.

### 6.2.2 - Critical Criteria in Designing Flexible Riser Catenary Shapes

The critical parameters in the shape design of a flexible riser configuration are as follows:

- a) The bending radius at the sag part of the catenary must be limited by the given minimum radius of curvature of the riser.
- b) The vertical distance of the lowest point of the catenary from the sea bed should not be less than a given value.
- c) Tension along the riser should not exceed the maximum specified by the manufacturer.
- d) The angles at the top and bottom terminations should not be greater than the limiting values specified by the type of end connectors employed.

For a given combination of water depth and excursion envelope of the floating support, each particular configuration in figure 6.5 corresponds to a set of extreme values of the above parameters. That is criteria (a) and (b) in the near position and criteria (c) and (d) in the far position of the riser.

An initial guess of the riser length is usually obtained using a configuration similar to that shown in figure 6.6. However, geometry of the test cases for this study are obtained by proportioning the riser used in the Balmoral Oil Field.

### 6.2.3 - Optimization of Program FLEXSTATIC

As only the eventual static equilibrium solution is required, optimized fictitious mass components, obtained using the

stability criteria equation 6.1, are used in the equations of motion.

$$M = \Delta t^2 \cdot \frac{S}{2} \quad (6.1)$$

where  $\Delta t$  = an arbitrary constant.

$S$  = the greatest possible direct stiffness at

a node =  $\sum (EA/L)$  for adjacent members

$M$  = the fictitious nodal mass.

Further optimization is achieved by using reduced element stiffnesses. In computing the riser equilibrium shape, the length of the riser is adjusted to that of the given length in the stressed state. Therefore, the accuracy in the computed equilibrium shape is not affected by using reduced element stiffnesses.

The choice of the value for the element stiffness is the most important iteration control factor. The optimized value of the reduced element stiffness is dependent on self-weight and shape of the structure. The parameter study showed that for catenary flexible risers the minimum number of iterations is achieved when the non-dimensionalised parameter,  $EA/(W.L/N)$ , was approximately 25, figure 6.7.

where  $EA$  = Axial stiffness of one metre length.

$W$  = Self-weight per metre length.

$L$  = Length of riser.

$N$  = Number of elements.

$W.L/N$  = Average nodal force.

A further parameter study was carried out to optimize the number of iterations by controlling the number of computed kinetic

energy peaks between each "initial" length modification during the computation. The most efficient procedure was found to be the resetting of specified initial lengths of elements at every third kinetic energy peak, figure 6.8.

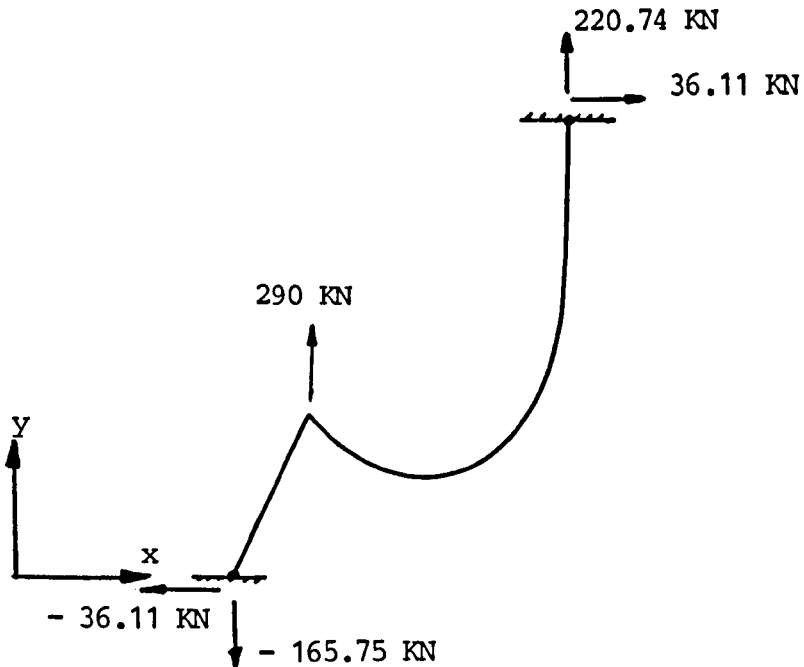
#### 6.2.4 - Validation of Program FLEXSTATIC

The accuracy of the computed equilibrium shape of a riser can be examined from the equilibrium of the vertical and horizontal external forces.

Total vertical forces = apparent self-weight  
+ vertical reaction forces  
+ buoyancy force of sub-buoy = 0.

Total horizontal forces = horizontal reaction forces = 0.

The above criteria are checked for a single catenary riser test case as follows:



Computed reaction forces of a single catenary riser

Apparent self-weight of riser = -344.99 kN

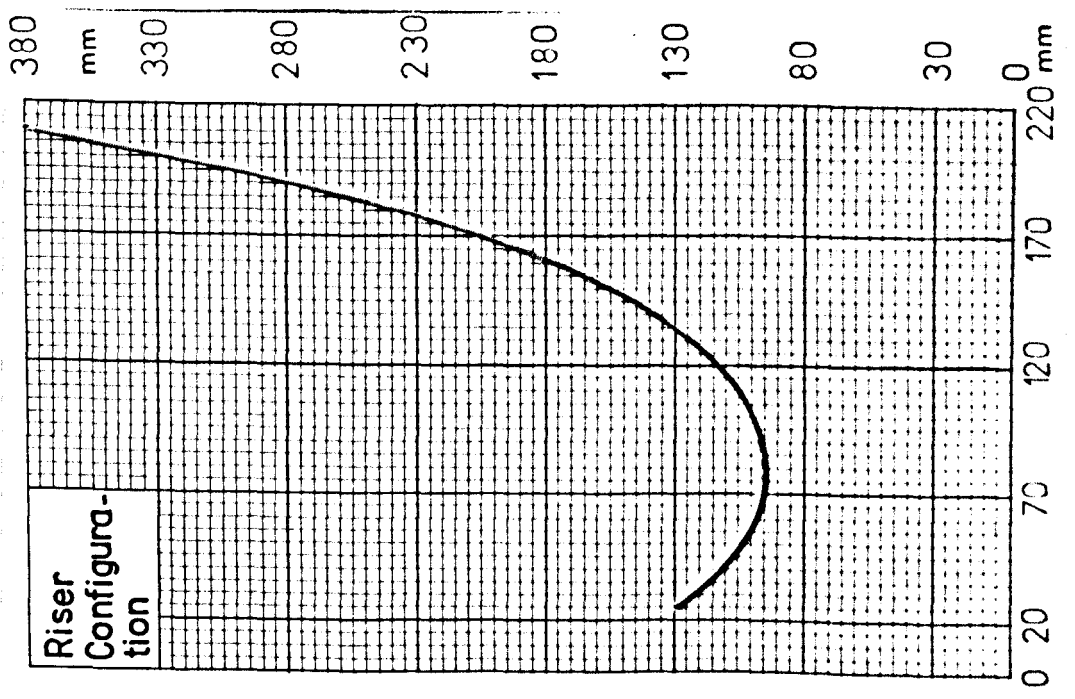
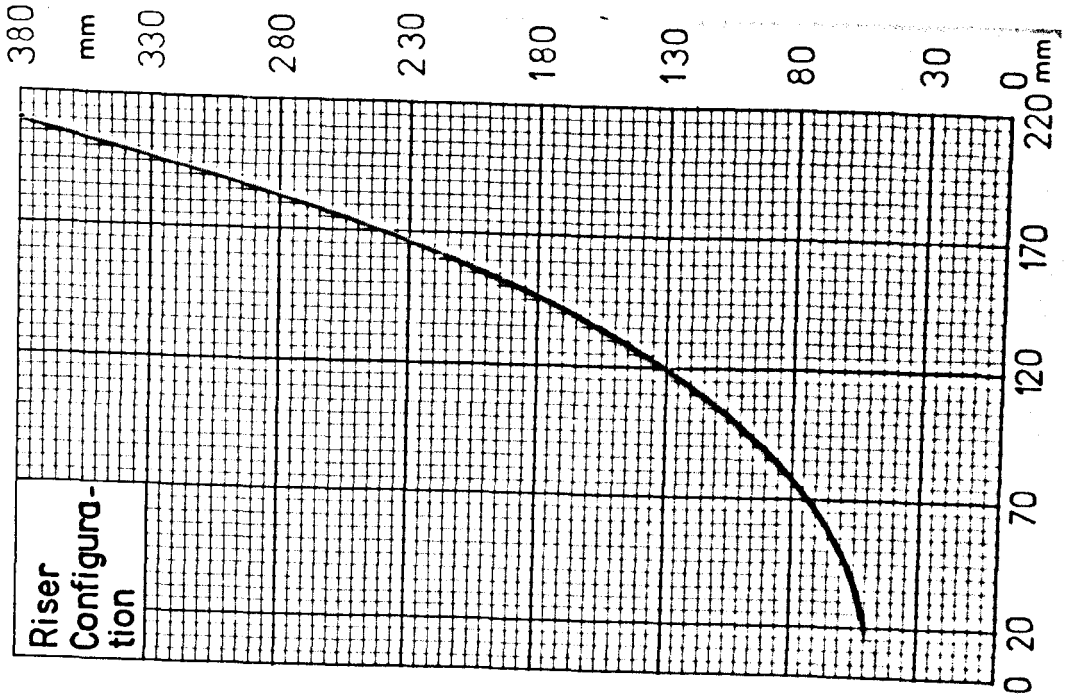
Total vertical force =  $-344.99 + 220.74 - 165.75 + 290 = 0$ .

Total horizontal force =  $-36.11 + 36.11 = 0$ .

A snake chain of 2mm in diameter and 400mm in length was hung in two shapes in order to compare with computed equilibrium shapes. The first shape was arranged in the shape of the upper catenary part of a single or double catenary riser (plate 1). The second shape was arranged in the form of a free hanging riser (plate 2). These arrangements were photographed and digitized and then compared with the computed shapes, figures 6.9 and 6.10 respectively. The number of elements for both computations was 11. The comparisons were in good agreement.

#### **6.2.5 - Parameter Study on the Number of Elements Used to Compute the Riser Equilibrium Shape**

Element size in dynamic analysis of a flexible riser is a crucial parameter regarding the computation effort. This is because the integration time step,  $\Delta t$ , is proportional to the element length. Thus, a parameter study was carried out to determine the minimum required number of elements to give acceptable accuracy in the analysis. The single catenary riser, for which data is given in table 6.2, was adopted as the test case. The tests were carried out by computing the static solution of the riser with differing numbers of elements and then comparing the reaction forces and nodal co-ordinates. The numbers of elements used in the analyses were 7, 11 and 22 (figure 6.11). The comparisons of the reactions and nodal co-ordinates are given in tables 6.4 and 6.5 respectively. These comparisons show that an analysis with 11 elements produces acceptable results for engineering applications.



6.3 - Implementation of Dynamic Solution

6.3.1 - Program STOKWAVE

The theory to determine the wave parameters of any order (1-5) of the Stokes Wave Theory, which was described in Chapter 4 Section 4.3, has been implemented in the program STOKWAVE. The program solves the simultaneous equations (4.49) for  $\lambda$  and  $K$  and then calculates the wave constants  $A_{ij}$ ,  $B_{ij}$  and  $C_i$  using the relations given in Appendix A.

where 
$$\lambda = \frac{2 \pi a}{L}$$

$a$  = Wave amplitude.

$L$  = Wave length.

$K$  = Wave number,  $\frac{2 \pi}{L}$ .

The program was validated by using the example which is given in the paper presented by Skjelberia and Hendrickson (1960). The wave which was considered in the example had the following parameters:

Water depth,  $h = 30$  ft (9.137m)

Wave height,  $H = 18 \frac{2}{3}$  ft (5.685m)

Wave period,  $T = 7.72$  sec.

The results of the example are given in Table 6.6 and those obtained from program STOKWAVE are given in Table 6.7.

$d/L = 0.12,$	$\lambda = 0.1885$	
$B_{22} = 2.5024,$	$B_{33} = 5.7317,$	$B_{44} = 14.034$
$B_{24} = -3.7216,$	$B_{35} = -4.8893,$	$B_{55} = 37.200$
$A_{11} = 1.2085,$	$A_{22} = 0.7998,$	$A_{35} = -1.5042$
$A_{13} = -5.1153,$	$A_{24} = -4.9710,$	$A_{44} = 0.0587$
$A_{15} = -10.6530,$	$A_{33} = 0.3683,$	$A_{55} = -0.0750$

Table 6.6 - Results of the example given by Skjelberia and Hendrickson

### 6.3.2 - Program FLEXDYNAMIC (Program 2)

The theory and flow chart for the program were presented in Chapters 4 and 5 and figure 5.3 respectively. The program calculates the 3-dimensional dynamic behaviour of a flexible riser due to the effects of waves and currents from any direction, vessel movements, vortex-shedding and structural damping. The input data is established in the following two data files:

- 1) A data file which is created by program 1 containing the nodal geometry, nodal external forces due to riser self-weight, and tensions in the elements in the equilibrium shape.
- 2) A data file which contains the data associated with the wave and current profile, magnification factors for nodal drag coefficients in the drag-inertia force direction due to the vortex-shedding, and vessel movement. The list of required input data is given by a user-friendly program which is incorporated in FLEXDYNAMIC.

The vessel movement associated with wave motion is considered to have six degrees of freedom: three translational and three rotational, with each having an amplitude and a phase angle. The translational motions are: surge, sway and heave and rotational motions are: roll, pitch and yaw. These motions are illustrated in figure 6.12.

The sub-buoy is considered as part of the flexible riser and its mass and the hydrodynamic forces exerted on it are lumped at the node to which it is attached.

### 6.3.3 - Optimization of Program FLEXDYNAMIC

The single catenary riser which is described by table 6.2., was chosen as the test case and wave and current loadings with no platform motions were applied.

Descriptions of the data are given in table 6.8a. Table 6.8b gives the wave parameters for the 5th order Stokes Wave Theory computed by program STOKWAVE.

The dynamic response of the test case was computed three times to observe the effect of the different optimizing effects described in Chapter 5, Section 5.2.4. The influence of these is summarised below:

- 1) With no optimization the CPU computing time on a Gould 9005 computer system was 15 minutes and 50 seconds,
- 2) with hydrodynamic forces on the riser calculated at every 30 time steps, the CPU computing time was 2 minutes and 24 seconds,
- 3) with EA values reduced by a factor of 10 (allowing a time integration step  $\sqrt{10}$  times larger), and hydrodynamic forces on the riser calculated at every 10 time steps, the CPU computing time was just 1 minute and 22 seconds. Four further runs were made for this test case with the hydrodynamic forces calculated at every 1, 5, 10 and 15 time intervals. Comparisons of the results for the horizontal top tension and the horizontal displacement of node 10 for these runs are given in figure 6.13. The comparisons show that the differences are negligible.

The results from all of the above sets of computations were in good agreement and the maximum difference in the results was 0.5 percent. Figure 6.2 shows the static equilibrium shape of the riser and figure 6.14 shows "snap shots" of the riser dynamic response at the 5th wave cycle. The time histories of the horizontal and vertical nodal displacements are given by figure 6.15 and 6.16 respectively. The important conclusion from these time history graphs is that the steady uniform response of the riser is closely approached after only one wave cycle. Thus 3 wave cycles are sufficient to analyse a flexible riser using program FLEXDYNAMIC.

Another set of runs was carried out using the above test riser subject to platform motion. The data is given in Table 6.9. The static equilibrium shape, figure 6.2., corresponds to the initial configuration of the riser with the platform having the maximum heave and zero surge motions at time zero. Runs were made with and without optimization with the following results:

- 1) With no optimization the CPU computing time on a Gould 9005 computer system was 16 minutes and 57 seconds,
- 2) with hydrodynamic forces on the riser calculated at every 30 time steps, the CPU computing time was only 2 minutes and 25 seconds.

The results from both runs were in good agreement. Figures 6.17, 6.18 and 6.19 show respectively the "snap shots" at the 5th wave cycle and the time histories of horizontal and vertical nodal displacements.

The comparison of the snap shots of the riser with and without platform motion shows that the response of the sag part of the riser is strongly dependent on the platform motion.

The computed dynamic response of a flexible riser by program FLEXDYNAMIC is postprocessed and presented in the form of tables at required time intervals, together with time history graphs, and snap shots of riser displacements.

#### 6.4 - Program FLEXCURRENT (Program 3)

The same theory used for the static program (FLEXSTATIC) is implemented in the program FLEXCURRENT. The flow chart for the program is given in figure 6.20.

The program computes the response of a riser due to steady current motion, any static loading on the riser and static displacement of the platform. It is well suited to investigate critical design criteria for a flexible riser as outlined in section 6.2.2 of this chapter. Of particular interest is the extreme position of the platform induced by waves, or drifting of the platform due to the failure of any platform anchoring chain. The iterative use of programs FLEXSTATIC and FLEXCURRENT allow potential designs to be quickly investigated.

The simple catenary riser for which data is given in Table 6.2 was chosen as the test case. Figure 6.21 shows the static response of the riser due to the current loading described by Table 6.10. Figures 6.22 and 6.23 show respectively the response of the riser due to current forces together with heave and surge displacement of the platform. The amplitude of the heave and surge were 9 and 10 metres respectively. The CPU computing times in a Gould computer system for these runs were only 5 to 6 seconds.

The program is incorporated with a user-friendly program which gives the list of the required input data. The results are output in both tabular and graphical forms.

#### 6.5 - Validation of Programs FLEXSTATIC, FLEXCURRENT and FLEXDYNAMIC Computations by Hand Calculations

The results from every computation of the programs were checked with those obtained by lengthy hand calculations for two simple test cases (figures 6.24 and 6.25) for the first two time steps. This procedure ensured that the theories described in Chapters 4 and 5 were implemented correctly.

#### 6.6 - Implementation and Numerical Validation of the Method Used to Determine Structural Natural Frequencies

The theory which was described in Chapter 5, Section 5.5, is implemented into a computer program and is used to obtain the structural natural frequencies of any type of flexible riser.

Triantafyllou et. al. (1983) presented an analytical method and gave graphs to calculate the natural frequencies of catenary cables. The graphs give the first four structural natural frequencies for different top angles of the cable configuration for any constant value of  $WL/H$ , where  $W$  = self-weight of cable per metre length,  $L$  = cable length, and  $H$  = horizontal component of top tension. The specifications of a cable and a typical natural frequency graph are given in figures 6.26 and 6.27 respectively.

A catenary riser was chosen as the test case and its static

equilibrium shape was obtained using program FLEXSTATIC, figure 6.28. The parameters for the test case were:

$$WL/H = 1.5, \text{ top angle} = 59 \text{ degrees}$$

Figure 6.27 was then used to obtain the first four structural natural frequencies and these are given in Table 6.11.

These natural frequencies were also evaluated by the method described in Chapter 5, Section 5.5. This was carried out by displacing a node, (say node 8, along the riser) by applying a horizontal load of -10 kN and a vertical load of 10 kN at the node and computing the displaced equilibrium shape of the riser using program FLEXCURRENT. This new equilibrium shape (but without the applied vertical and horizontal nodal forces), was then used as input data for the program FLEXDYNAMIC and the natural vibration of the node following release from the displaced state was traced, figure 6.29. A section of the displacement trace between any two maxima, figure 6.29, was chosen and discretized using the Fourier analysis to evaluate the Fourier coefficients  $A_r$  and  $B_r$ . These coefficients are plotted against the variable  $r$ , figure 6.30. Each maximum or minimum value of  $A_r$  and  $B_r$  corresponds to a structural natural frequency. Figure 6.30 shows the first four natural frequencies of the riser. It can be seen that each frequency possesses a close spectrum rather than a single value. This is explained by the fact that the flexible riser is a mechanism system. The above procedures were repeated also for node 7 and the resulting natural frequencies were found to be in good agreement with those calculated using an initial displacement of node 8.

The natural frequencies which were obtained from the Trianafyllou et. al. method and the method used in this work are presented in Table 6.11. The comparison shows that the results are generally in good agreement.

Water depth	300 m
Water density	1.025 t/m <sup>3</sup>
Riser outside diameter	0.275 m
Riser and its contents weight in air	1.34 kN/m
Axial stiffness, EA	98 E4 KN
Total length	381 m
Horizontal span	180 m
Vertical span	320 m
Number of elements	11

Table 6.1 - Input data for the free hanging riser

Water depth	300 m
Water density	1.025 t/m <sup>3</sup>
Riser outside diameter	0.275 m
Riser and its contents weight in air	1.34 kN/m
Axial stiffness, EA	98 E4 KN
Catenary length	325 m
Taut length	112 m
Horizontal span	180 m
Vertical span	320 m
Buoyancy of sub-buoy	290 KN
Number of elements for catenary part	11
Number of elements for taut part	1

Table 6.2 - Input data for the single catenary riser

Water depth	300 m
Water density	1.025 t/m <sup>3</sup>
Riser outside diameter	0.275 m
Riser and its contents weight in air	1.34 kN/m
Axial stiffness, EA	98 E4 KN
Upper catenary length	325 m
Lower catenary length	118 m
Horizontal span	320 m
Vertical span	180 m
Buoyancy of sub-buoy	150 KN
Tethered length	111 m
Horizontal distance of tether base from riser base	50.5 m
Number of elements for upper catenary	10
Number of elements for lower catenary	4

Table 6.3 - Input data for the double catenary riser

Number of elements	Reaction at Riser Top (KN)		Reaction at Riser Base (KN)	
	Hor.	Vert.	Hor.	Vert.
6	35.8	221.1	-35.8	-165.4
11	36.1	220.7	-36.1	-165.7
22	36.1	220.6	-36.1	-165.5

Table 6.4 - Reaction forces of the single catenary riser with different number of elements

Corresponding Node Numbers along riser			6 Elements		11 Elements		22 Elements	
6	11	22	x-coords (m)	y-coords (m)	x-coords (m)	y-coords (m)	x-coords (m)	y-coords (m)
1	1	1	0.	0.	0.	0.	0.	0.
2	2	3	19.0	110.7	19.2	111.	19.4	111.1
3	4	7	76.3	86.0	75.1	89.5	75.1	90.3
4	6	11	122.9	128.1	122.1	129.4	121.9	129.6
5	8	15	149.1	187.2	148.7	187.9	148.7	188.1
6	8	19	166.8	251.8	166.6	252.2	166.6	252.2
7	12	23	180.0	320.0	180.0	320.0	180.0	320.0

Table 6.5 - Horizontal and vertical co-ordinates of the single catenary riser with different number of elements

```
=====
HEIGHT OF WAVE = 5.685
PERIOD OF WAVE = 7.72
DEPTH OF STILL WATER = 9.137
=====
```

```
=====
LANDA                                K
=====
0.1885                                0.0825
CONVERGENCE IS OBTAINED
ITERATION NUMBER=1
=====
RATIO OF STILL WATER DEPTH TO WAVE LENGTH (D/L) = 0.1200
=====
```

```
=====
A11                                A13                                A15
=====
0.12085E+01                        -0.51153E+01                        -0.10653E+02
=====
```

```
=====
A22                                A24                                A33
=====
0.79984E+00                        -0.49709E+01                        0.36827E+00
=====
```

```
=====
A35                                A44                                A55
=====
-0.15042E+01                        0.58722E-01                        -0.74979E-01
=====
```

```
=====
B22                                B24                                B33
=====
0.25024E+01                        -0.37215E+01                        0.57317E+01
=====
```

```
=====
B35                                B44                                B55
=====
-0.48890E+01                        0.14034E+02                        0.37200E+02
=====
```

Table 6.7 - Predicted wave parameters  
for Stokes 5th order

Wave height	25 m
Wave period	16 sec.
Wave phase angle at the centre of gravity of the platform	0°
Rise is situated at the centre of gravity of the platform	
Current velocity profile is	
at water-free surface	1.5 m/sec
at 100 metres below water level	1.0 m/sec
at sea bed	1.0 m/sec
Axial stiffness, EA	98 E4 KN
Bending stiffness, EI	480 KN/m <sup>2</sup>
Buoy diameter	4 m
Buoy overall height	5 m
Buoy volume	46.0 m <sup>3</sup>
Buoy mass	16500 kg
Drag coefficient, $C_d$ , for riser	0.6
Inertia coefficient, $C_m$ , for riser	1.5
Tangential drag coefficient, $C_{dt}$ , for riser	0.02
Drag coefficient for buoy	0.6
Inertia coefficient for buoy	1.5

Table 6.8a - Data for dynamic run with no platform motion

=====

HEIGHT OF WAVE = 25. m  
 PERIOD OF WAVE = 16. sec  
 DEPTH OF STILL WATER = 300. m

=====

=====

LANDA	K
0.1872	0.0152
0.1869	0.0152
0.1869	0.0152

CONVERGENCE IS OBTAINED  
 ITERATION NUMBER=3

=====

RATIO OF STILL WATER DEPTH TO WAVE LENGTH (D/L) = 0.7243

=====

A11	A13	A15
0.21114E-01	-0.13209E-01	-0.16303E-01
A22	A24	A33
0.74521E-07	-0.11153E-03	0.26197E-09
A35	A44	A55
-0.19726E-06	0.76623E-12	-0.18090E-14
B22	B24	B33
0.50045E+0	-0.70917E+00	0.37550E+00
B35	B44	B55
-0.11973E+01	0.33394E+00	0.32627E+00

Table 6.8b - Predicted wave parameters of  
 Stokes 5th order wave theory  
 for the dynamic test case

Wave height	25 m
Wave period	16 sec
Wave phase angle at the centre of gravity of the platform	0°
Riser is situated at the centre of gravity of the platform	
Current velocity profile is	
at water-free surface	1.5 m/sec
at 100 metres below water level	1.0 m/sec
at sea bed	1.0 m/sec
Axial stiffness, EA	98 E4 KN
Bending stiffness, EI	480 KN/m <sup>2</sup>
Buoy diameter	4 m
Buoy overall height	5 m
Buoy volume	46.0 m <sup>3</sup>
Drag coefficient, $C_d$ , for riser	0.6
Inertia coefficient, $C_m$ , for riser	1.5
Tangential drag coefficient, $C_{dt}$ , for riser	0.02
Drag coefficient for buoy	0.6
Inertia coefficient for buoy	1.5
Platform surge amplitude	7 m
Surge phase angle	90°
Platform heave amplitude	7 m
Heave phase angle	0.

Table 6.9 - Data for dynamic run of the single  
catenary riser with platform motion

Current velocity profile is	
at water-free surface	1.5 m/sec
at 100 metres below water level	1.0 m/sec
at sea bed	1.0 m/sec
Axial stiffness, EA	98 E4 KN
Buoy diameter	4 m
Buoy overall height	5 m
Buoy volume	46.0 m <sup>3</sup>
Buoy mass	16500 kg
Drag coefficient, $C_d$ , for riser	0.6
Inertia coefficient for buoy	0.6

Table 6.10 - Data for static run with  
current loadings

		$f_{n1}$			$f_{n2}$			$f_{n3}$			$f_{n4}$		
$f_n$ (published paper)		2.57			3.91			5.28			6.58		
Present Work	r	15	16	17	25	26	27	33	34	35	45	46	47
	$f_n$	2.17	2.32	2.46	3.62	3.76	3.91	4.77	4.92	5.06	6.51	6.66	6.80

Table 6.11 - Comparison of structural natural frequencies predicted by Triantifyllou et. al. (1983) and the present work

$$\text{(From equation (5.48), } f_n = \frac{1}{2 \times 3.456} r = 0.1447r)$$

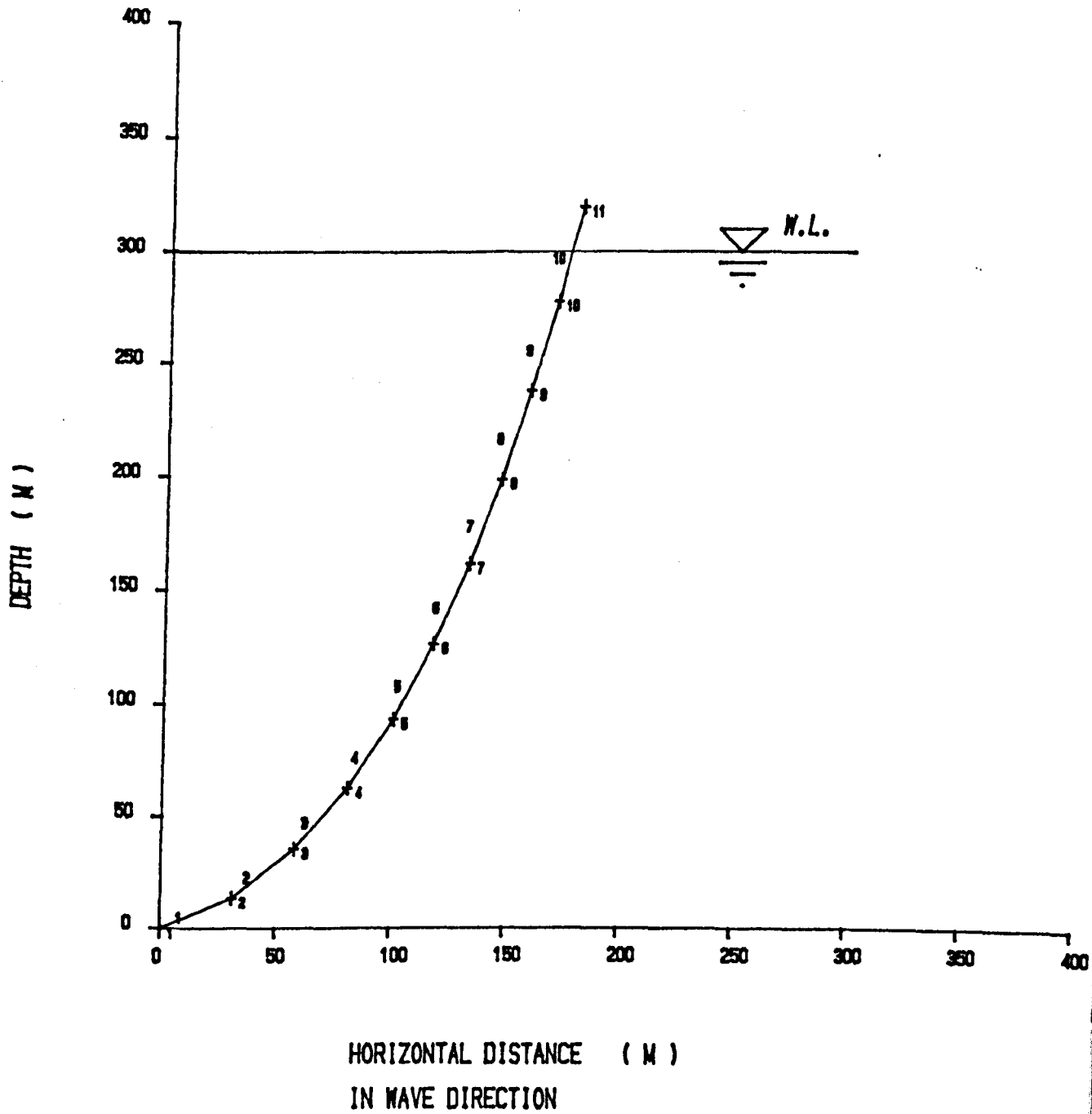


Figure 6.1 - Computed static equilibrium shape of a free hanging riser

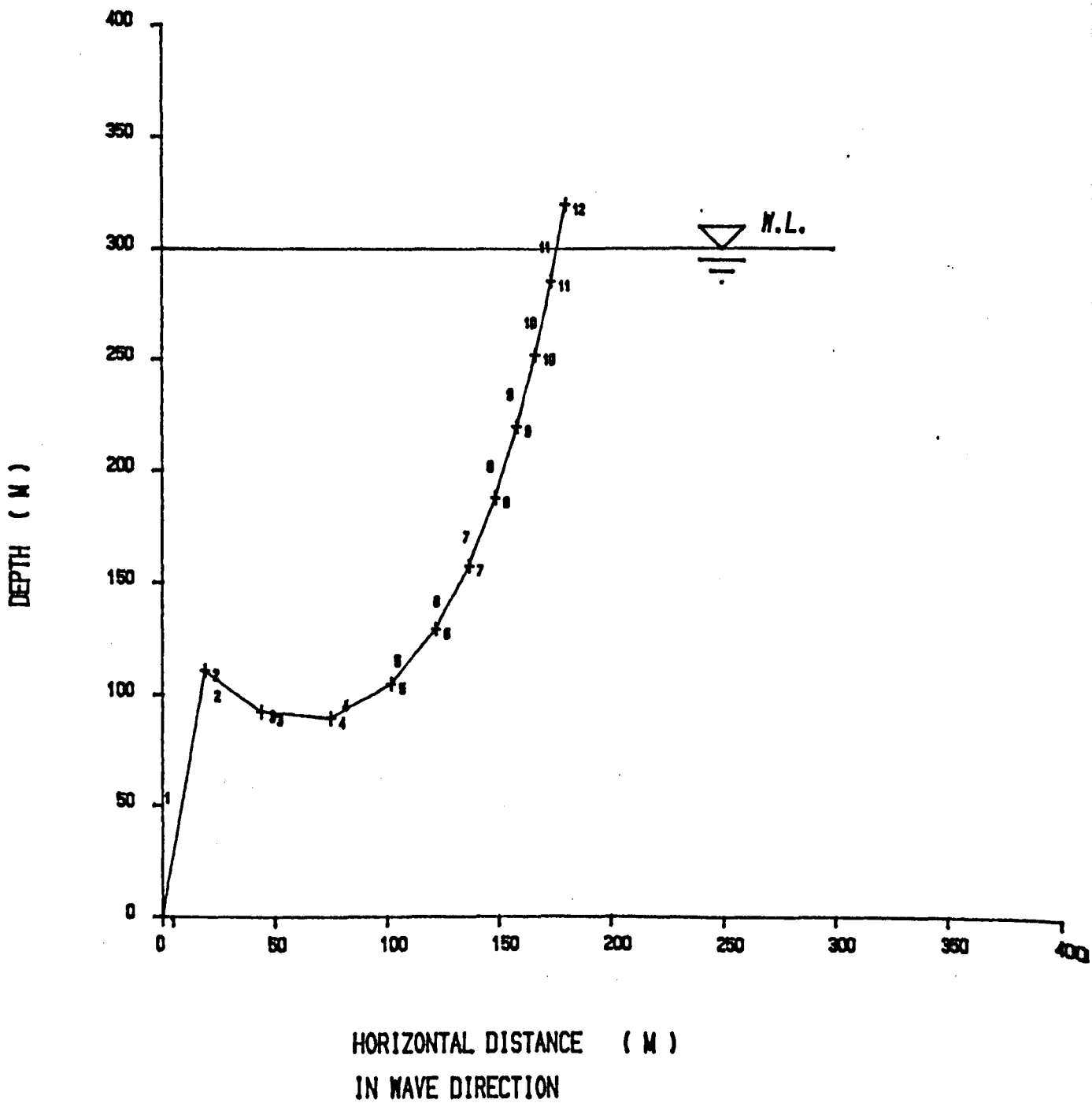


Figure 6.2 - Computed static equilibrium shape of a single catenary riser

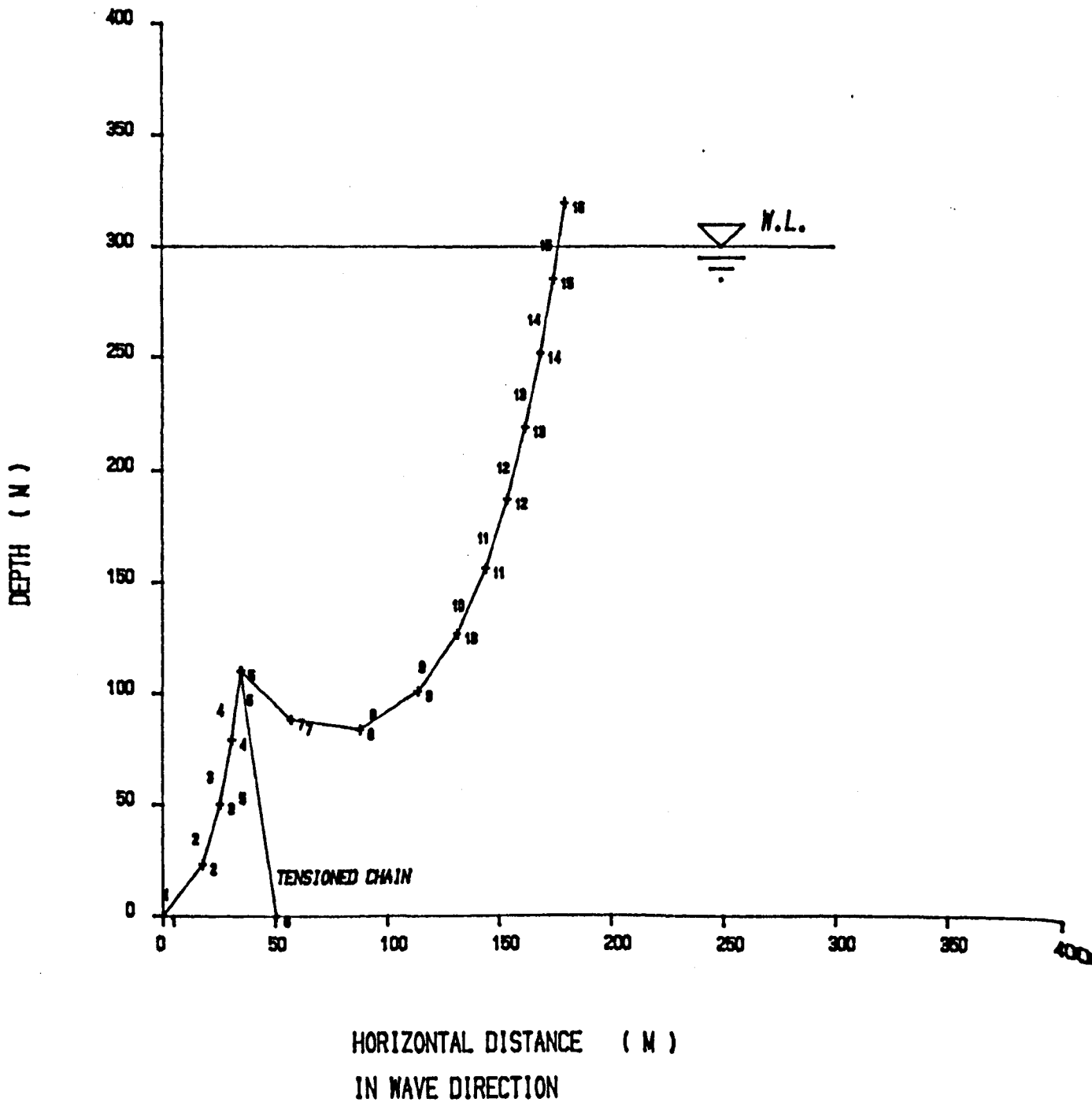


Figure 6.3 - Computed static equilibrium shape of a double catenary riser

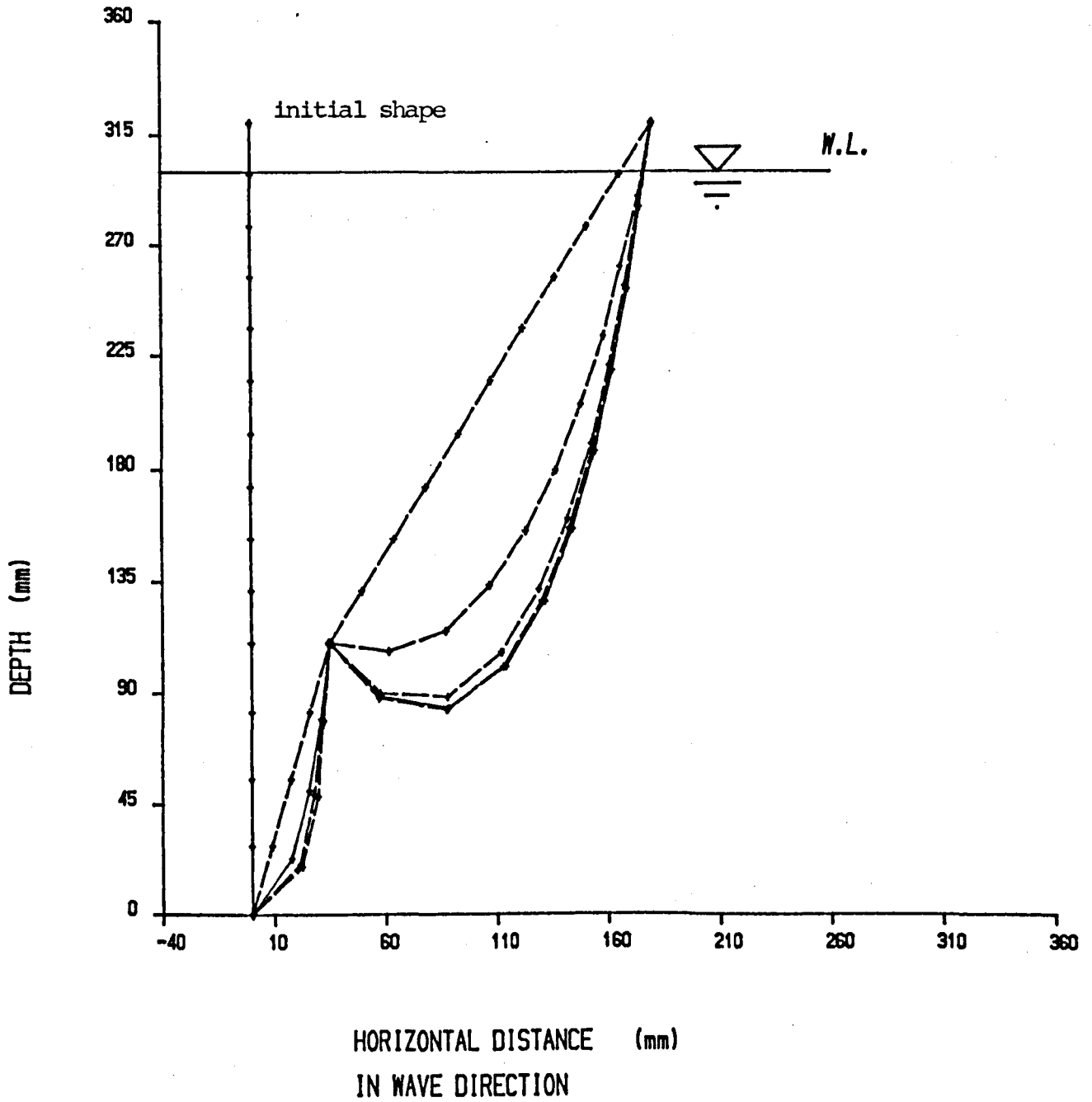


Figure 6.4 - Computation of static equilibrium shape of a double catenary riser from the initial input shape

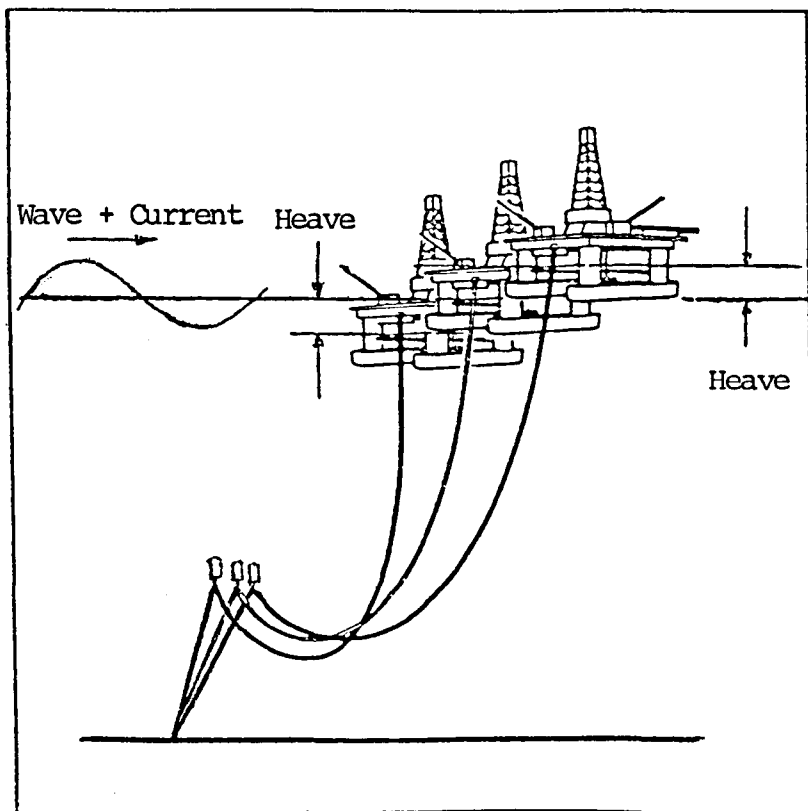
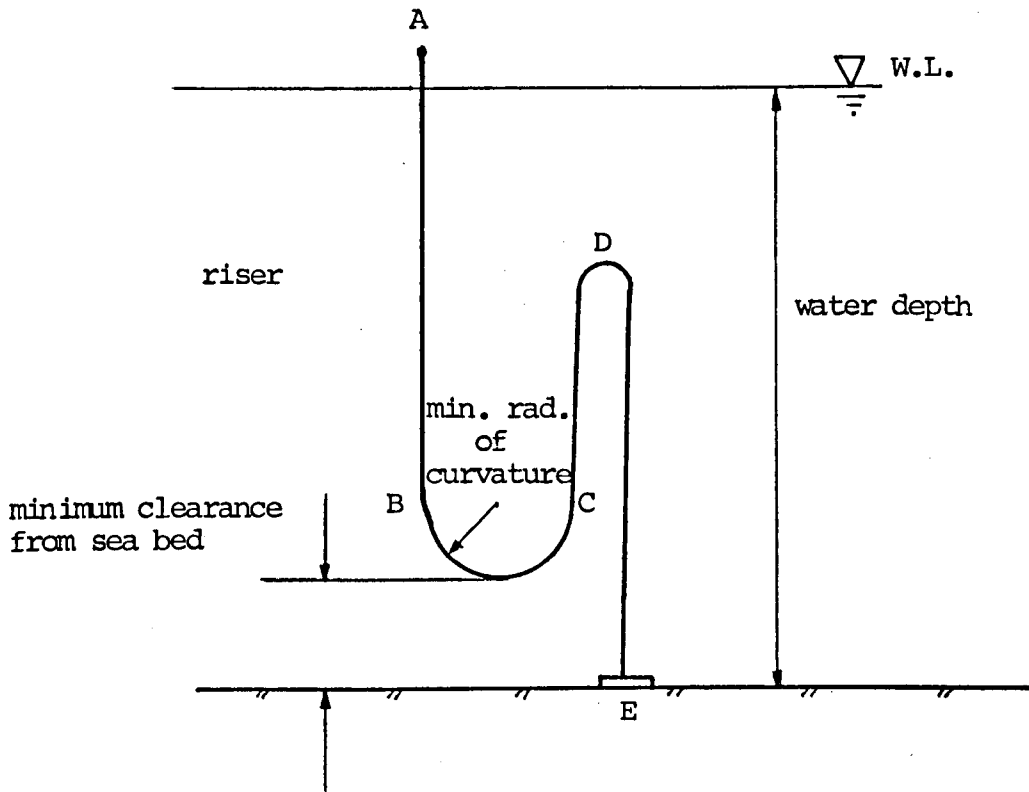


Figure 6.5 - Critical Configurations of a single catenary riser corresponding to far and near movements of the platform



$$\text{total riser length} = AB + BC + CD + DE$$

Figure 6.6 - Key configuration to estimate the length of a single catenary riser

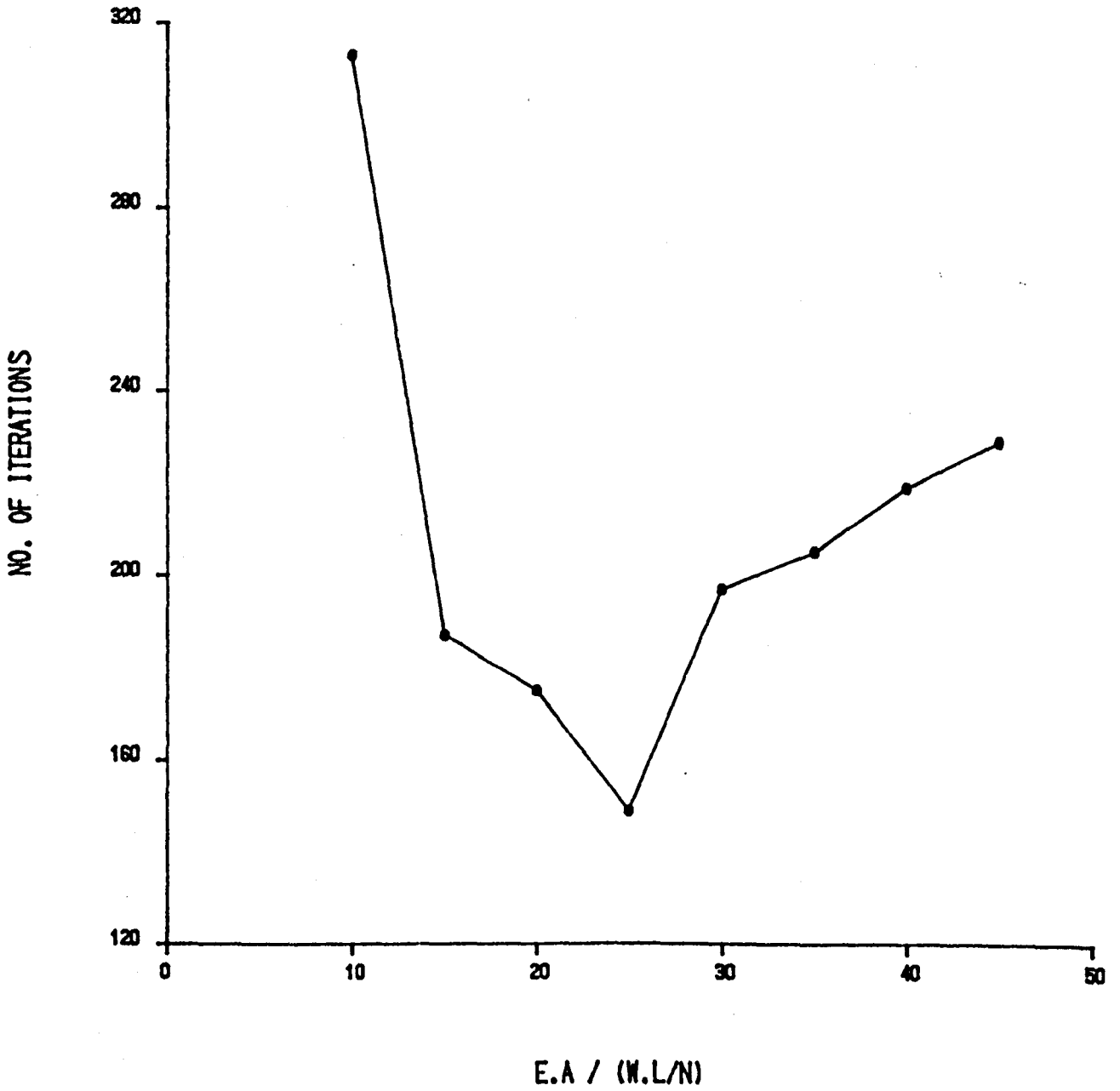


Figure 6.7 - Optimization of static solution with reduced axial stiffness

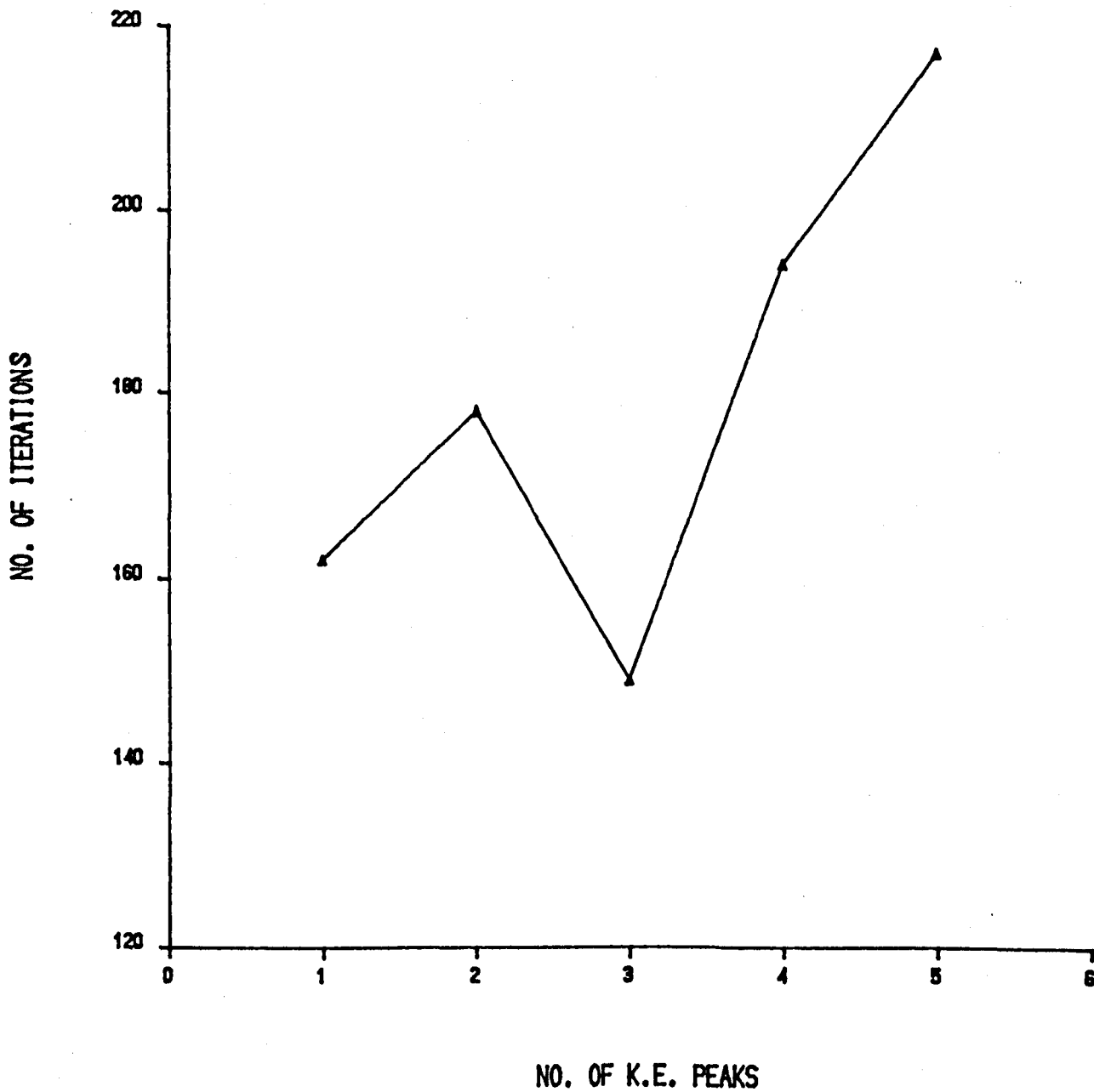


Figure 6.8 - Optimization of static solution with number of kinetic energy peaks at which the riser length is corrected

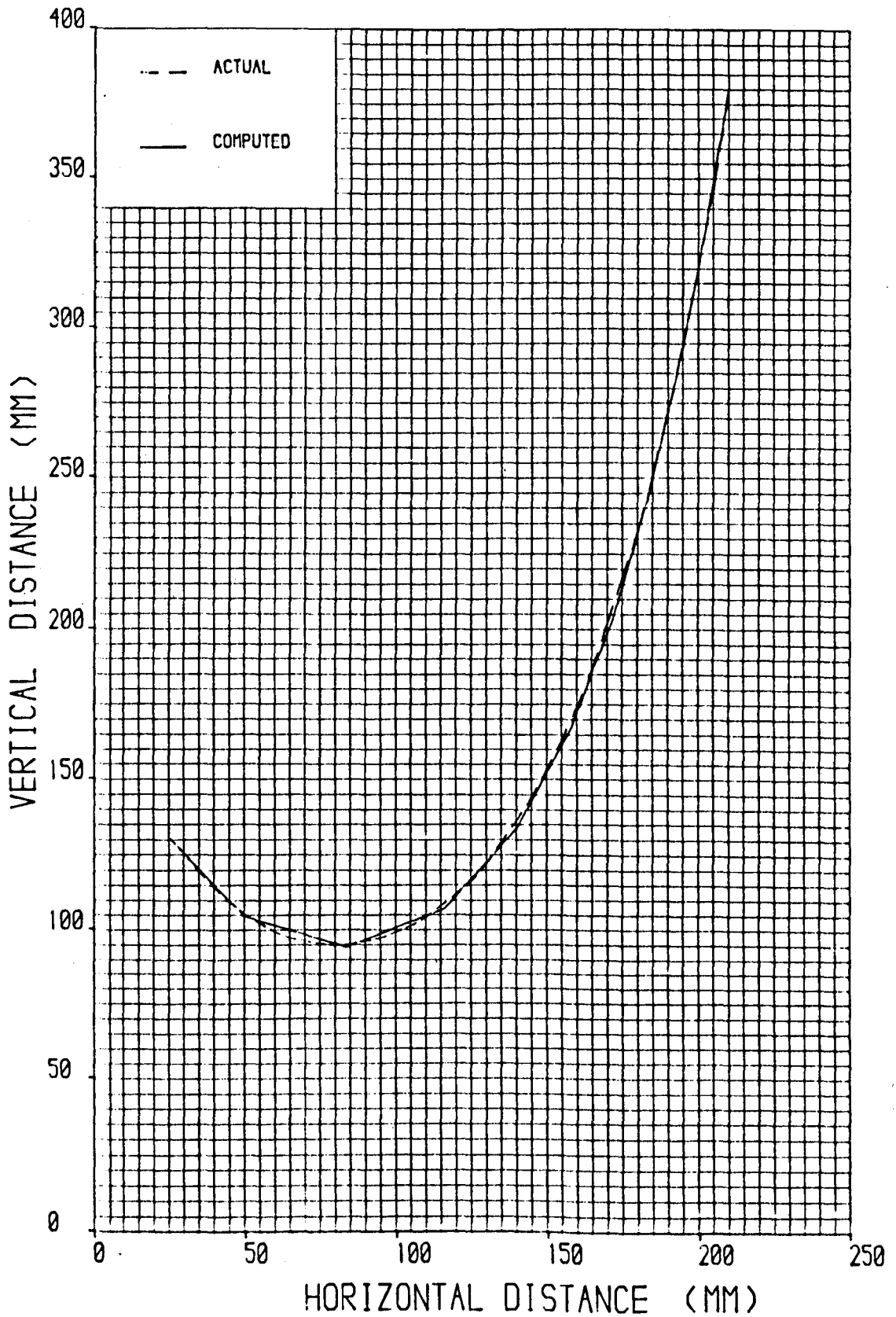


Figure 6.9 - Comparison of the digitized and computed static configurations of the catenary snake chain representing the upper part of a single or double catenary riser

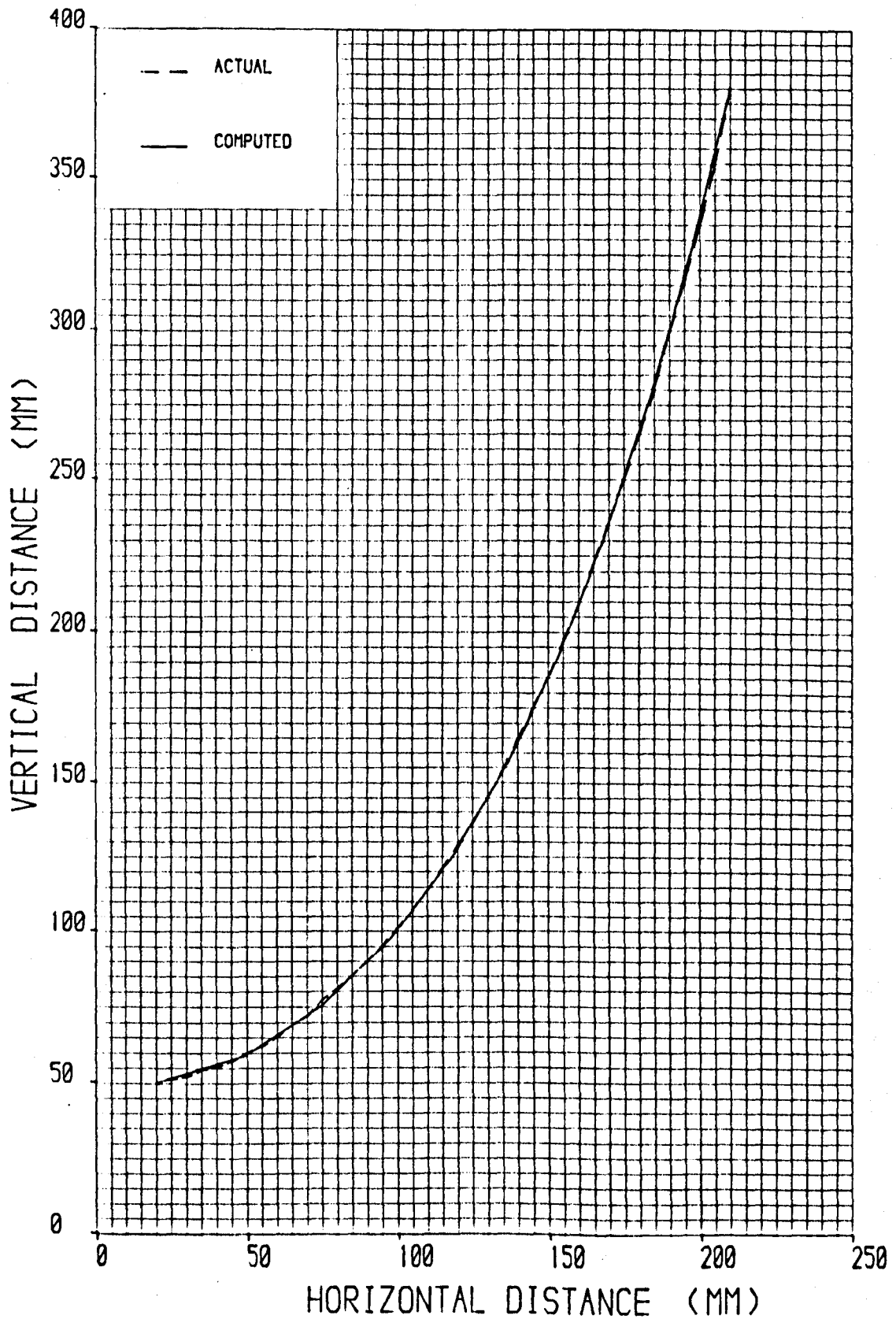


Figure 6.10 - Comparison of the digitized and computed static configurations of the catenary snake chain representing a free hanging riser

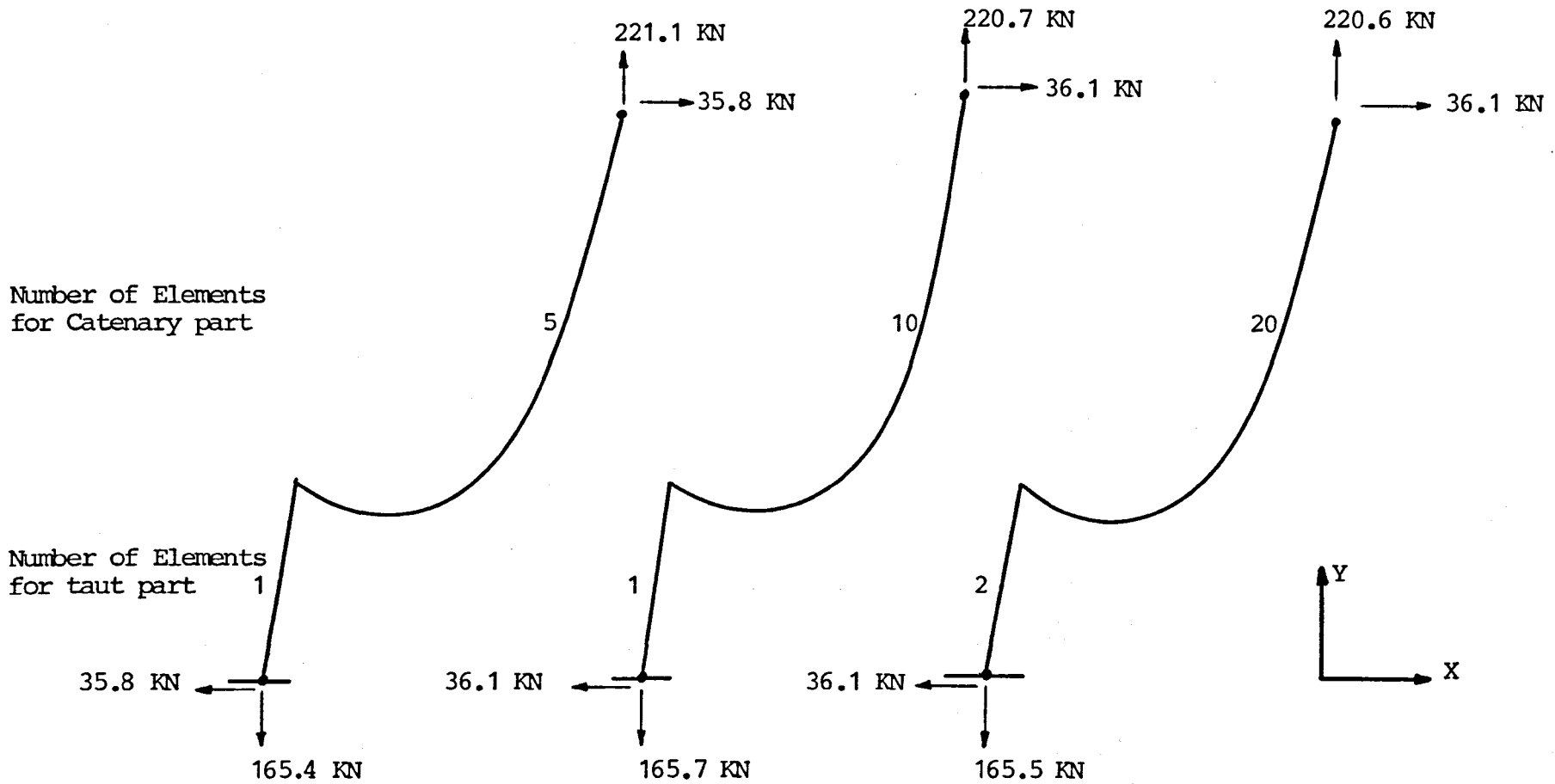


Figure 6.11 - Reaction forces of a Single Catenary Riser with Different Number of Elements

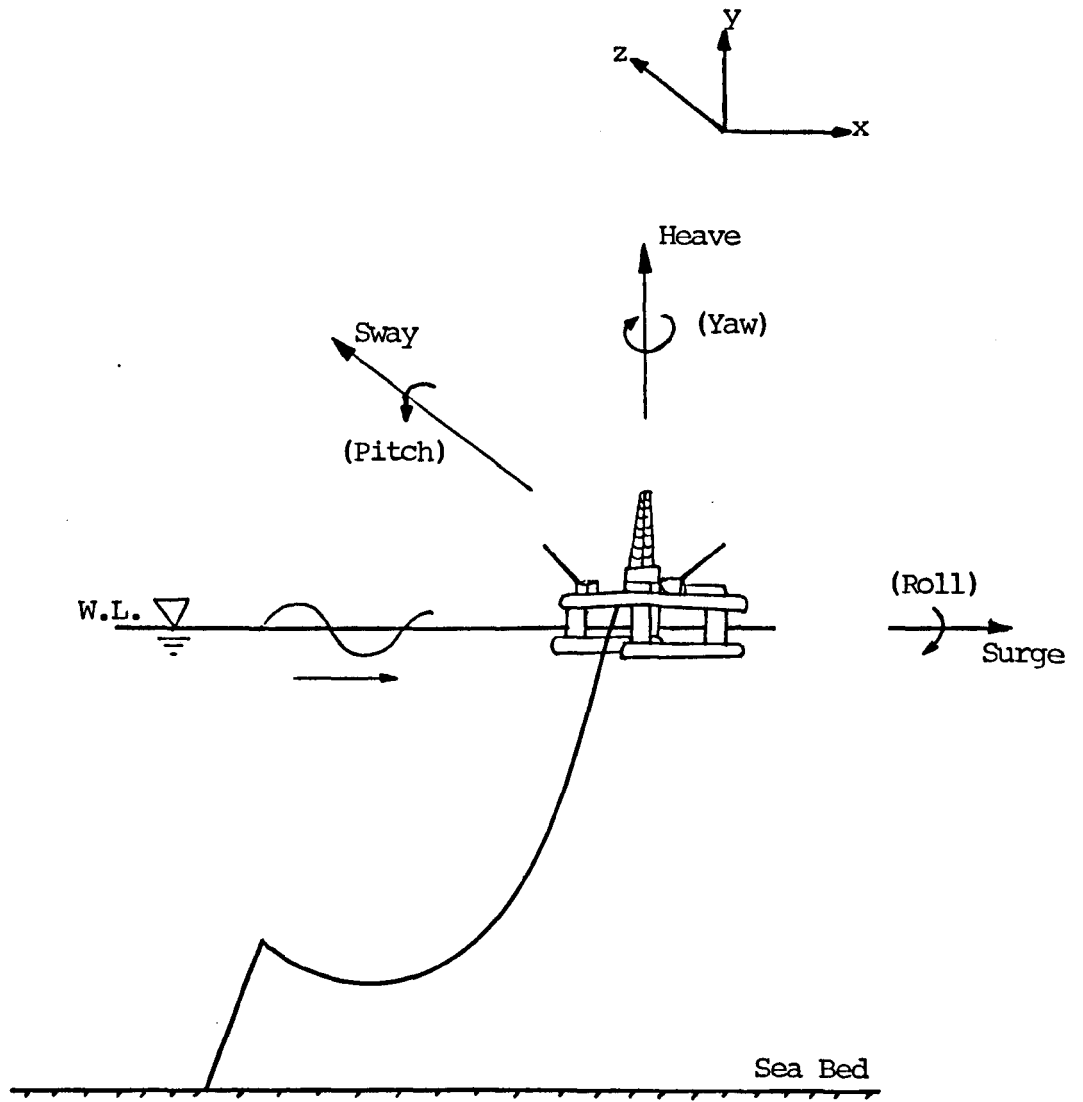


Figure 6.12 - Definition Sketch of Platform Motion

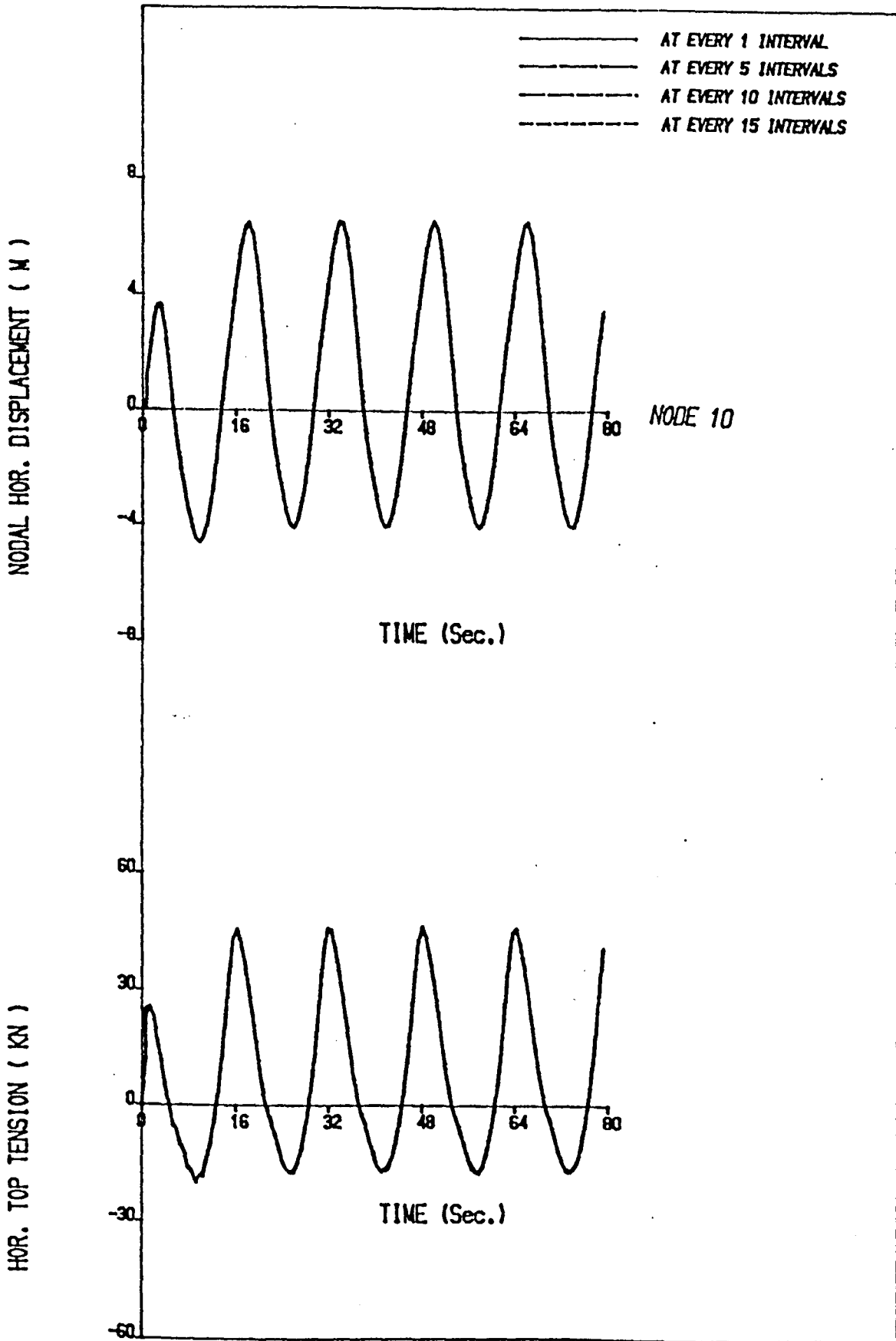


Figure 6.13 - Comparison of the computed dynamic responses of a single catenary riser with calculating the wave and current induced hydrodynamic forces at every 1, 5, 10 or 15 integration time intervals

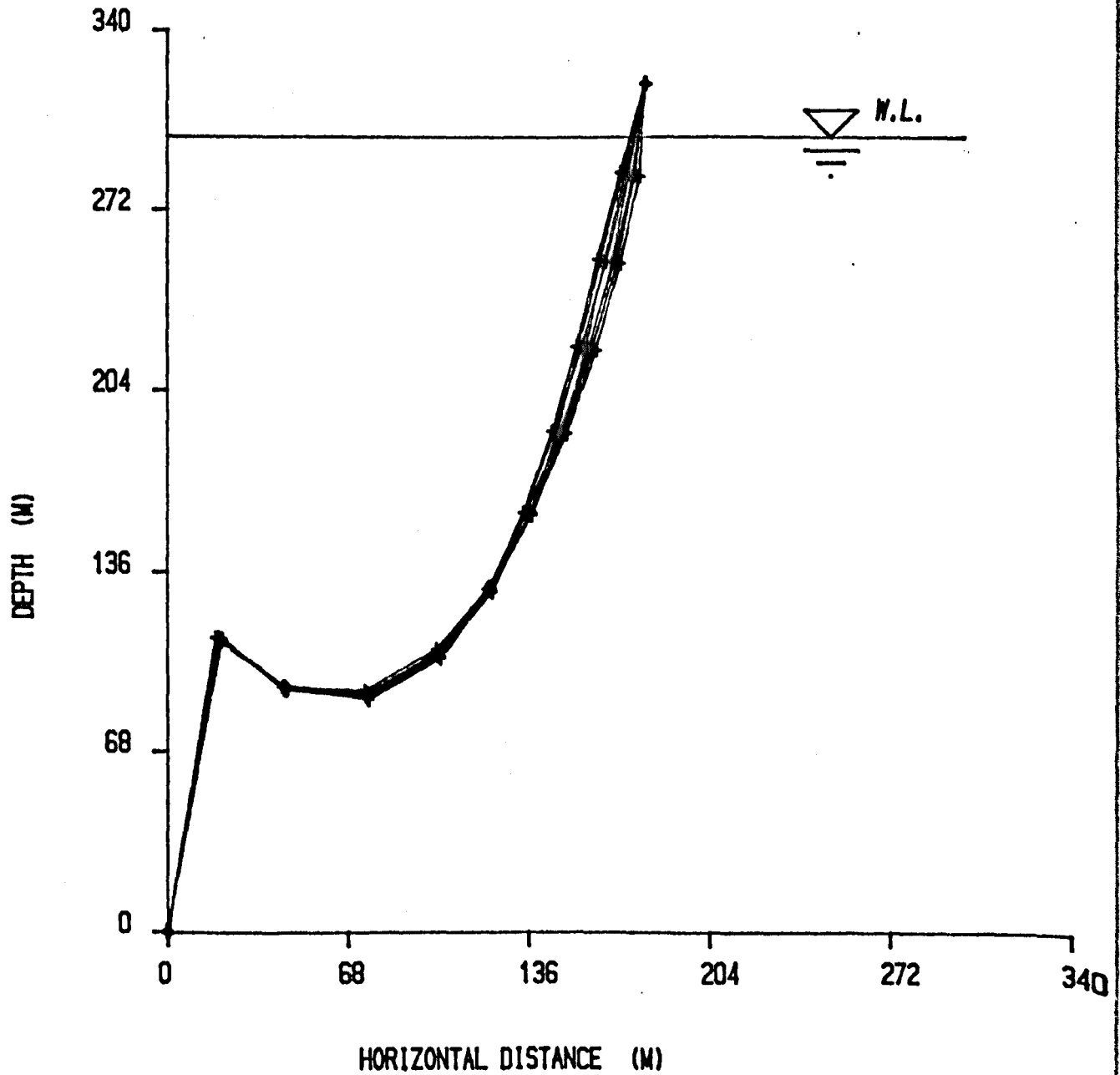
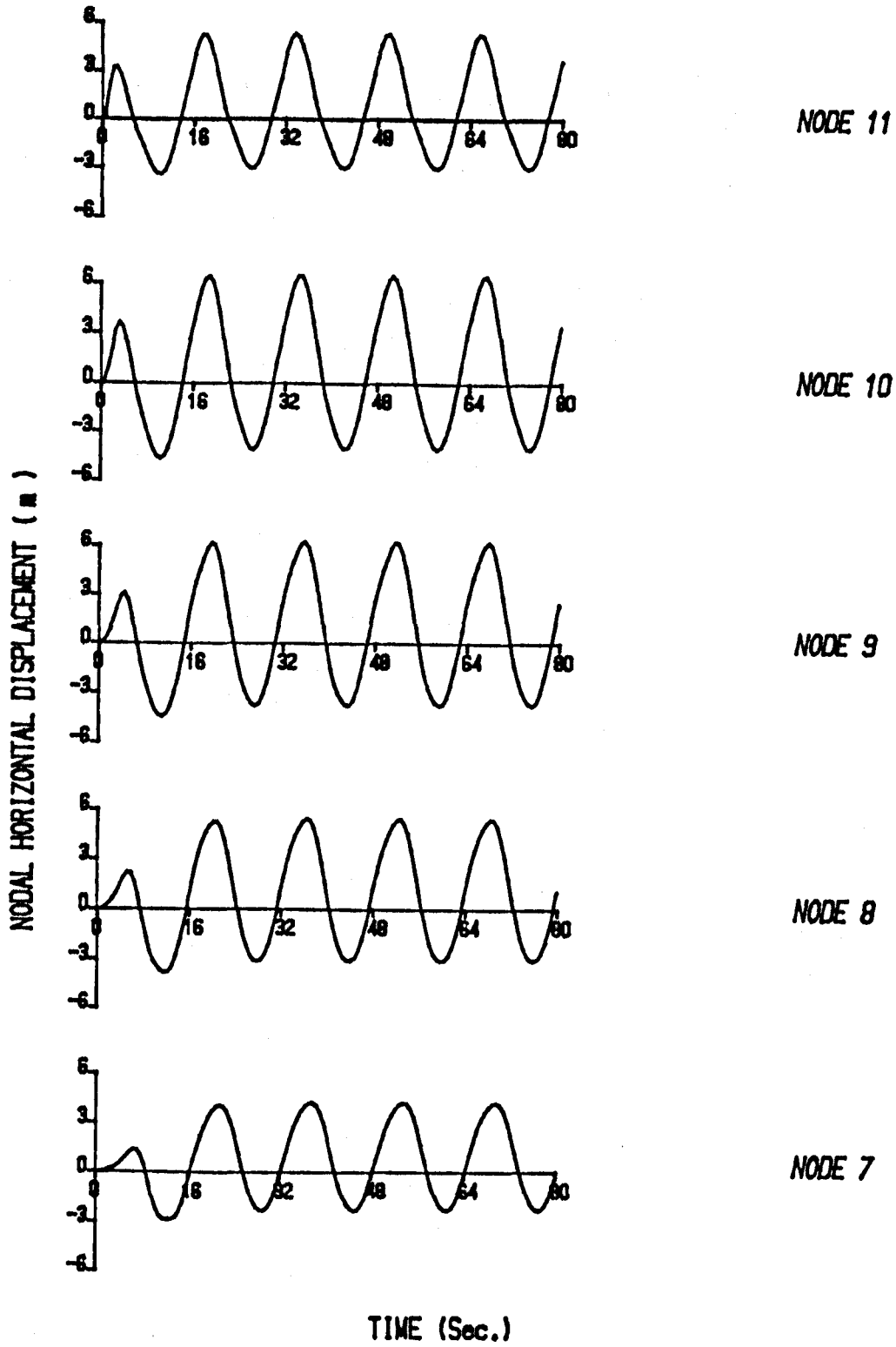


Figure 6.14 - Snap-shots of the dynamic response of a single catenary riser subjected to wave and current induced hydrodynamic loadings



TIME (Sec.)

(Continued ...)

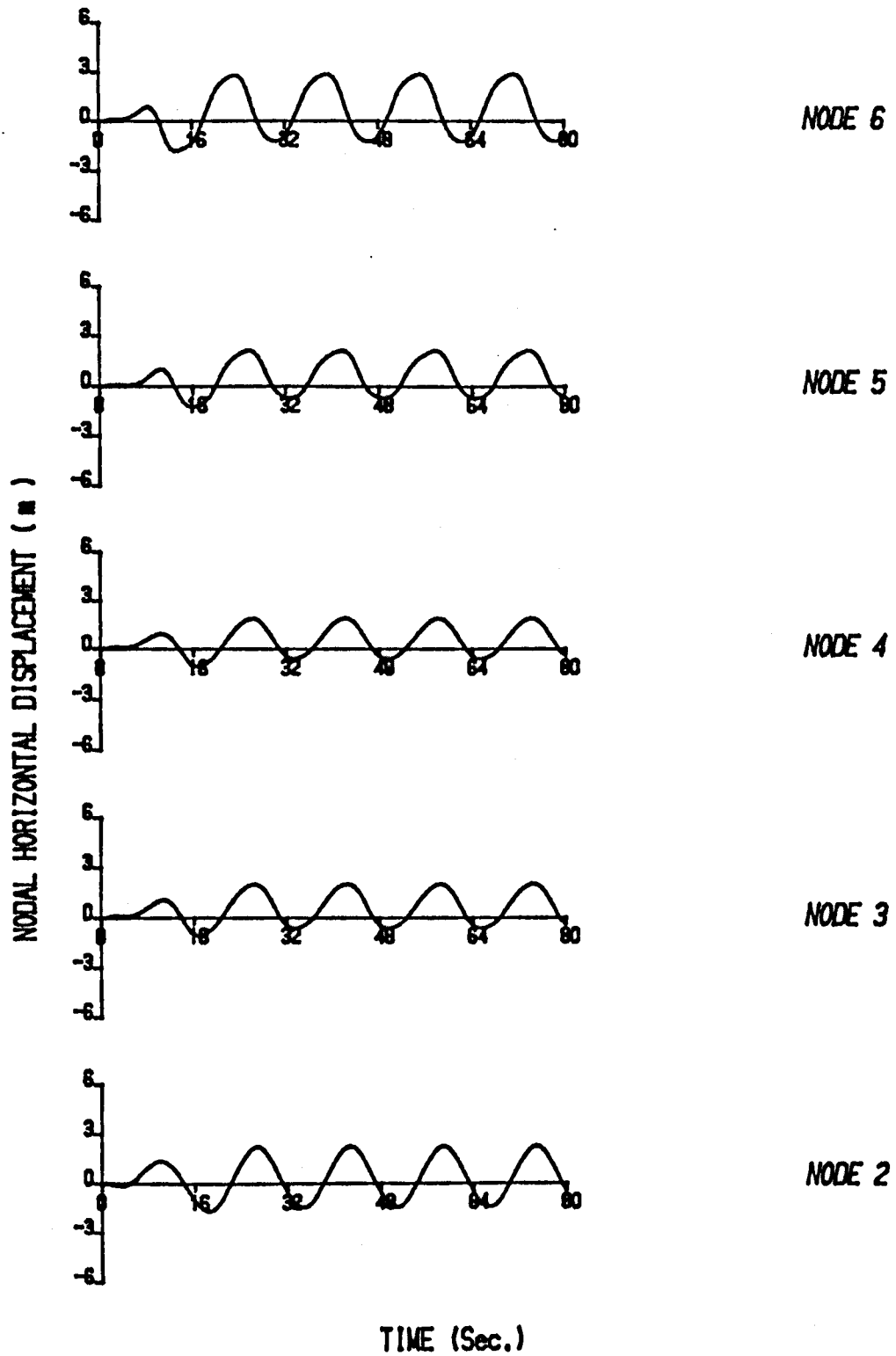
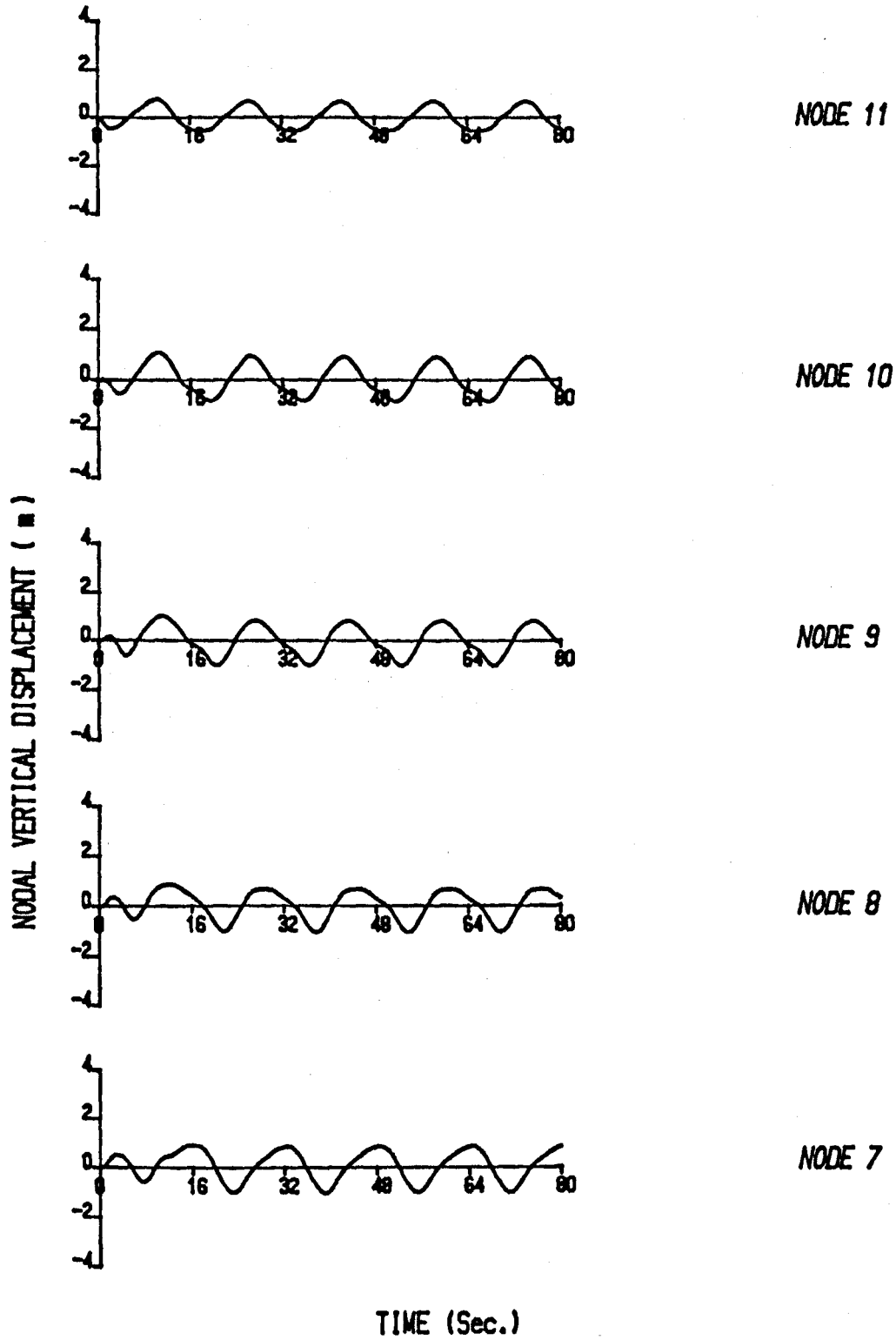


Figure 6.15 - Time histories of horizontal nodal displacements of a single catenary riser subjected to wave and current induced hydrodynamic loadings



TIME (Sec.)

(Continued ...)

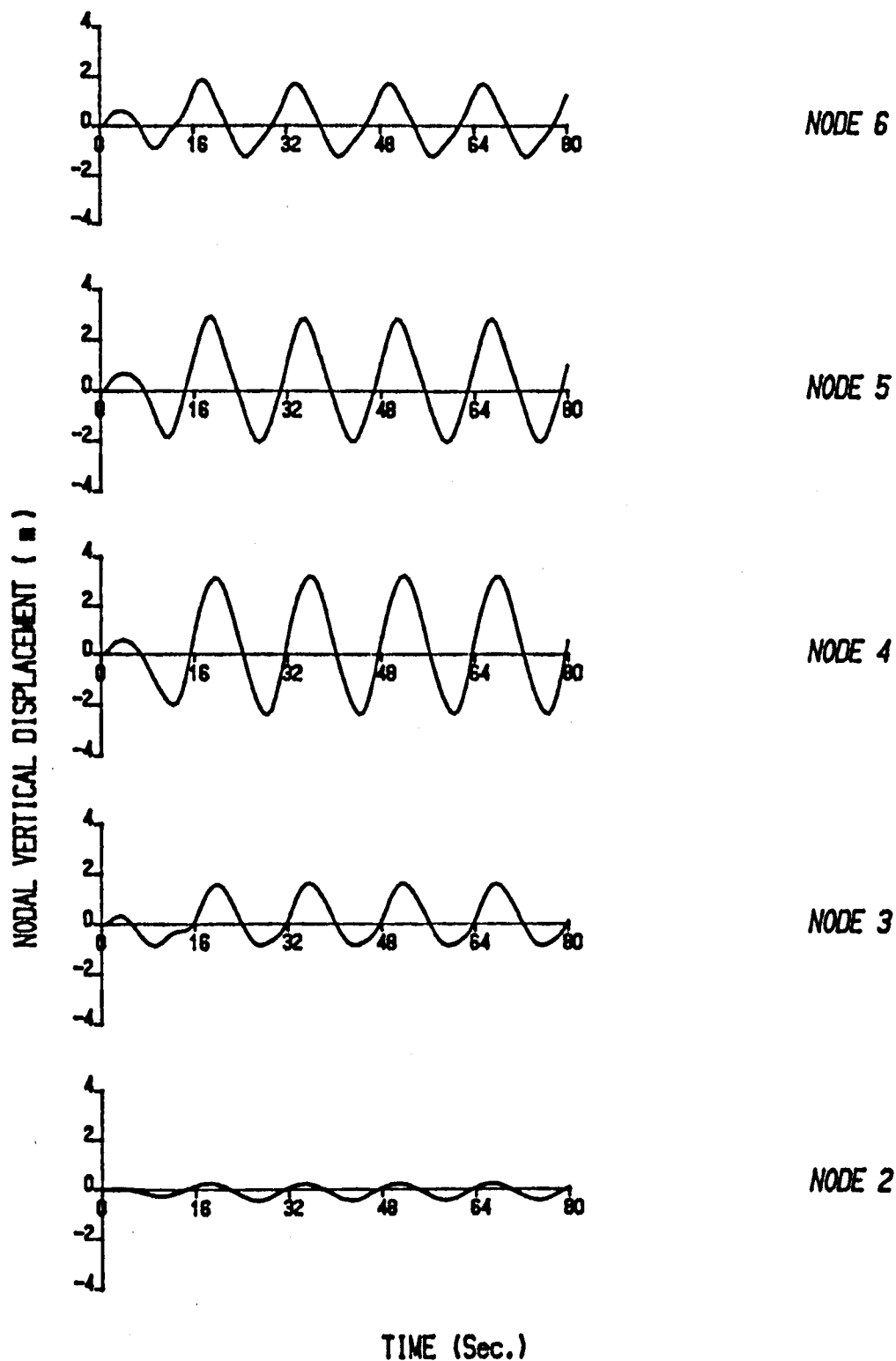


Figure 6.16 - Time histories of vertical nodal displacements of a single catenary riser subjected to wave and current induced hydrodynamic loadings

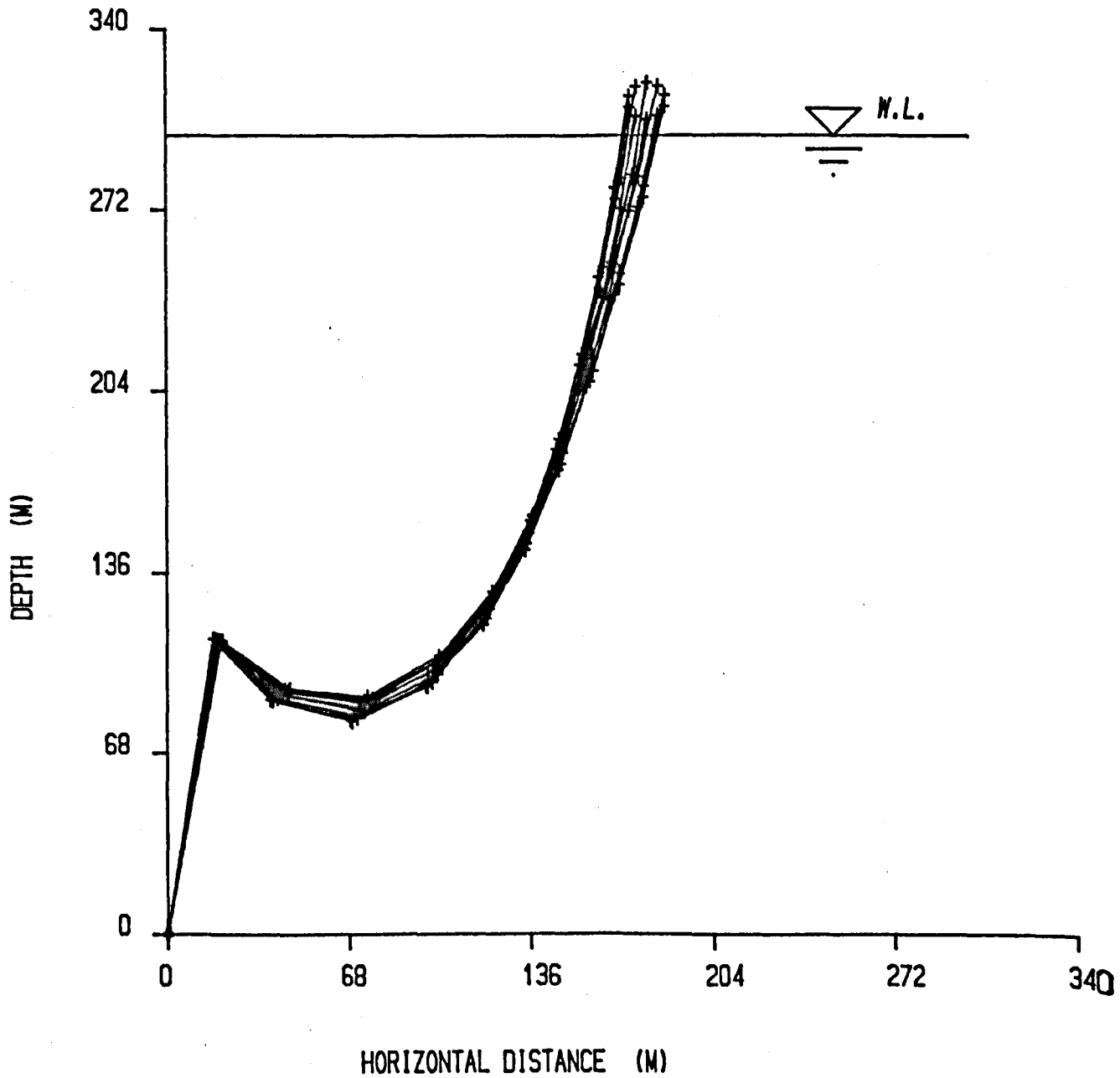
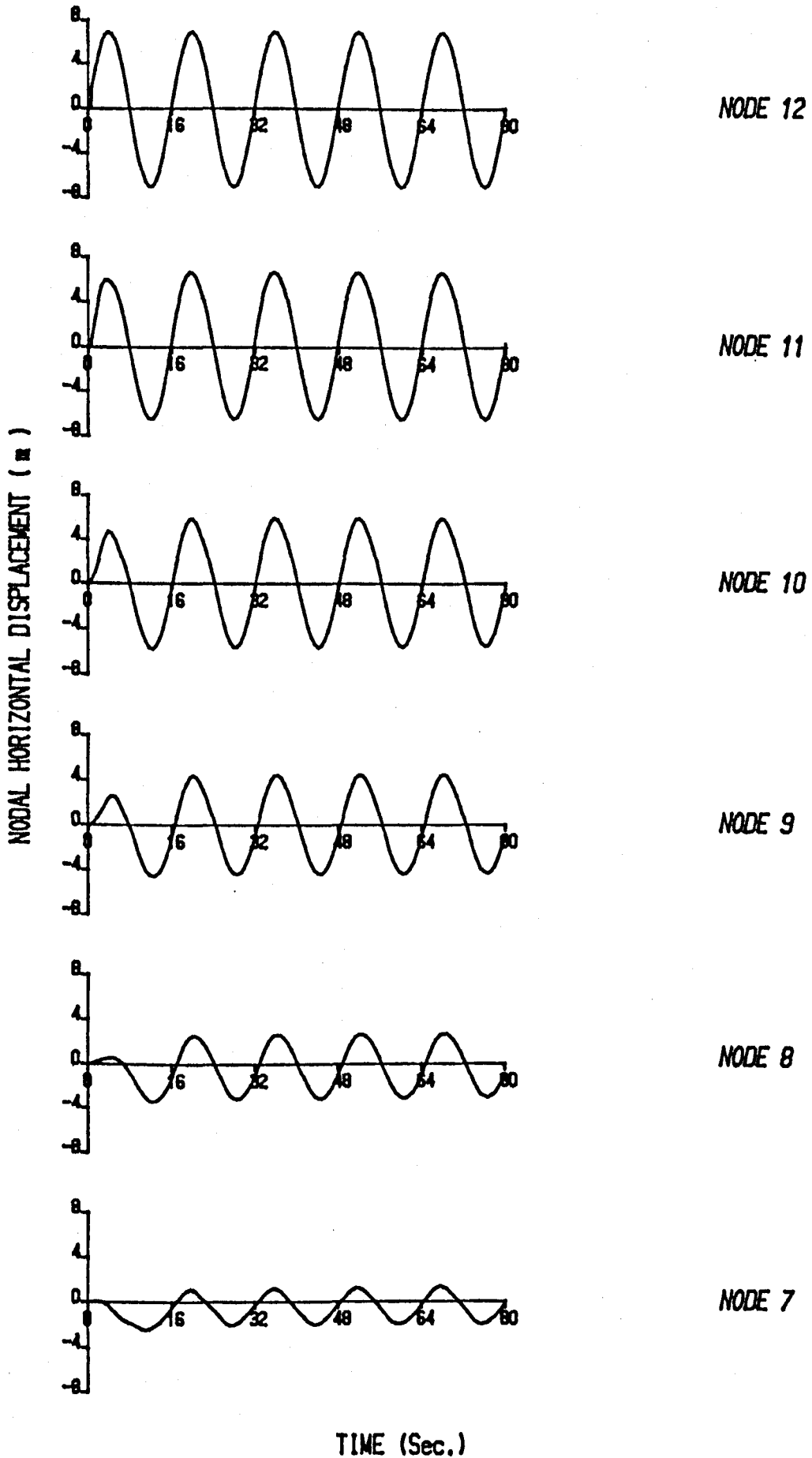


Figure 6.17 - Snap-shots of the dynamic response of a single catenary riser subjected to wave and current induced hydrodynamic forces and platform motion



TIME (Sec.)

(Continued ...)

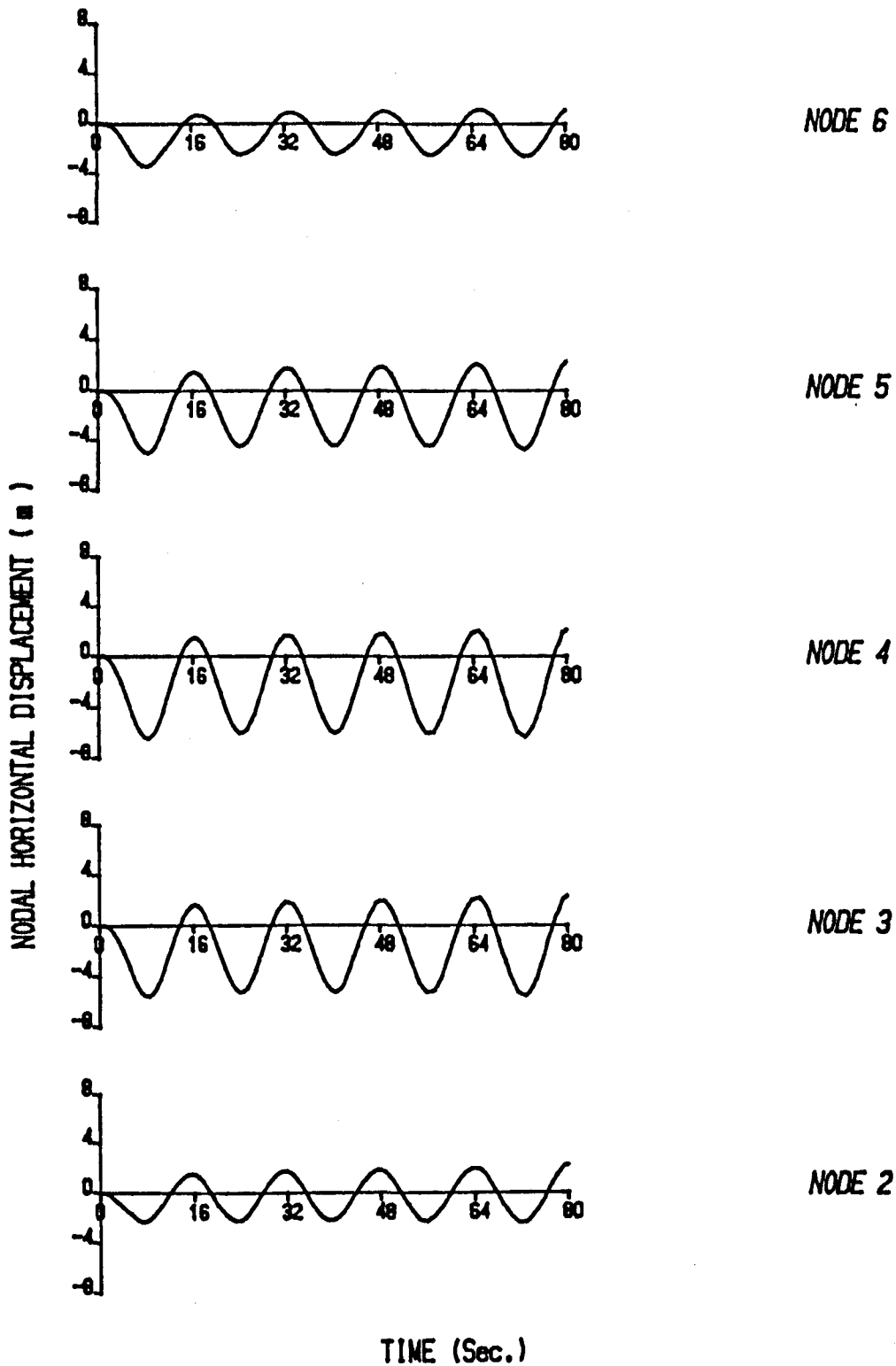
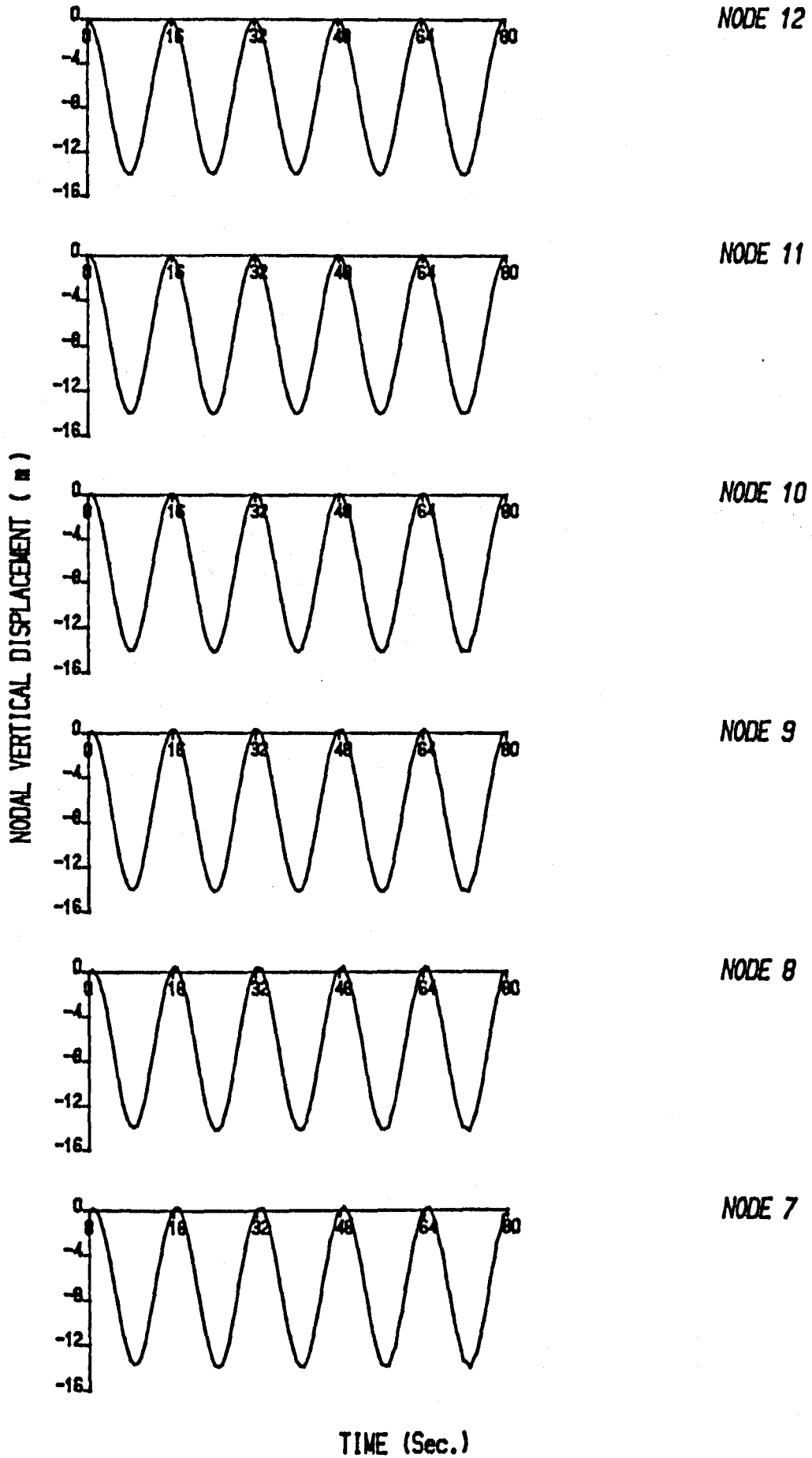


Figure 6.18 - Time histories of horizontal nodal displacements of a single catenary riser subjected to wave and current induced hydrodynamic loadings and platform motion



(Continued ...)

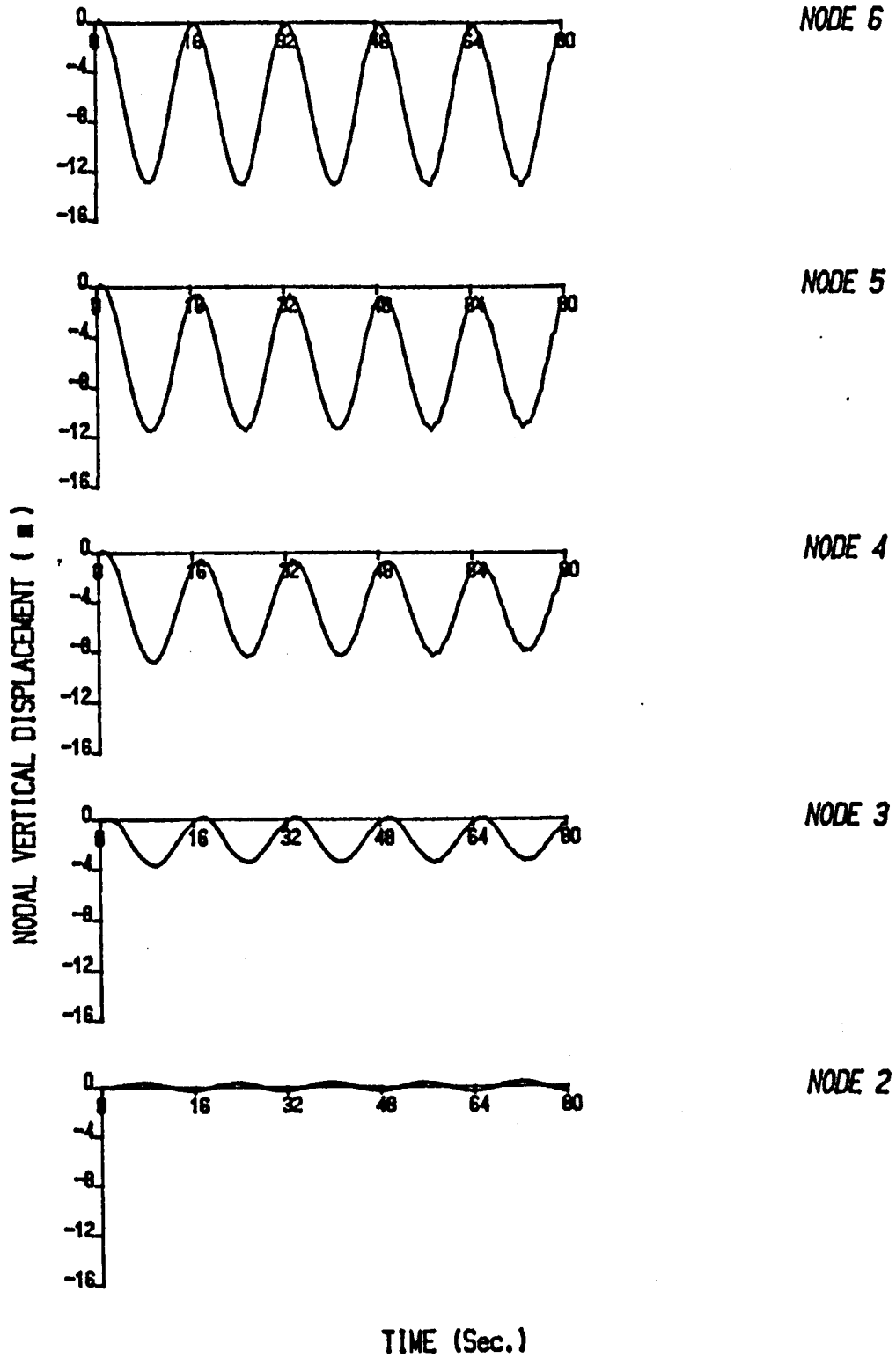


Figure 6.19 - Time histories of vertical nodal displacements of a single catenary riser subjected to wave and current induced hydrodynamic forces and platform motion

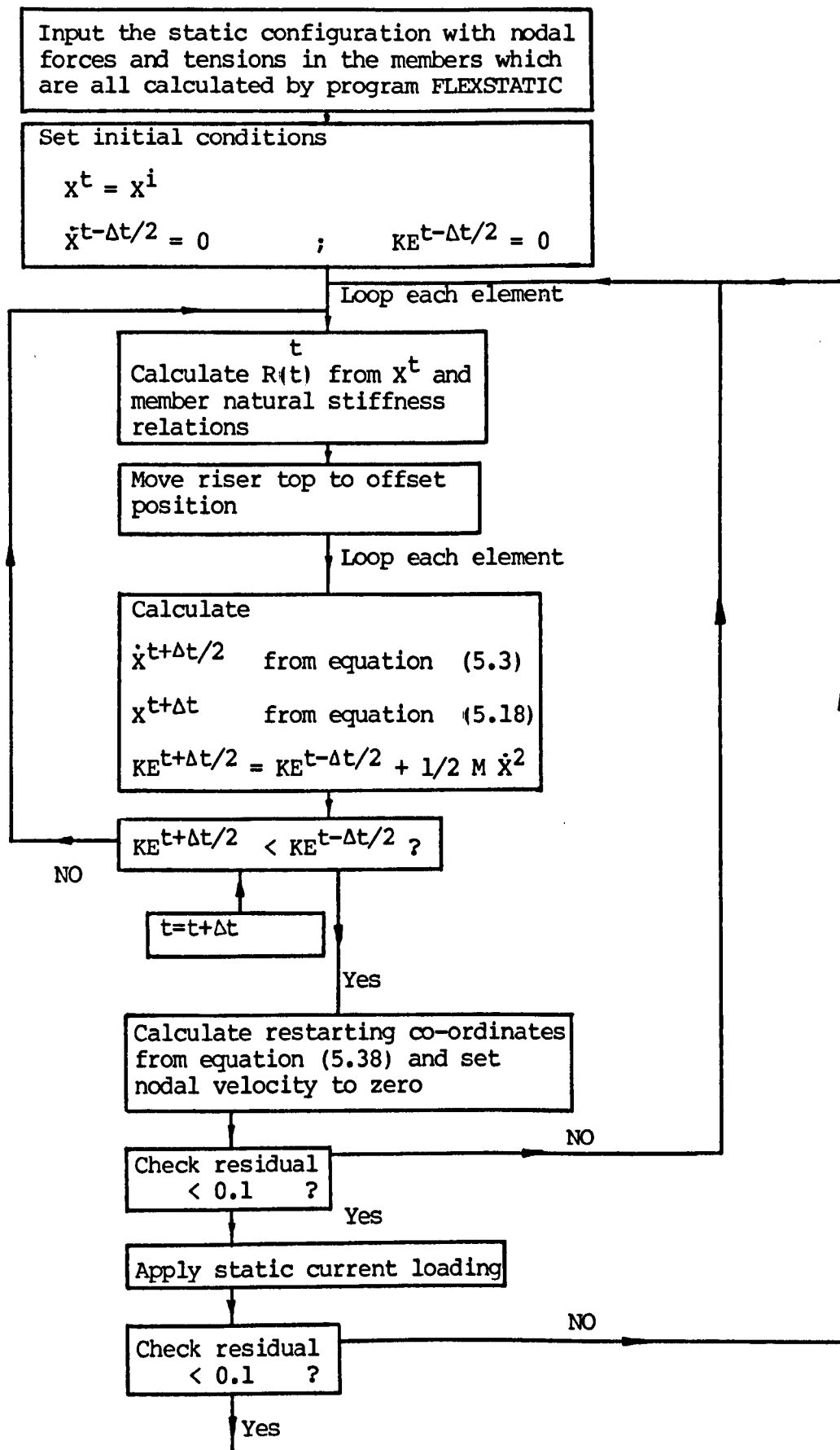


Figure 6.20 - Flow chart for static solution of a flexible riser subjected to current induced loadings and platform movements

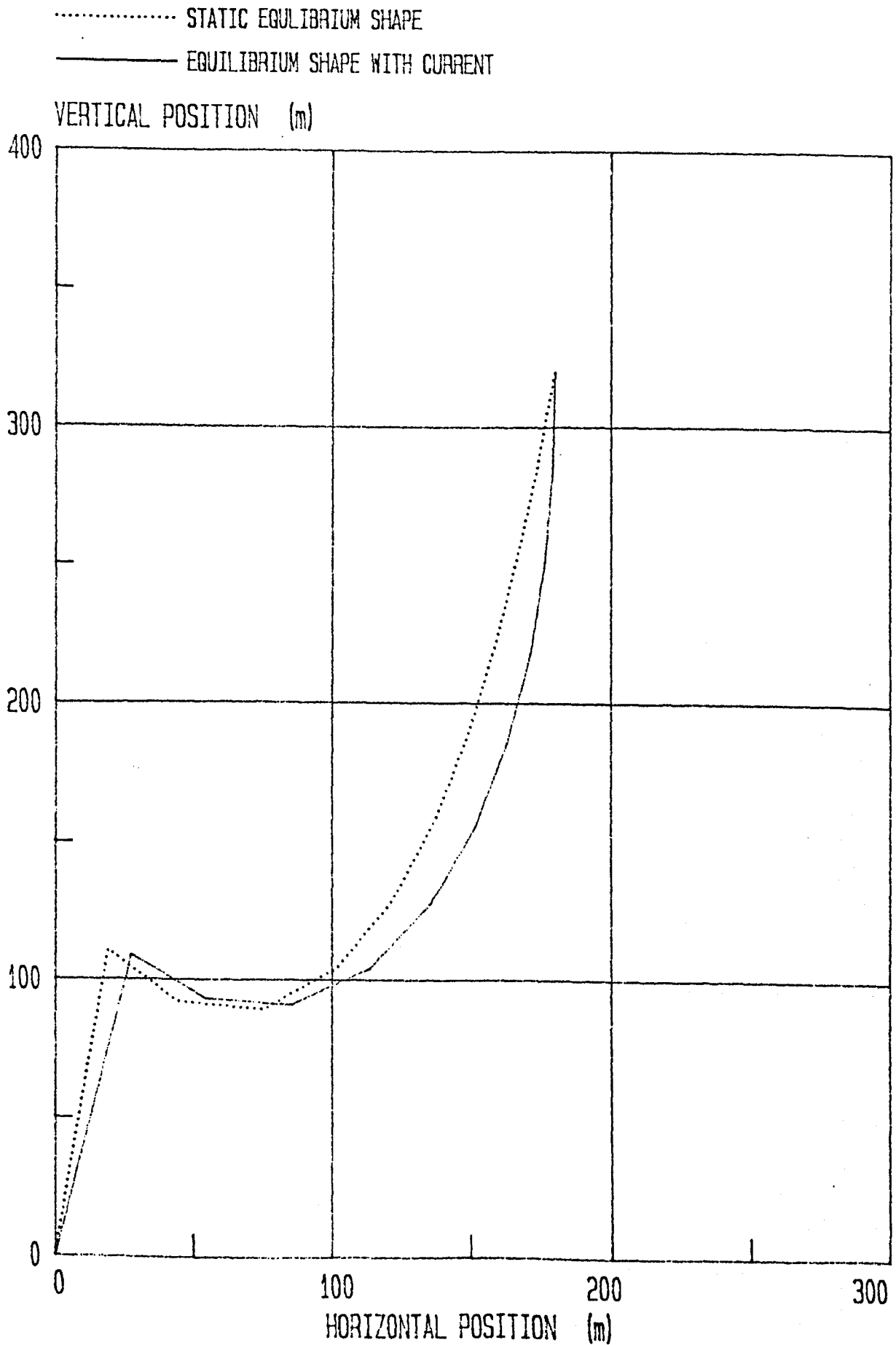


Figure 6.21 - Computed static equilibrium shapes of a single catenary riser with and without current induced hydrodynamic loadings

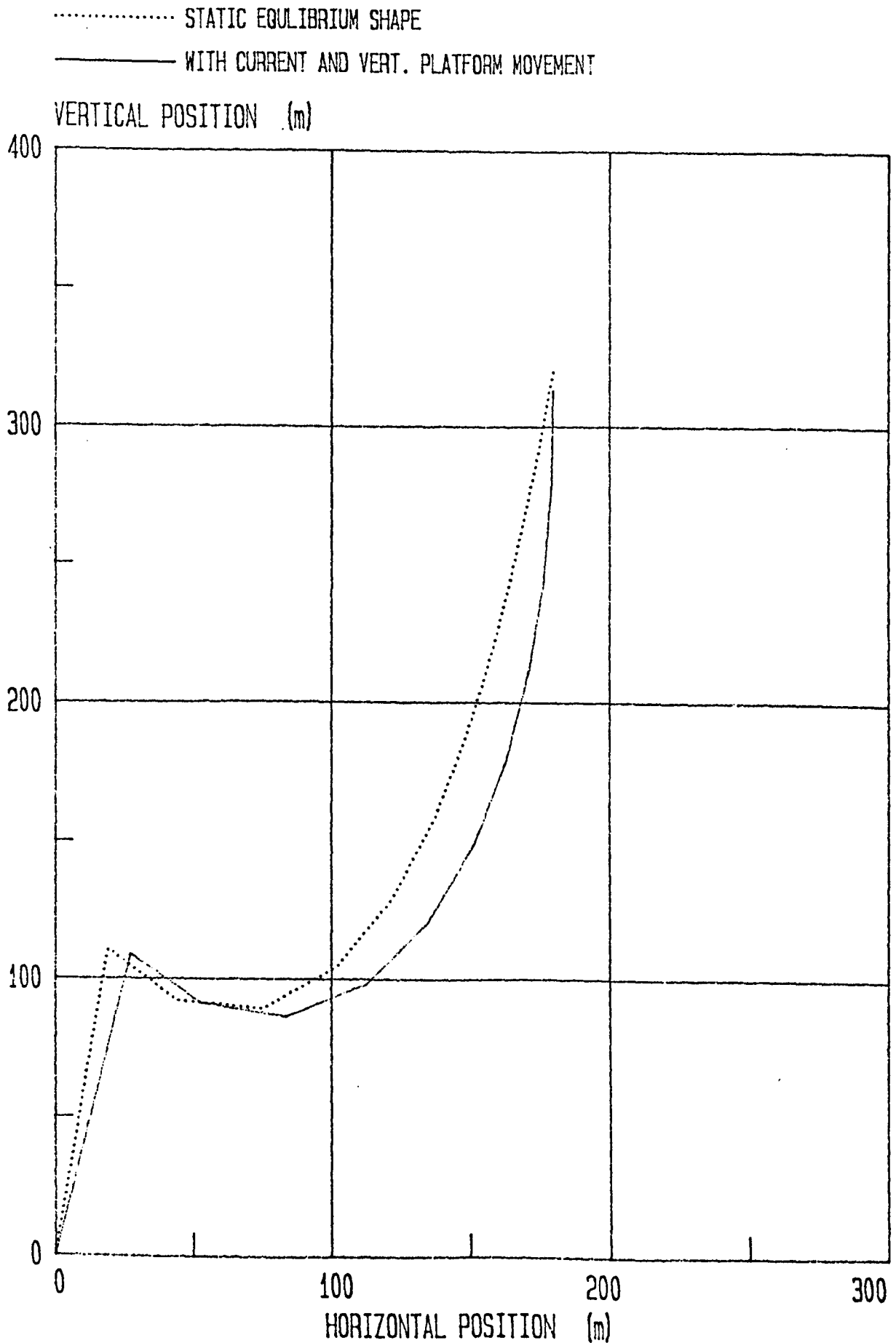


Figure 6.22 - Computed static equilibrium shapes of a single catenary riser with and without current induced loadings and vertical platform movement

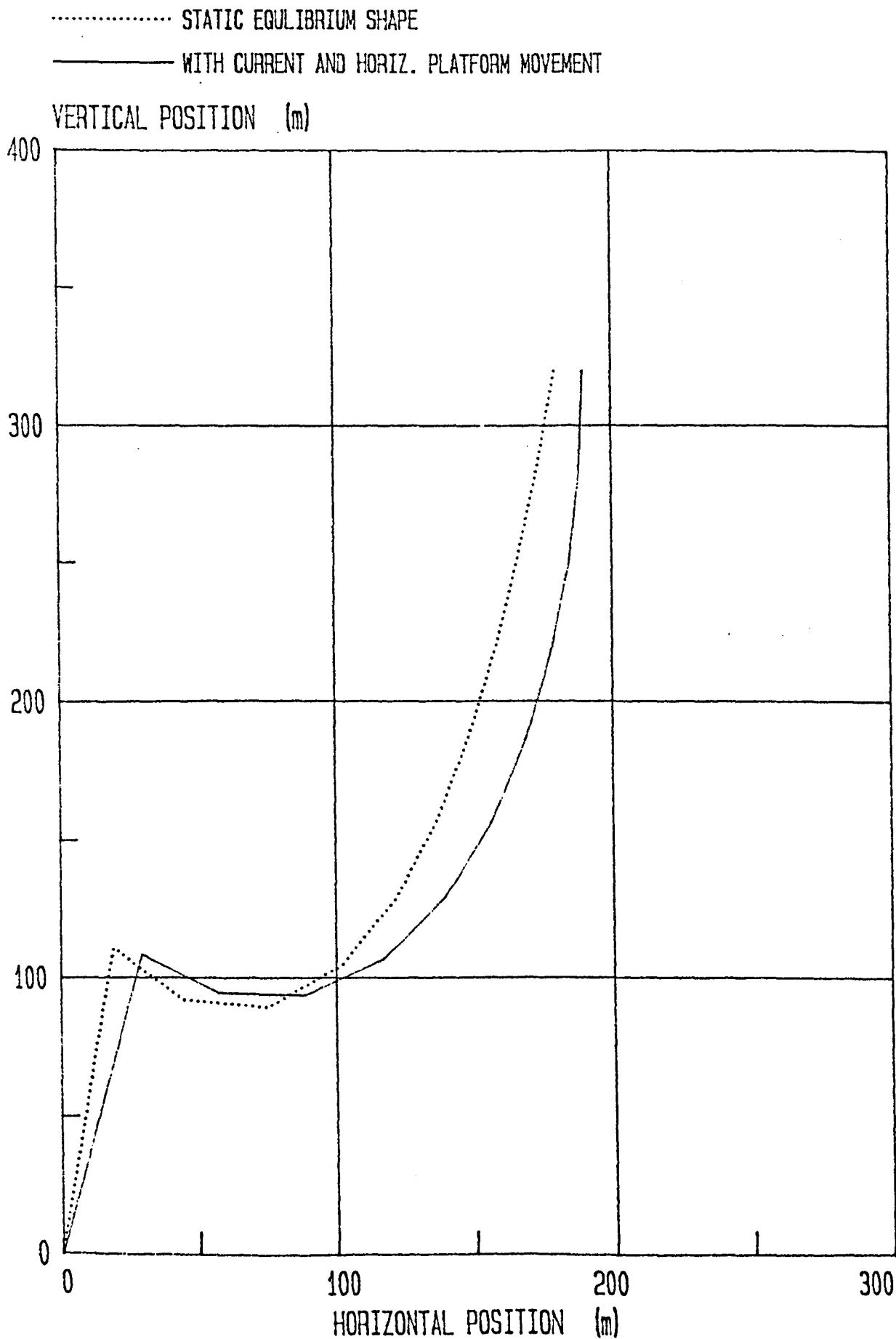


Figure 6.23 - Computed static equilibrium shapes of a single catenary riser with and without current induced hydrodynamic loadings and horizontal platform movement

Wave height 25 m

Wave period 16 sec

Current velocity profile : At water-free surface 1.5 m/sec  
At 100 metres below water 1 m/sec  
At sea bed 1 m/sec

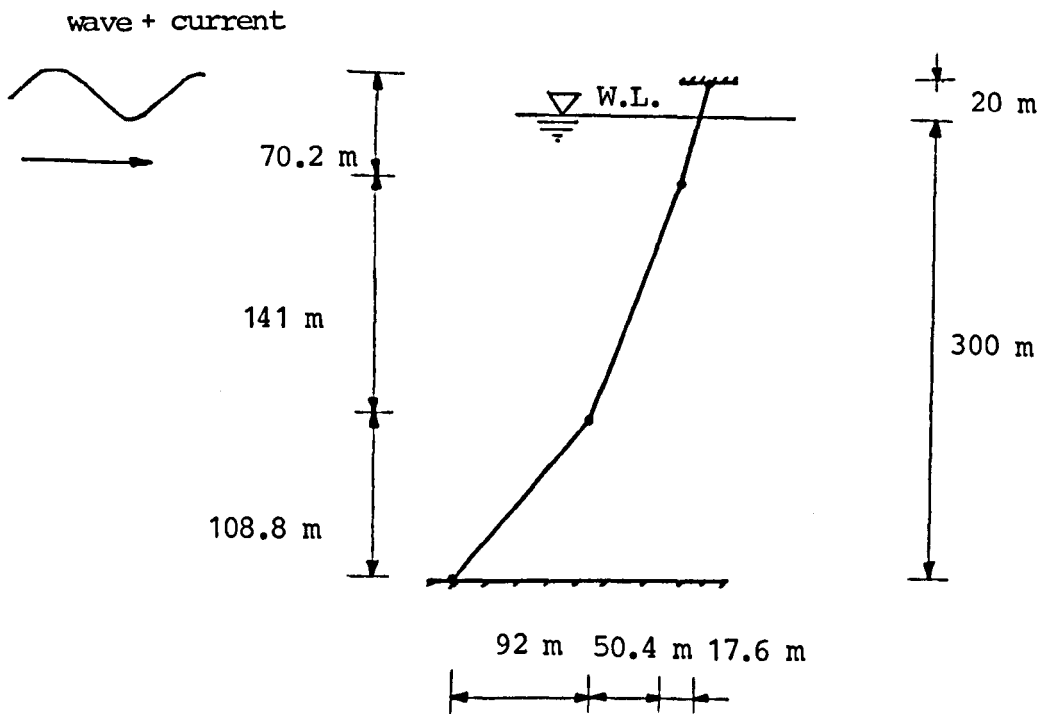


Figure 6.24 - Hand calculation test case

Wave height 25 m

Wave period 16 sec

Current velocity profile : At water-free surface 1.5 m/sec  
At 100 metres below water 1 m/sec  
At sea bed 1 m/sec

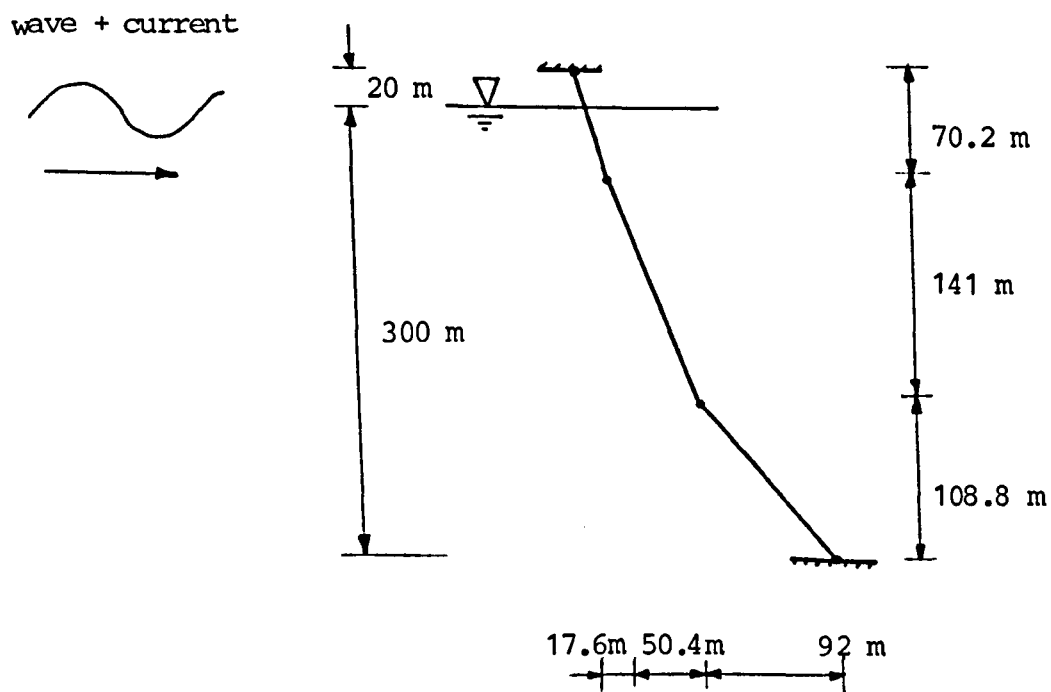


Figure 6.25 - Hand calculation test case

Weight of cable per unit length =  $W$

Length of Cable =  $L$

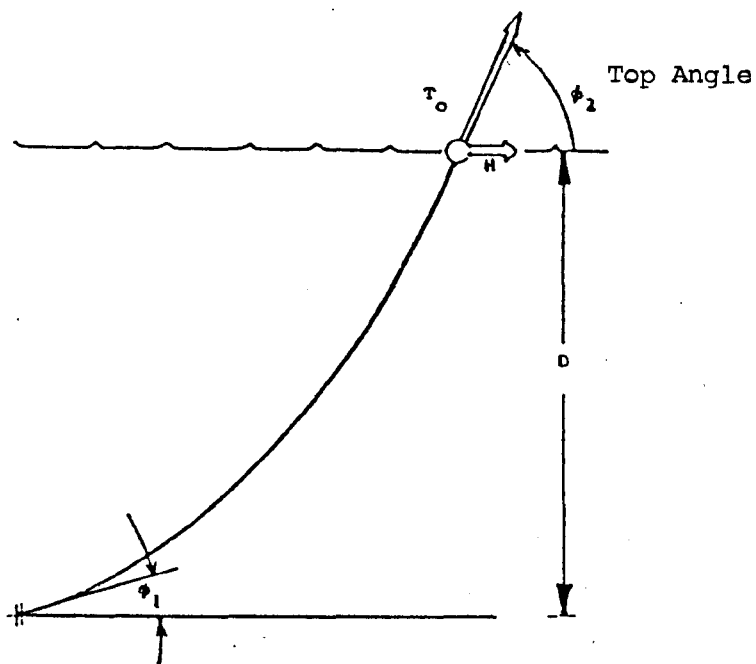


Figure 6.26 - Specifications of a catenary cable used by Triantafyllou et. al. (1983) to calculate the structural natural frequencies.

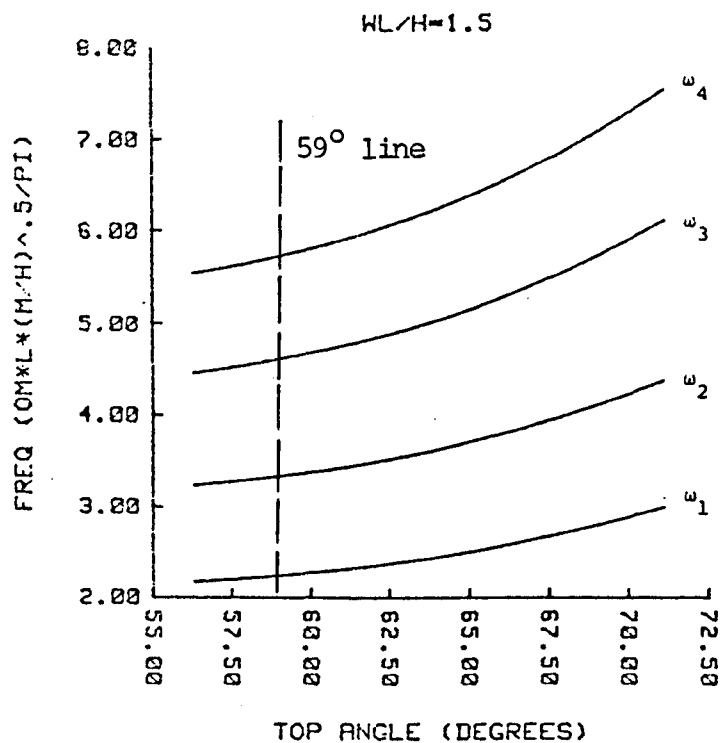


Figure 6.27 - The first four natural frequencies of a catenary for  $WL/H = 1.5$  as a function of the static angle at the top after Triantafyllou et. al. (1983) (the value in the vertical axis corresponds to non-dimensional circular natural frequencies. For the test case considered in the present work, the values in the vertical axis correspond to  $0.139158 \omega_n$ )

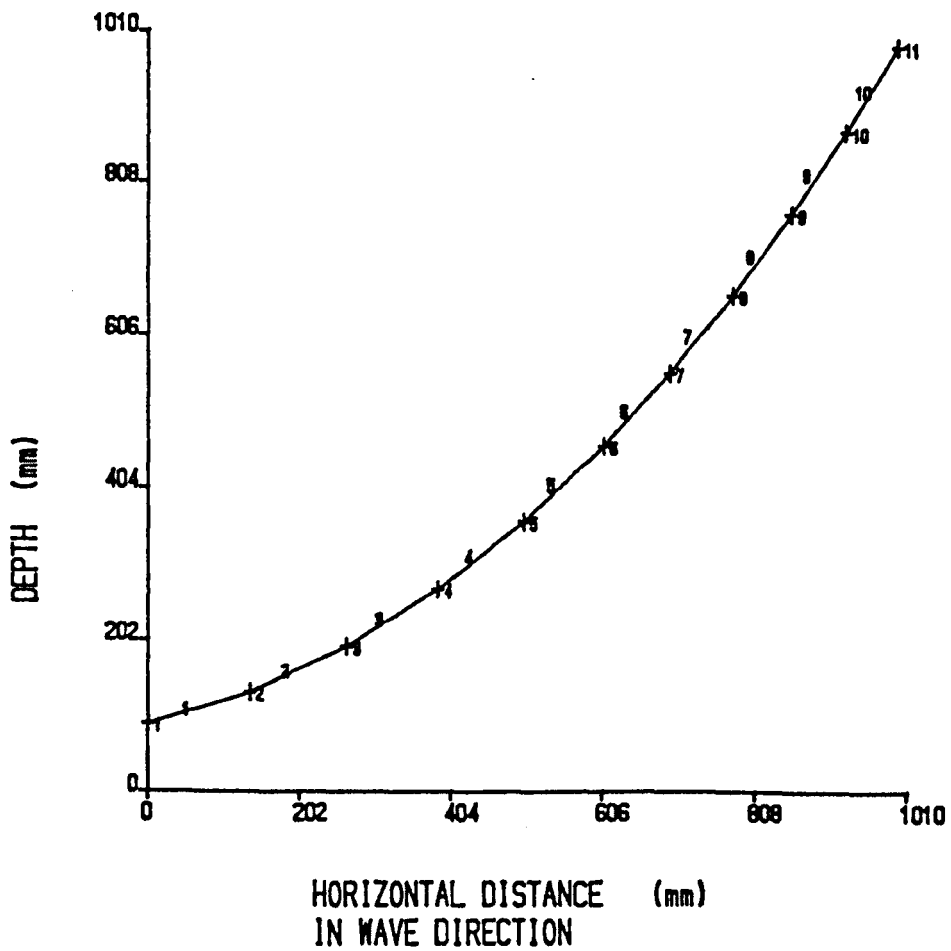


Figure 6.28 - Static equilibrium shape of the natural frequency validation test case

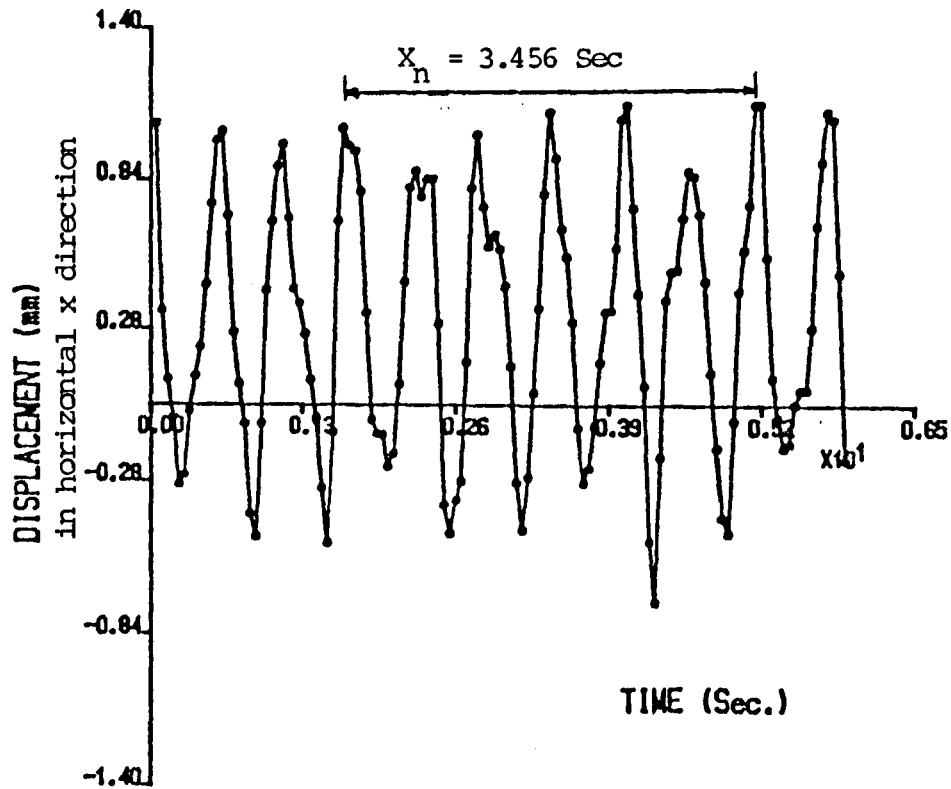


Figure 6.29 - Time history of the "poked" natural frequency validation test case

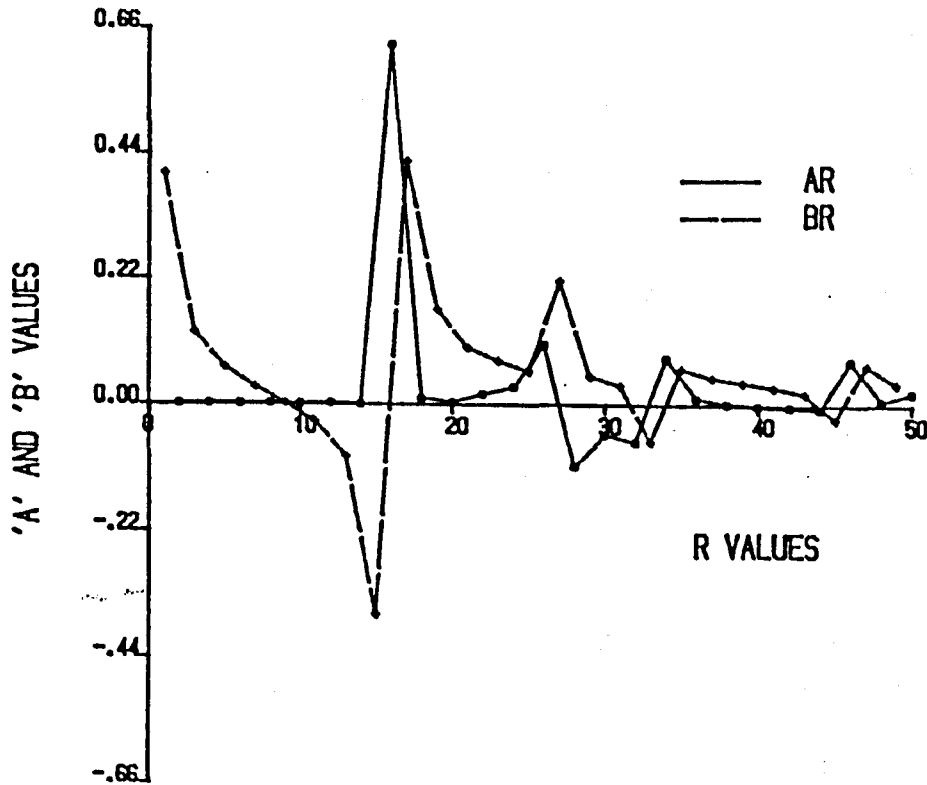


Figure 6.30 - Values of coefficients A and B against r for the natural frequency validation test case

## CHAPTER 7

### EXPERIMENTAL WORK TO VALIDATE NUMERICALLY

#### COMPUTED RESULTS

##### 7.1 - Introduction

Experimental investigations of the behaviour of flexible risers under hydrodynamic loading have usually been carried out in two categories; prototype testing and small scale laboratory tests. The former procedure is notoriously expensive to carry out and also the resulting data is difficult to analyse. In contrast, small scale testing is not expensive to perform but suffers from the major disadvantage of not being able to simulate high Reynold's numbers. Thus, the correlation between predicted results and those of the real sea conditions may be poor.

##### 7.2 - Objectives of the Experiments

The main aim of the experimental work was to validate the computer programs for; a) assessment of hydrodynamic loading on the riser, and b) the material properties and physical performance of the riser. To achieve this it was decided to carry out the testing in two stages. The first series required a model with negligible material damping and bending stiffness so that the assessment of current and wave loadings on different shapes of risers could be validated. Having validated the load modelling, a further series of tests was carried out in a large wave flume using a bigger model with significant material damping. The purpose of these tests was to investigate the effects of material damping and vortex-shedding.

### 7.3 - Model Scaling and Description of Test Models, Regular Waves and Current Flows

For each test series the model, current and wave flows were scaled from prototype conditions.

#### 7.3.1 - First Series of Experiments

##### 1 - Scaling the riser

- a) prototype riser - a Dunlop high pressure drilling flexible riser with the following properties was considered as the typical prototype:

pipe internal diameter = 250 mm

pipe external diameter = 326 mm

body weight in air = 99.3 kg/m

assumed mud density = 3000 kg/m<sup>3</sup>

$$\text{Thus, density of pipe + mud} = \frac{99.3}{(0.326^2 \pi / 4)} + 3000 = 4190 \text{ kg/m}^3$$

- b) model riser - a geometric scaling factor of 1/200 was adopted.

$$\text{From equation (5.58) } \frac{D_m}{D_p} = \frac{1}{200}, \text{ thus } D_m = \frac{326}{200} = 1.63 \text{ mm}$$

Modelling the mass properties requires  $\rho_{rm} = \rho_{rp}$

thus, the density of the model = 4190 kg/m<sup>3</sup>

A snake chain with the following properties was found to meet reasonably well the required model specifications:

Chain diameter = 2 mm

Chain density = 5882 kg/m<sup>3</sup> (7.1)

2 - Scaling the current flow

a) prototype current flow:

$$\text{current velocity} = 1.4 \text{ m/sec}$$

b) model current flow:

$$\text{from equation (5.64) } K_V = K_L^{1/2} = \left(\frac{1}{200}\right)^{1/2} = \frac{1}{14.14}$$

$$\text{Thus, } V_C = \frac{1.4}{14.14} = 0.099 \text{ m/sec} \quad (7.2)$$

3 - Scaling the wave

a) prototype wave:

$$\text{wave height, } H = 13.6 \text{ m}$$

$$\text{wave period, } T = 12 \text{ sec}$$

$$\text{water depth, } h = 100 \text{ m}$$

This wave is almost a deep water wave considering the following definitions:

$$\text{for shallow water waves } Kh < \pi/10$$

$$\text{for deep water waves } Kh > \pi \quad (7.3)$$

Where K is the wave number and h is the still water depth.

Using the linear wave theory, equation (7.3) can be expressed as:

$$\text{for shallow water waves } \frac{4\pi^2 h}{gT^2} < \pi/10 \quad (7.4)$$

$$\text{for deep water waves } \frac{4\pi^2 h}{gT^2} > \pi$$

For the chosen wave:

$$\frac{4 \pi^2 h}{gT^2} = \frac{4 \pi^2 \cdot 100}{g \times 12^2} \cong 0.9 \pi \quad \text{deep water waves} \quad (7.5)$$

b) model wave:

$$\text{From equation (5.58), } \frac{H_m}{H_p} = \frac{h_m}{h_p} = K_L = \frac{1}{200}$$

$$\text{From equation (5.61), } K_T = K_L^{1/2} = \left(\frac{1}{200}\right)^{1/2}$$

Thus,  $H_m = 0.068 \text{ m}$ ,  $h_m = 0.5 \text{ m}$ , and  $T_m = 0.85 \text{ sec}$

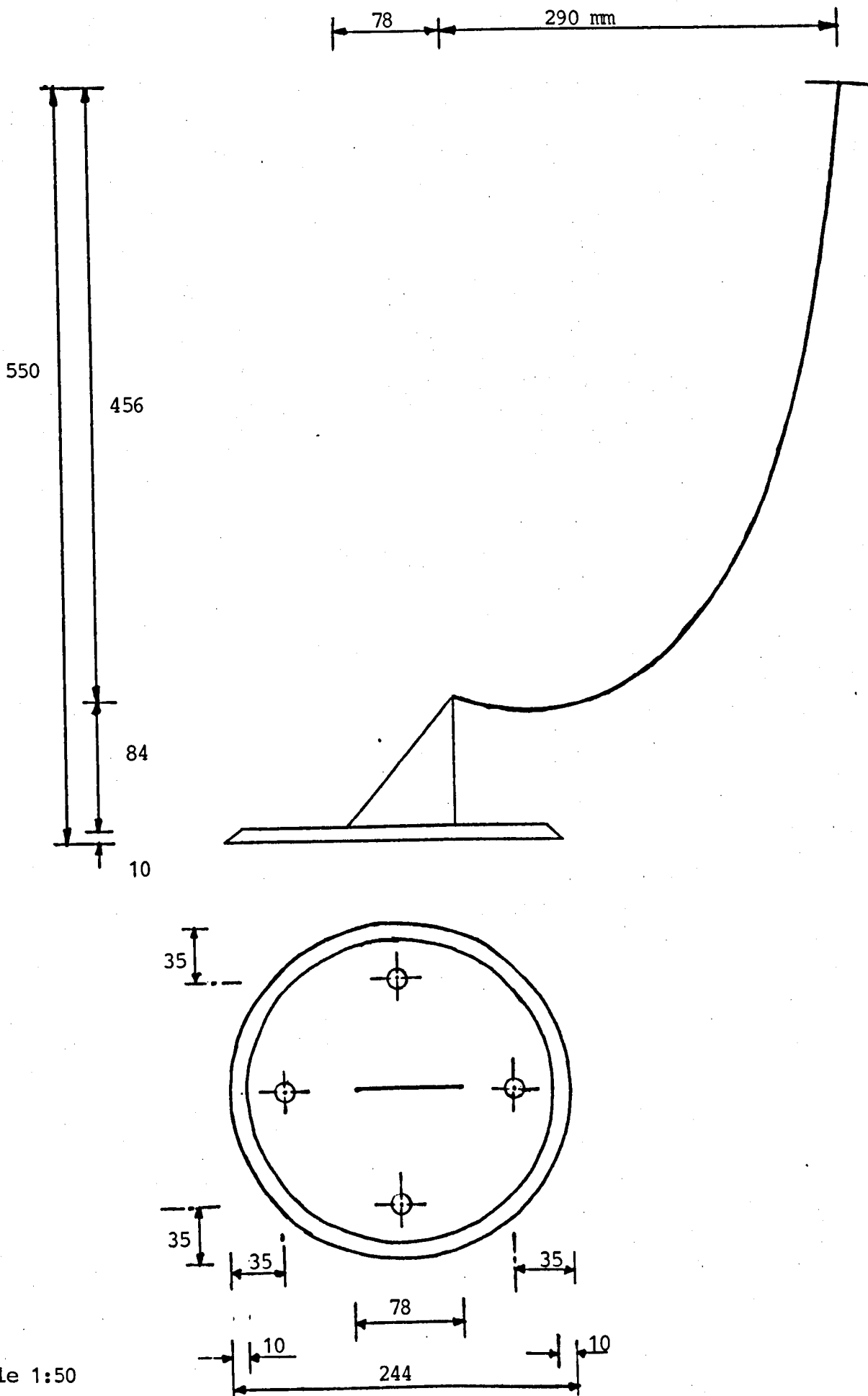
(7.6)

4 - Scaling the arrangement of the chain in the wave flume - this arrangement was obtained by scaling the dimensions of the single catenary flexible riser used in the Balmoral Oil Field. The shape of the single catenary riser was simplified because of the limited size of the flume and water depth. This was done by replacing the lower stretched part of the riser by a thin plate with sharpened edges to minimize its disturbance on the wave flow, plate 6. The plate was made of PVC (Polyvinyl Chloride). The dimensions of the chain arrangement and the plate are given in figure (7.1).

### 7.3.2 - Second Series of Experiments

The scaling factors for the second series of tests were obtained from water depth criteria corresponding to the maximum water depth which could be used in the large wave flume at The City University. Assuming the same prototype conditions as before:

$$K_L = \frac{h_m}{h_p} = \frac{1.20}{100} = \frac{1}{83}$$



Scale 1:50

Figure 7.1 - Arrangement of the snake chain in catenary shape at  $0^\circ$  to wave flow

Thus, the ratio of geometric scaling factor between the two test

$$\text{series is } \frac{83}{200} \approx \frac{1}{2.4} .$$

The scalings for the second series are thus obtained by multiplying the first series parameters by 2.4 for dimensions and by  $(2.4)^{1/2}$  for wave period.

1 - Scaling the riser model

$$D_m = 2.4 \times 2 \text{ mm} = 4.8 \text{ mm}$$

$$\rho_{rm} = 4190 \text{ kg/m}^3$$

In order to model material damping a plastic tube filled with mercury was chosen. This had the following properties:

$$\begin{aligned} D_m &= 5.23 \text{ mm} \\ \rho_{rm} &= 5543 \text{ kg/m}^3 \end{aligned} \quad (7.7)$$

## 2 - Scaling the wave flow

The scaled properties of the prototype wave flow are:

$$\begin{aligned} H_m &= 2.4 \times 0.068 = 0.163 \text{ m} \\ h_m &= 2.4 \times 0.5 = 1.2 \text{ m} \\ T_m &= (2.4)^{1/2} \cdot 0.85 = 1.32 \text{ sec} \end{aligned}$$

However, to ensure initially that there would be no vortex-shedding effect the following wave was adopted:

$$\begin{aligned} H_m &= 0.15 \text{ m} \\ h_m &= 1.2 \text{ m} \\ T_m &= 1.22 \text{ sec} \end{aligned} \quad (7.8)$$

In a further set of tests on the same model, intended to examine the effects of the vortex-shedding, a bigger wave with the following description was generated:

$$\begin{aligned} H_m &= 0.25 \text{ m} \\ h_m &= 1.2 \text{ m} \\ T_m &= 1.4 \text{ sec} \end{aligned} \quad (7.9)$$

## 5 - Scaling the arrangements of the model in the wave flume

Again the dimensions were obtained by scaling the single catenary flexible riser used in the Balmoral Oil Field. In this series of tests, however, there were two different tube arrangements. In the first arrangement the lower stretched part of the single catenary riser was replaced by a thin plate made of PVC. This simplification was used in order to avoid employing an

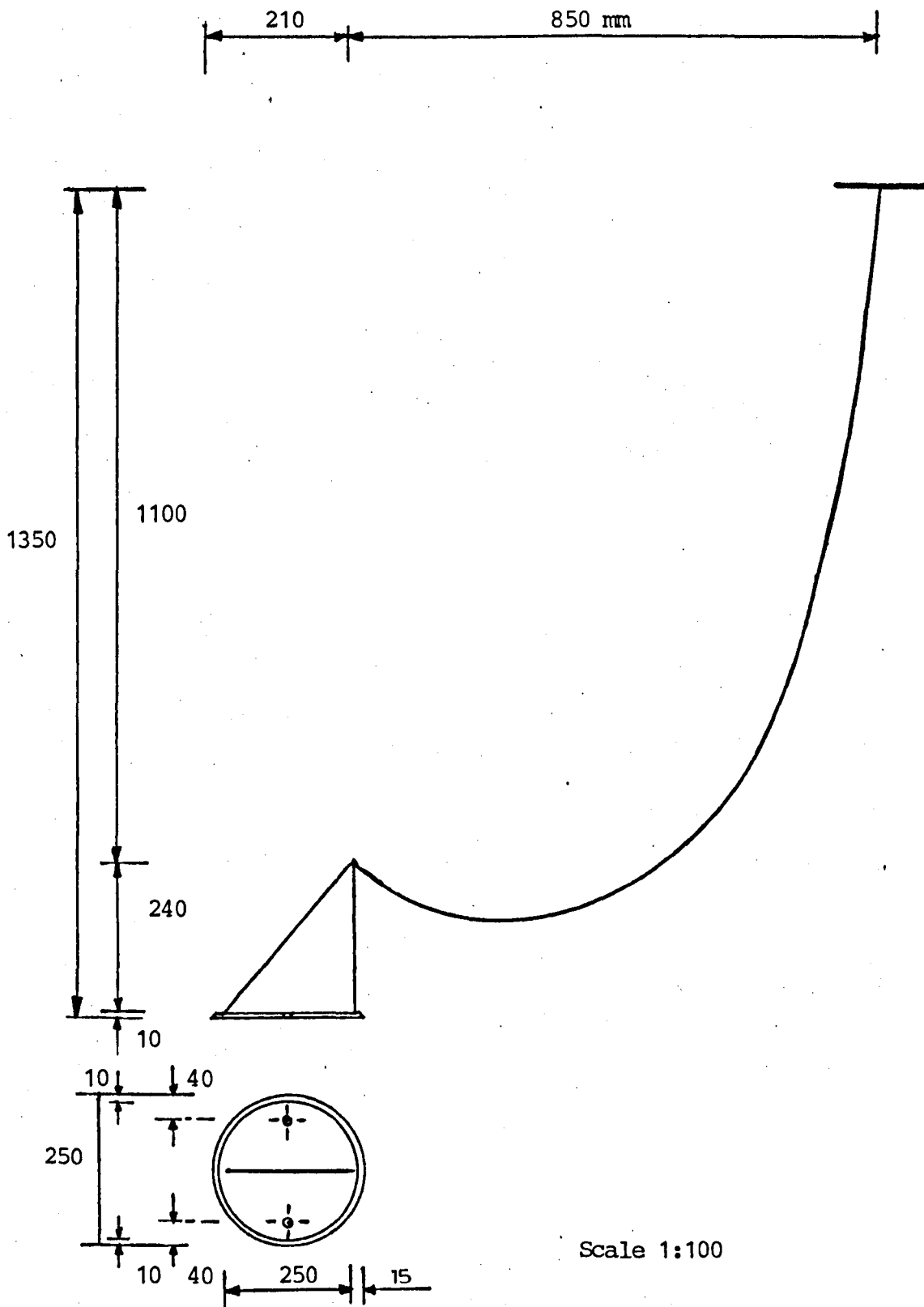


Figure 7.2 - Arrangement of the tube model in catenary shape at 0° to wave flow

intermediate sub-buoy. The arrangement was used principally for examining the effects of material damping and to assess the chosen force coefficients  $C_d$  and  $C_m$ . The dimensions of the arrangement and the base plate are given in figure (7.2).

The second tube arrangement had an intermediate sub-buoy system consisting of the sub-buoy and a cradle system, plate 10. A smooth ball was chosen as the sub-buoy and its size was governed by the approximate required buoyancy force which was calculated from the static solution. The point on the cradle, at which the ball was attached, was obtained by considering the equilibrium of the overturning moments as follows:

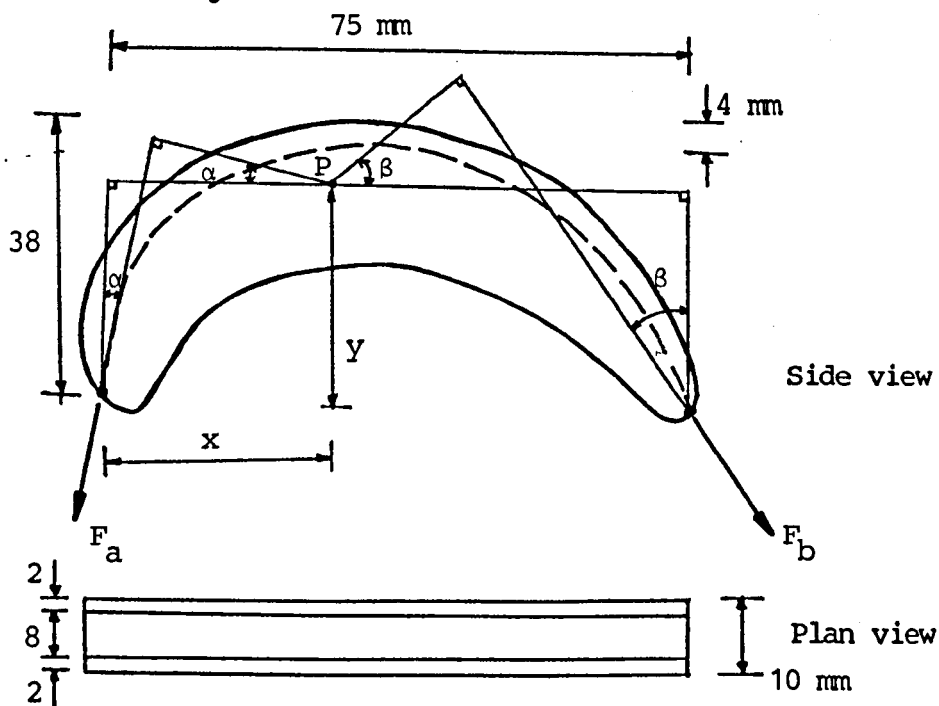


Figure 7.3 - Experimental cradle system

The position of point P was obtained by using simple geometry from figure 7.3:

Taking moment about point P:

$$\left(\frac{x-y \tan \alpha}{\cos \beta}\right) F_a = \left(\frac{(7.5-x)-y \tan \beta}{\cos \alpha}\right) F_b \quad (7.10)$$

from the static solution:

$$F_a = 938 \text{ N} \times 10^{-3}$$

$$F_b = 271 \text{ N} \times 10^{-3}$$

$$\alpha = 12.3 \text{ degrees}$$

$$\beta = 47.4 \text{ degrees}$$

Giving  $y = 30 \text{ mm}$ , from equation (7.10),  $x = 27 \text{ mm}$

(7.11)

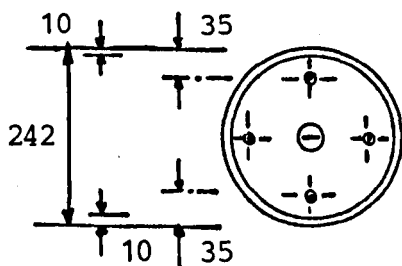
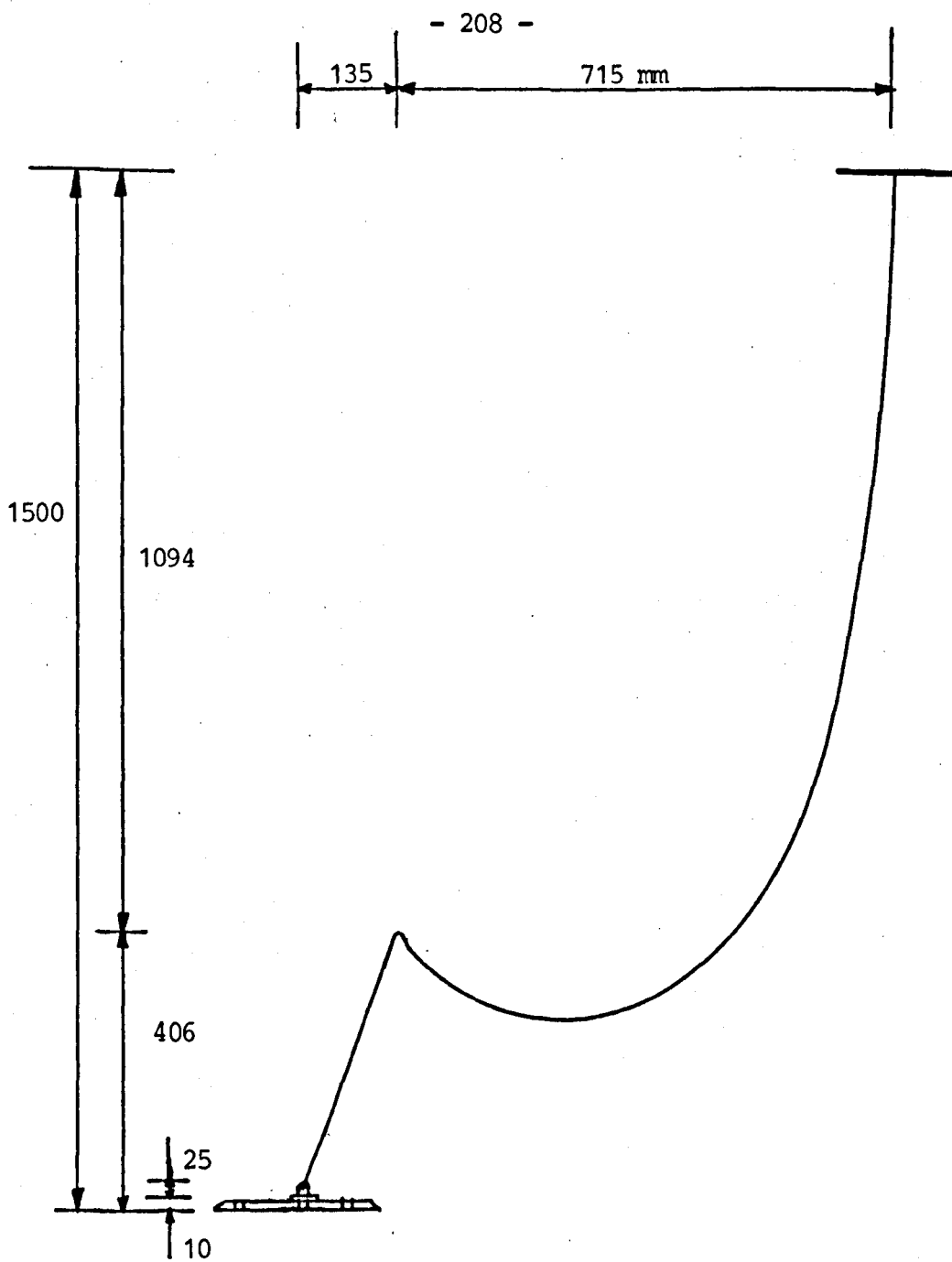
The dimensions of the tube arrangement are given in figure (7.4).

#### 7.4 - Experimental Apparatus

The experiments were carried out in a current channel and in the small and large wave flumes in the Department of Civil Engineering at The City University.

##### 7.4.1 - Current Channel

The channel was glass-sided and was 16 metres long and 300 mm wide with a maximum working water depth of 250 mm. There was a controlling tap at one end and a gate at the other end of the channel. The current velocity and the desired water depth in the channel were controlled by adjusting the tap and raising or lowering the gate.



Scale 1:100

Figure 7.4 - Arrangement of the tube model in single catenary riser shape

#### 7.4.2 - Small Wave Flume

The flume was glass-sided, and was 750 mm in width and 18 metres in length and had a maximum working water depth of 500 mm.

Regular waves were generated by means of a wedge oscillating vertically to the surface of the water at one end of the flume. The generated wave energies were absorbed by installing a sloping beach at the other end (i.e. downstream end) of the flume. The beach had a 9 degree slope and terminated at the still water level.

A well known phenomenon associated with laboratory generated waves is the presence of higher harmonics due to; a) the secondary effect of the wedge type wave maker, b) reflected waves from the beach. These phenomena have been considered for this particular wave flume by Ellix (1984). The wave which was chosen for this study (Section 7.3) was selected from Ellix's work which had negligible secondary wave components and this fact was also observed during the present work.

#### 7.4.3 - Large Wave Flume

This flume measured 62 m long by 1.8 m wide with a 1.2 m maximum working water depth. It was equipped at one end with a wedge type wave maker and at the other end with a wave absorbing beach. The beach was fixed at 8 degrees and finished at undisturbed water level. Half of one side of the flume, near the downstream side, had glass windows for viewing.

Two sets of waves were generated in this flume which were an increased scale of the waves used in the small flume in order to minimize the secondary effects on the waves due to the beach and the generator.

## 7.5 - Description of Measuring Instrumentation

### 7.5.1 - Current Meter

A current meter was used to measure the velocity of the current flow. The system consisted of a propeller attached to a digital counter box by means of a wire. The box had a button which when depressed set the digital counter to zero, and when released recorded the number of revolutions of the propeller. The velocity of the flow was calculated using the formula:

$$V_c = \frac{0.1827 N + 0.098}{3.25} \quad (7.12)$$

where  $V_c$  = current velocity

$$N = \frac{\text{number of revolutions}}{60}$$

### 7.5.2 - Wave Probe

The wave probe was used to measure the wave profile. The measurement was carried out by detecting the change of voltage due to the change of resistance of the wire probe using the equation.

$$\bar{I} \times \bar{R} = \bar{V}$$

where  $\bar{I}$  = the constant alternating current

$\bar{V}$  = the variable D.C Voltage

$\bar{R}$  = the variable resistance of the probe wire due to the change of the wave profile

Alternating current prevented polarization of the water in the region of the probe.

The probe itself consisted of two stainless wires having a diameter of 3 mm and a length of 500 mm with a resistance of 0.006 ohms per metre. The two wires were separated by a constant distance of 25 mm, perpendicular to the direction of wave propagation, and were fixed to a perspex plate suspended over the flume by means of an adjustable boom. The probe formed one element of a wheatstone bridge circuit. The output voltages were monitored by a Bryans X-Y plotter Model 26000 A3 and the graphs of voltage against time were plotted. The height and period of the generated wave were measured from this graph.

#### 7.5.3 - Horizontal Top Tension Measuring Strain Gauges

The horizontal components of top tension in the tube for the second series of tests was obtained by employing two 120 ohm SR-4 strain gauges, one each side of a vertical stainless cantilever beam supporting the tube at the top. These gauges were coupled with an ultra violet (U.V.) recorder model SE0 6012. The changes in the strain in the cantilever beam due to the horizontal component of top tension in the tube were plotted against time by the U.V. recorder. The traces of these horizontal components with time were evaluated from the U.V. graphs.

#### 7.5.4 - Ultra Violet Recorder

The U.V. recorder was used to plot graphs of output voltages against time. This system was coupled with the strain gauges to record top tension components, and with a frictionless transducer

to record displacements of the tube with time in the material damping test (see plate 15).

#### 7.5.5 - High Speed Camera

A 16 mm motion picture (Handland Rotating Prism) High Speed Camera with a 30 mm focal length lens and running at 100 frames per second was used to record the displacements of the points along the models in the wave direction. It was also used to film the wave profiles.

#### 7.5.6 - The Modular Film Analysis System (Digitizer System)

This system was used to digitize all the filmed data and outputs from the U.V. recorder.

The system was composed of:

- a) motion analyser
- b) SAC GP7 Sonic digitizer
- c) BBC microcomputer
- d) printer.

The Sonic digitizer itself consisted of a screen and an electronic eye pen. The particular frame of the film was fed on to the screen by the motion analyser and then the points of interest on the frame were digitized and the results stored in the BBC microcomputer. In the case of the U.V. output, the graph was attached on the screen and the points were digitized directly.

The first stage in utilizing this technique was to calibrate the data. In this calibration stage, an initial reference point was fixed and the scales to be used for the axes were computed

directly by digitizing marked distances along both axes. Once this calibration was completed the data was stored and the film was digitized frame by frame.

## **7.6 - Calibration of Measuring Instruments**

### **7.6.1 - Wave Probe**

The aim of the wave probe calibration was to determine the relationship between the amplitude of the graphically obtained and the actual water surface displacement.

The calibration was achieved by recording the variation in the amplitude of the graph by raising and lowering the probe by 10 cm in 1 cm steps in still water. The results of the calibration in the small and large flumes show a linear relationship between the output and the variation of the immersion depth.

### **7.6.2 - Strain Gauges**

The strain gauged cantilever beam was clamped in a horizontal position and known weights of 0.1 Newton were hung from the hook at the free end of the beam. These weights were added up to a total of 1 Newton and then removed. The corresponding changes in the strain of the beam were recorded to calibrate the U.V. recorder.

### **7.6.3 - Displacement Transducer**

The transducer was calibrated by applying known constant incremental displacements to the transducer by a Digimatic Head instrument with 0.001 mm sensitivity. The resulting output voltages were recorded on the U.V. recorder.

## 7.7 - Experimental Procedure

The experimental procedures were carried out in two stages as previously described. The first series employed the snake chain and the second series the plastic tube filled with mercury.

### 7.7.1 - The First Series of Tests

#### 7.7.1.1 - Current Channel Experiment

The aim of this test was to obtain a value for the drag coefficient,  $C_d$ , and to validate the static analysis program 3.

The snake chain of 402 mm in length was subdivided into 6 elements and the nodes of the elements were marked, figure (7.5). The chain was then placed in the middle of the channel and a surveying theodolite camera was set up beside the channel aligned with the model chain so that the ray from the camera to the chain was normal to the channel longitudinal axis. The purpose of employing this camera was to obtain the nodal displacements of the chain due to current flow by measuring the angles between the initial and displaced positions of the nodes. The horizontal distance between the theodolite and the chain was established by measuring the distance and vertical angle to a point above the model chain. The horizontal and vertical angles of the nodes at their initial positions were then recorded.

A current flow was established by opening the tap situated at the inlet of the channel, and the water depth was adjusted to 0.25 m by raising or lowering the gate at the end of the channel. The propeller of the current meter was placed at the middle of the channel width and at mid-depth. The velocity of the current was

adjusted to 0.097 m/sec and the water depth to 0.25 m by controlling the inlet tap and outlet gate. The propeller was situated at different depths and the current velocities were measured to obtain a profile.

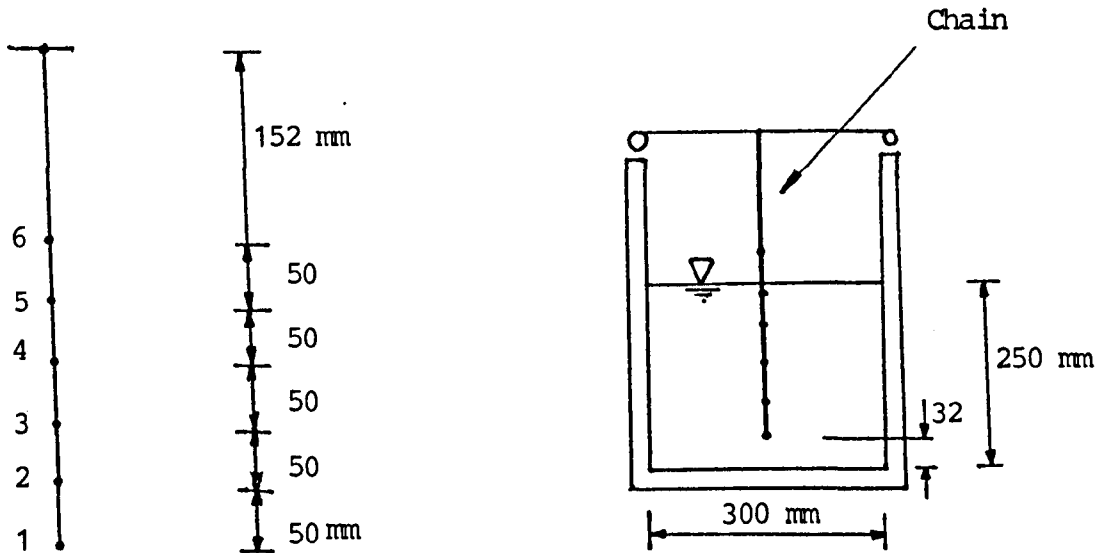


Figure 7.5 - Model chain and current channel

### Deflections of the Chain

The nodal displacements were calculated as follows:

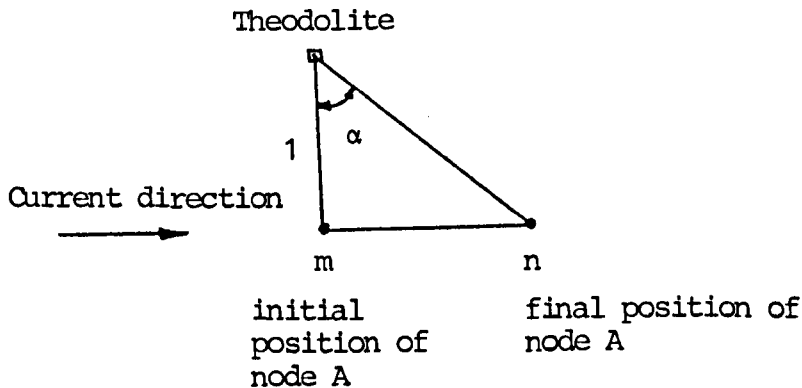


Figure 7.6 - Geometry of nodal displacement

From figure (7.6),

$$\text{displacement (mm)} = l \tan \alpha$$

where  $l$  = distance of the initial position of node A from the theodolite.

$\alpha$  = measured horizontal angle.

$$l = l_h / \cos (\beta_1).$$

$l_h$  = horizontal distance of the theodolite from the chain.

$\beta_1$  = vertical angle of node A at its initial position.

The vertical co-ordinate of node A was obtained by:

$$\text{Vertical co-ordinate of node A} = l_h \tan (\beta_1) - \text{co-ordinate of node 1}$$

#### 7.7.1.2 - Wave Flume Experiments

The main concern of these tests was to validate the assessment of wave loadings on various arrangements of the chain. The arrangements used simulated the following conditions:

- a) a catenary riser at zero degrees to the wave direction
- b) a catenary riser at 30 degrees to the wave direction
- c) a u-shape flexible riser at 30 degrees to the wave direction (u-shaped risers may be used between two platforms)
- d) disconnected flexible riser (such as may occur in emergency situations).

Plates 4, 5, 7 and 8 show respectively the above arrangements.

The base plate used for cases a and b is shown in plate 6.

The following experimental procedure was carried out for all of the 4 chain arrangements.

The chain was subdivided into 10 elements and the shape of the catenary chain was found from the numerical analysis. Then 3 representative nodes along the chain were selected and marked. The chain was placed inside the wave flume and 3 cross shape reference points at the same levels of the marked nodes were established on one flume wall with a coloured tape. These reference points were used in digitizing the nodal displacements.

The specified wave was generated by adjusting the frequency and amplitude of the wave generator and the wave height and period were evaluated from the graphs plotted by the X-Y plotter attached to the wave probe system.

The nodal displacements of the 3 marked nodes were filmed by the high speed camera for a duration of ten wave periods. In filming the displacements of each node, special care was taken to fix the camera on the same horizontal level as the node in order to minimize the errors caused by the filming. When the filming of the nodal displacements was finished a 30 mm wide stainless steel ruler was placed in the locations of the nodes and then was filmed. This was done in order to establish the scale factors for the nodal displacements which were used in digitizing the displacements.

The films were fed into the Modular Film Analysis System and were digitized.

## **7.7.2 - The Second Series of Tests**

### **7.7.2.1 - Current Channel Experiment**

The purpose of this test was to evaluate the drag coefficient for

the plastic tube. The same testing procedure, current channel and current flow as in the first experimental tests were used.

The arrangement of the tube in the current channel is shown in plate 9.

#### 7.7.2.2 - Wave Flume Experiments

The tests were carried out in the large wave flume and can be classified in two main groups. The aim of the first group was to examine the validity of the numerically predicted behaviour of the tube which had significant material damping to wave loadings. The second group was performed to verify experimentally the applicability of the adopted vortex-shedding model.

The first group consisted of three tests. The first of these used a simplified form of a single catenary riser as in the preliminary series of tests. The purpose of the simplification was to avoid the influence of the intermediate sub-buoy on the behaviour of the tube due to wave loadings. This test was carried out to confirm the selected values of the force coefficients,  $C_d$  and  $C_m$ , and to observe the simulation and the effect of the material damping on the response of the tube to wave loadings. The model was placed at zero degrees to the wave direction, plate 11. The second and third tests used a single catenary riser model with an intermediate sub-buoy. The model was placed at zero and 45 degrees to the wave direction for these second and third tests respectively, plates 12 and 13.

The model with an intermediate sub-buoy was mounted at zero degrees to the wave direction for the next section of the tests, and a larger wave was generated in which the transverse vibration of the tube due to vortex-shedding was visible.

The buoyancy force of the intermediate sub-buoy was obtained by subtracting the weight of the sub-buoy and cradle from that of the volume of water displaced by the sub-buoy and the cradle.

The experimental procedures were carried out in the same way as in the first series of the tests. In addition, the U.V. recorder was calibrated and was used to obtain the trace of the horizontal top tensions with time.

The films and the graphs obtained from the U.V. recorder were digitized, as before, by the Modular Film Analysis System.

#### **7.7.2.3 - Material Damping Test**

The aim of this test was to determine the material damping constants  $a$  and  $b$  and the short term modulus of elasticity of the tube.

The displacement transducer attached to the U.V. recorder was calibrated. Two equal straight segments of the empty tube, 500 mm in length, were arranged as shown in figure (7.7) and plates 14 and 15. A dead weight corresponding to the self-weight of the tubes when filled with mercury was applied on the hanger and the system was allowed to settle down for 5 hours. Since constants  $a$  and  $b$  depend on the initial stress level in the tube the tests were carried out five times with different imposed loadings. Four of these loadings employed weights corresponding to the

maximum top tension in the second series of tests. The fifth was a slightly larger weight of 0.5 Newton which was applied for greater clarity in observing the tube response. A thin wire was installed in the middle of the system and the applied imposed load was initially carried by this wire. The wire was then suddenly cut without causing any lateral movement in the tubes, and the trace of the tube displacements was recorded by the U.V. recorder attached to the transducer.

The plots for all five tests were digitized using the digitizer system.

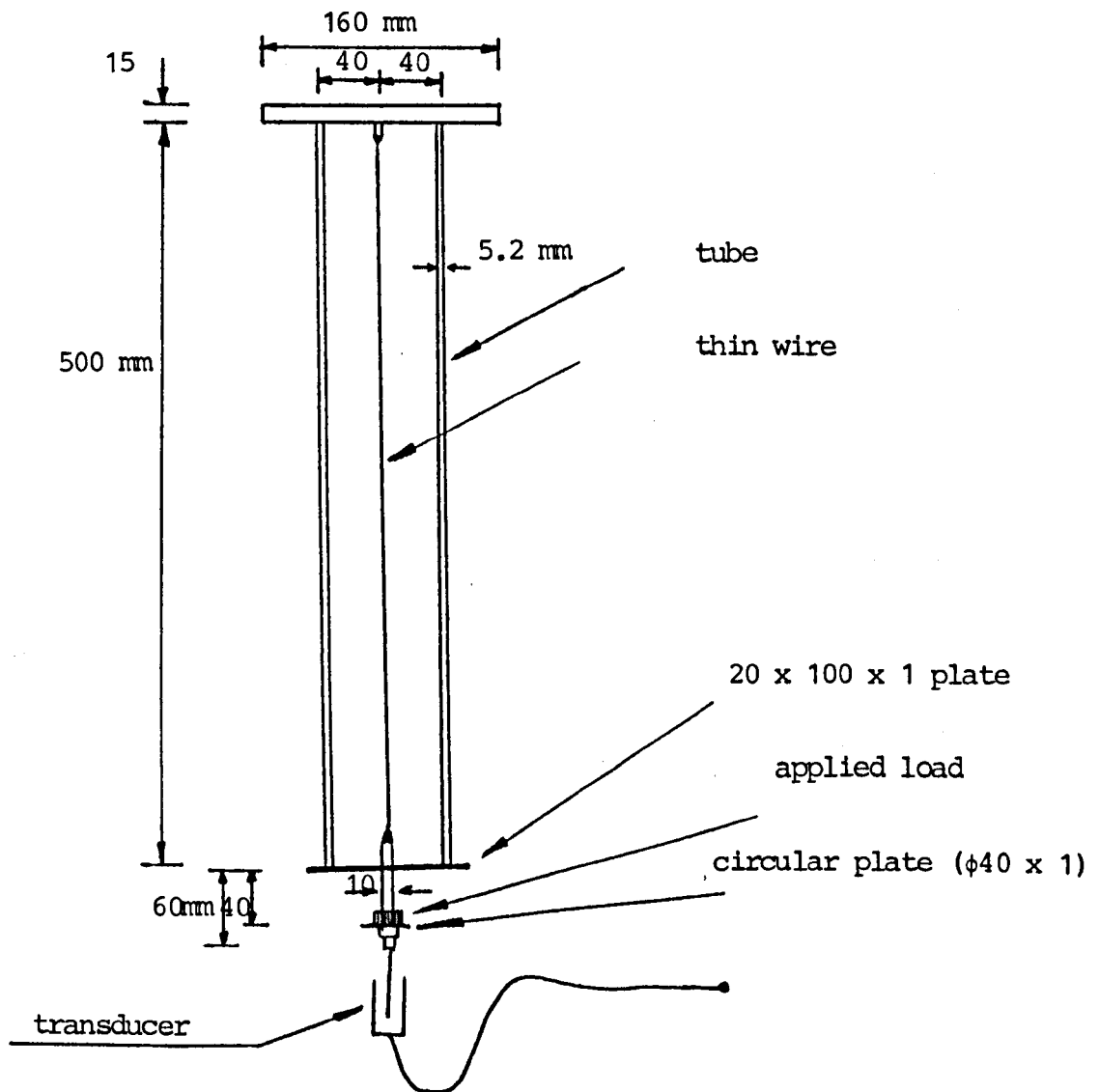


Figure 7.7 - Material damping test arrangement

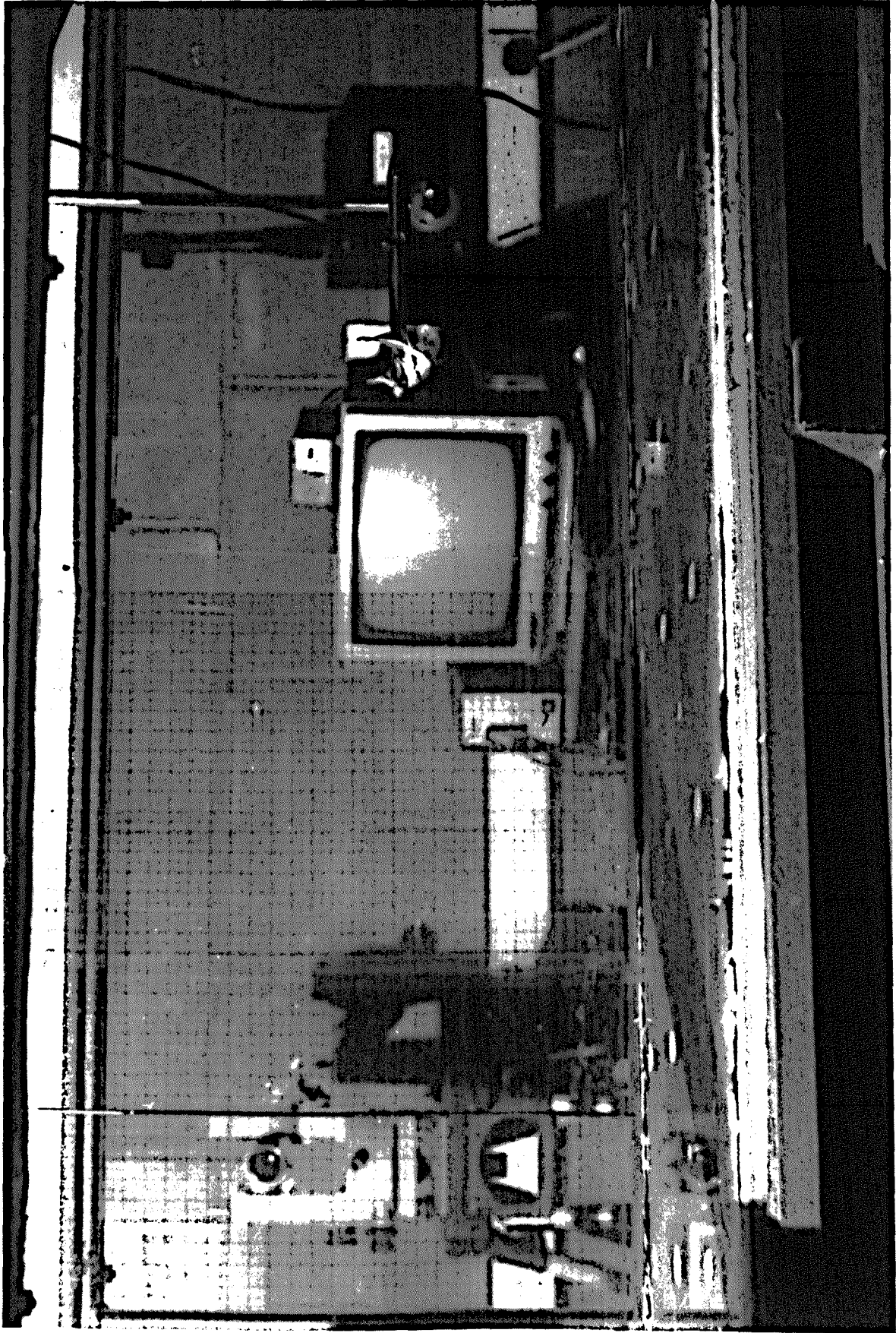


Plate 3

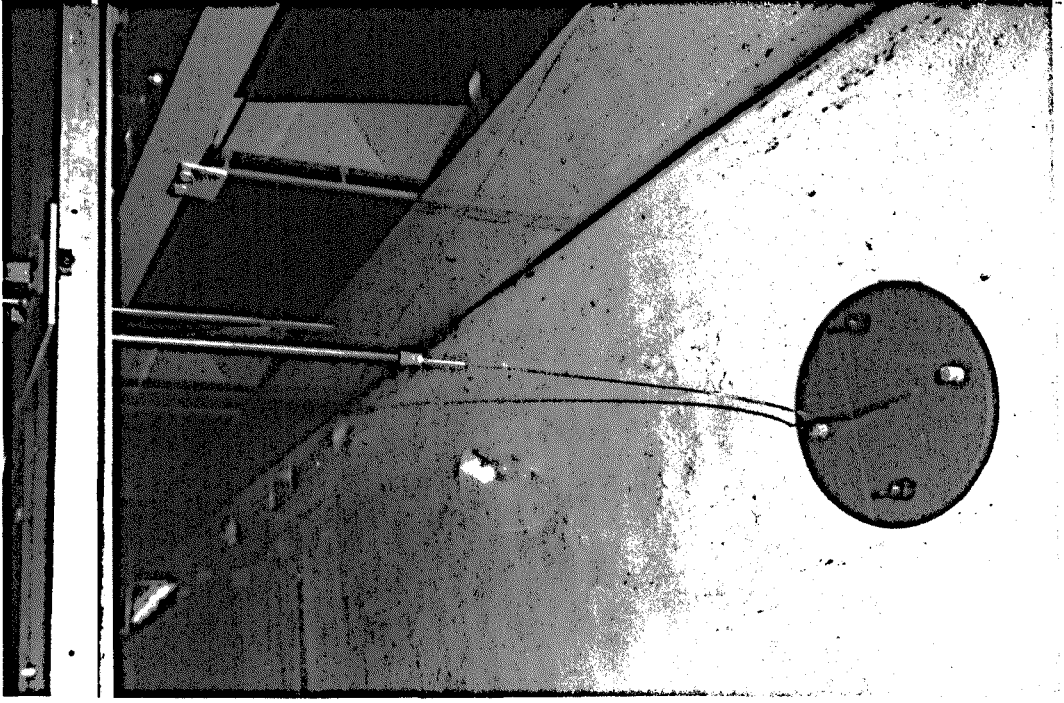


Plate 5

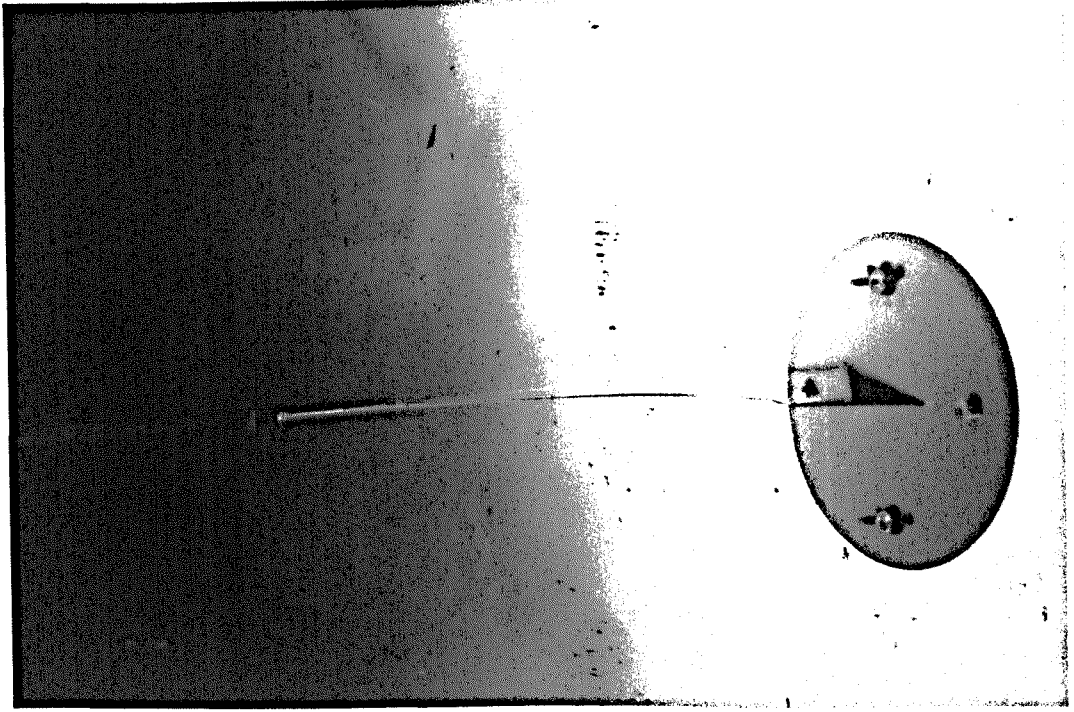


Plate 4

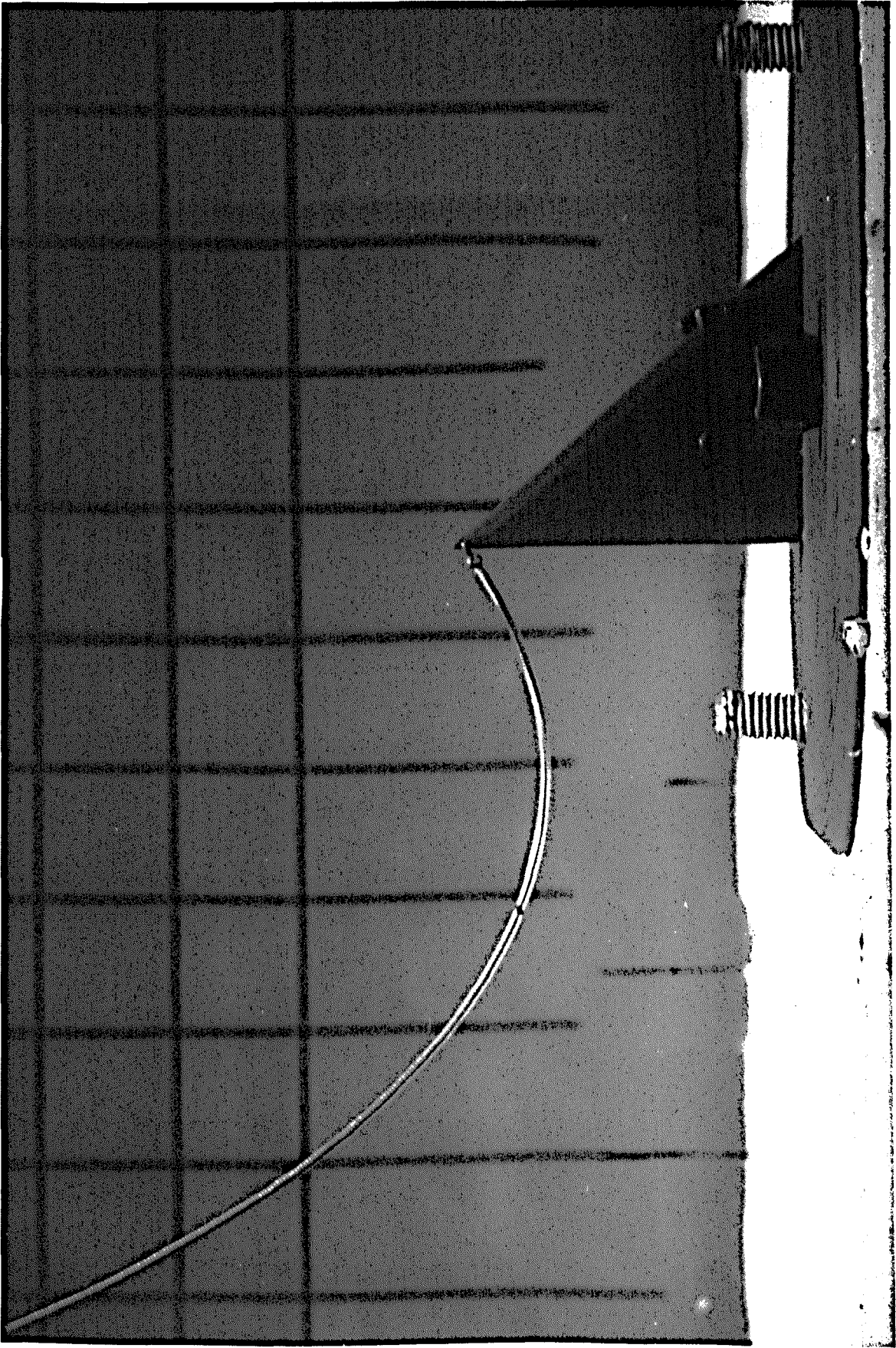


Plate 6

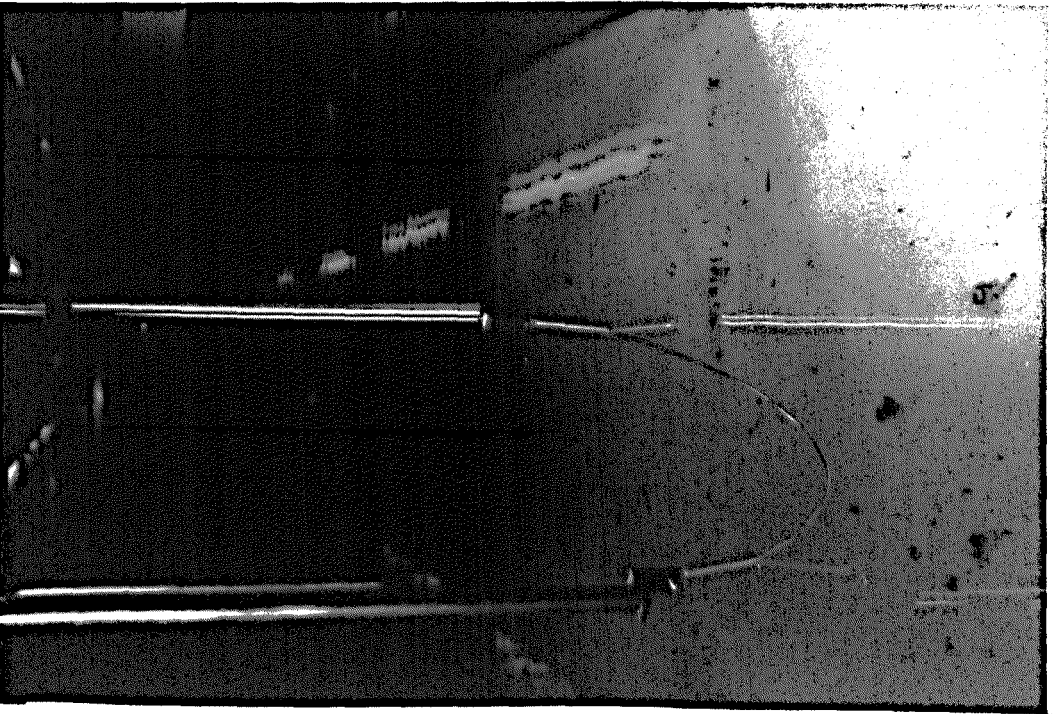


Plate 7



Plate 8

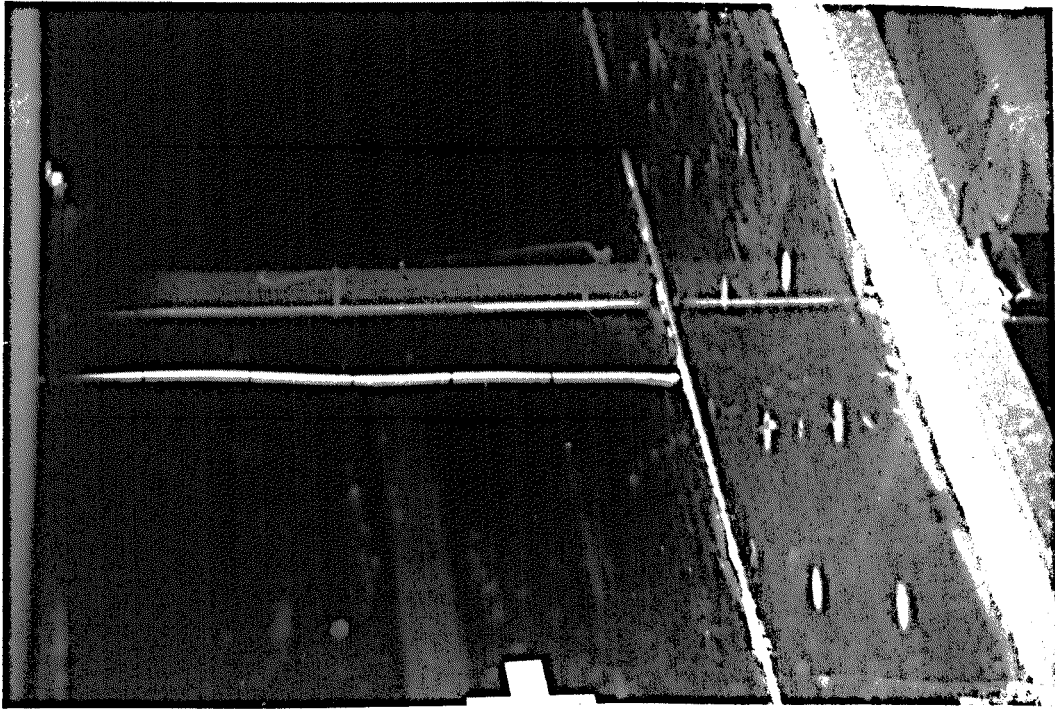


Plate 9

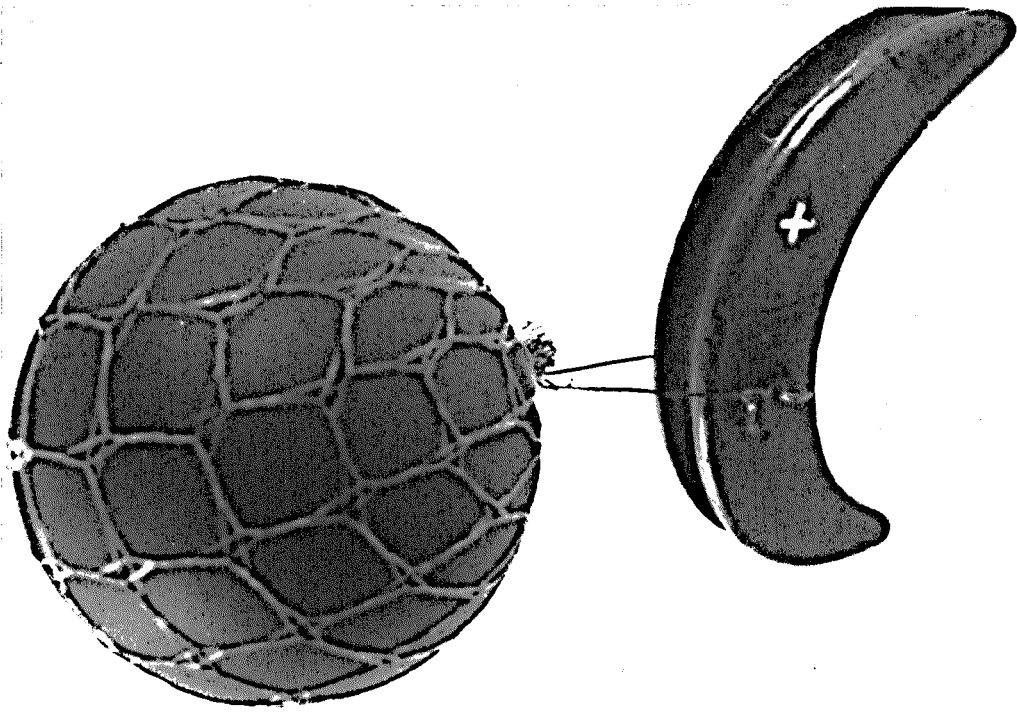


Plate 10

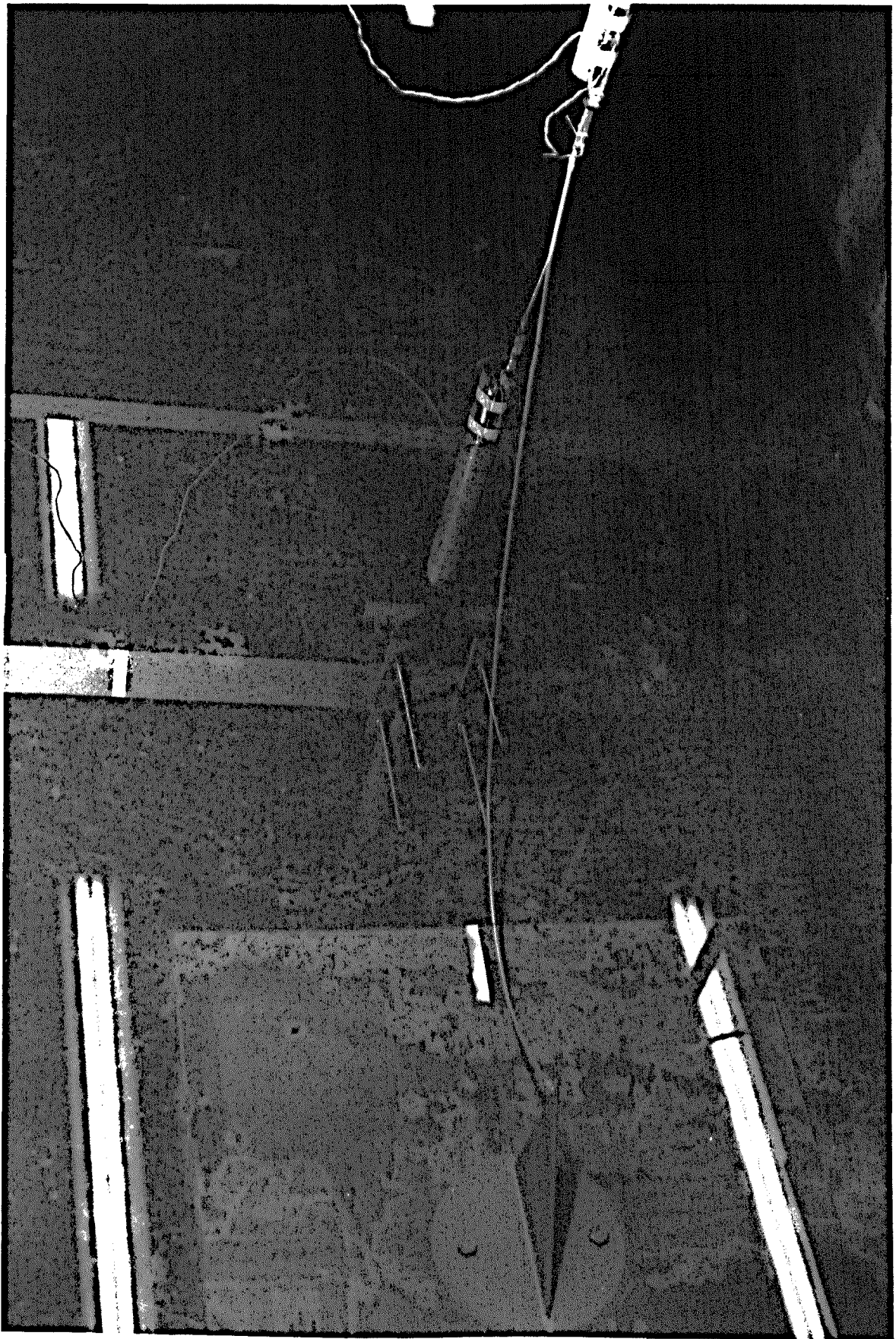


Plate II

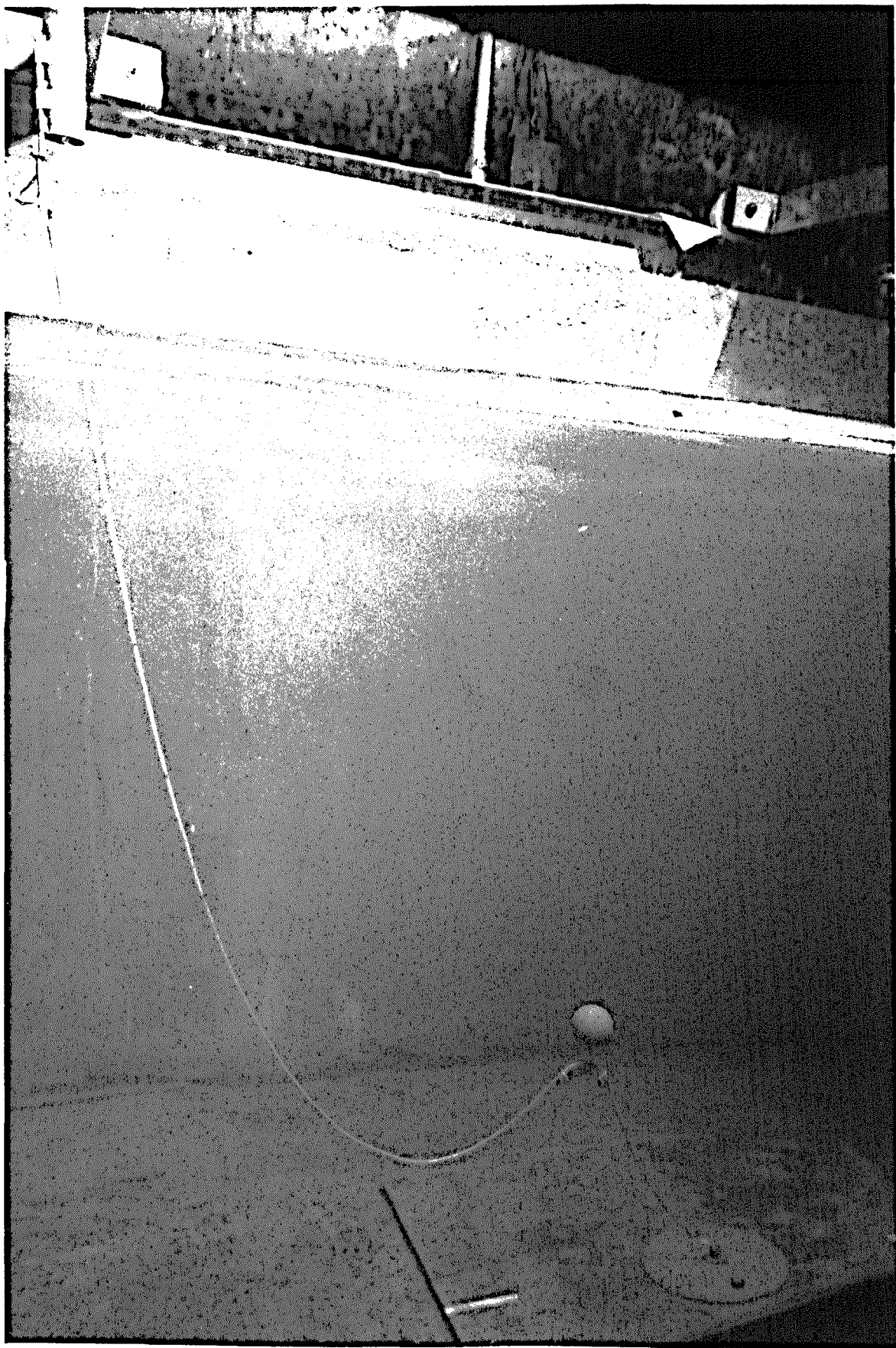


Plate 12

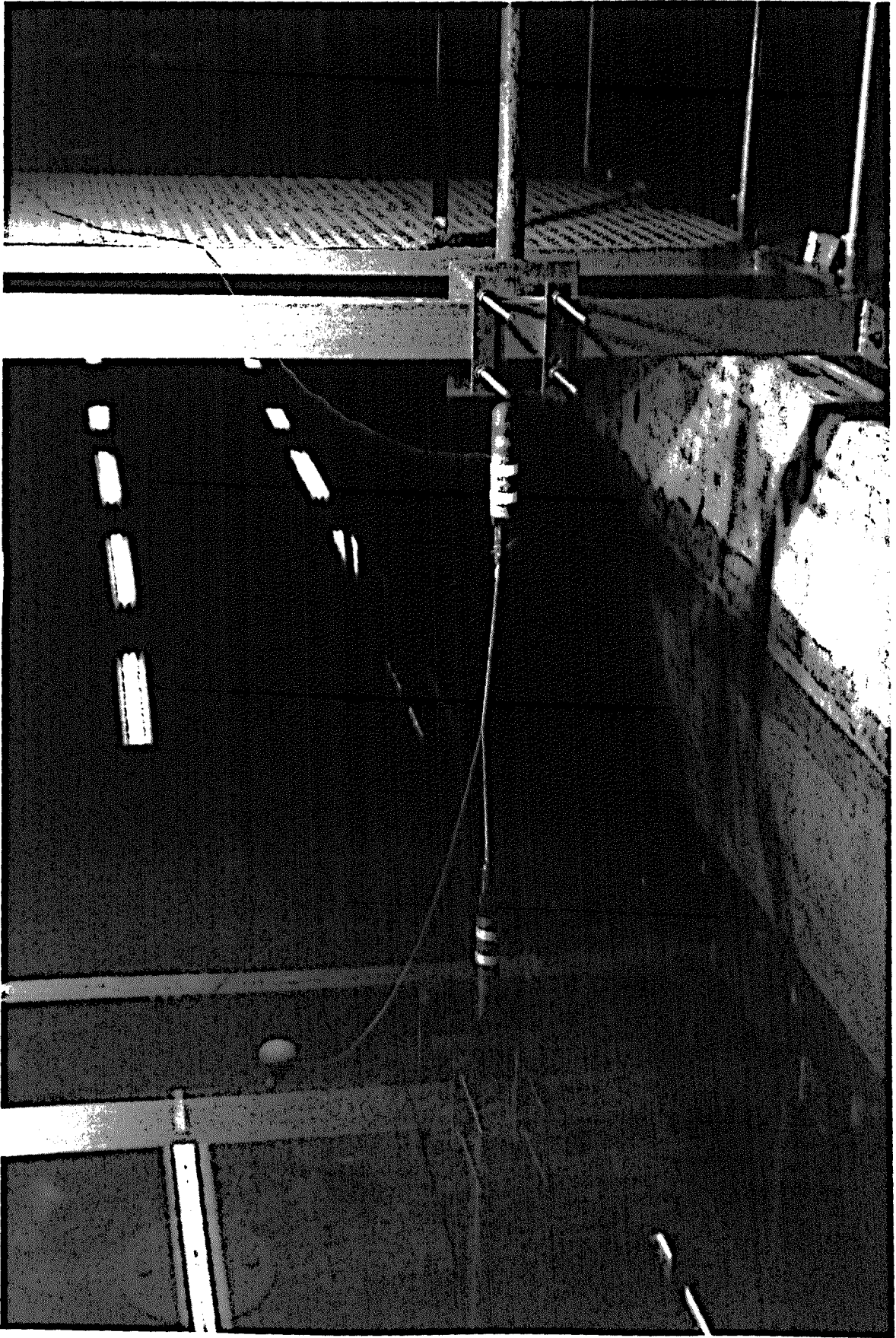


Plate 13

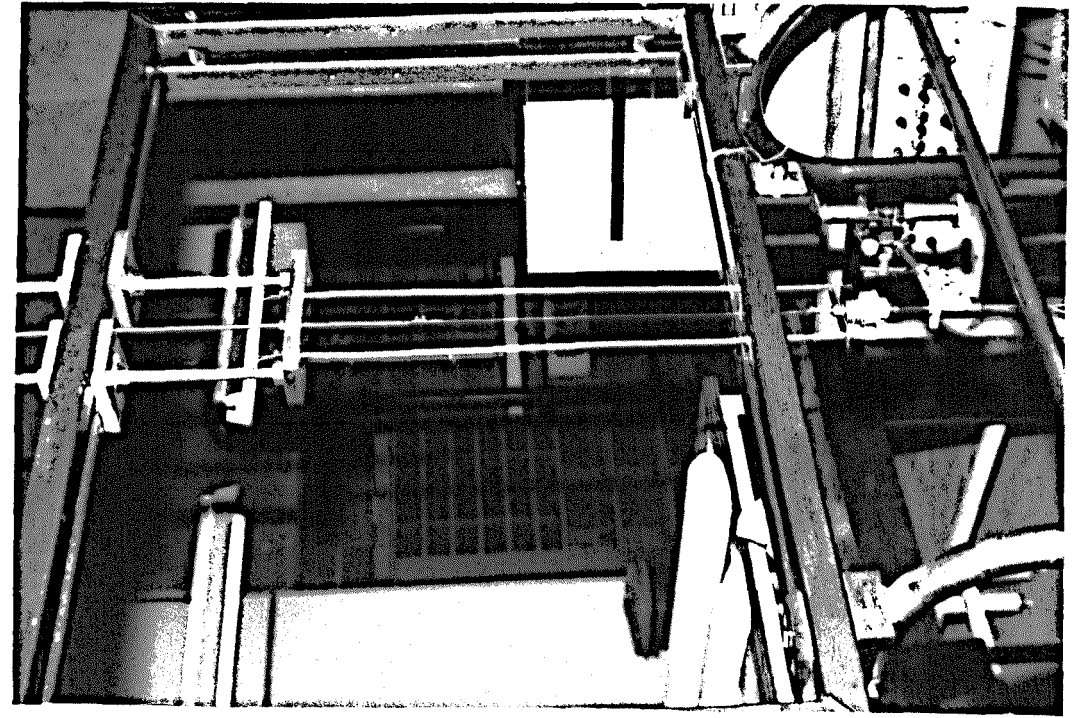


Plate 14

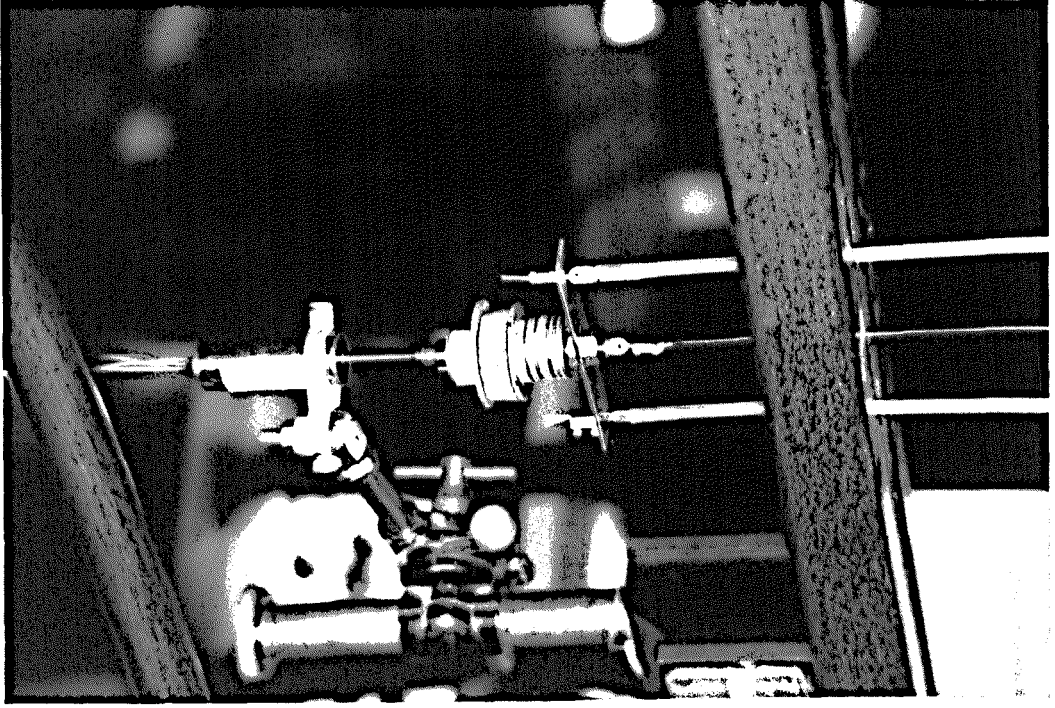


Plate 15

## CHAPTER 8

### RESULTS

#### 8.1 - Introduction

This chapter describes and compares the experimentally and numerically predicted results of the test cases which were presented in chapter 7. It is divided into the following two sections:

1 - results for the chain model

2 - results for the tube model

Each section consists of the results from tests carried out in the current channel and the wave flume. The numerical results for the model in the current channel were obtained by determining the model configuration using program 1, and then program 3 was used to compute the response of the model induced by the current loading. The configuration and dynamic response of the model in waves were obtained using programs 1 and 2 respectively.

#### 8.2 - Results for the Chain Model

##### 8.2.1 - Determination of Young's Modulus, $E$ , for the Chain

An extensometer machine was used to obtain the  $E$  value for the chain. A graph of load against deflection was recorded and Young's modulus was calculated from the slope of this graph. The  $E$  value for the chain was  $26.1 \text{ N/mm}^2$ .

##### 8.2.2 - Determination of the Drag Coefficient, $C_D$ , for the Model in Steady Current Flow and Validation of Static Program 3

The distance and vertical angle of the point above the model from the theodolite were 1395 mm and  $9^\circ 36' 50''$  respectively. Thus,

the horizontal distance of the model from the theodolite =  
 $1395. \cos (9^{\circ} 36' 50'') = 1374 \text{ mm.}$

The chain configuration was obtained using program 1, figure 7.5, and the nodes along the chain were marked. The nodal displacements of the chain, due to current forces, were measured and calculated as described in chapter 7, Section 7.7.1.1. These results are given in table 8.1.

The variations of the current velocity with water depth, which were measured by the current meter, are given in table 8.2. An equivalent current velocity profile along the chain was calculated as shown in figure 8.1. This velocity profile was input into static program 3. Trial values of the drag coefficient,  $C_D$ , were then considered and the corresponding nodal displacements were computed. A solution for  $C_D$  was obtained when the experimental and computed values of the nodal displacement corresponding to the lowest node were in close agreement. The value of  $C_D$  was determined as 1.37. The proportionality of the other nodal displacements confirmed the validity of program 3. The comparison is given in table 8.3 and figure 8.2.

### 8.2.3 - Determination of Drag Coefficient, $C_D$ , and Inertia Coefficient, $C_m$

An approximate value of the drag coefficient for the chain was obtained from the current channel test as described above. Sarpakaya et. al. (1974) measured drag-inertia forces on cylinders for sub-critical Reynolds numbers in oscillating flow. They determined the drag coefficient,  $C_D$ , and inertia

Node	Intitial Position				Initial Co-ords		Final Position			Horizontal angle = $[\beta_f - \beta_i]$ 0 ' "	Final Position	
	Horizontal angle ( $\beta_i$ ) 0 ' "	Vertical angle reading 0 ' "	Vertical angle $\theta$ 0 ' "	Distance from Theodolite $l = l_h / \cos \theta$	Horizontal mm	Vertical mm	Horizontal angle ( $\beta_f$ ) 0 ' "	Vertical angle reading 0 ' "	Vertical angle 0 ' "		Horizontal displacement mm	Vertical co-ords mm
1	8 39 20	98 59 40	8 59 40	1391	1.5	0.0	7 26 30	99 08 40	9 08 40	1 12 50	29.5	0.8
2	8 41 20	96 59 40	6 59 40	1384	0.7	50.4	7 38 20	97 02 40	7 02 40	1 03 00	25.4	50.6
3	8 42 00	94 58 20	4 58 20	1379	0.5	100.2	7 48 50	94 59 10	4 59 10	0 53 10	21.3	100.5
4	8 42 00	92 55 10	2 55 10	1376	0.5	150.0	7 59 00	92 55 00	2 55 00	0 43 00	17.2	150.4
5	8 42 30	90 50 20	0 50 20	1374	0.3	200.0	8 10 00	90 50 20	0 50 20	0 31 50	12.7	200.2
6	8 43 10	88 44 20	-1 15 40	1374	0.0	250.4	8 21 50	88 45 40	1 14 20	0 21 20	8.5	250.1
7	8 43 10	82 29 50	-7 30 10	1386	0.0	402.7	8 43 10	82 28 10	7 31 50	0 00 00	0.0	402.0

Table 8.1 - Computation of the experimental nodal displacements induced by the Current

Depth from Channel Bed (mm)	Number of Propeller Revolution	Velocity m/sec
230	65	0.091
220	66	0.092
210	70	0.096
200	71	0.097
155	71	0.097
65	71	0.097
55	66	0.092
45	63	0.089
35	62	0.088

Table 8.2 - Variation of the current velocity with water depth

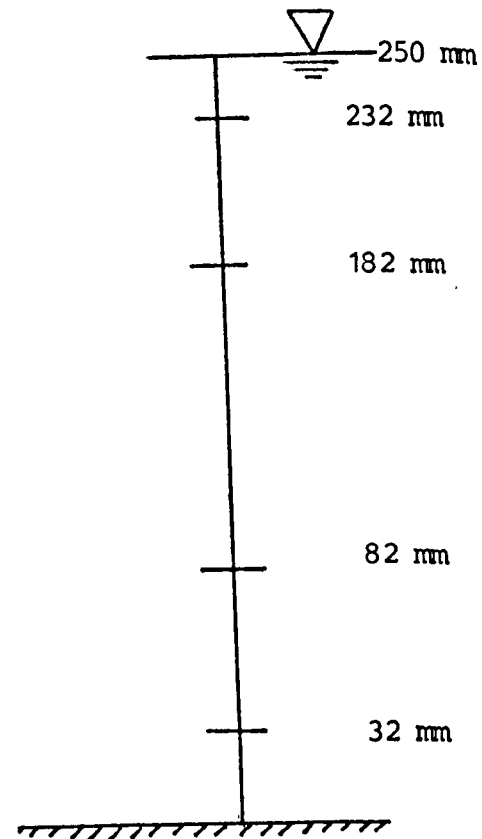
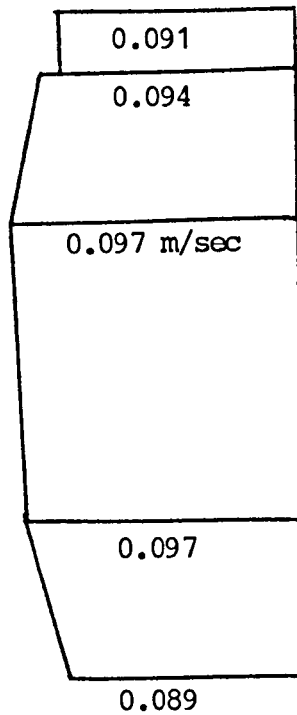


Figure 8.1 - Equivalent current velocity variation with water depth

Node	Experimental displacement (mm)	Computed displacement (mm)
1	29.5	29.4
2	25.4	25.5
3	21.3	21.1
4	17.2	16.9
5	12.7	12.3
6	8.5	8.3
7	0.	0.

Table 8.3 - Comparison of the computed and experimental horizontal nodal displacements

coefficient,  $C_m$ , as a function of KC. These are shown in figures 8.3 and 8.4 respectively. The force coefficients for the chain in waves were obtained as follows:

The horizontal velocity of water particles induced by waves at mean water level using the linear wave theory for deep water waves is:

$$V_x = \pi H/T \quad (8.1)$$

where H and T are the wave height and period respectively.

The Keulegan Carpenter number for the considered wave is:

$$KC = \frac{V_x T}{D} \quad (8.2)$$

where D is the diameter of the chain.

Substituting equation (8.1) into equation (8.2) and evaluating the KC number for the wave:

$$KC = \frac{\pi H}{D} = \frac{\pi \times 0.068}{0.002} = 106.8 \quad (8.3)$$

Thus, from graphs 8.3 and 8.4 for  $KC > 50$ :

$$C_d = 1.37$$

$$C_m = 1.25$$

#### 8.2.4 - Results of the Generated Wave in the Small Plume

It was essential to ensure that the input criteria for the generated wave was accurate. This was achieved by measuring the wave profile using both the X-Y plotter and the high speed camera. Results from the X-Y plotter are shown in figure 8.5. The height and period of the wave were measured from figure 8.5a. The values were 0.068 metres and 0.85 seconds respectively.

These results were in conformity with those obtained from the filming. Figure 8.5b shows the uniformity of the wave in the flume and hence confirms the fact that the effect of the secondary components of the wave are negligible as reported by Ellix (1984).

The most suitable wave theory for the considered wave was determined from figure 4.4 which was the Stokes 3rd order theory. A comparison of the computed and filmed wave profiles is given in figure 8.6. This indicates that the adopted wave theory represents the wave accurately.

The wave parameters which were obtained using the program STOKWAVE, are given in table 8.4.

Wave Height mm	Wave Period sec	Water Depth mm	$\lambda$	K	A <sub>11</sub>	A <sub>13</sub>	A <sub>15</sub>	A <sub>22</sub>	A <sub>24</sub>
68	0.85	500	0.1824	0.0054	0.13264	-0.08614	0.	0.116E-3	0.

A <sub>33</sub>	A <sub>35</sub>	A <sub>44</sub>	A <sub>55</sub>	B <sub>22</sub>	B <sub>24</sub>	B <sub>33</sub>	B <sub>35</sub>	B <sub>44</sub>	B <sub>55</sub>
-.266E-5	0.	0.	0.	0.51769	0.	0.39514	0.	0.	0.

Table 8.4 - Wave parameters of the wave generated in the small flume

### 8.2.5 - Results of the Tests in the Small Wave Flume

The chain model was arranged in the following four different configurations in the wave flume:

- 1 - Catenary shape at zero degrees to the wave direction.
- 2 - Catenary shape at 30 degrees to the wave direction.

3 - U-Shape at 30 degrees to the wave direction.

4 - Straight line shape.

For each arrangement, the static equilibrium shape of the chain was obtained using program 1. Then program 2 was used to compute the dynamic response of the chain due to the wave motion. Comparisons of the computed and experimental dynamic response of 3 nodes are presented graphically.

The computed static configuration of the chain in the first case is given in figure 8.7. The computed and experimental envelopes of the dynamic response of the chain are given in figure 8.8. Figure 8.9 shows a comparison of the computed and experimental nodal displacements.

Graphs corresponding with those listed above for the second, third and fourth cases are given in figures 8.10 to 8.12, 8.13 to 8.15 and 8.16 to 8.18 respectively.

The above comparisons show a very close agreement between the computed and experimentally measured amplitudes of the nodal displacements. The degree of accuracy is partly due to employing the Simpson's rule to calculate the wave loadings on the chain. These results complete the validation of the adopted scheme for assessing the hydrodynamic loadings on a flexible catenary riser.

### 8.3 - Results for the Tube Model

#### 8.3.1 - Results of the Material Damping Tests

The applied dead load on the system was 1.4 Newtons and the live loads were 0.09, 0.18, 0.32 and 0.5 Newtons. The time history of the system displacements associated with the applied live loads were obtained from the U.V. recorder and were then digitized.

A curve fitting procedure was carried out for the case with 0.5 N live load by giving trial values for the material constant,  $a$ , and the Young's modulus,  $E$ , and computing the corresponding displacement curve. This curve was then compared with that obtained from the test. The criteria for fitting the curves were to satisfy the first peak and the rate of displacement decay with time. These fitted curves are shown in figure 8.19. The corresponding values for the material damping constants,  $a$ , and  $b$ , and the Young's modulus,  $E$ , were as follows:

$$a = 4.9 \times 10^{-6} \text{ m}^2/\text{N}\cdot\text{sec.} , b = 30 \text{ 1/sec.} , E = 8.3 \times 10^6 \text{ N/m}^2$$

The above values of  $a$ ,  $b$  and  $E$  were used to compute the system response for the other live load cases. The resulting graphs fitted well with those obtained from the experiments.

#### 8.3.2 - Determination of the Drag Coefficient, $C_d$ , for the Model in Steady Current Flow

The same current velocity field which was used for the chain model was generated. The computed and measured experimental nodal displacements due to the current flow are given in table 8.5 and figure 8.20. The value for  $C_d$  was 1.37.

Node	1	2	3	4	5	6	7
Experimental Displacements (mm)	55.8	43.1	35.3	29.4	20.	14.1	0.
Computed Displacements (mm)	55.2	45.0	37.2	29.5	21.6	14.3	0.

Table 8.5 - Comparison of the computed and experimental horizontal nodal displacements

### 8.3.3 - Determination of Drag Coefficient, $C_d$ , and Inertia Coefficient, $C_m$

The Keulegan number,  $KC$ , at the mean water level for the chosen wave, using equation (8.3), is:

$$KC = \frac{\pi H}{D} = \frac{\pi \times 0.15}{0.0053} = 88.9$$

Thus, from figures 8.3 and 8.4 for  $KC > 50$ :

$$C_d = 1.37$$

$$C_m = 1.25$$

### 8.3.4 - Results for the Generated Wave in the Large Wave Flume

The results for the wave height and period from the X-Y plotter, figure 8.21a, are 0.15 metres and 1.22 seconds respectively. These results were in conformity with those obtained from the filming process. Figure 8.21b shows reasonable uniformity of the wave in the flume.

The most suitable wave theory for the wave was Stokes 3rd order theory. A comparison of the computed and filmed wave profiles is given in figure 8.22. The wave parameters are given in table 8.6.

Wave Height mm	Wave Period sec	Water Depth mm	$\lambda$	K	A <sub>11</sub>	A <sub>13</sub>	A <sub>15</sub>	A <sub>22</sub>	A <sub>24</sub>
150	1.22	1200	0.1934	0.0026	0.0868	-0.0552	0.0	0.21E-4	0.0

A <sub>33</sub>	A <sub>35</sub>	A <sub>44</sub>	A <sub>55</sub>	B <sub>22</sub>	B <sub>24</sub>	B <sub>33</sub>	B <sub>35</sub>	B <sub>44</sub>	B <sub>55</sub>
-0.30E-6	0.	0.	0.	0.50756	0.	0.3836	0.	0.	0.

Table 8.6 - Wave parameters of the first wave generated in the large flume

### 8.3.5 - Calculation of the Buoyancy Force Induced by the Sub-Buoy and the Cradle

The mass of the cradle = 42.3 grams

The mass of the ball = 7.3 grams

Thus, total mass of the sub-buoy system = 49.6 grams

The total weight of the sub-buoy system = 0.486 N

Volume of the cradle = 23.2 cm<sup>3</sup>

Diameter of the ball = 6.25 cm

Thus, volume of the ball =  $(4/3) D^3 \pi / 8 = 127.8$

The total volume of the sub-buoy system = 151 cm<sup>3</sup>

Density of water  $\rho = 1000 \text{ Kg/m}^3$

Equivalent weight of displaced water =

$$151 \times 10^{-6} \times 1000 \times 10 = 1.51 \text{ N}$$

Buoyancy of the sub-buoy = 1.51 - 0.486 = 1.024 N

### 8.3.6 - Results of the Tests in the Large Wave Flume

The model was arranged in the following three different configurations in the wave flume:

- 1 - Catenary shape at zero degrees to the wave direction.
- 2 - Single catenary riser shape at zero degrees to the wave direction.
- 3 - Single catenary riser shape at 45 degrees to the wave direction.

For each arrangement, the static equilibrium shape of the tube was obtained using program 1. Program 2 was then used to compute the dynamic response of the tube due to wave motion. Comparisons of the computed and experimental dynamic horizontal top tension and nodal displacements of 3 nodes are presented graphically.

The computed static configuration of the tube in the first case is given in figure 8.23. The computed and experimental envelopes of the tube dynamic response are given in figure 8.24. Figure 8.25 shows a comparison of the computed and experimental horizontal top tension and nodal displacements in the wave direction. Figure 8.26 shows a typical output for the horizontal top tension from the U.V. recorder.

Graphs corresponding with those listed above for the second and third configurations of the tube are given in figures 8.27 to 8.29 and 8.30 to 8.32 respectively.

The above comparisons showed close agreement between the computed and experimental results. The program for the first configuration of the tube was also run without material damping. These results showed a 6% error (i.e. increase) in the amplitude of the horizontal top tension.

The results from the above comparisons complete the validation of the adopted scheme to model the physical characteristics and response of the flexible catenary riser due to drag-inertia hydrodynamic forces induced by wave and current motion.

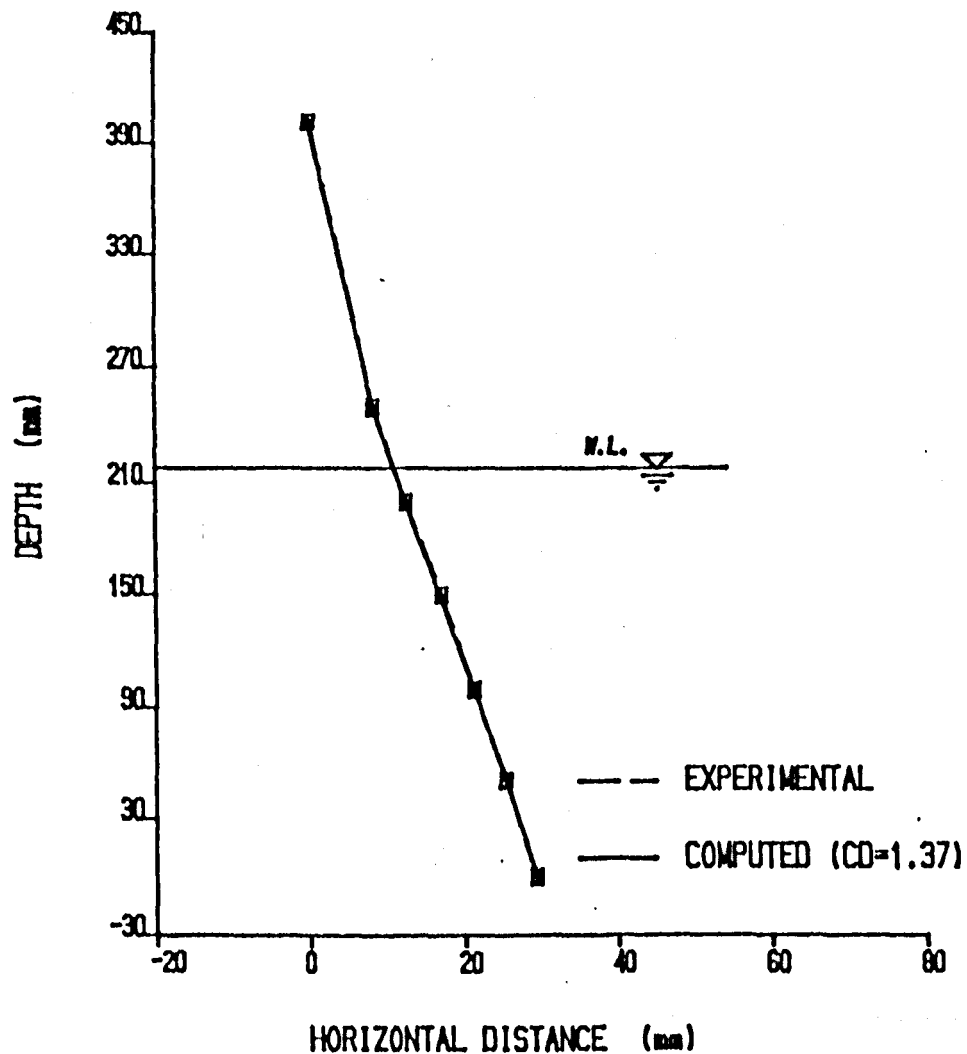


Figure 8.2 - Comparison of the measured and computed nodal displacements along the chain due to current induced hydrodynamic loadings

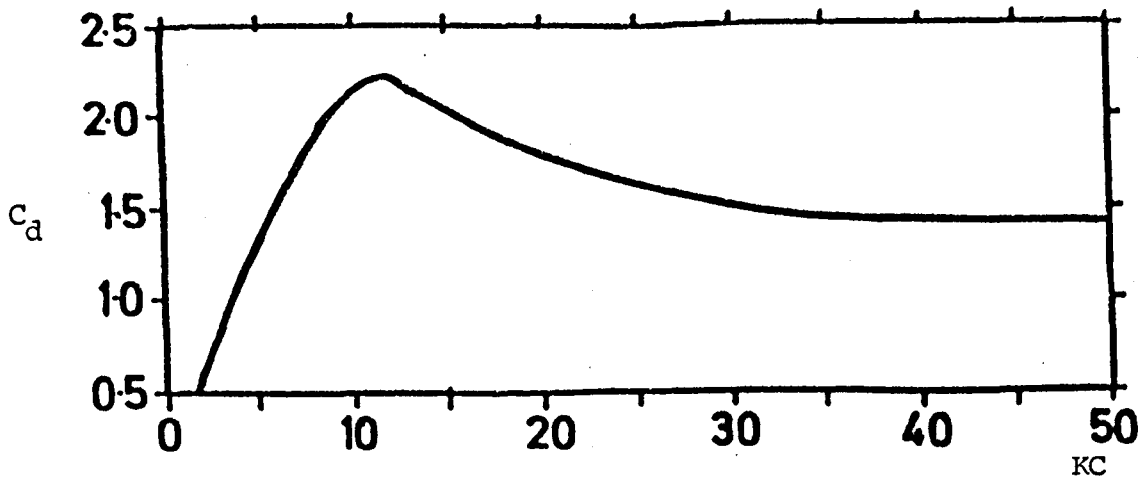


Figure 8.3 - Drag coefficient ( $C_d$ ) against Keulegan-Carpenter number ( $KC$ ) in subcritical Reynolds number region (after Sarpakaya et. al. (1974))

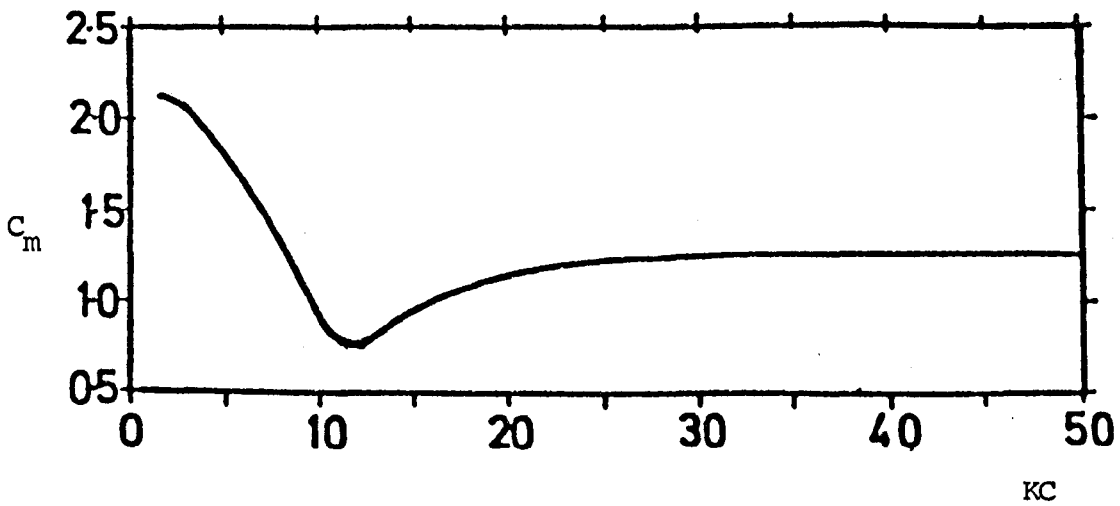


Figure 8.4 - Inertia coefficient ( $C_m$ ) against Keulegan-Carpenter number ( $KC$ ) in subcritical Reynolds number region (after Sarpakaya et. al. (1974))

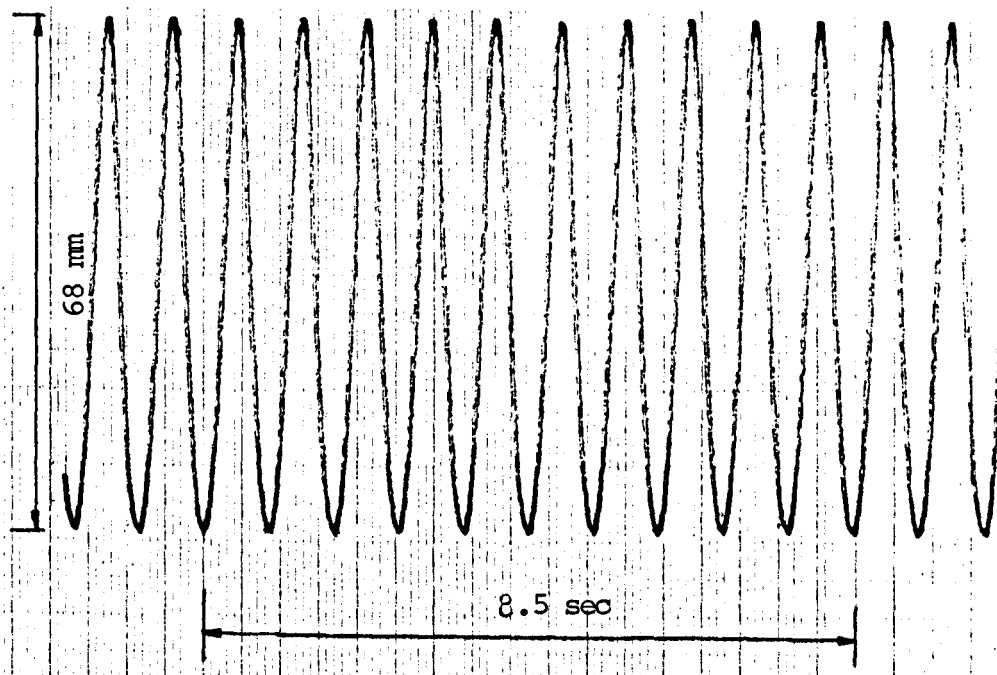


Figure 8.5a - Height and period of the wave generated in the small flume from X-Y plotter

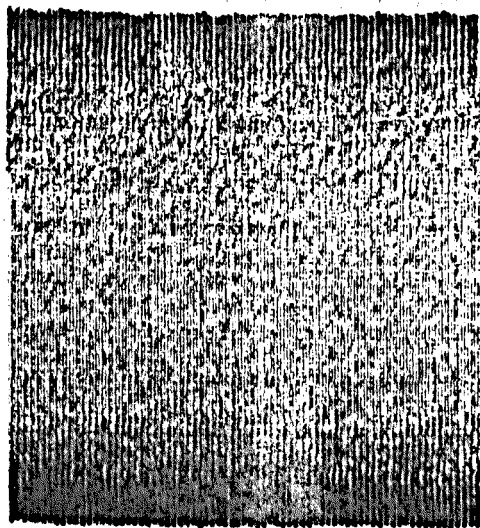


Figure 8.5b - The wave train generated in the small wave flume

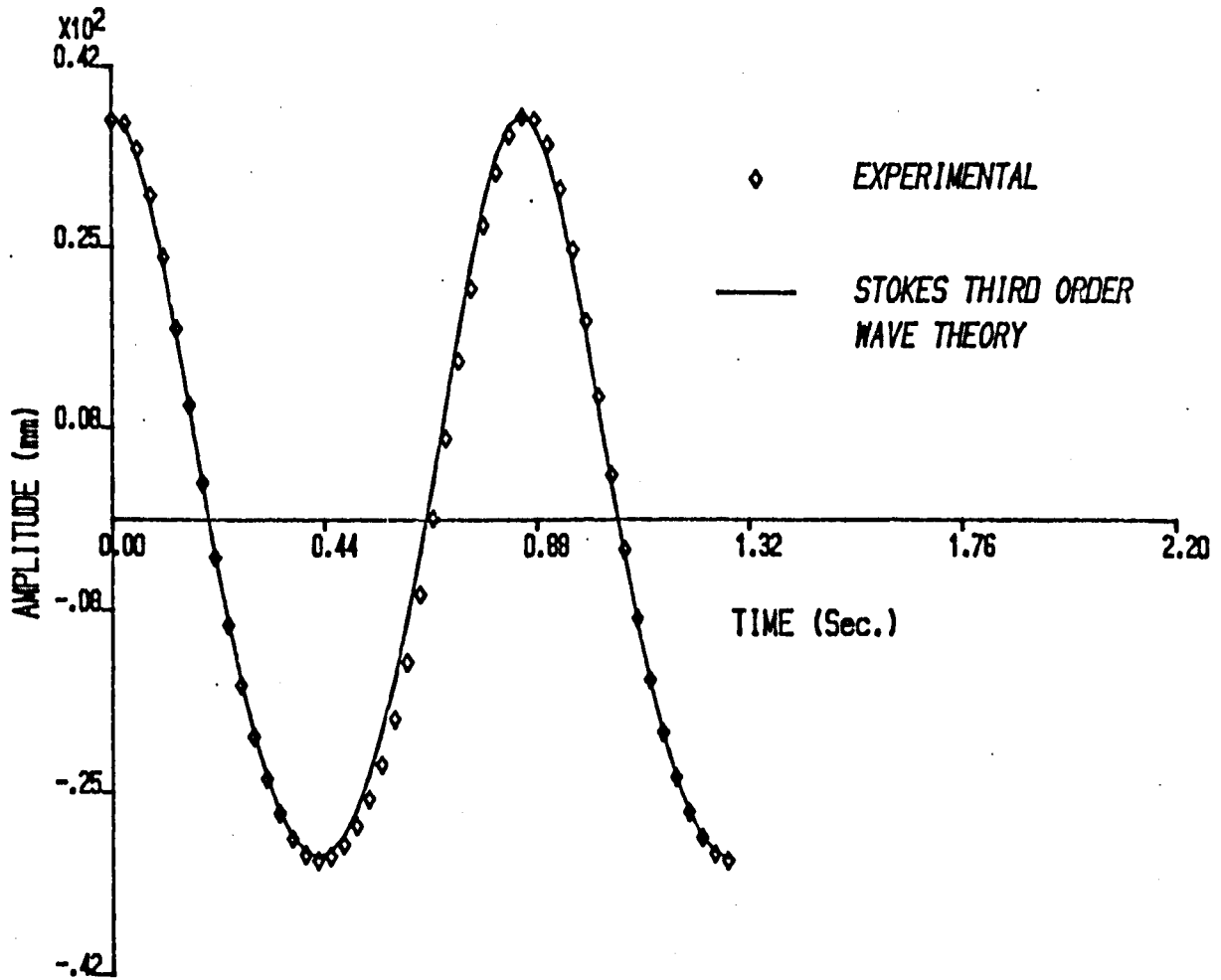


Figure 8.6 - Comparison of the computed and digitized wave profile for the wave generated in the small wave flume

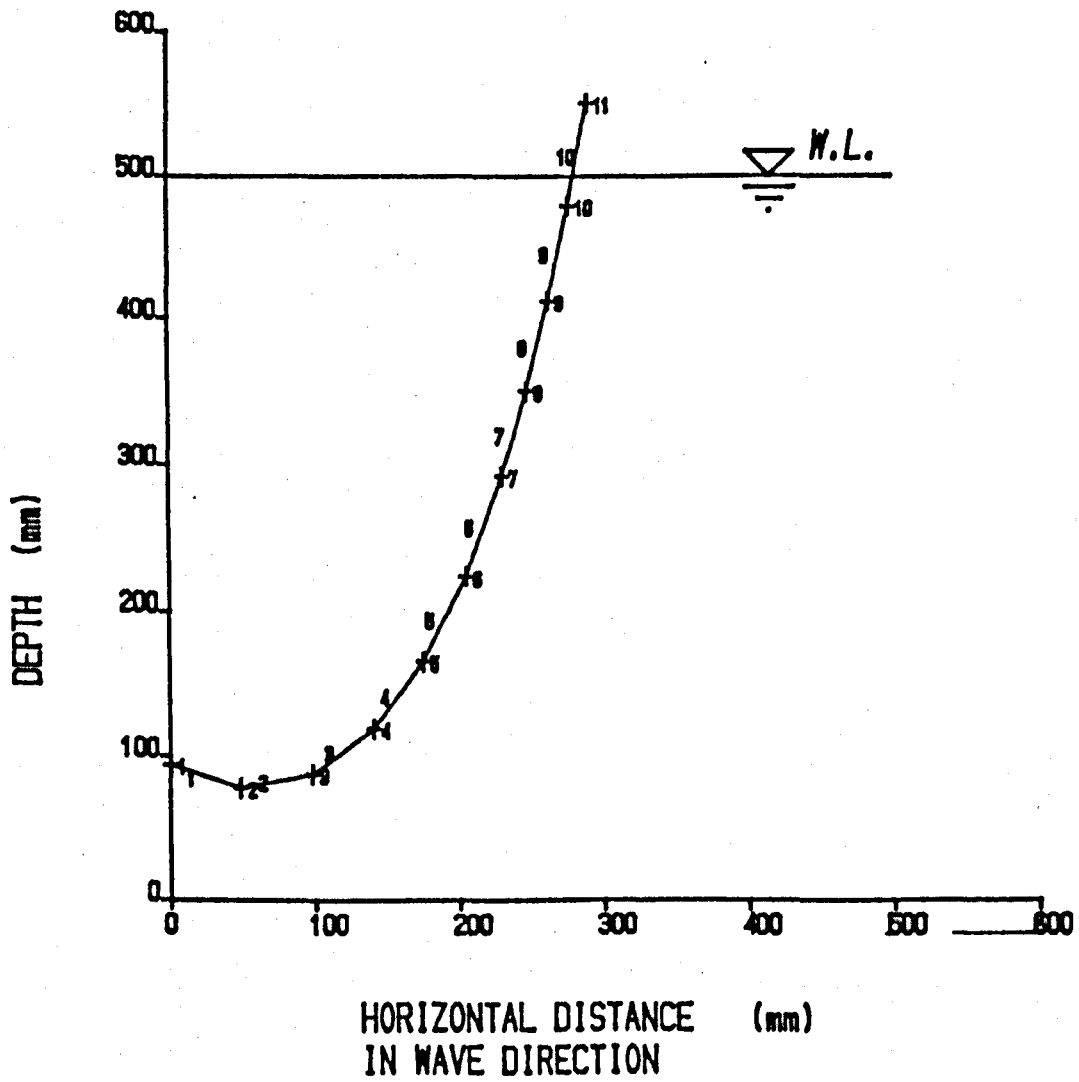


Figure 8.7 - Computed static equilibrium shape of the chain model at  $0^\circ$  to the wave direction

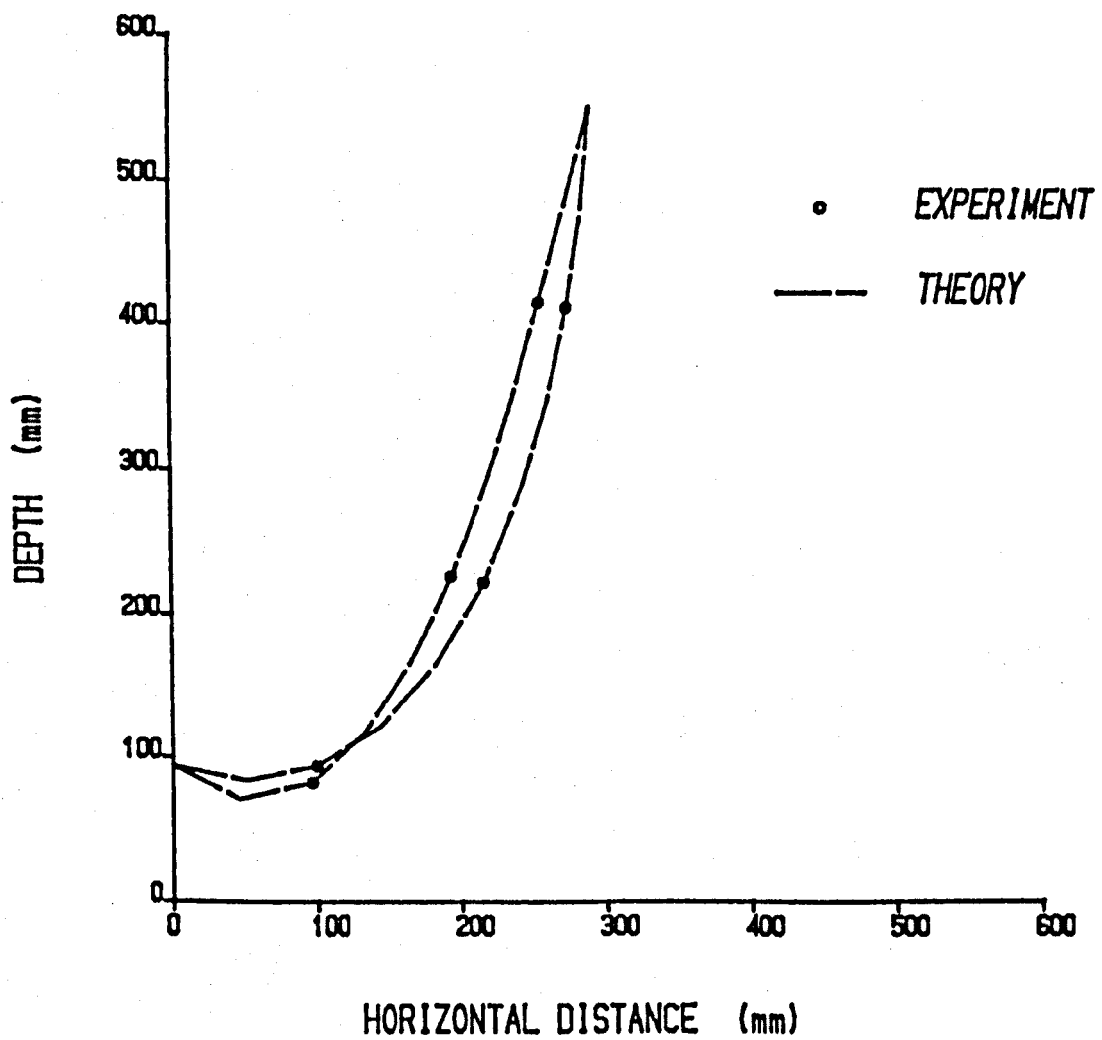


Figure 8.8 - Computed and measured envelopes for the dynamic response of the chain model at  $0^\circ$  to the wave direction

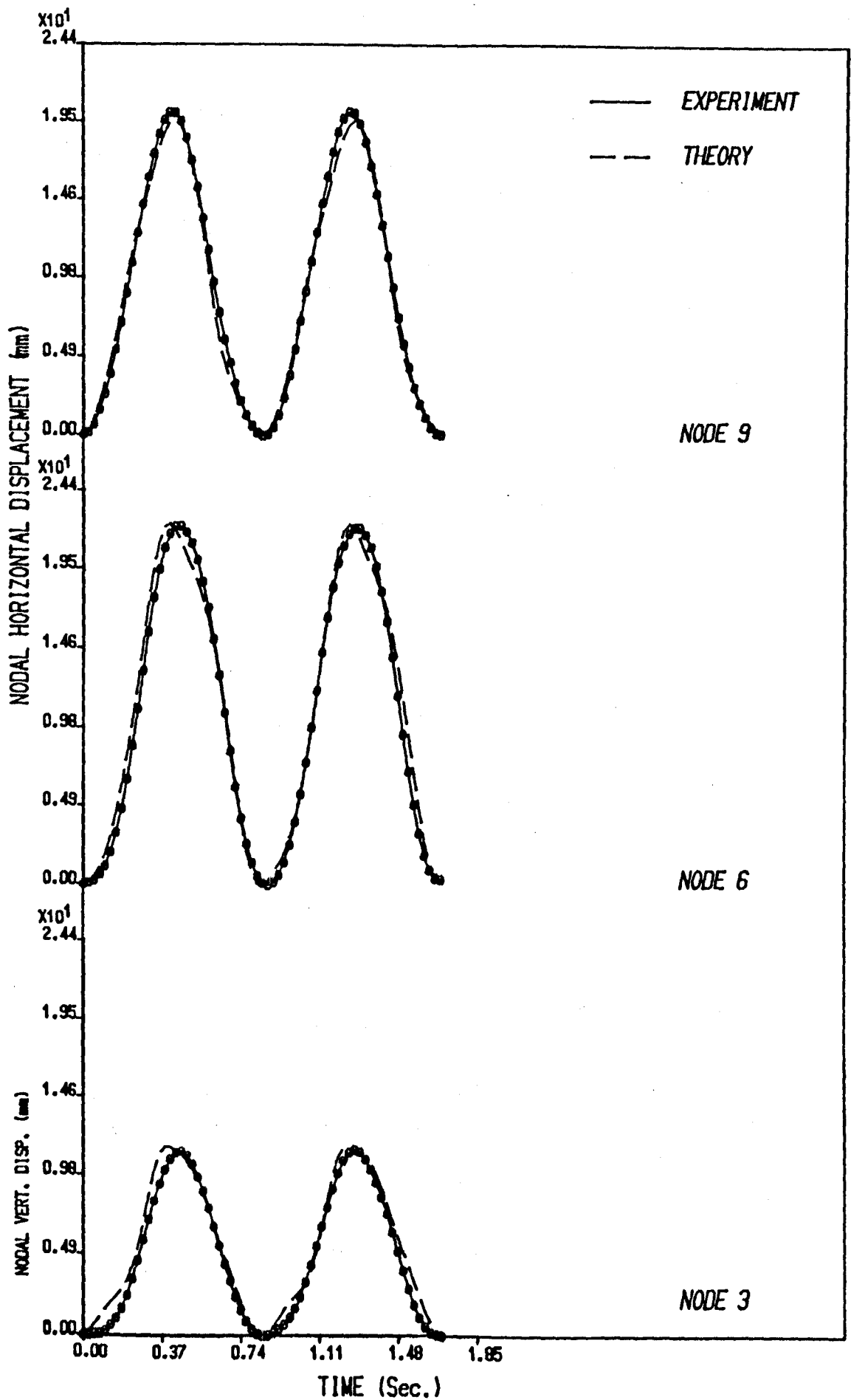


Figure 8.9 - Comparison of the computed and measured horizontal nodal displacements along the chain model at  $0^\circ$  to the wave direction

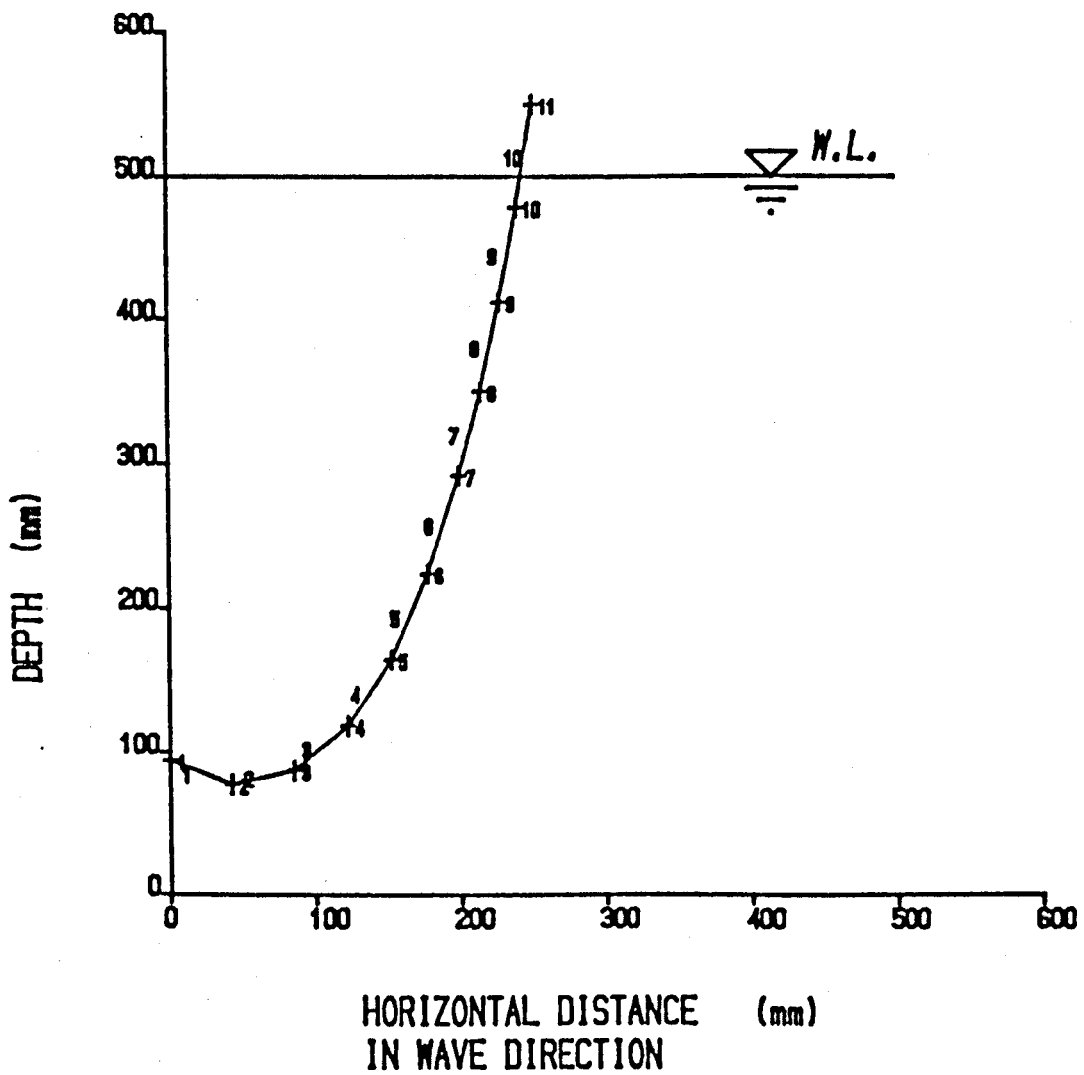


Figure 8.10 - Computed static equilibrium shape of the chain model at 30° to the wave direction

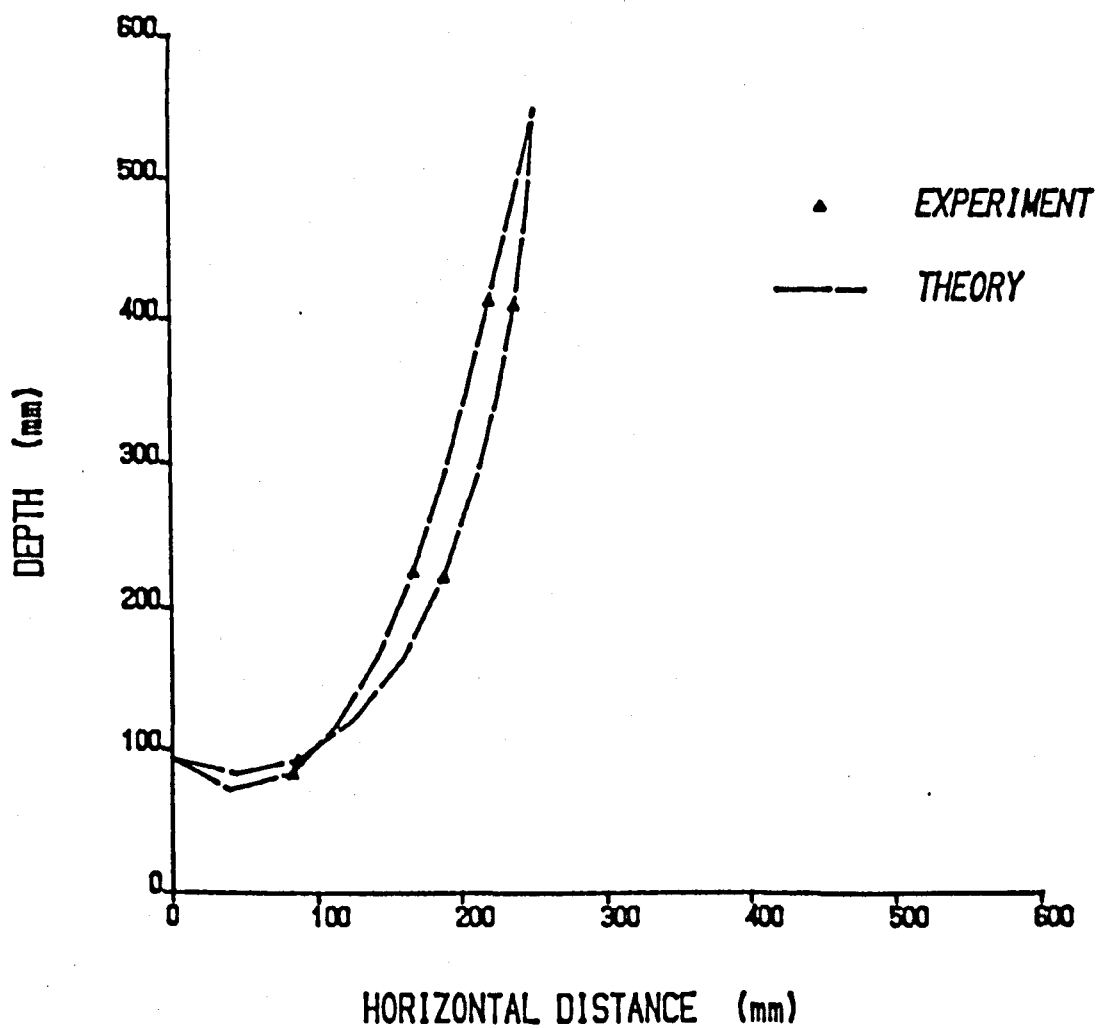


Figure 8.11 - Computed and measured envelopes in the wave direction for the dynamic response of the chain model at  $30^\circ$  to the wave direction

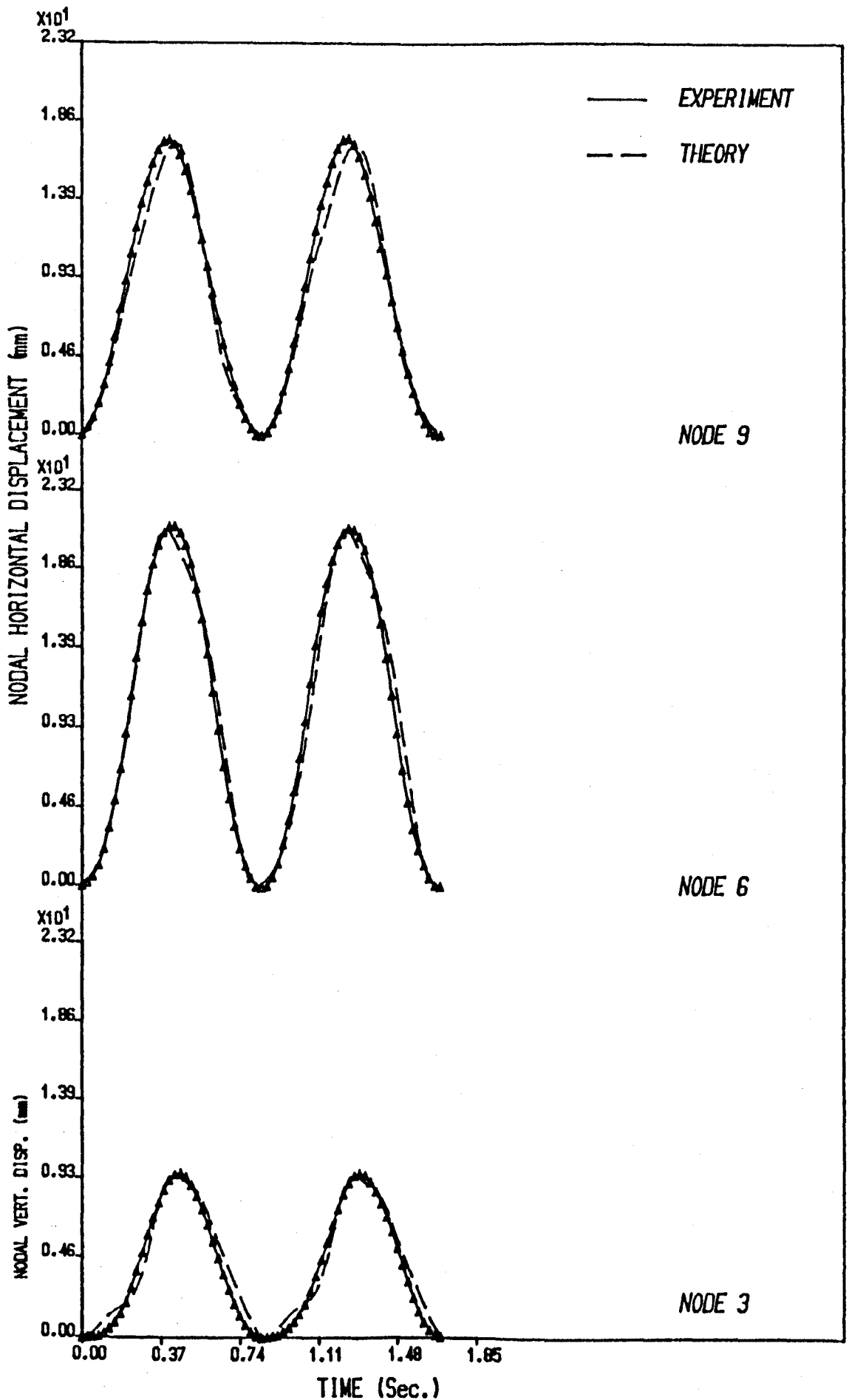


Figure 8.12 - Comparison of the computed and measured horizontal nodal displacements in the wave direction along the chain model at  $30^\circ$  to the wave direction

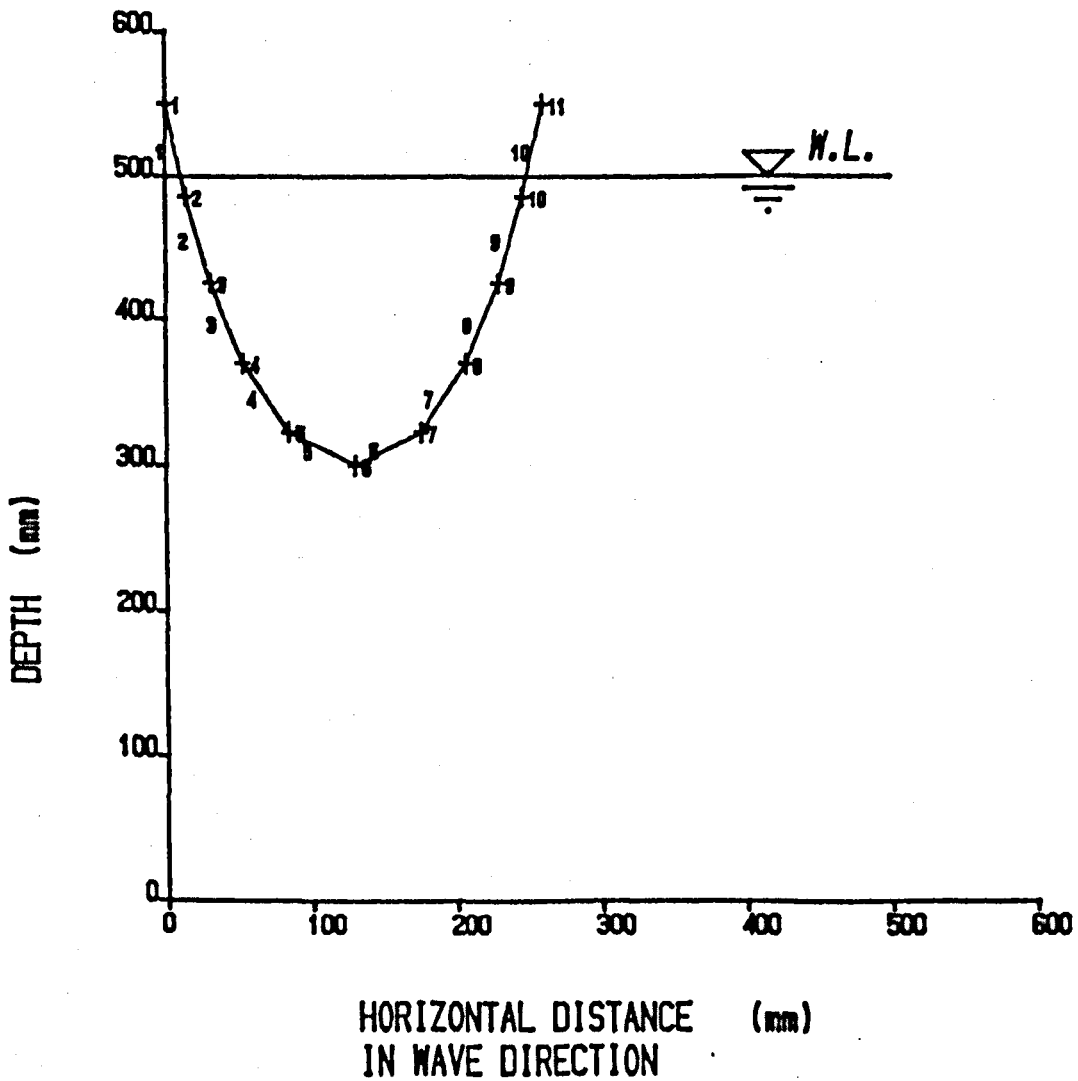


Figure 8.13 - Computed static equilibrium shape of the chain model in u-shape at  $30^\circ$  to the wave direction used as the initial shape for corresponding dynamic response calculations

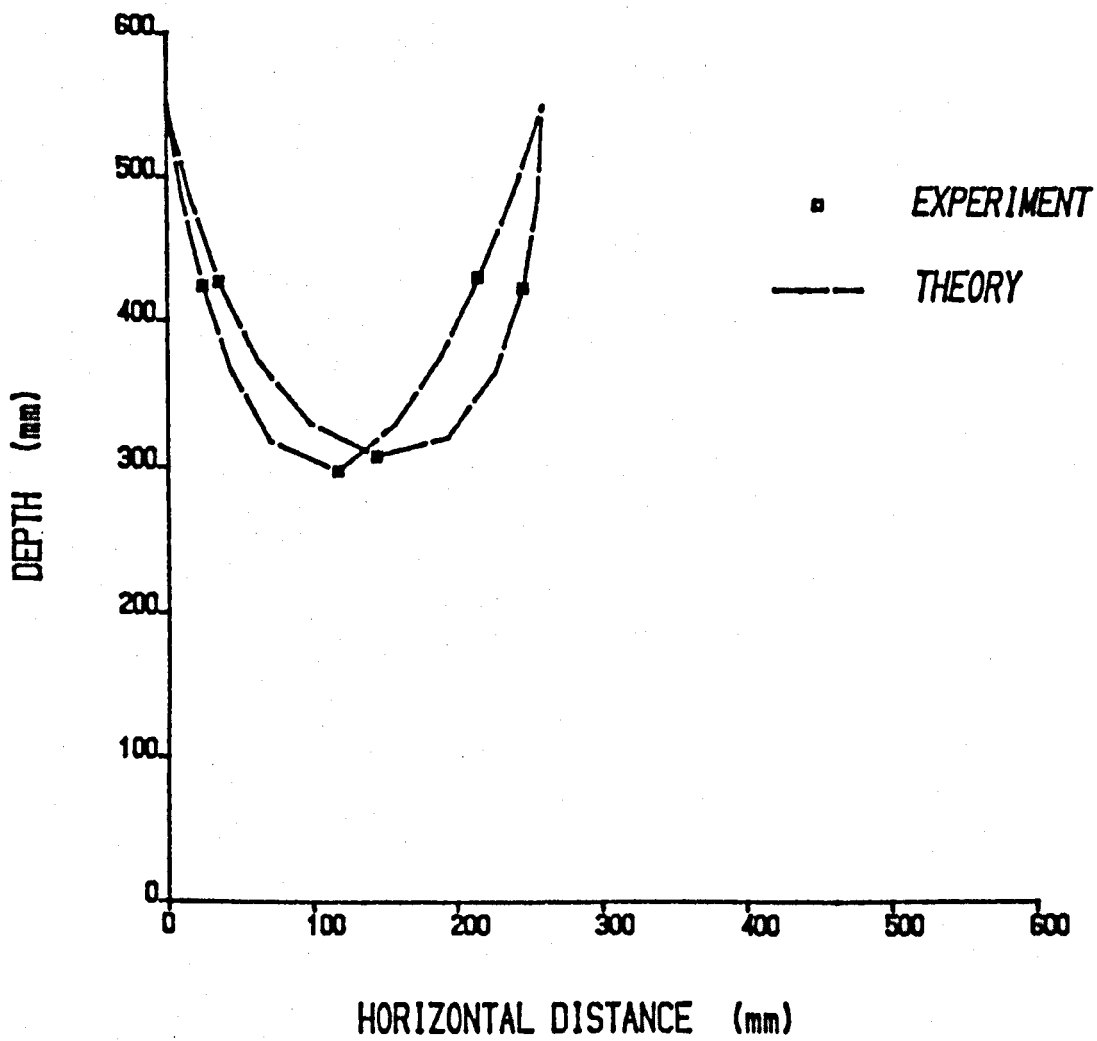


Figure 8.14 - Computed and measured envelopes in the wave direction for the dynamic response of the chain in u-shape at  $30^\circ$  to the wave direction

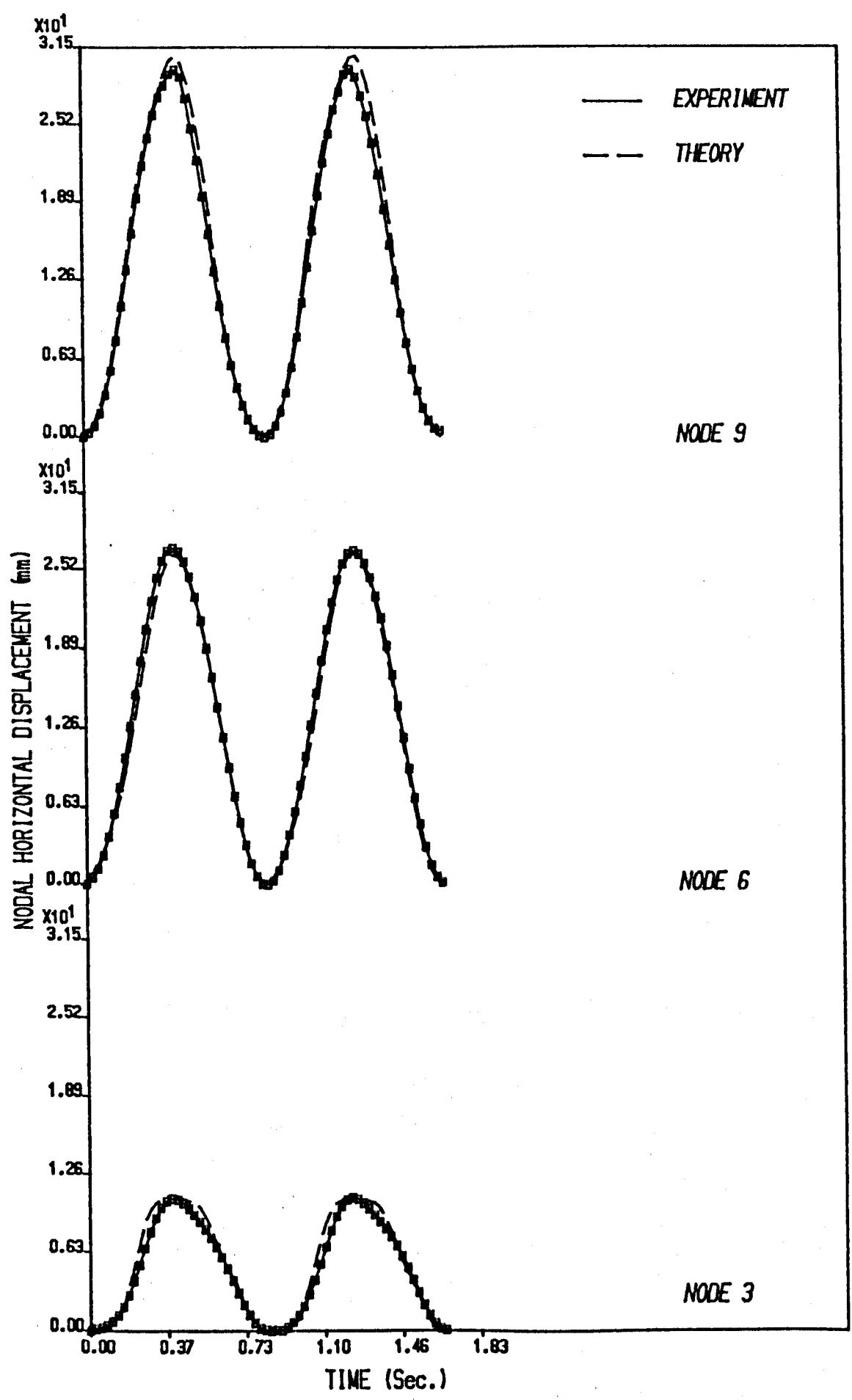


Figure 8.15 - Comparison of the computed and measured horizontal nodal displacements in the wave direction along the chain model in u-shape at  $30^\circ$  to the wave direction

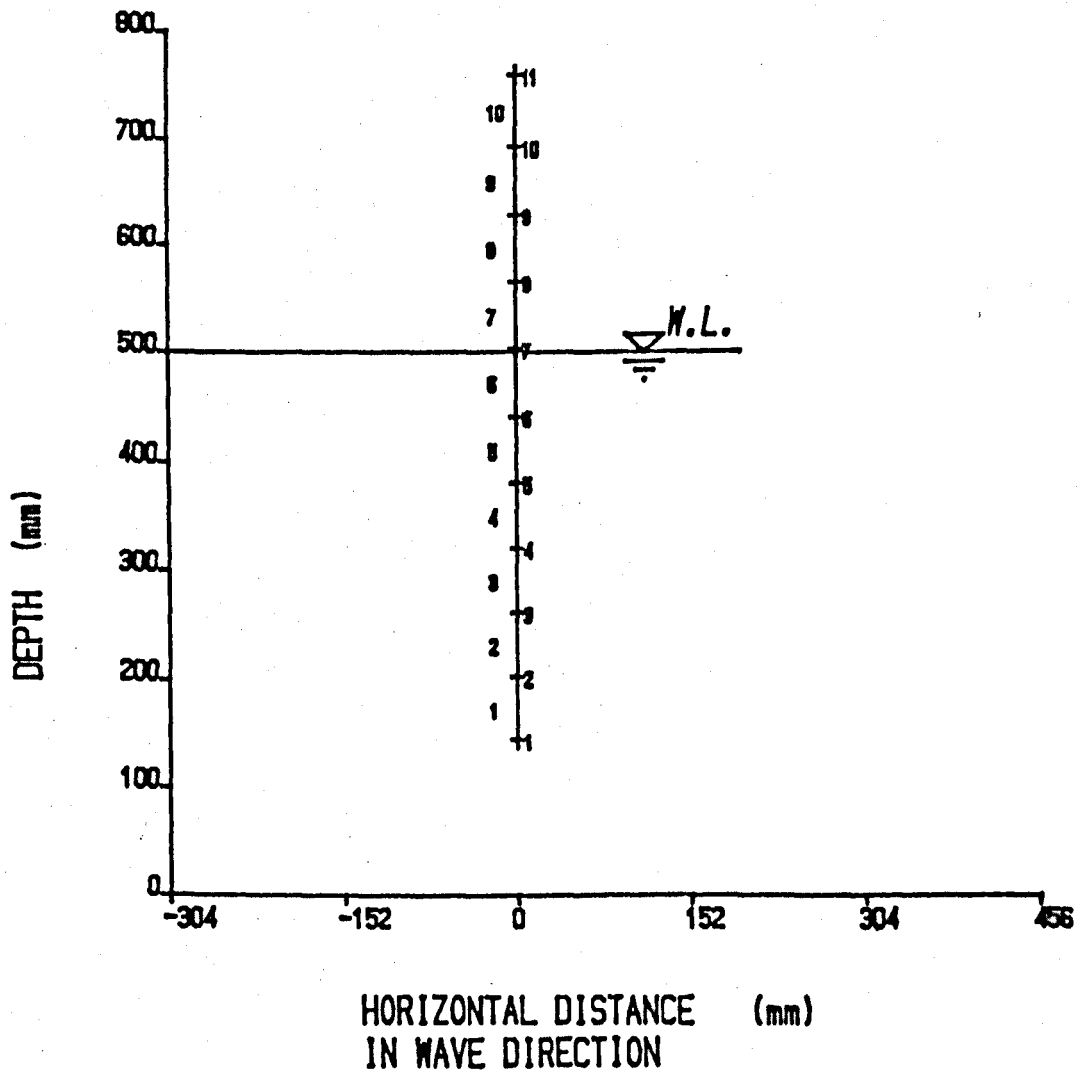


Figure 8.16 - Computed static equilibrium shape of the chain model in disconnected shape

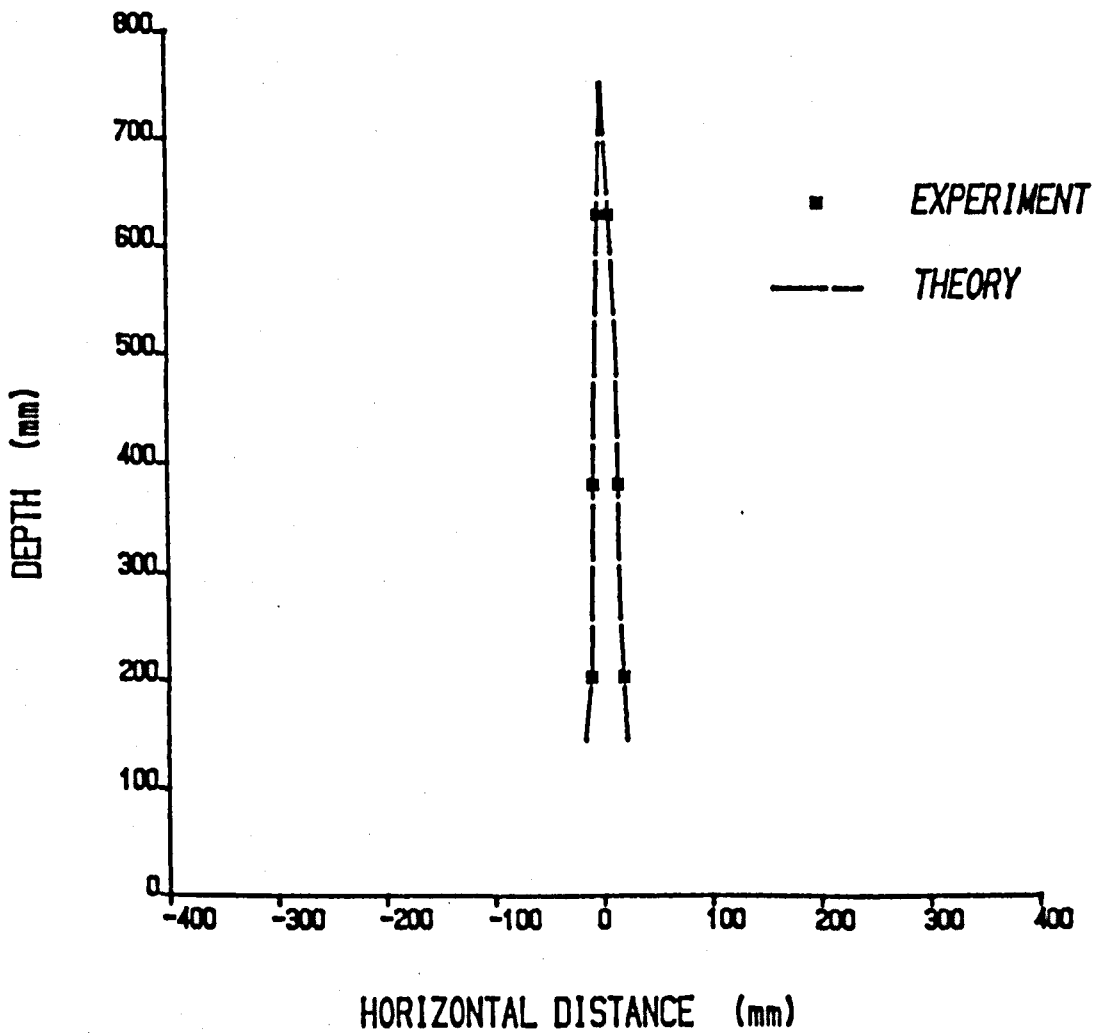


Figure 8.17 - Computed and measured envelopes for the dynamic response of the chain model in disconnected shape

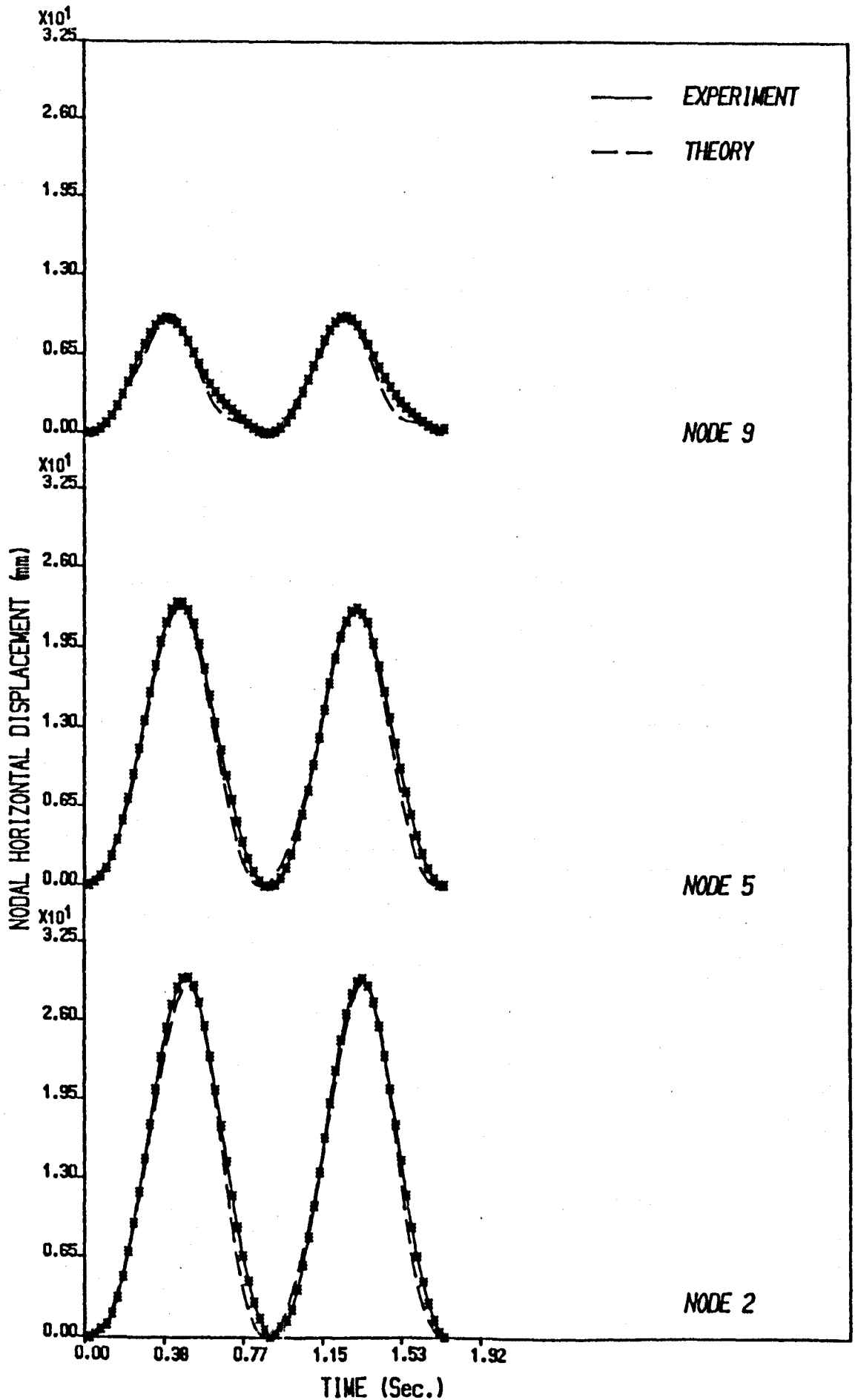


Figure 8.18 - Comparison of the computed and measured horizontal nodal displacements along the chain model in disconnected shape

8.4 - Results for the Vibrating Tube Model due to Vortex-Shedding

8.4.1 - Results for Higher Amplitude Wave Generated in the Large Wave Flume

The values for the wave height and period obtained from the X-Y plotter, figure 8.33a, are 0.25 metres and 1.40 seconds respectively. These results were in conformity with those obtained from the filming. Figure 8.33b shows the reasonable uniformity of the wave in the flume.

The most suitable wave theory for the wave was Stokes 3rd order theory. A comparison of the computed and filmed wave profiles is given in figure 8.34. The wave parameters are given in table 8.7.

Wave Height mm	Wave Period sec	Water Depth mm	$\lambda$	K	$A_{11}$	$A_{13}$	$A_{15}$	$A_{22}$	$A_{24}$
150	1.40	1200	0.2406	0.002	0.18945	-0.12794	0.	0.48E-3	0.

$A_{33}$	$A_{35}$	$A_{44}$	$A_{55}$	$B_{22}$	$B_{24}$	$B_{33}$	$B_{35}$	$B_{44}$	$B_{55}$
-0.14E-4	0.	0.	0.	0.53629	0.	0.41685	0.	0.	0.

Table 8.7 - Wave parameters of the second wave generated in the large flume

8.4.2 - Determination of Drag Coefficient,  $C_D$ , and Inertia Coefficient,  $C_m$

The Keulegan number,  $KC$ , at the mean water level for the chosen wave, using equation (8.3), is:

$$KC = \frac{\pi \times 0.25}{0.0053} = 148.2$$

Thus, from figures 8.3 and 8.4 for  $KC > 50$ :

$$C_d = 1.37$$

$$C_m = 1.25$$

#### 8.4.3 - Evaluation of the Model Natural Frequencies

The equilibrium configuration of the model was obtained using program 1. Then a node along the model (node 6) was displaced by applying horizontal and vertical point loads (-2N and -20N respectively), and the new equilibrium shape was obtained using the static program 3. This shape was the input into the dynamic program 2 and the natural vibration of node 6 with time was recorded when the loads were released, figure 8.35. Fourier analysis was carried out for a part of this recorded time history of displacement which was chosen so that the ends corresponded to maximum displacements, figure 8.35. The Fourier amplitude coefficients,  $A_r$  and  $B_r$ , were evaluated, figure 8.36; each peak value of  $A_r$  and  $B_r$  corresponding with a structural natural frequency. These frequencies were calculated using equation (5.48) as follows:

$$f_n = \frac{1}{2 \times 5.568} r = 0.090 r$$

The results are given in table 8.8.

r	6	7	10	11	20	21	32	33	40	41
$f_n$	0.539	0.629	0.898	0.988	1.796	1.886	2.874	2.963	3.592	3.682
$T=1/f_n$ (sec)	1.86	1.59	1.11	1.01	0.56	0.53	0.35	0.34	0.28	0.27

Table 8.8 - Natural frequencies of the single catenary model

#### 8.4.4 - Determination of the Model Response due to Vortex-Shedding

The effect of Vortex-Shedding on the tube was assessed by the method which was suggested by Rajabi et. al. (1984) as outlined in chapter 4 Section 4.4.2. This was achieved by using the calculated maximum nodal displacement in the direction of the lift force and the well known relationships to evaluate the amplification factors for the nodal drag coefficient,  $C_d/C_{d0}$ .

Nodal KC and Re values for the considered wave were calculated using the water particle velocity components normal to the members of the model; and possible vortex-shedding frequencies,  $f_v$ , along the model were determined from figure 4.9 and are given in table 8.9. These frequencies were compared with the structural natural frequencies ( $f_n$ ), figure 8.37, and the dominant values of  $f_v$  and corresponding  $f_n$  were determined. This was achieved by choosing the most closely agreeing values of  $f_v$  and  $f_n$ . From figure 8.37 these values are 2.857 and 2.874 respectively.

Node	Vert. Co-ords mm	Re	KC	$f_v/f_w$	$f_v$
1	0.	-	-	-	-
2	406	694	36	4	2.857
3	272	593	30	4	2.857
4	234	572	29	4	2.857
5	338	638	33	5	3.571
6	488	782	40	5	3.571
7	652	1022	52	6	4.286
8	818	1379	70	6	4.286
9	986	1901	97	6	4.286
10	1156	2654	136	6	4.286
11	1327	3733	191	6	4.286
12	1500	-	-	-	-

Table 8.9 - Possible vortex-shedding frequencies along the model from figure 4.9

The nodal reduced velocities,  $V_r$ , were then calculated. At the dominant vortex-shedding area along the tube (i.e. the area with  $f_v = 4f_n$ ), the reduced velocities varied from 7.28 to 8.11. Experimental results for a cantilever cylinder in a wave flume, obtained by Angrilli and Cossalter (1982), show that perfect resonance of a cylinder will occur at a reduced velocity of 8.98 when  $f_v$  is equal to  $4f_n$ . Therefore, the reduced velocity at perfect resonance,  $V_r^*$ , was assumed to be 8.98 for the present work. The nodal values  $V_r/V_r^*$  were calculated and the corresponding values of the lift amplification factor ( $CL/CL_0$ ) were determined from figure 4.11. The nodal lift coefficients,  $CL_0$ , were determined from figure 8.38 which is reproduced from the work by Sarpakaya et. al. (1974) who obtained the graph from experimental work in the subcritical region of Reynolds numbers. The dynamic program 2 was then used to find the maximum nodal displacements in the lift force direction and hence the nodal

amplification factors of the nodal drag coefficients,  $C_d/C_{d_0}$ . The results are summarized in table 8.10. These amplification factors were re-input into program 2 and the dynamic response of the tube in the drag-inertia force direction was computed.

Node	$V_r^*/V_r$	$CL/CL_0$	$C_{L0}$	Max. Displ. mm	$\frac{C_d}{C_{d_0}}$
1	-	-	-	-	-
2	0.98	2.80	1.11	23.15	4.1
3	0.84	2.63	1.33	21.32	4.3
4	0.81	2.50	1.35	17.96	4.0
5	0.90	2.75	1.22	15.34	3.5
6	1.11	2.71	1.0	12.82	2.8
7	1.45	2.23	0.9	11.56	2.2
8	1.95	1.83	0.9	10.17	1.6
9	2.69	1.67	0.9	8.18	1.0
10	3.76	1.62	0.9	5.61	1.0
11	5.29	1.62	0.9	2.75	1.0
12	-	-	-	-	-

Table 8.10 - Computed results from the vortex-shedding model

**8.4.5 - Comparison of the Model Response to the Wave with and without taking account of Vortex-Shedding Effects**

The static configuration of the tube in the wave flume was obtained using program 1, figure 8.39. Program 2 was then used to compute the dynamic response of the tube with and without taking account of the nodal drag amplification factors,  $C_d/C_{d_0}$ , in the drag-inertia force direction. A comparison of the computed results is given in figure 8.40. Figure 8.41 shows a comparison of both of these computed results with the experimental horizontal top tension and nodal displacements induced by the wave loadings. The comparison shows close agreement between the experimental results and those computed by taking account of the vortex-shedding effect. The results

computed without taking vortex-shedding into account show a 10 to 15% error in both the amplitude of the horizontal top tension and the nodal displacements.

The vortex-shedding, which was experienced in the present test, (i.e. with  $f_v = 4f_n$ ) tended to have a beneficial effect on damping the dynamic response of the tube in the drag-inertia force direction. However, the lift force had a frequency of 4 times that of the wave. This is important in the context of fatigue life, particularly at the end connections.

The results of this comparison may be considered as an experimental verification of the vortex-shedding theory suggested by Rajabi et. al. (1984).

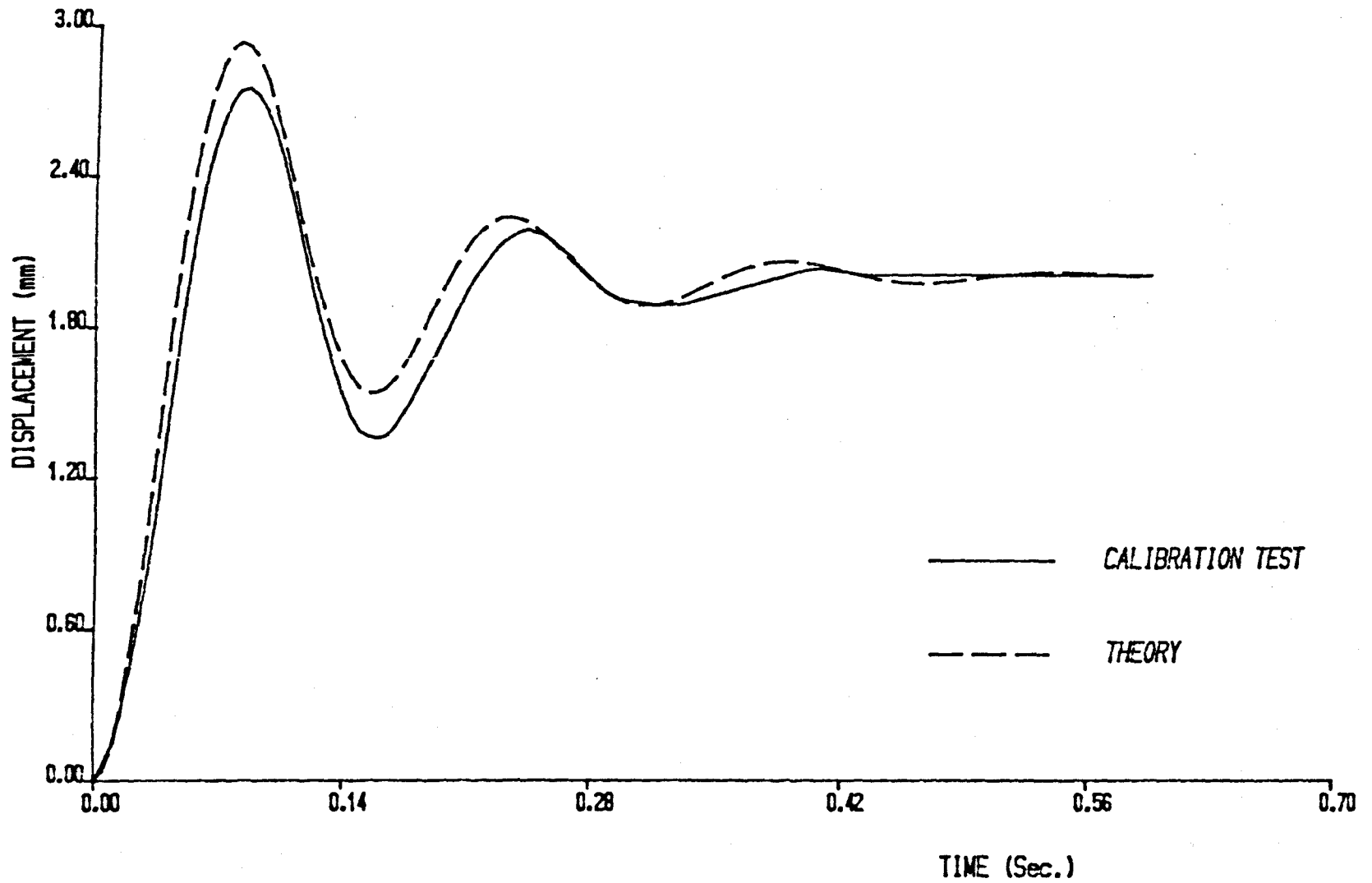


Figure 8.19 - Curve-fitting for material damping constants :

$$E = 8.3 \times 10^6 \text{ N/m}^2, a = 4.9 \times 10^{-6} \text{ m}^2/\text{N}\cdot\text{sec} \text{ and } b = 30 \text{ sec}^{-1}$$

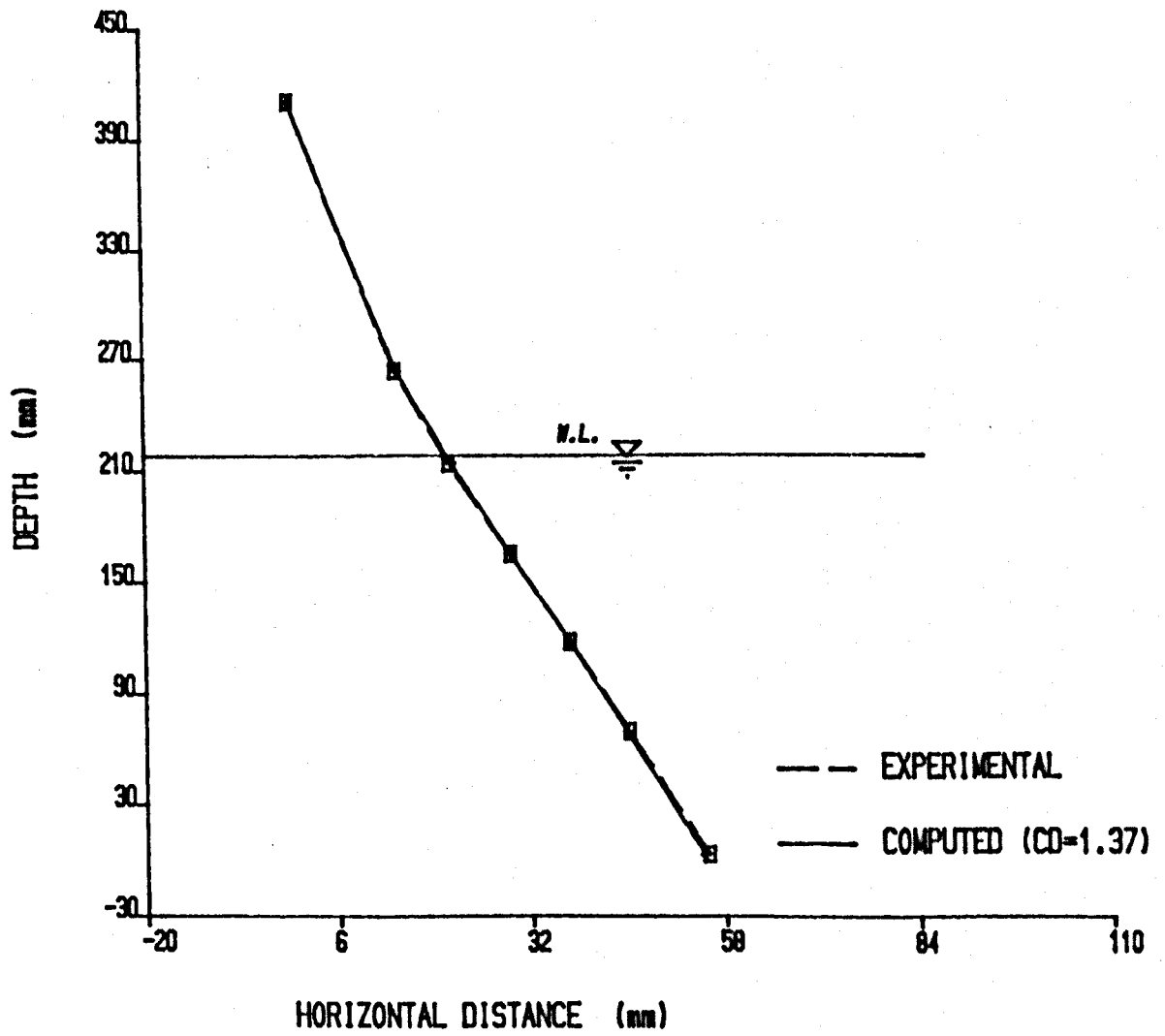


Figure 8.20 - Comparison of the measured and computed nodal displacements along the tube model due to current induced hydrodynamic loadings

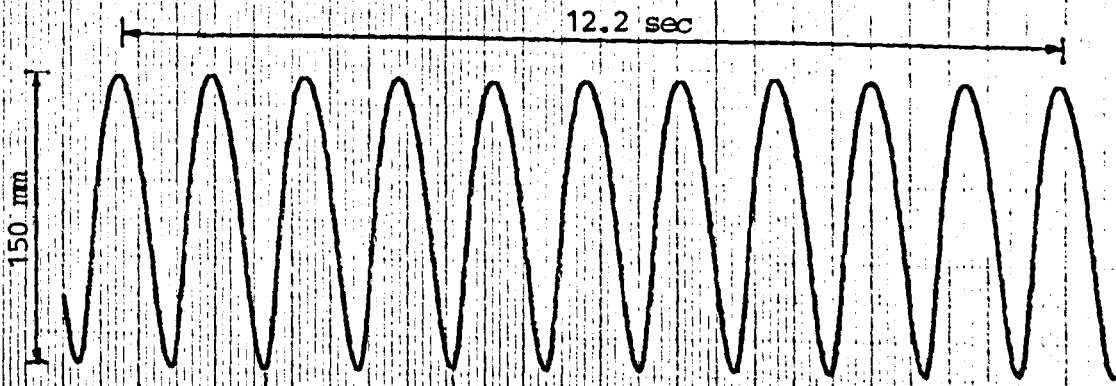


Figure 8.21a - Height and period of the first wave generated in the large wave flume

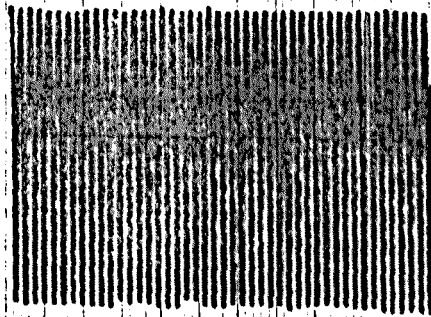


Figure 8.21b - The first wave train generated in the large wave flume

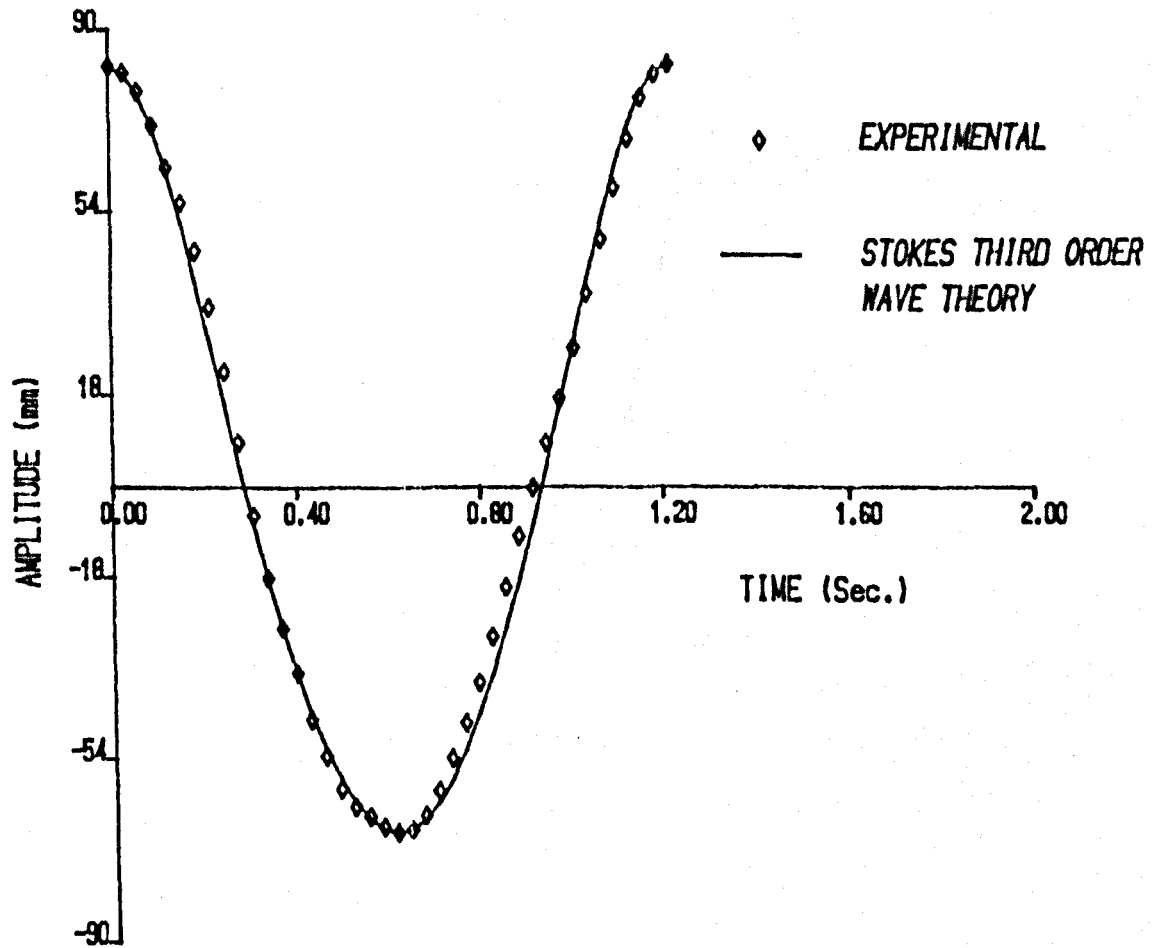


Figure 8.22 - Comparison of the computed and digitized wave profile for the first wave generated in the large wave flume

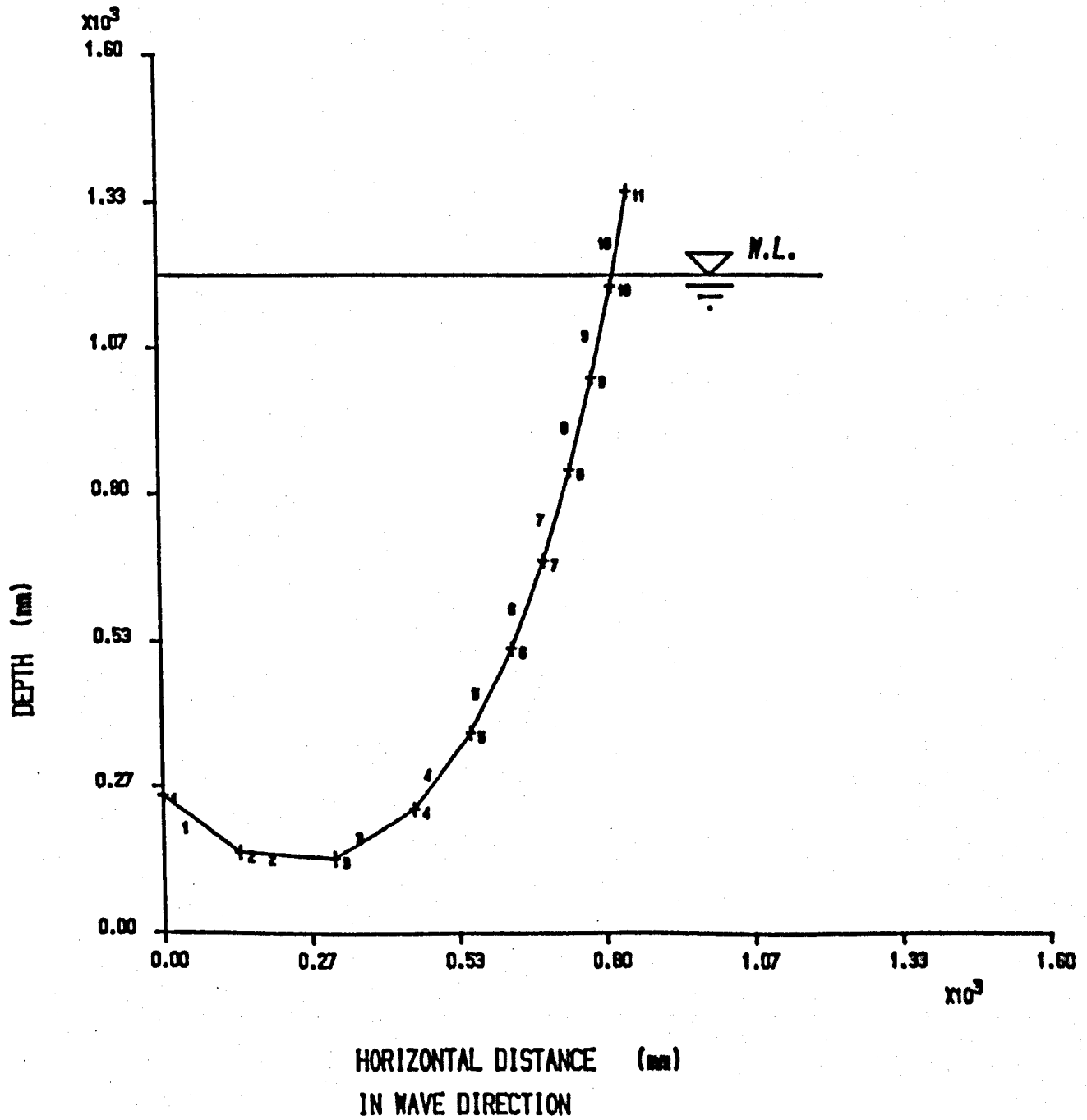


Figure 8.23 - Computed static equilibrium shape of the tube model in catenary shape at  $0^\circ$  to the wave direction

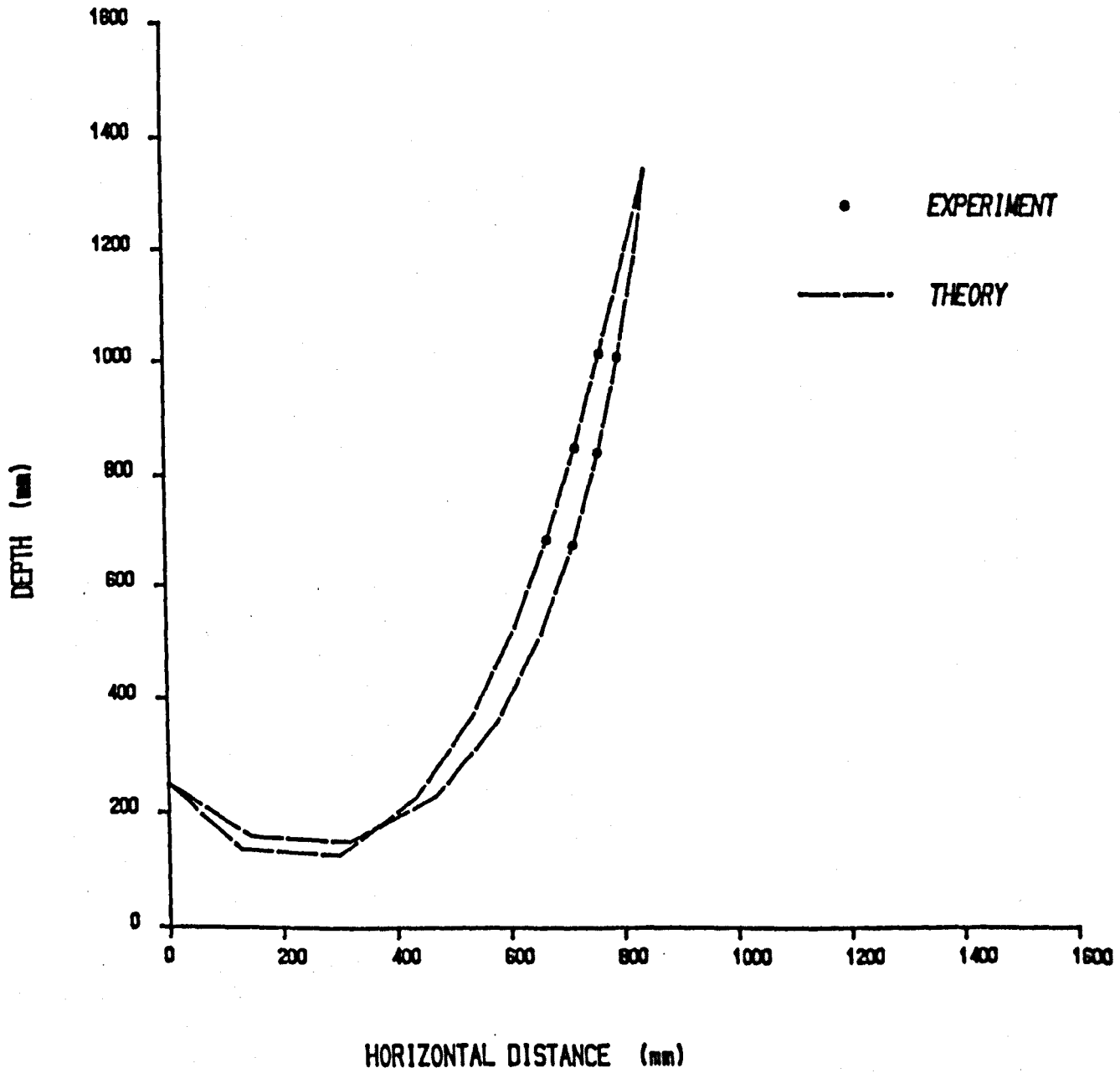


Figure 8.24 - Computed and measured envelopes for the dynamic response of the tube model in catenary shape at  $0^\circ$  to the wave direction

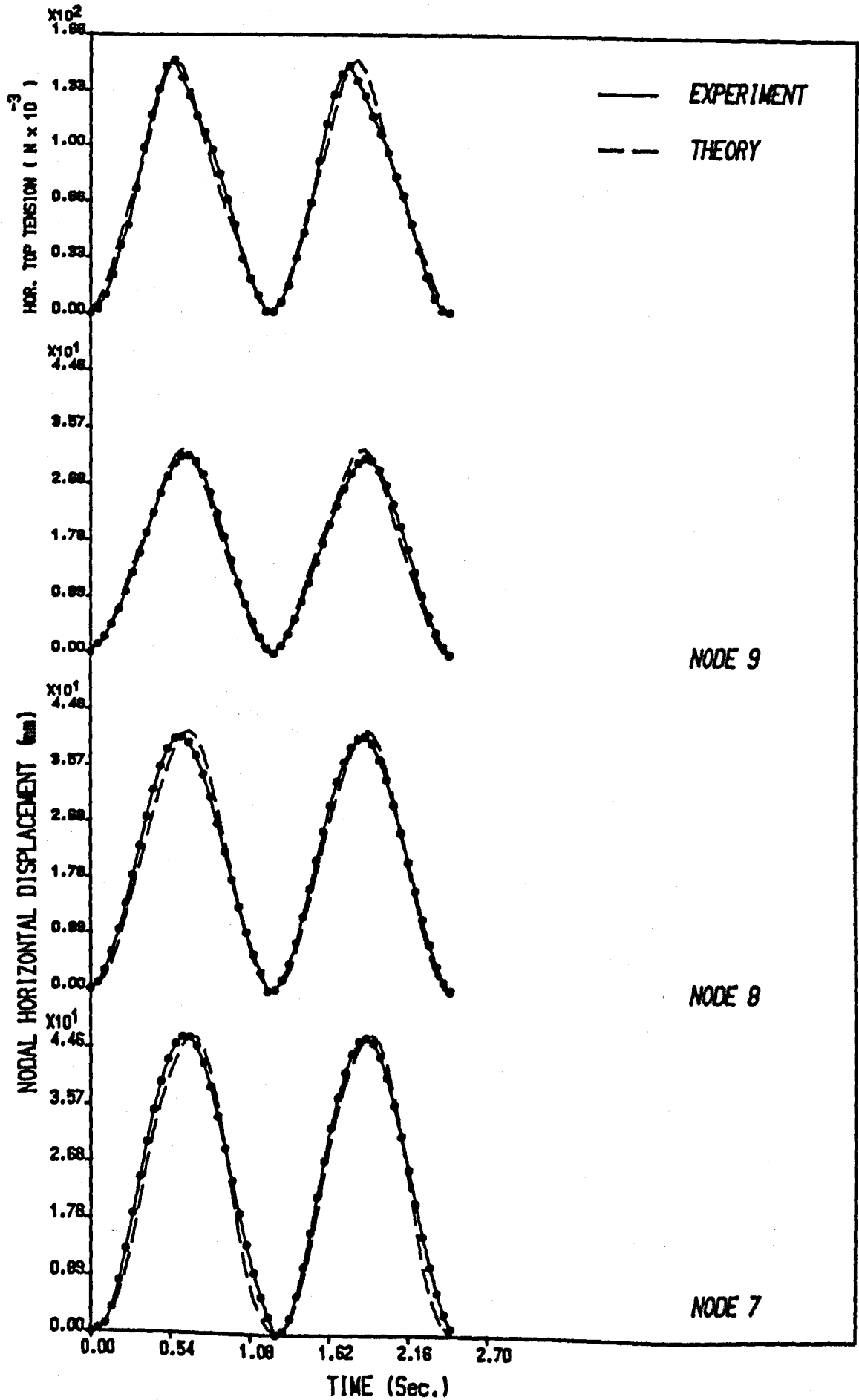


Figure 8.25 - Comparison of the computed and measured horizontal top tension and nodal displacements along the tube model in catenary shape at  $0^\circ$  to the wave direction

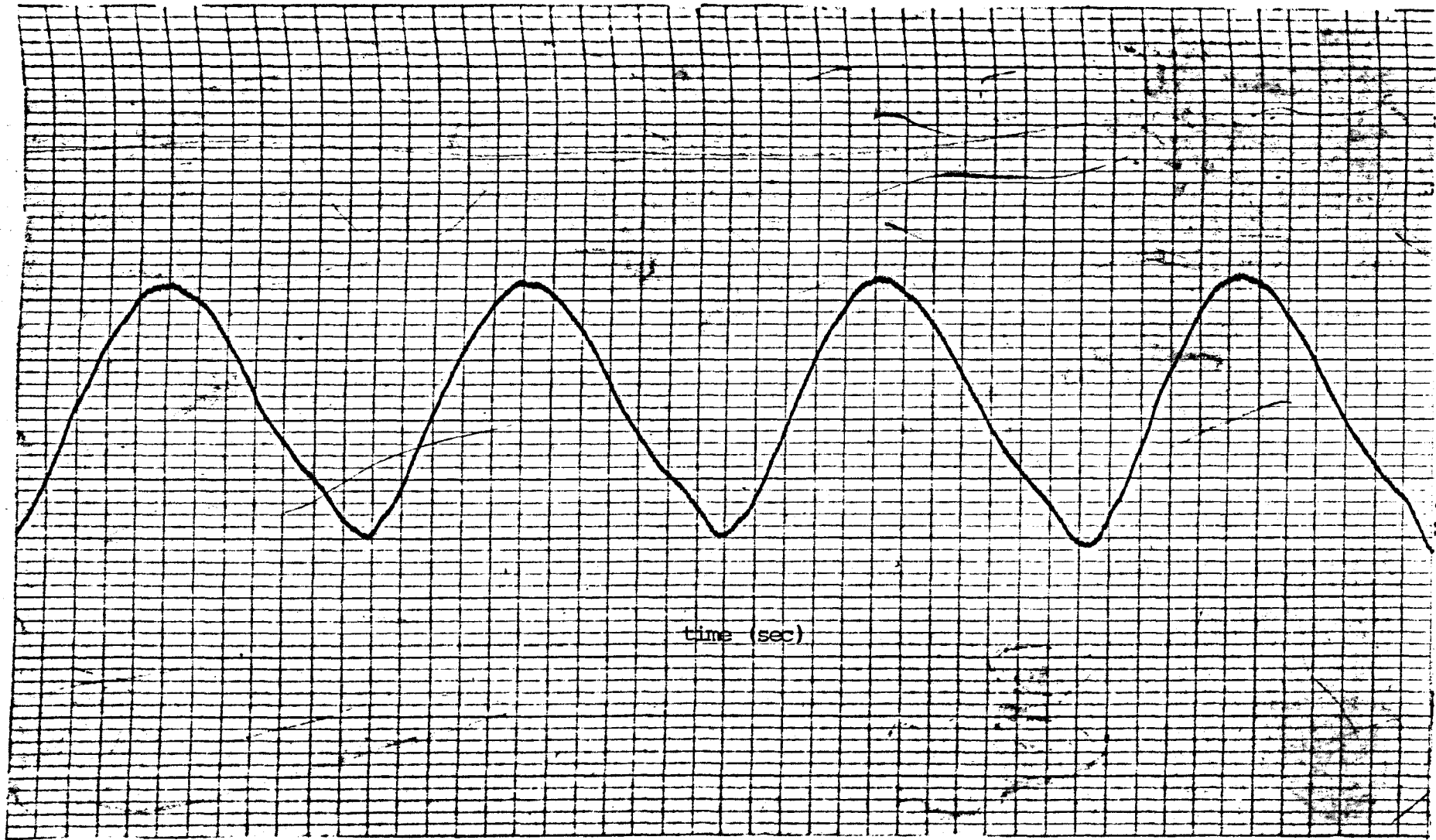


Figure 8.26 - A typical graph output from the U.V. recorder for the horizontal top tension of the tube model in the large wave flume

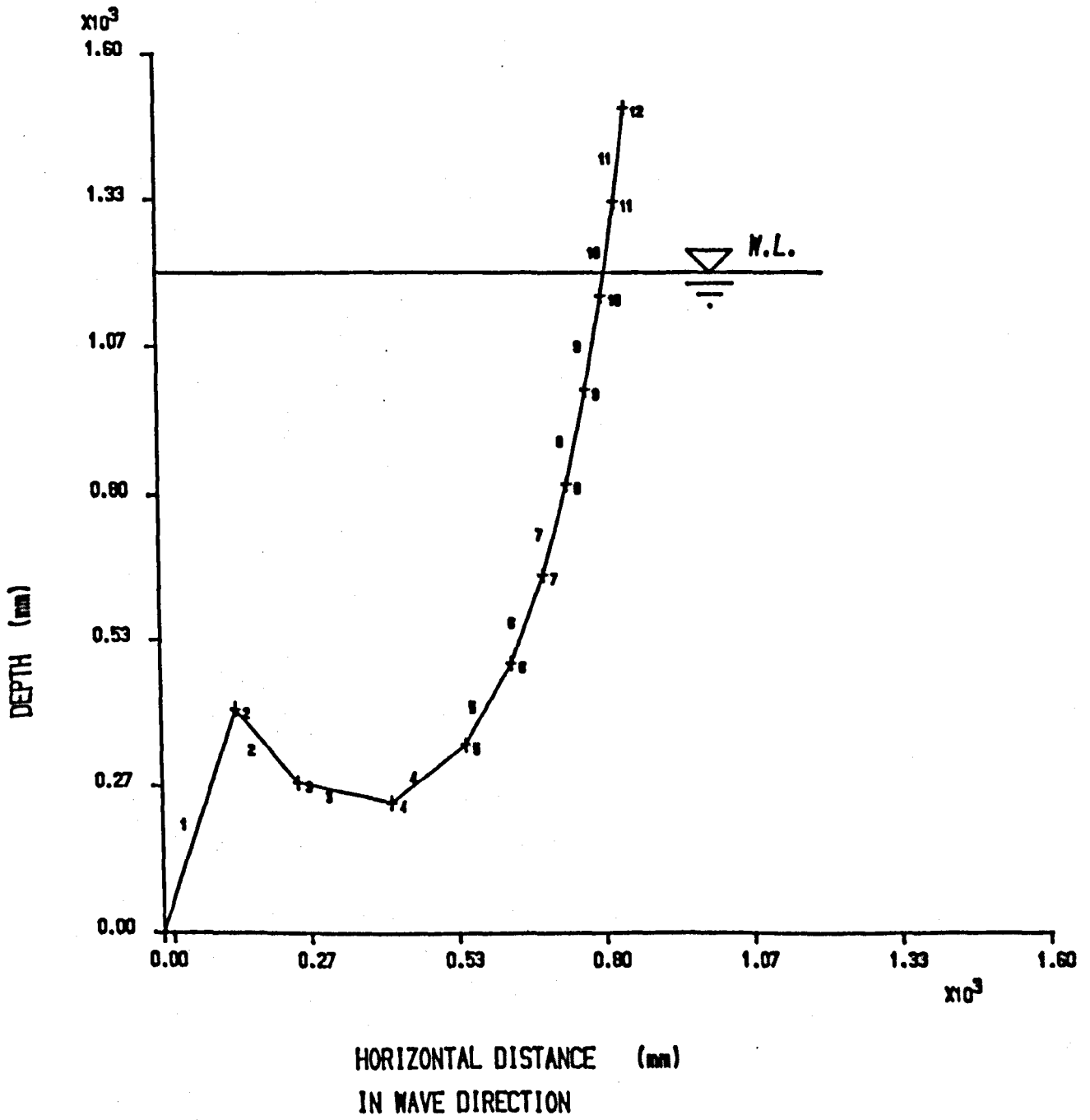


Figure 8.27 - Computed static equilibrium shape of the tube model at 0° to the wave direction

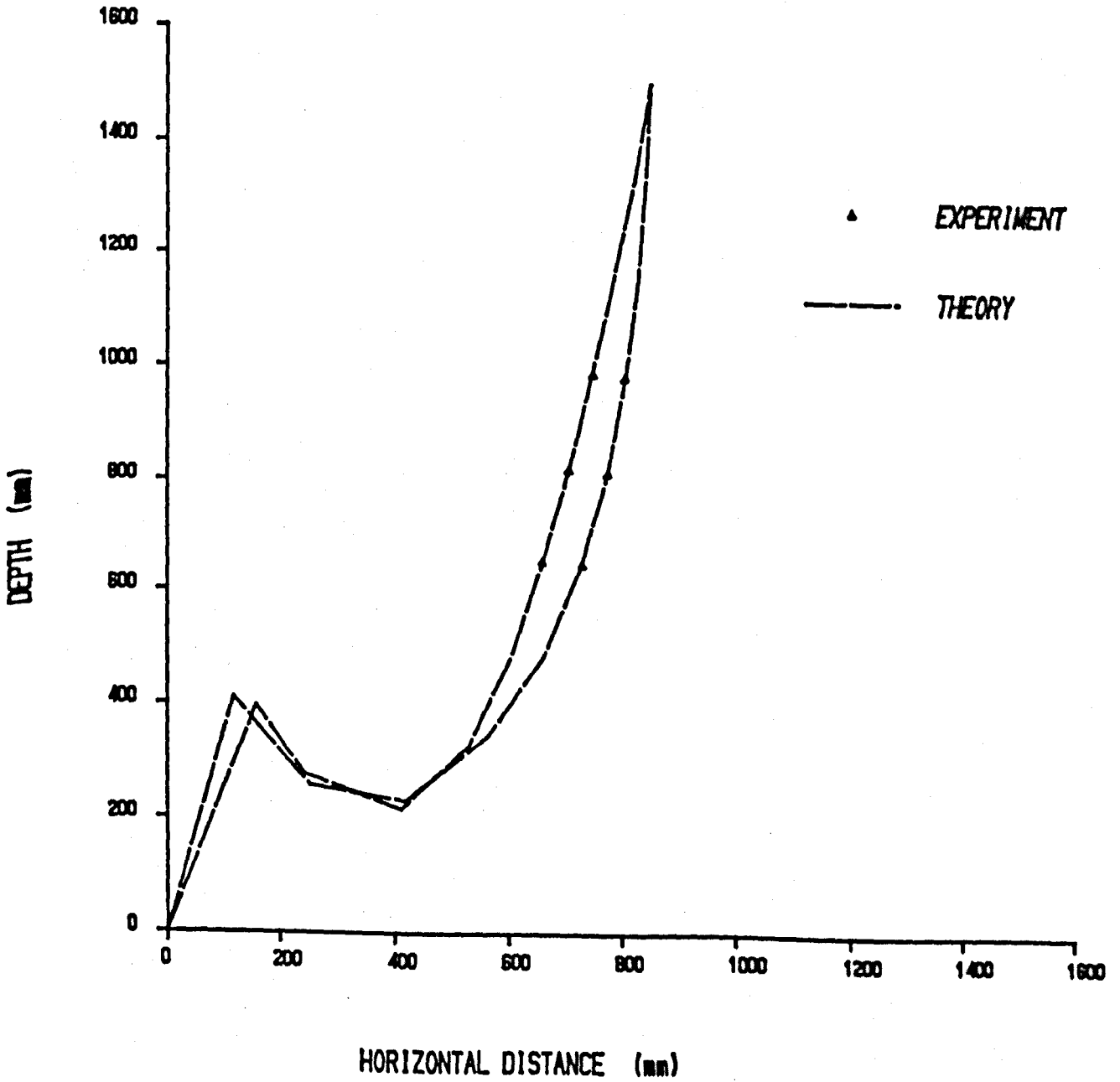


Figure 8.28 - Computed and measured envelopes for the dynamic response of the tube model at  $0^\circ$  to the wave direction

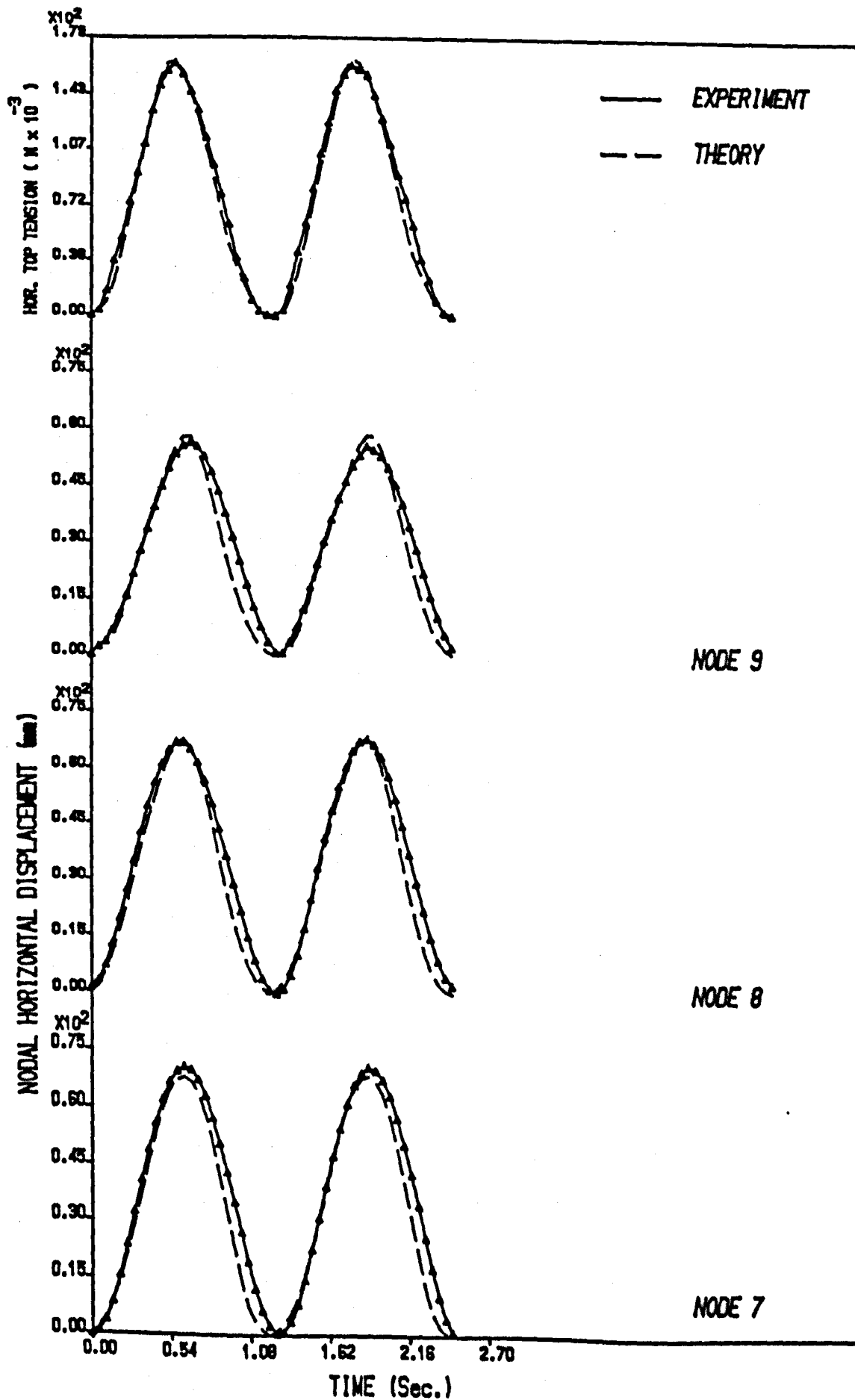


Figure 8.29 - Comparison of the computed and measured top tension and nodal displacements along the tube model at 0° to the wave direction

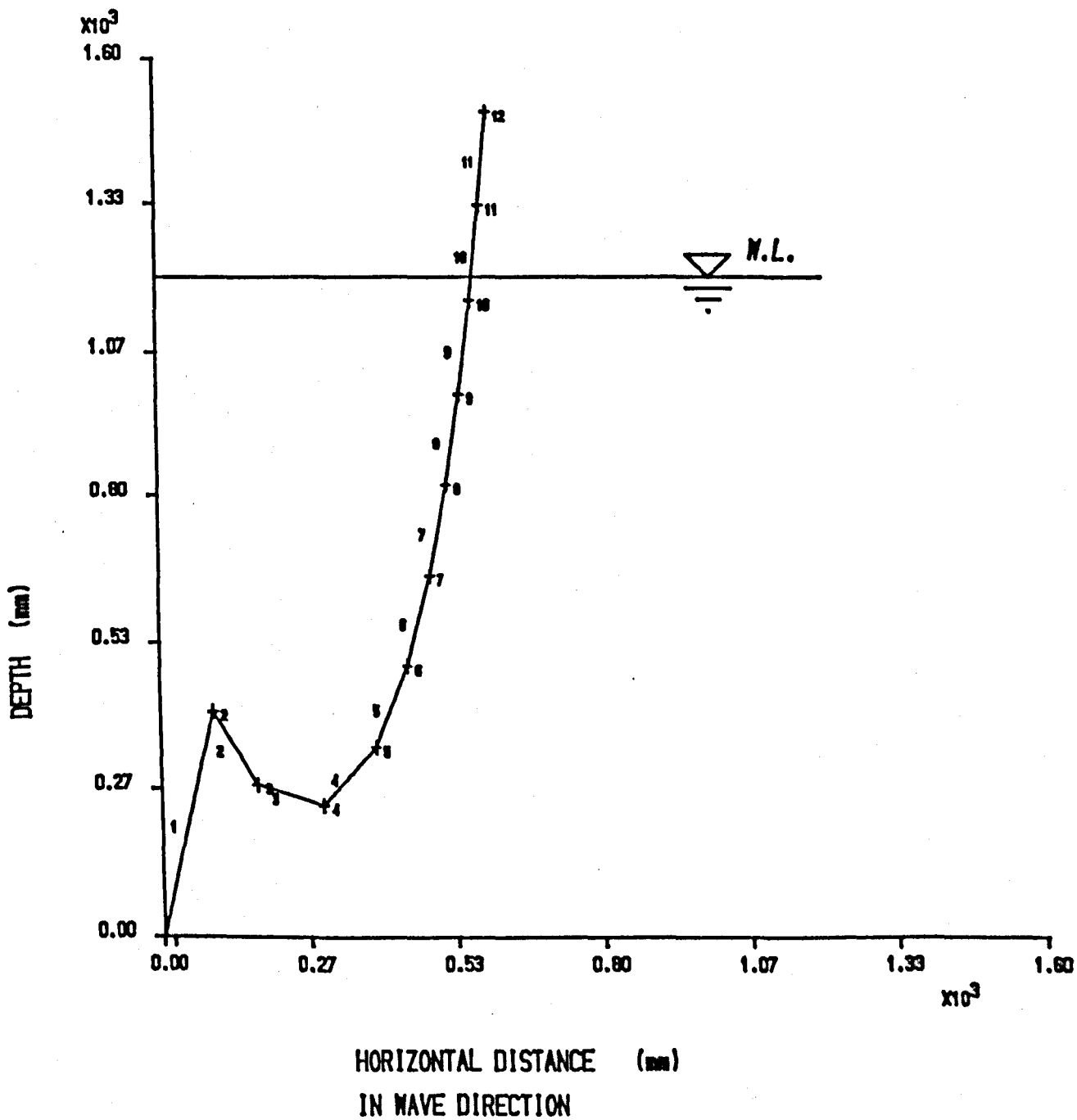


Figure 8.30 - Computed static equilibrium shape of the tube model at 45° to the wave direction

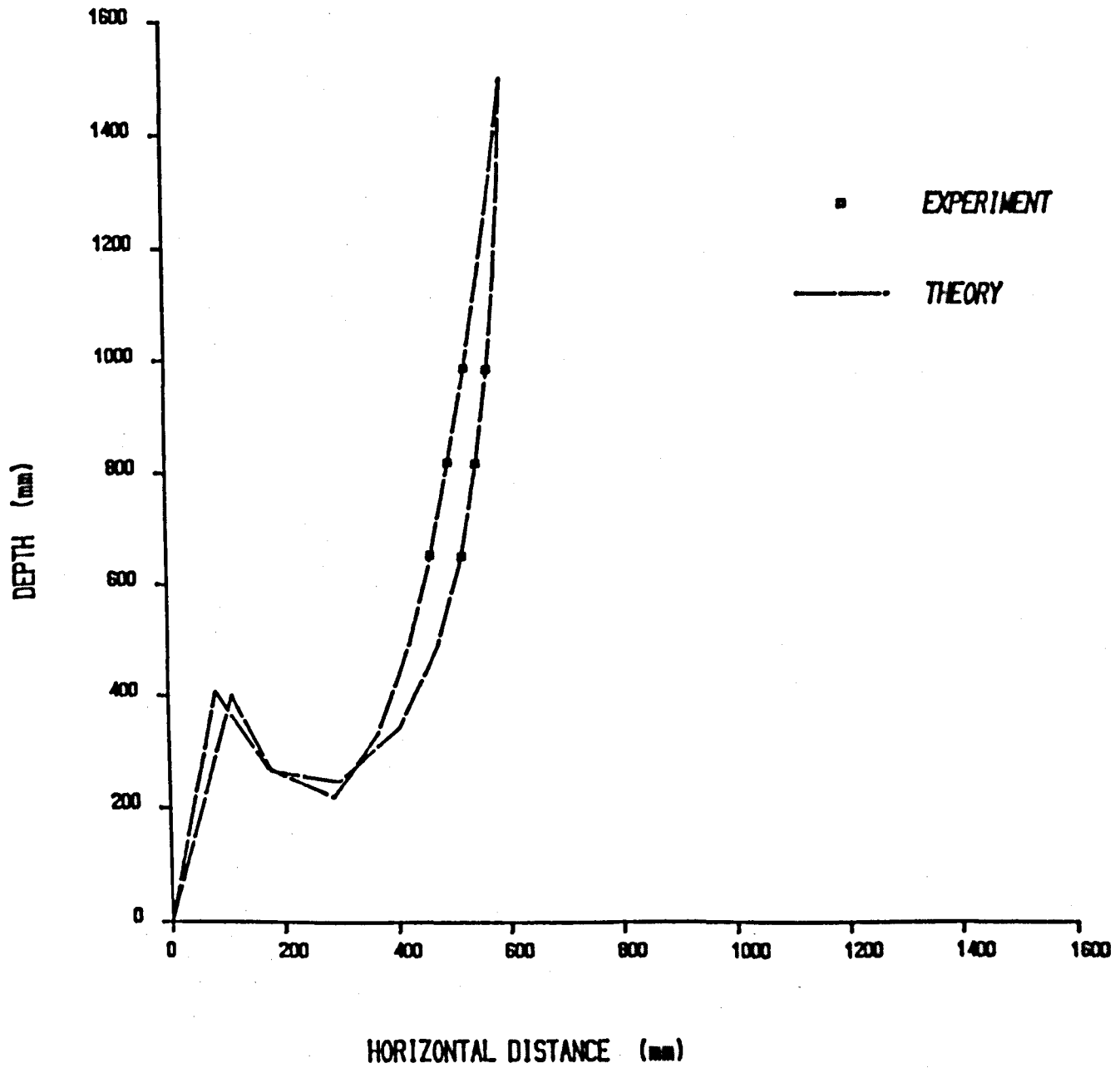


Figure 8.31 - Computed and measured envelopes in the wave direction for the dynamic response of the tube model at  $45^\circ$  to the wave direction

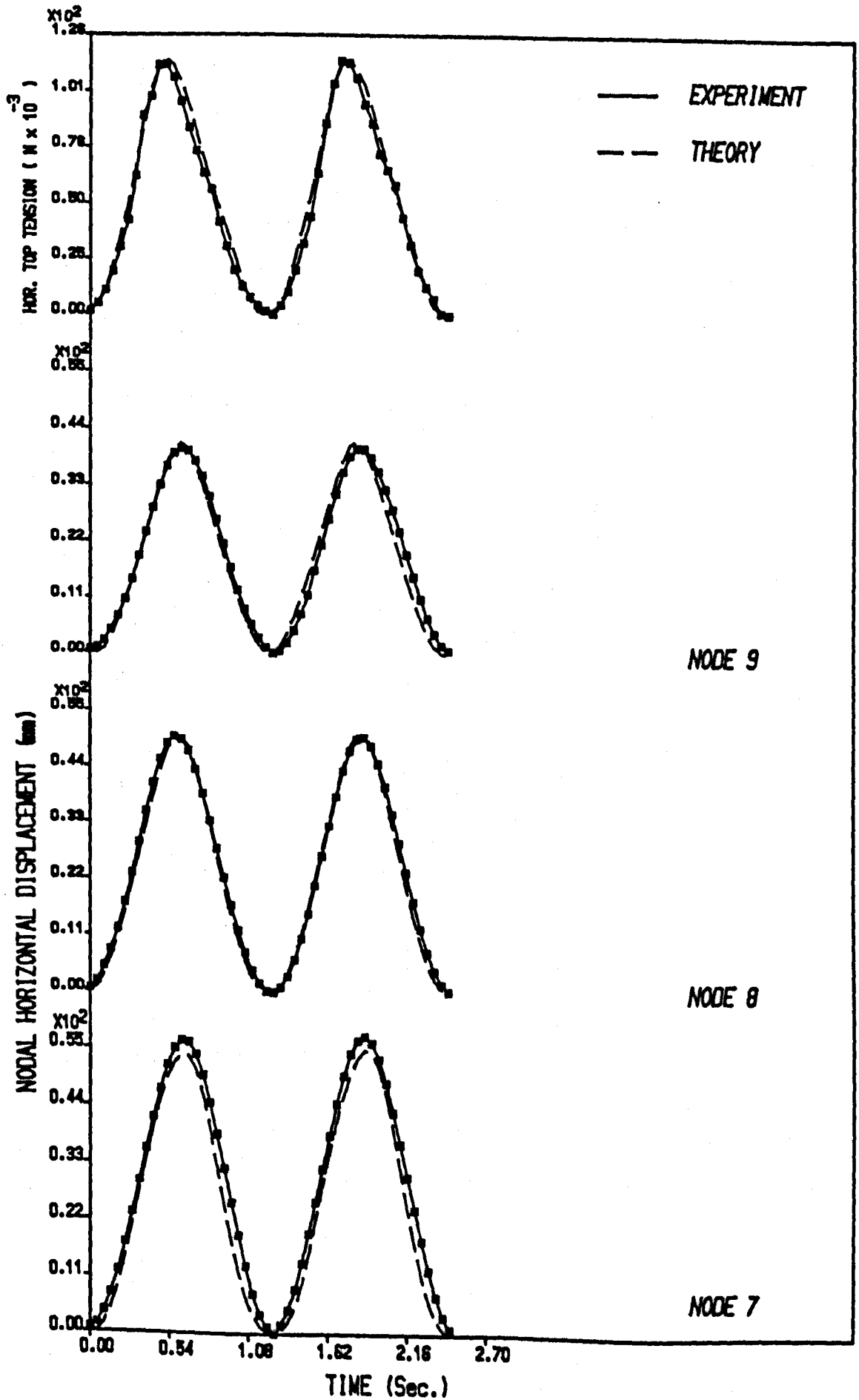


Figure 8.32 - comparison of the computed and measured horizontal top tension and nodal displacements in the wave direction along the tube model at 45° to the wave direction

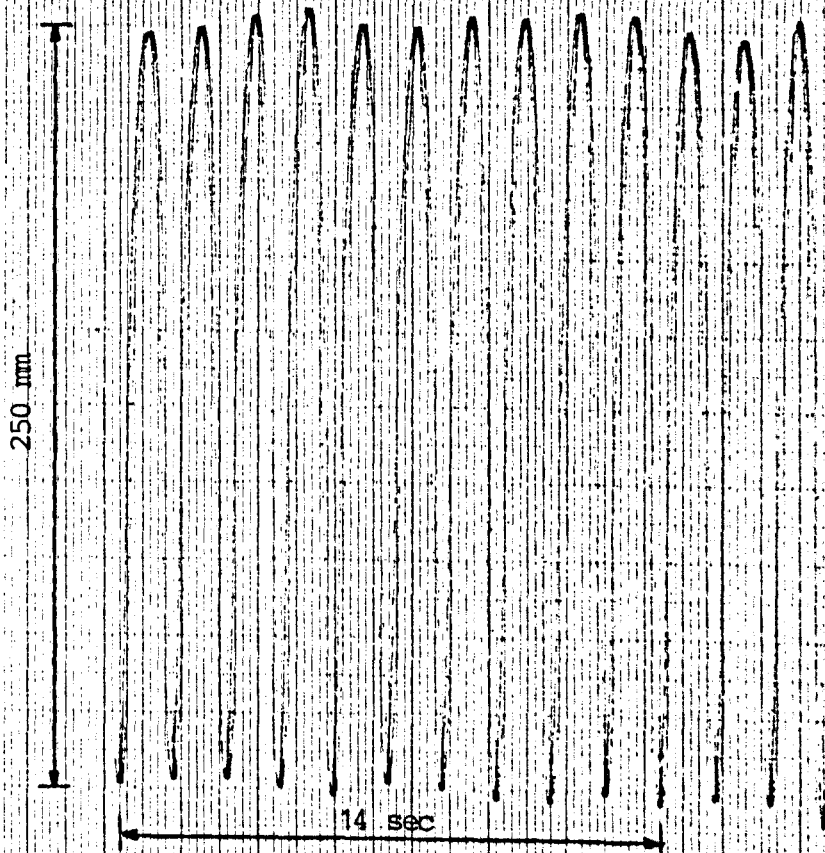


Figure 8.33a - Height and period of the large wave generated in the large wave flume (from X-Y plotter)

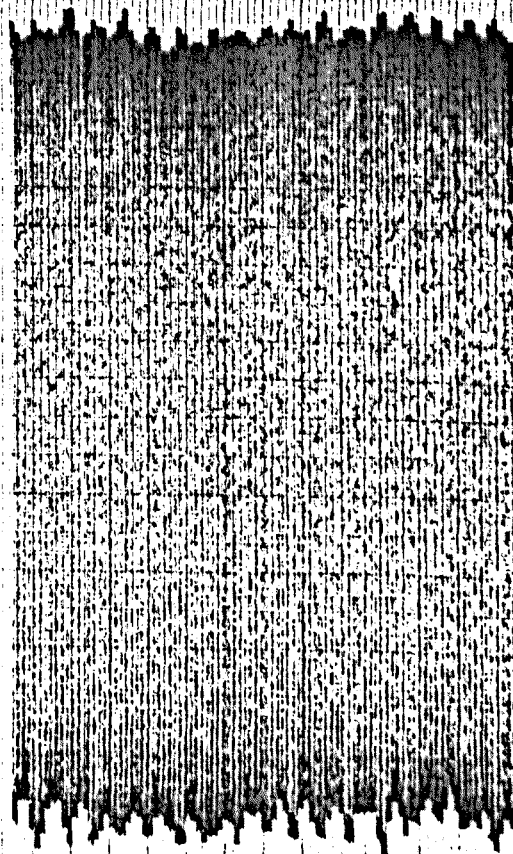


Figure 8.33b - The wave train of the large wave generated in the large wave flume

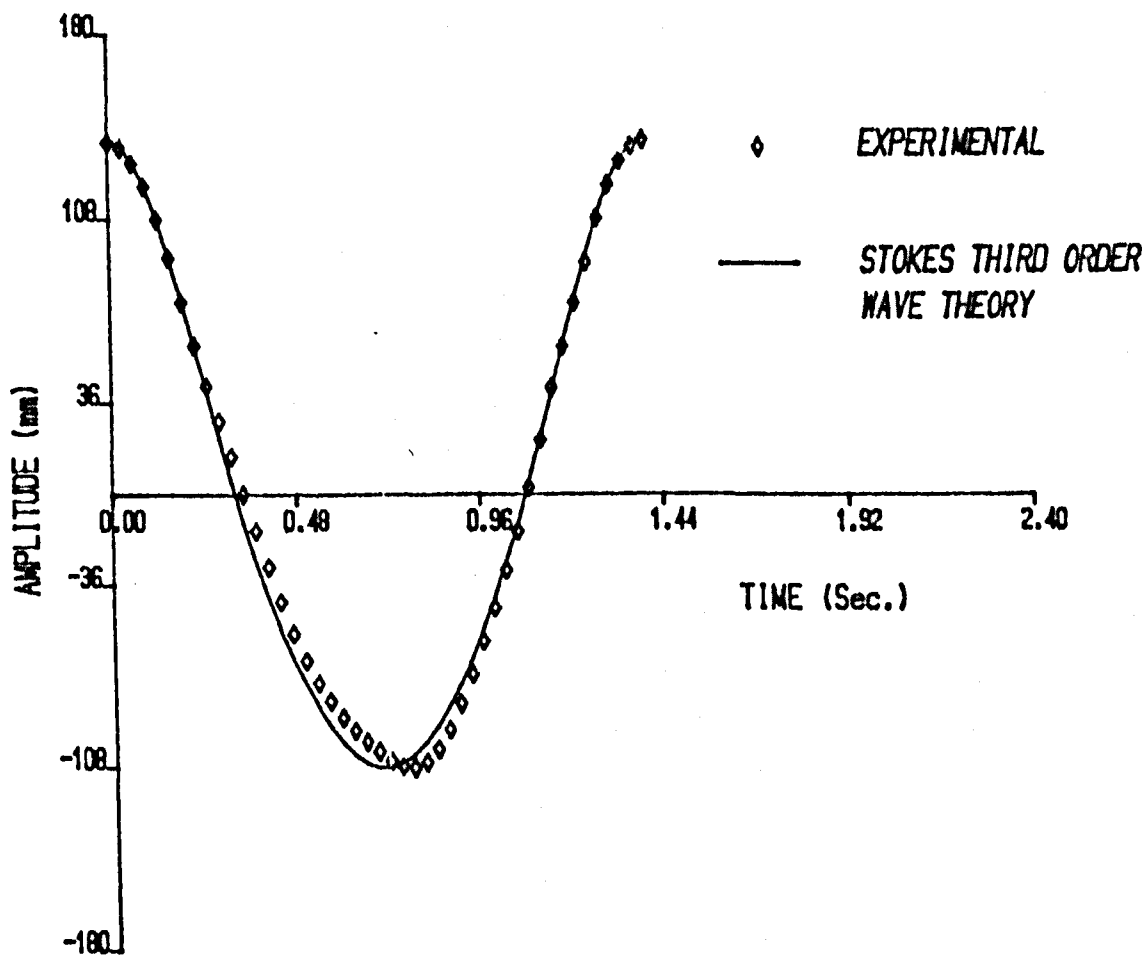


Figure 8.34 - Comparison of the computed and digitized wave profile for the large wave generated in the large wave flume

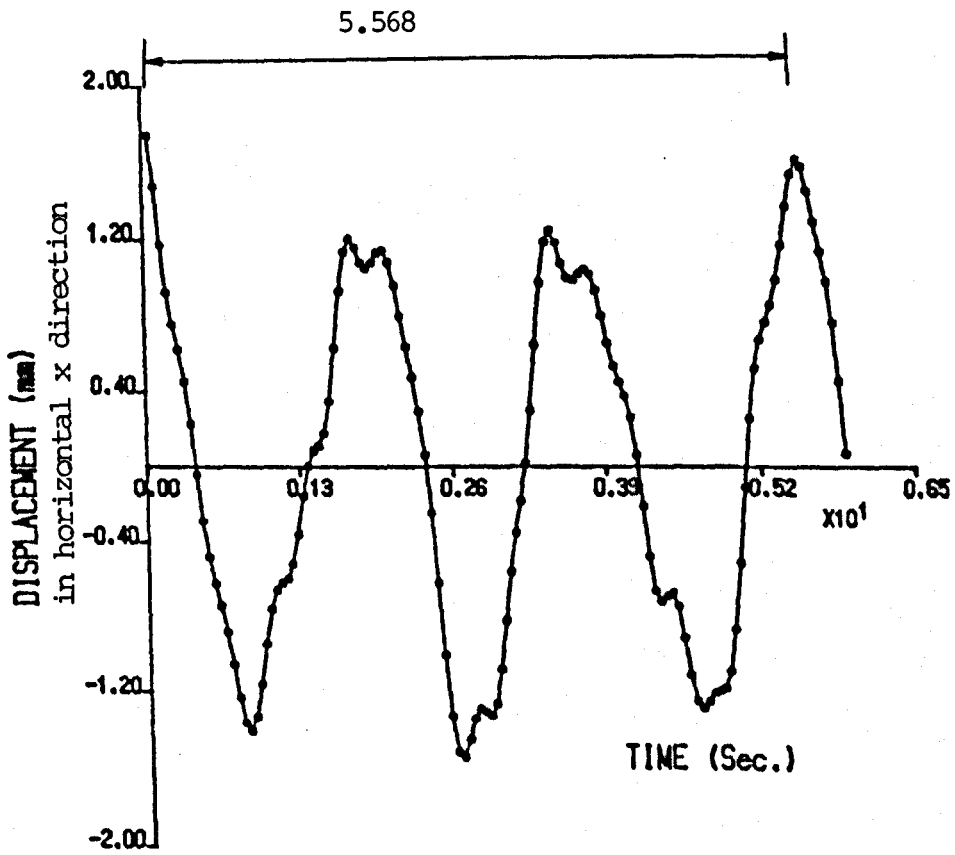


Figure 8.35 - Time history of the nodal displacements of node 7 induced by "poking"

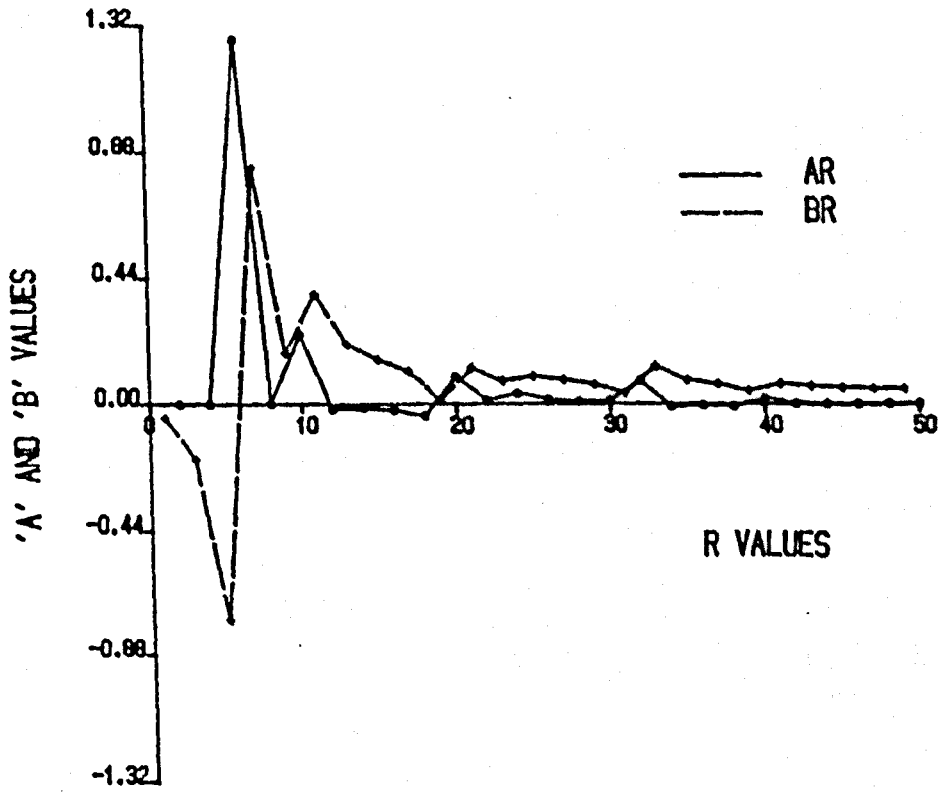


Figure 8.36 - Values of coefficients A and B against r for the tube model

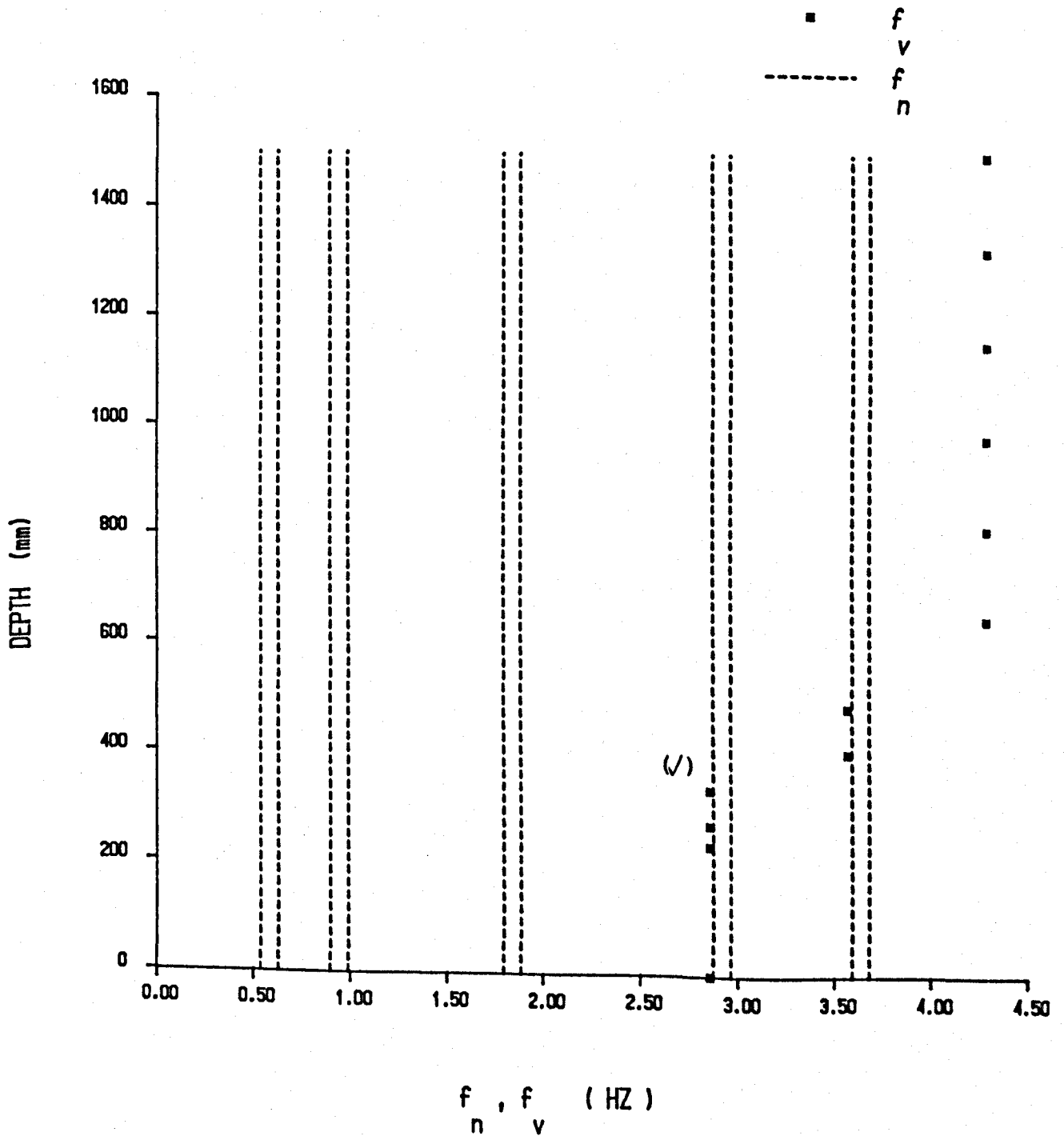


Figure 8.37 - Determination of the dominant vortex-shedding frequency and corresponding structural natural frequency for the tube model (these are marked by (✓))

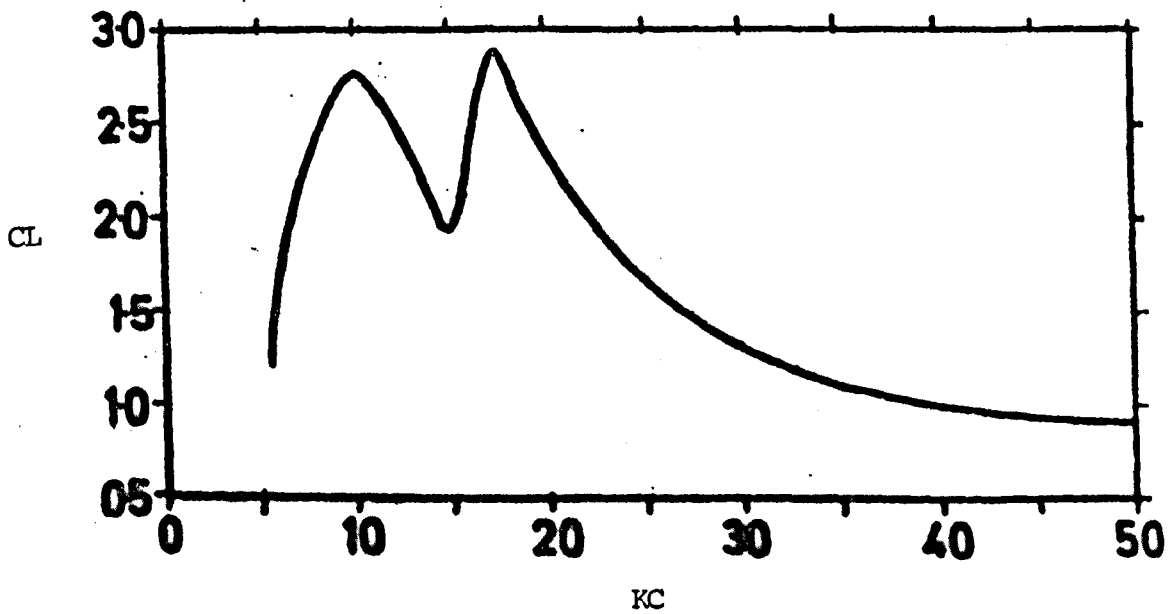


Figure 8.38 - Lift coefficient ( $CL_o$ ) against Keulegan-Carpenter number (KC) in subcritical Reynolds number region for a rigid cylinder (after Sarpakaya et. al. (1974))

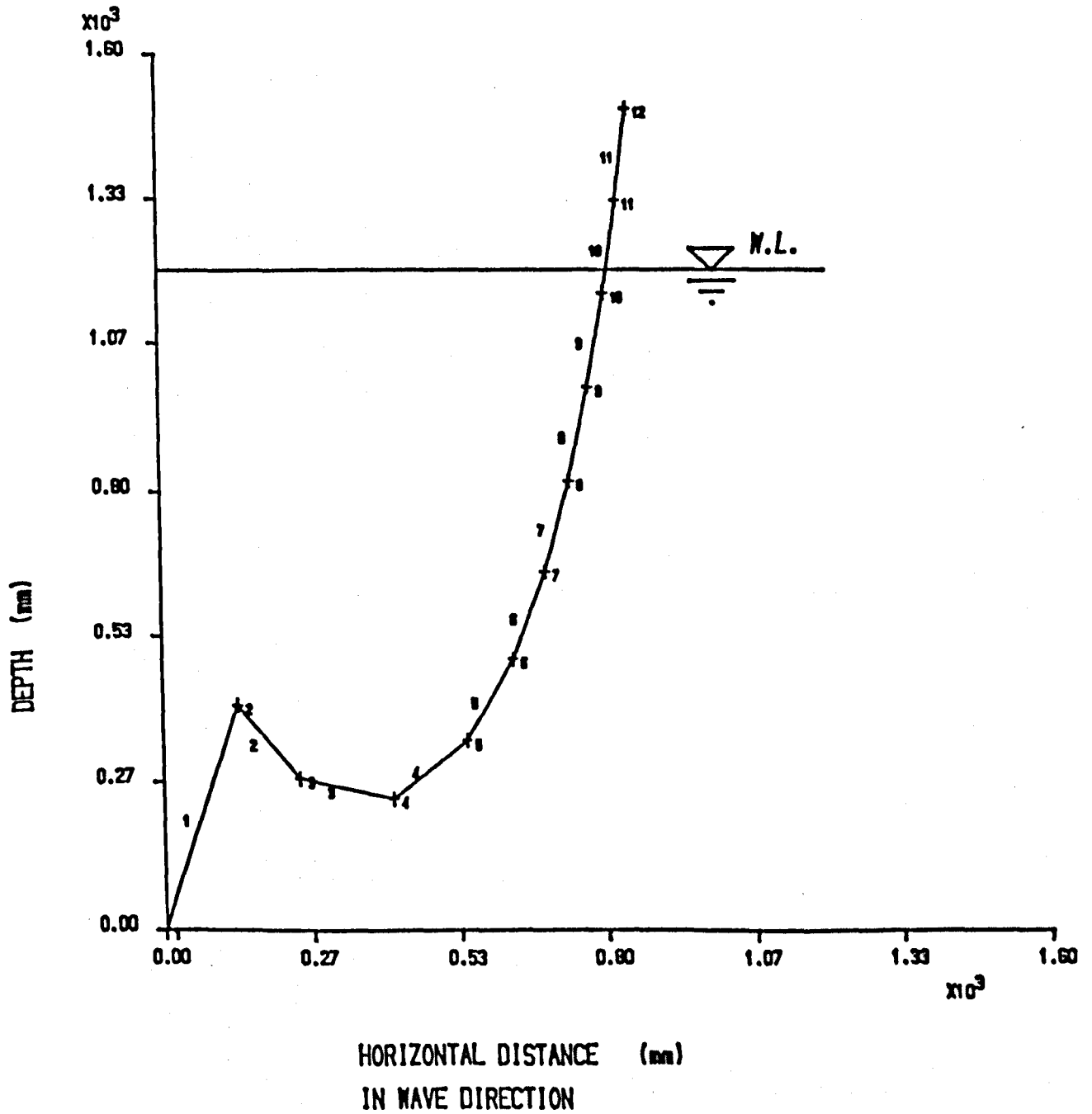


Figure 8.39 - Computed static equilibrium shape of the tube model at  $0^\circ$  to the wave direction

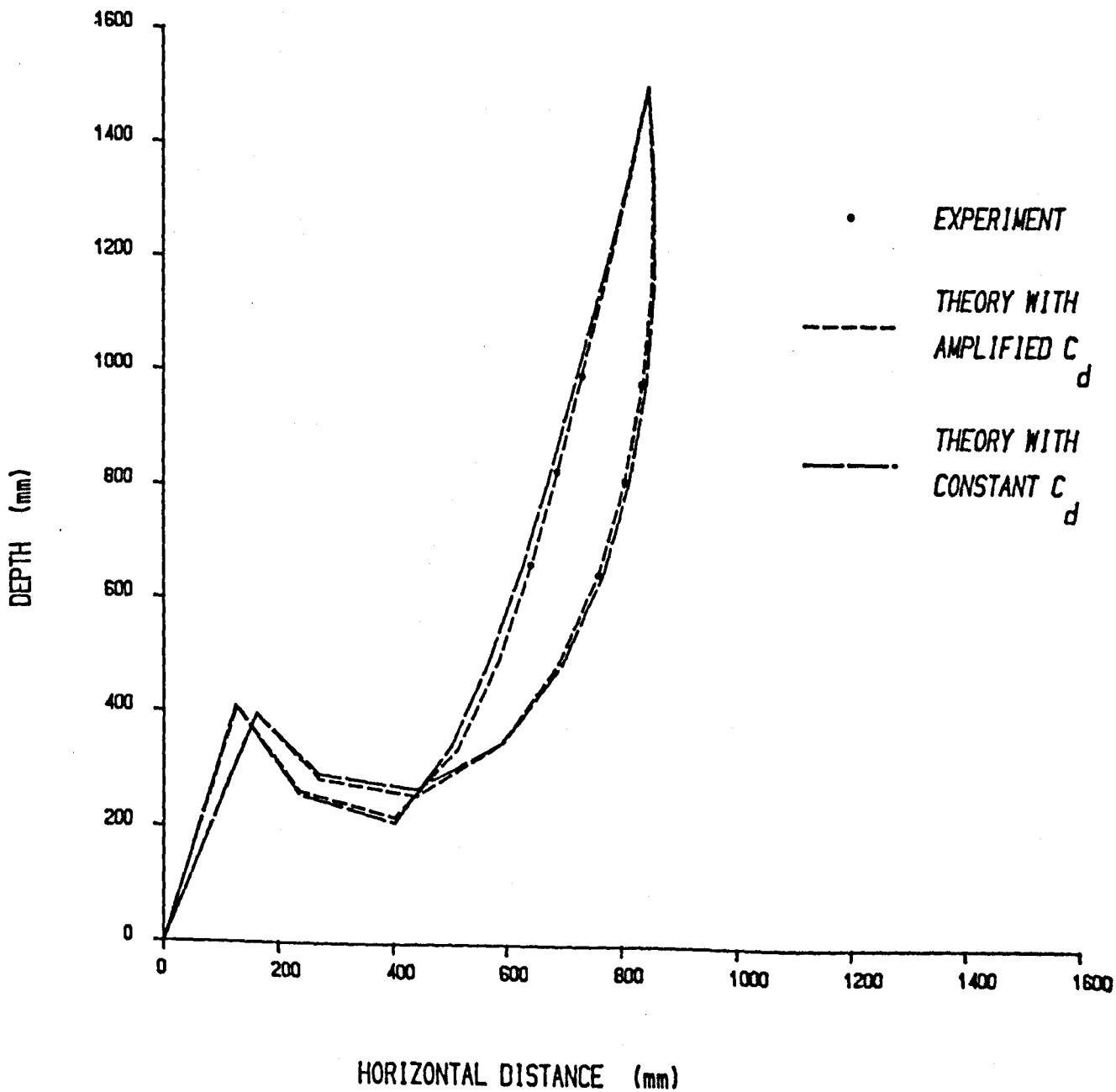


Figure 8.40 - Comparison of the measured and computed envelopes of the dynamic response of the tube model (with and without account of the effects of vortex-shedding)

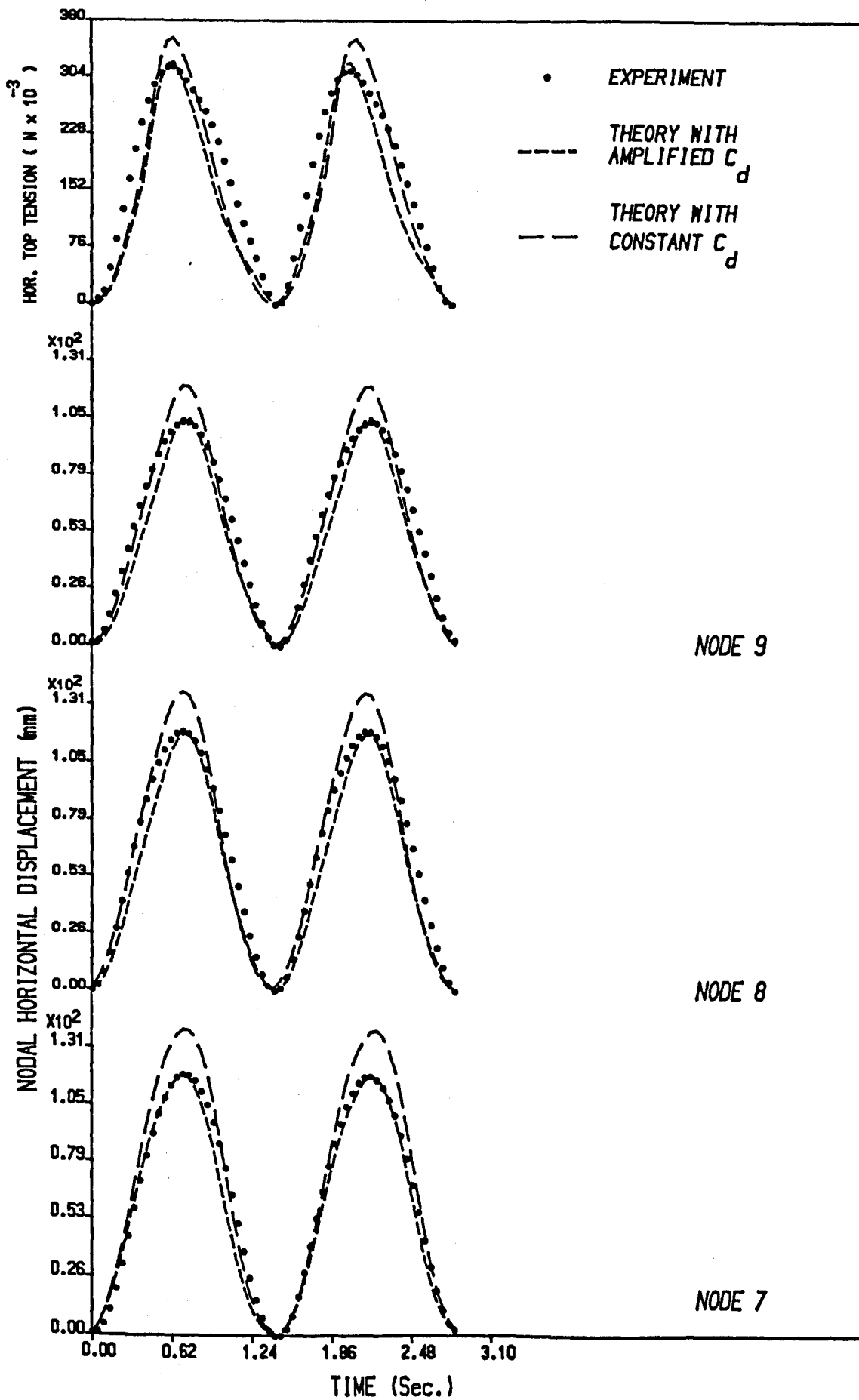


Figure 8.41 - Comparison of the measured and computed horizontal top tension and nodal displacements along the tube model (with and without account of the effects of vortex shedding)

## CHAPTER 9

### NUMERICAL VALIDATION

#### 9.1 - Introduction

This chapter is concerned with a comparison of the numerically predicted results using the programs developed in the present work (termed FLEXSTATIC, FLEXCURRENT and FLEXDYNAMIC) with those obtained from the well known general purpose program "FLEXRISER".

Program FLEXRISER is a 3-dimensional flexible riser program which has been developed by Zentech Consultants of London in conjunction with Professor Larsen of the Royal Institute of Technology in Stockholm. FLEXRISER has undergone comparative checks with well known Finite Element Packages such as ABAQUS and FENRIS. The analysis and the numerical Solution Scheme which are used by FLEXRISER to predict the behaviour of a flexible riser are completely different from those used by the programs developed in this thesis. FLEXRISER uses a solution scheme which is analogous to the system describing the hydrodynamics of an open channel flow and the equation of motion is solved using an implicit numerical scheme.

The chapter includes comparisons for the static equilibrium configurations with and without current loadings, and the dynamic behaviour induced by wave and current loadings and platform motions for various flexible risers. The number of elements used to model the riser were the same for program FLEXRISER and the three programs developed in the present work for each test case. Most of the test cases used in this chapter were data corresponding to real cases. The input for these data are given

in Appendix E.

The static comparisons without current loadings include the following test cases:

- a) Free hanging risers - this type of riser is further divided into the following two configurations:
  - 1) Single hanging riser - a riser which is attached to the platform at the top and to the sea bed manifold at the sea bed, figure 9.1.
  - 2) Double hanging riser - a riser which forms a U shape and connects two platforms, figure 9.2.
- b) Single catenary risers - these risers are divided into the following two configurations with respect to the type of sub-surface sub-buoys employed:
  - 1) Steep-S risers - in this type of riser the buoyancy at the sub-surface is supplied by a discrete sub-buoy, figure 9.3.
  - 2) Steep wave risers - in this type the buoyancy is supplied by employing buoyant collars which are installed along a certain length of a riser with constant or varying gaps between them, figure 9.4.
- c) Double catenary risers - this type of riser, like single catenary risers, is divided into two configurations in respect of their sub-surface buoyancy systems as follows:
  - 1) A Lazy-S riser - which has a discrete sub-buoy, figure 9.5.
  - 2) A Lazy wave riser - which has a collar buoyancy system, figure 9.6.

The static comparisons with current loadings, and the dynamic comparisons, include the following test cases:

- a) Double hanging riser which is referred to in the text as the simple catenary riser.
- b) Steep-S riser.

All the comparisons are presented in graphical form. The results predicted by program FLEXRISER are plotted as full lines and those predicted by the programs which have been developed in the present work are plotted as dotted lines.

## 9.2 - Static Test Cases without Current Loadings

Figures 9.1 to 9.6 show the comparison of the static configurations for flexible risers with no current loadings predicted by programs FLEXRISER and FLEXSTATIC. The comparisons are in close agreement. The sequence of the figure numberings for the test cases are as follows:

- Figure 9.1 Single hanging riser
- Figure 9.2 Double hanging riser
- Figure 9.3 Steep-S riser
- Figure 9.4 Steep wave riser
- Figure 9.5 Lazy-S riser
- Figure 9.6 Lazy wave riser

Program FLEXSTATIC had to be modified to take account of sea bed reaction forces when the riser was lying on the sea bed. This was done by setting the negative vertical velocities and vertical co-ordinates of the nodes on the sea bed to zero. The same modifications were made for both FLEXDYNAMIC and FLEXCURRENT programs.

### 9.3 - Static Test Cases with Current Loadings

Figures 9.7 and 9.8 show respectively the comparison of the static equilibrium shapes for a double hanging riser and a Steep-S riser, subjected to current loadings, predicted by programs FLEXRISER and FLEXCURRENT. The comparisons are in close agreement.

### 9.4 - Dynamic Test Cases

The comparison of the dynamic behaviour for the test cases was carried out by computing the riser response for 6 wave cycles by programs FLEXRISER and FLEXDYNAMIC and comparing the snap shots of the riser response (i.e. frozen riser response with respect to time) at the 6th wave cycle. Four snap shots corresponding to times  $5T$ ,  $5T + T/4$ ,  $5T + T/2$ , and  $5T + 3T/4$  (where  $T$  is the wave period) are considered for the comparisons. In all the test cases the hydrodynamic loadings included both wave and current induced loadings.

The Steep-S riser for which the static configuration was computed in section 9.2, figure 9.3, was considered as the test case to carry out the dynamic comparisons. The comparisons were carried out in four steps. First the catenary part of the riser was considered as a double hanging riser (it is referred to in the text as the simple catenary riser). The dynamic response of this riser section due to hydrodynamic loadings with and without platform motion were then compared. The whole Steep-S riser was subsequently considered. Again first the riser response with hydrodynamic loading and no platform motion and then with platform motion was computed and compared. All comparisons show

close agreement. The sequence for the figure numbering is as follows:

Figure 9.9 Snap shots of simple catenary riser with no platform motion

Figure 9.10 Snap shots of simple catenary riser with platform motion

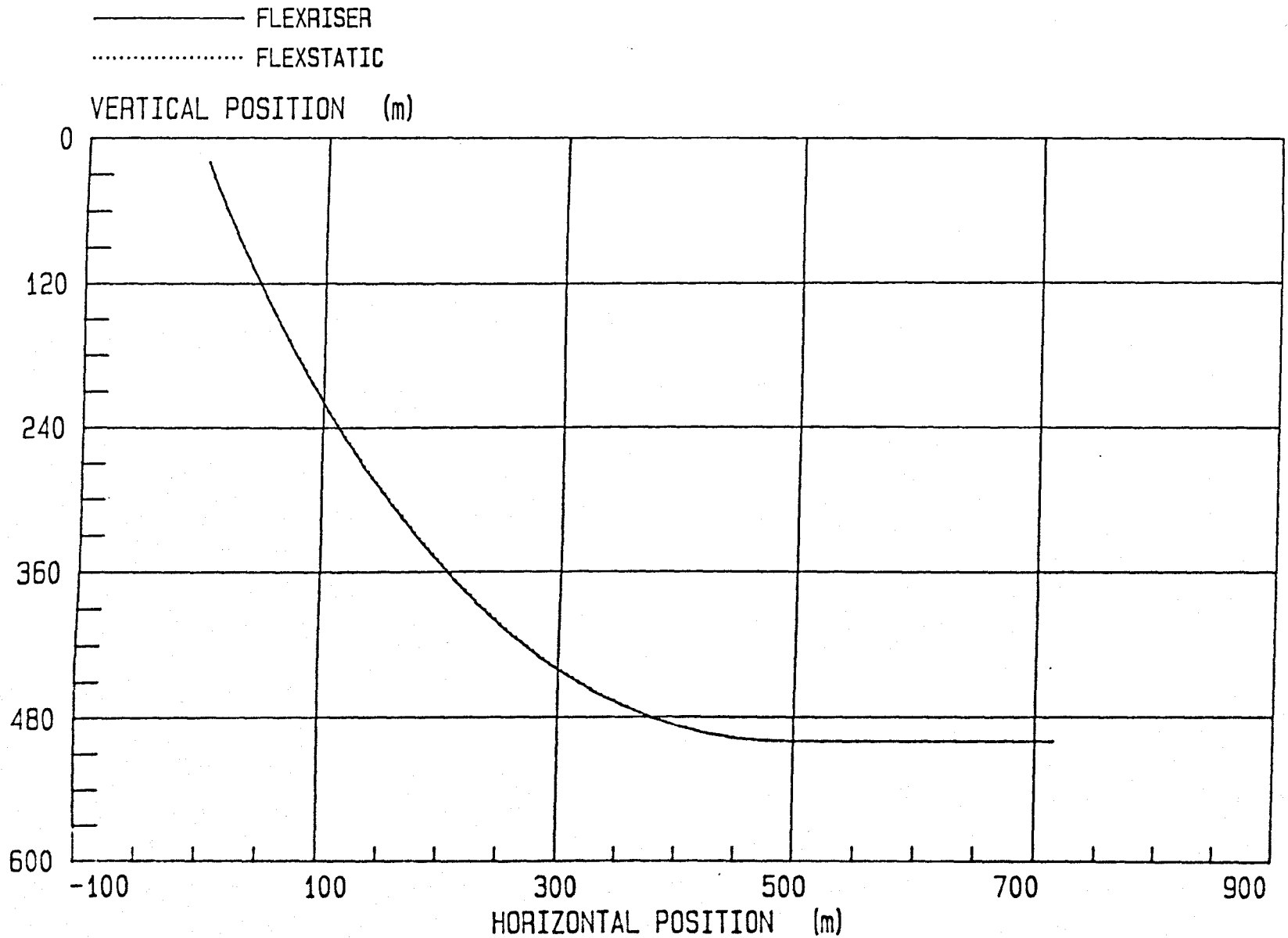
Figure 9.11 Snap shots of steep-S riser with no platform motion

Figure 9.12 Snap shots of steep-S riser with platform motion

# FREE HANGING FLEXIBLE-RISER COMPARISON OF STATIC CONFIGURATION



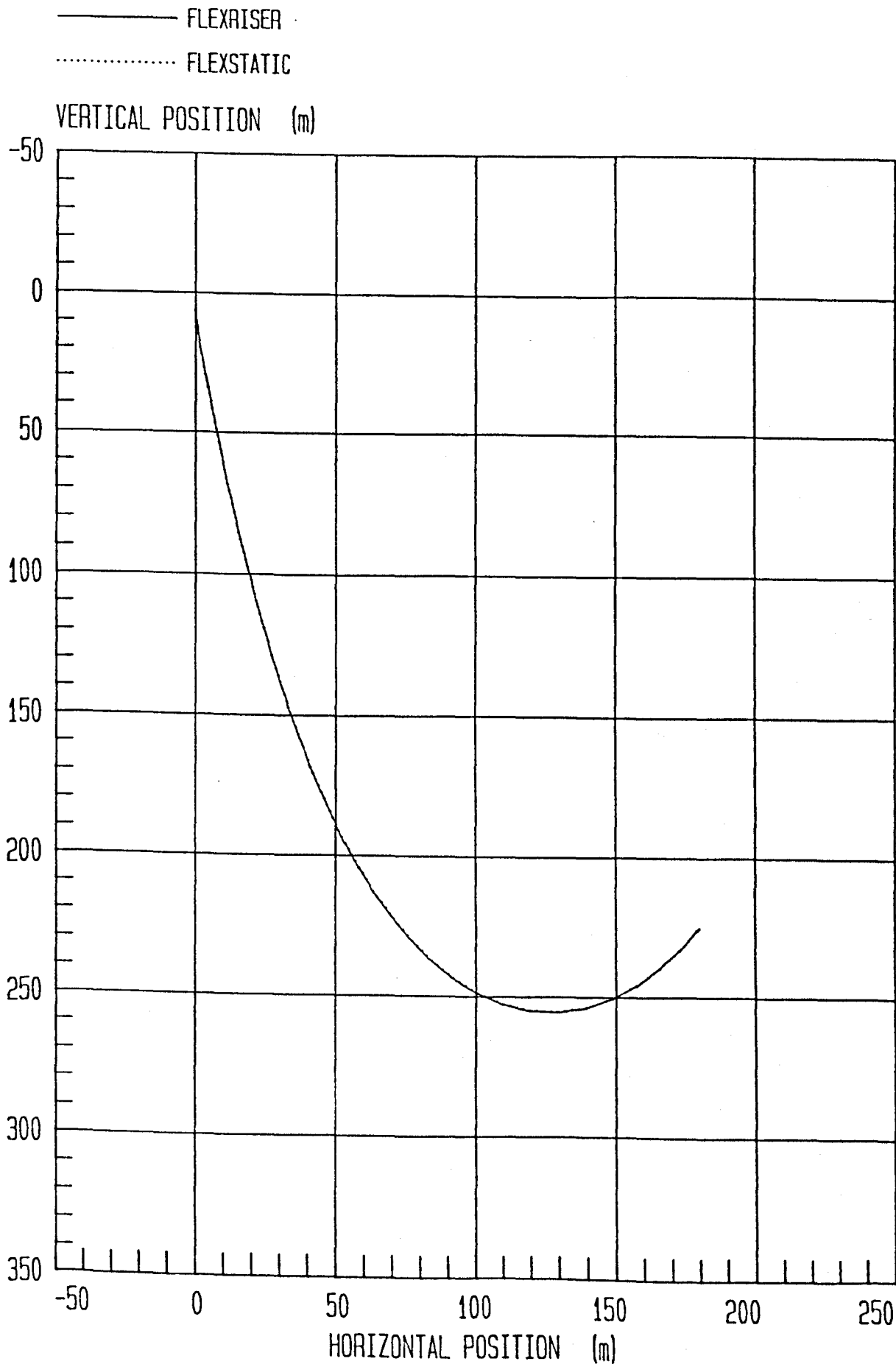
FIG. 9.1



# FREE HANGING FLEXIBLE-RISER COMPARISON OF STATIC CONFIGURATION



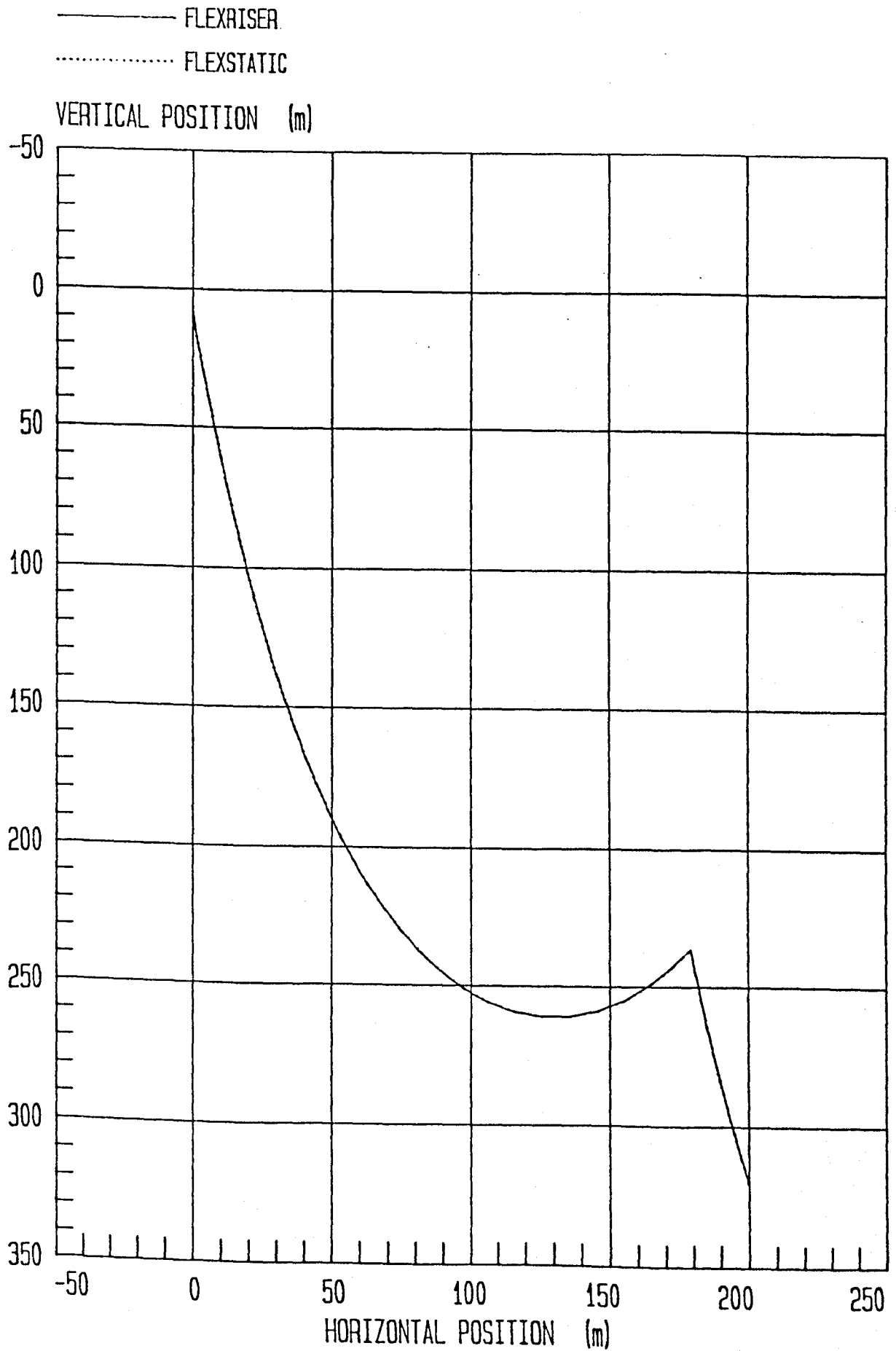
FIG. 9.2



# STEEP S FLEXIBLE-RISER COMPARISON OF STATIC CONFIGURATION



FIG. 9.3



# STEEP WAVE FLEXIBLE-RISER COMPARISON OF STATIC CONFIGURATION

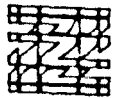
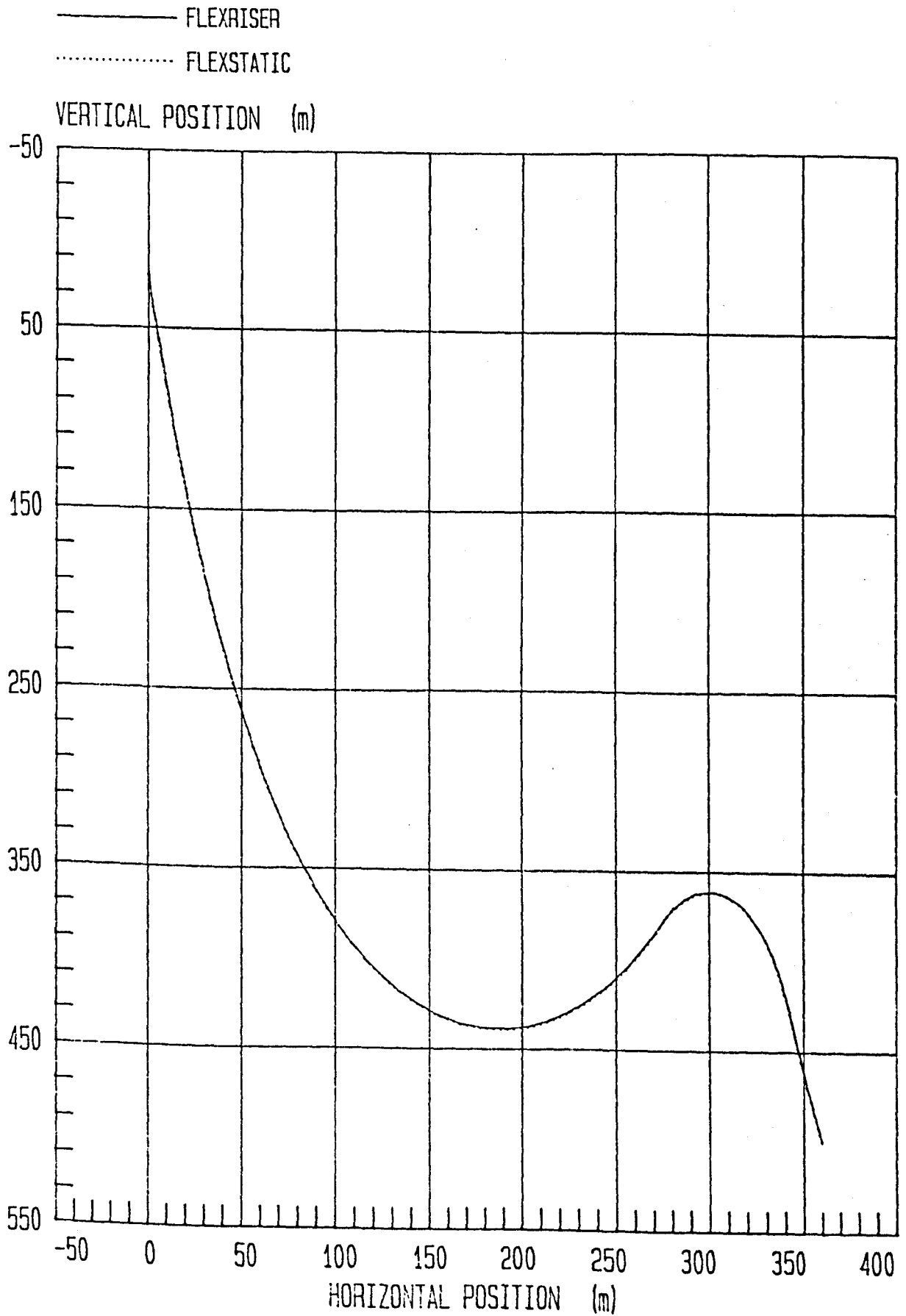


FIG. 9.4

ZENTECH  
CONSULTANTS

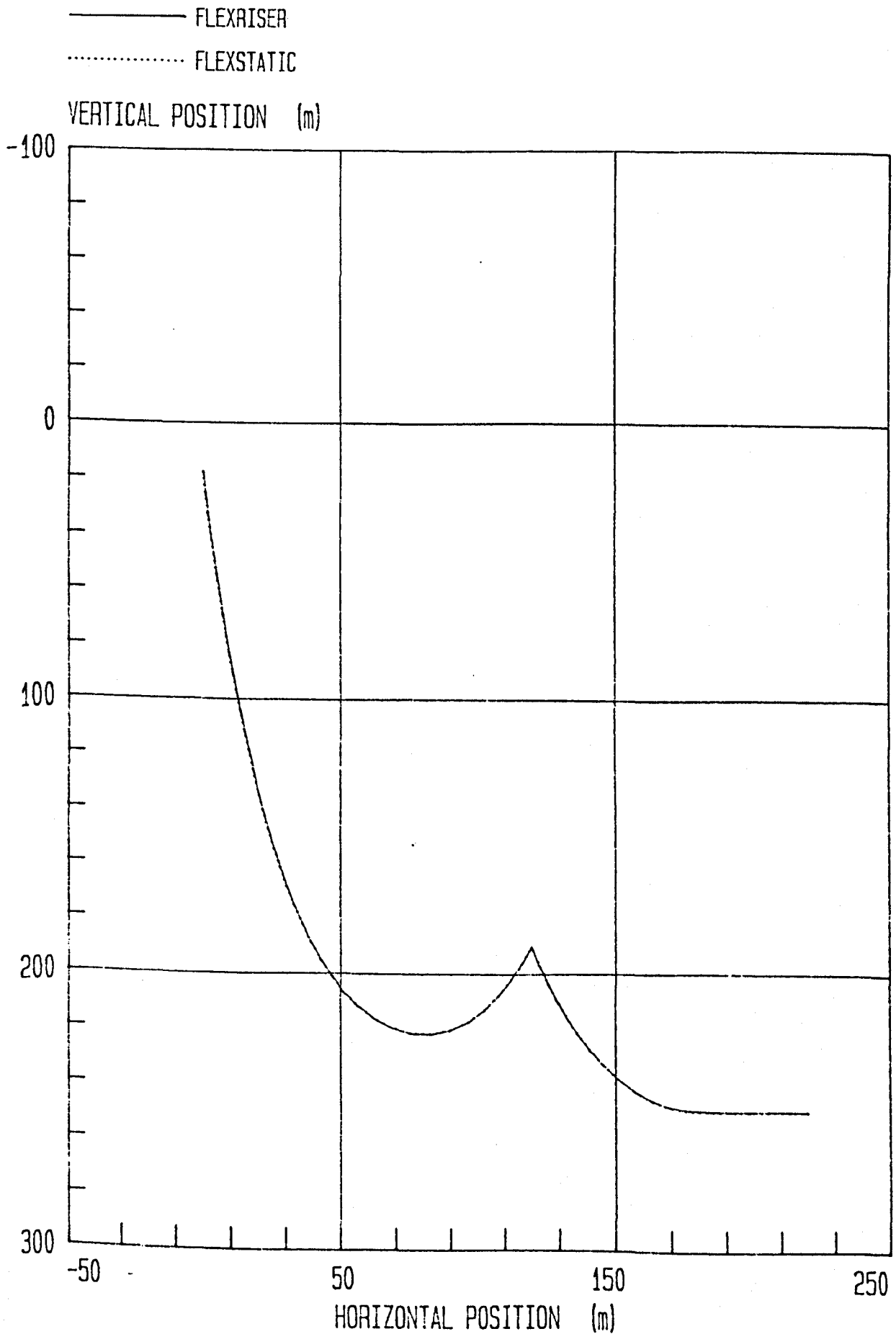


# LAZY S FLEXIBLE-RISER

COMPARISON OF STATIC CONFIGURATION



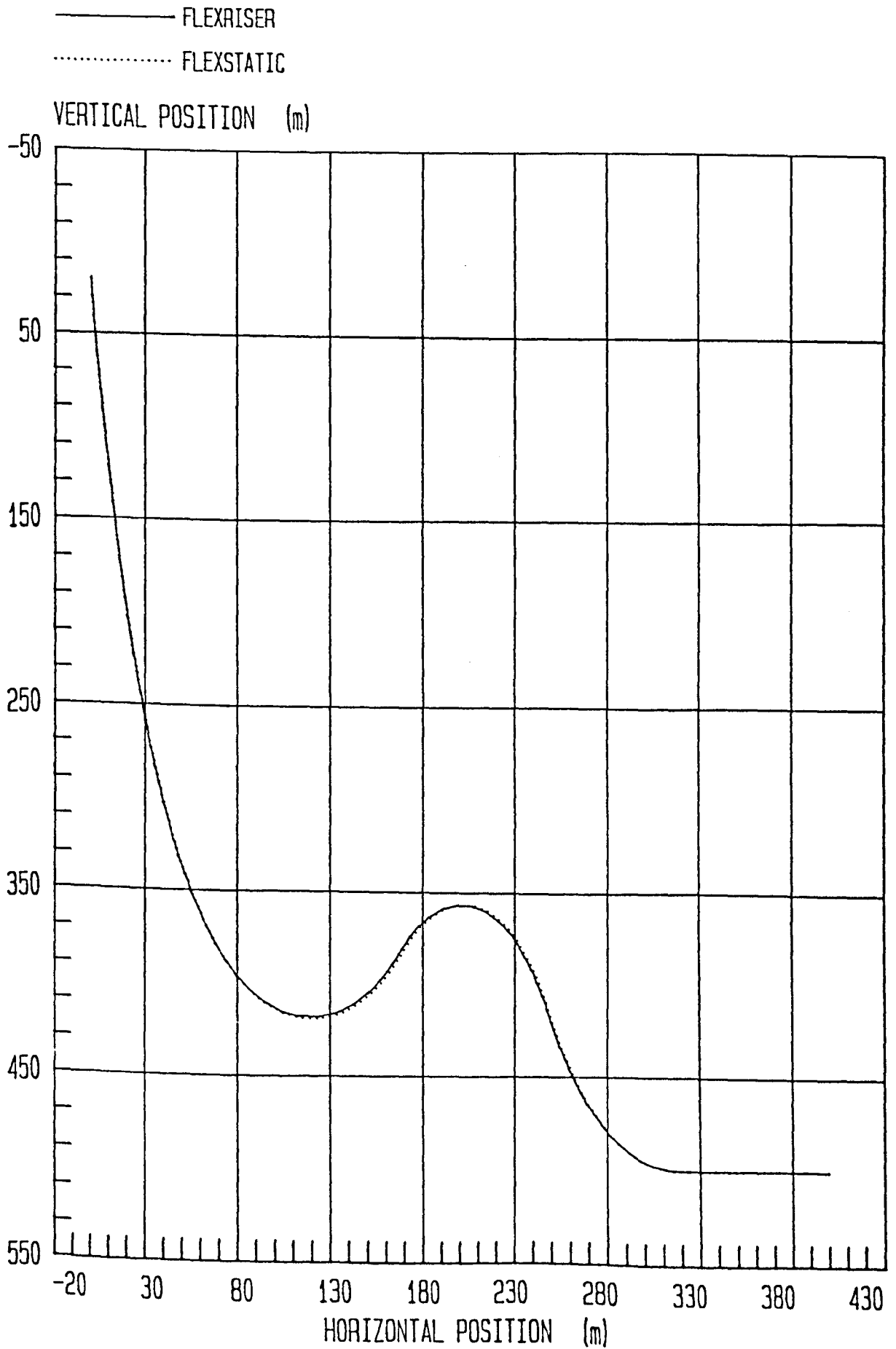
FIG. 9.5



# LAZY WAVE FLEXIBLE-RISER COMPARISON OF STATIC CONFIGURATION



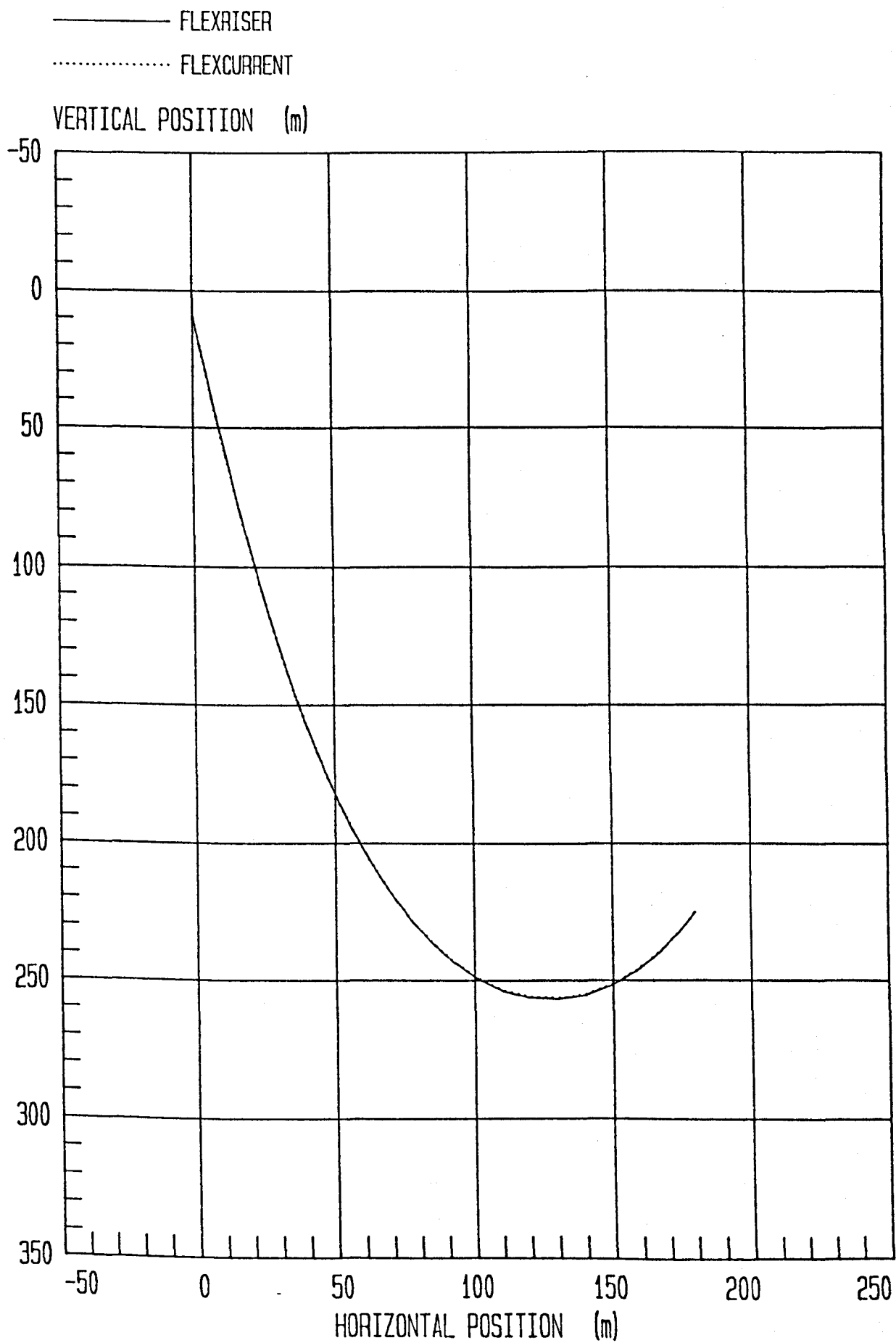
FIG. 9.6 ZENTECH CONSULTANTS



# SIMPLE CATENARY FLEXIBLE RISER COMPARISON OF STATIC CONFIGURATION WITH CURRENT



FIG. 9.7

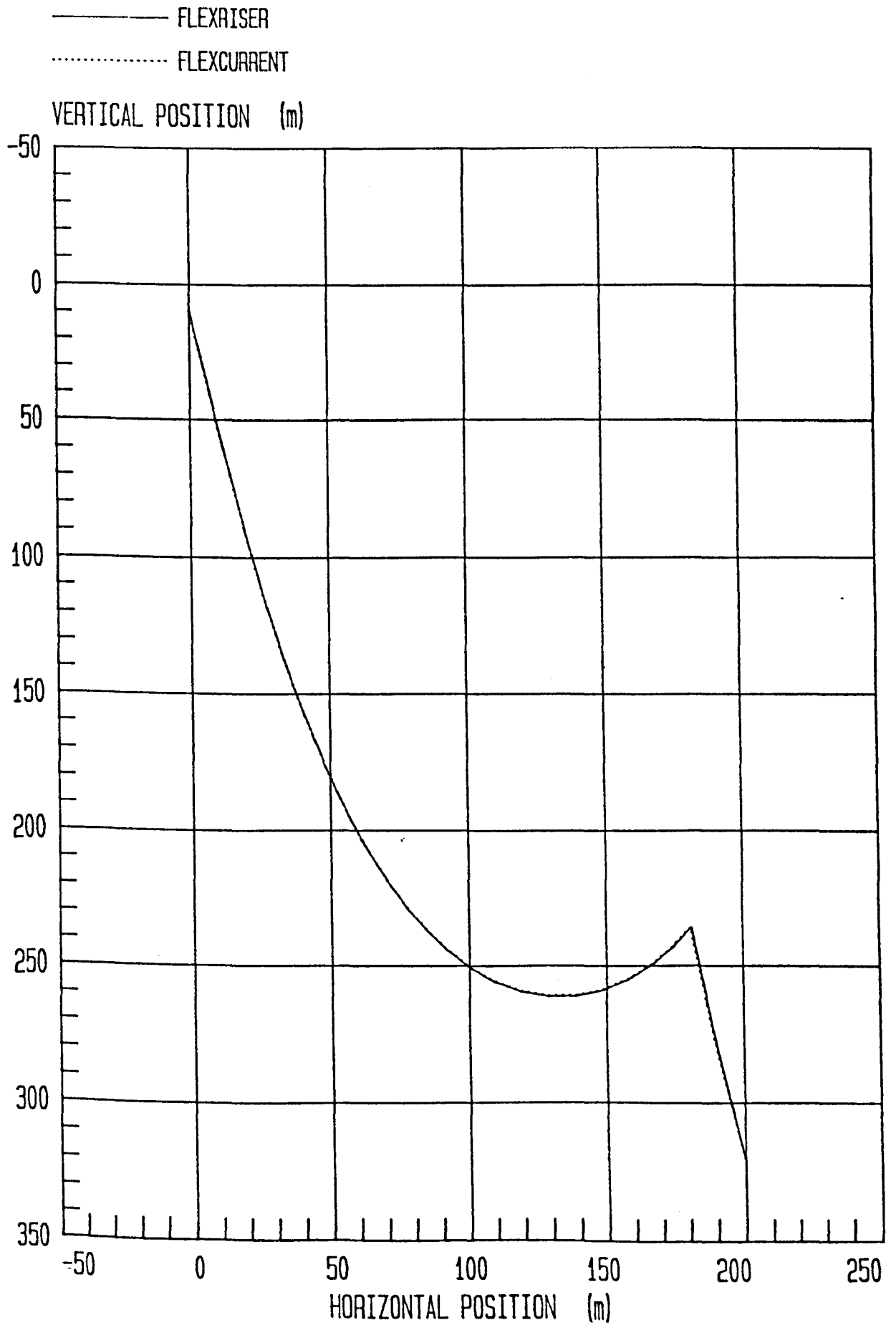


# STEEP S FLEXIBLE-RISER

COMPARISON OF STATIC CONFIGURATION WITH CURRENT



FIG. 9.8



# SIMPLE CATENARY FLEXIBLE RISER

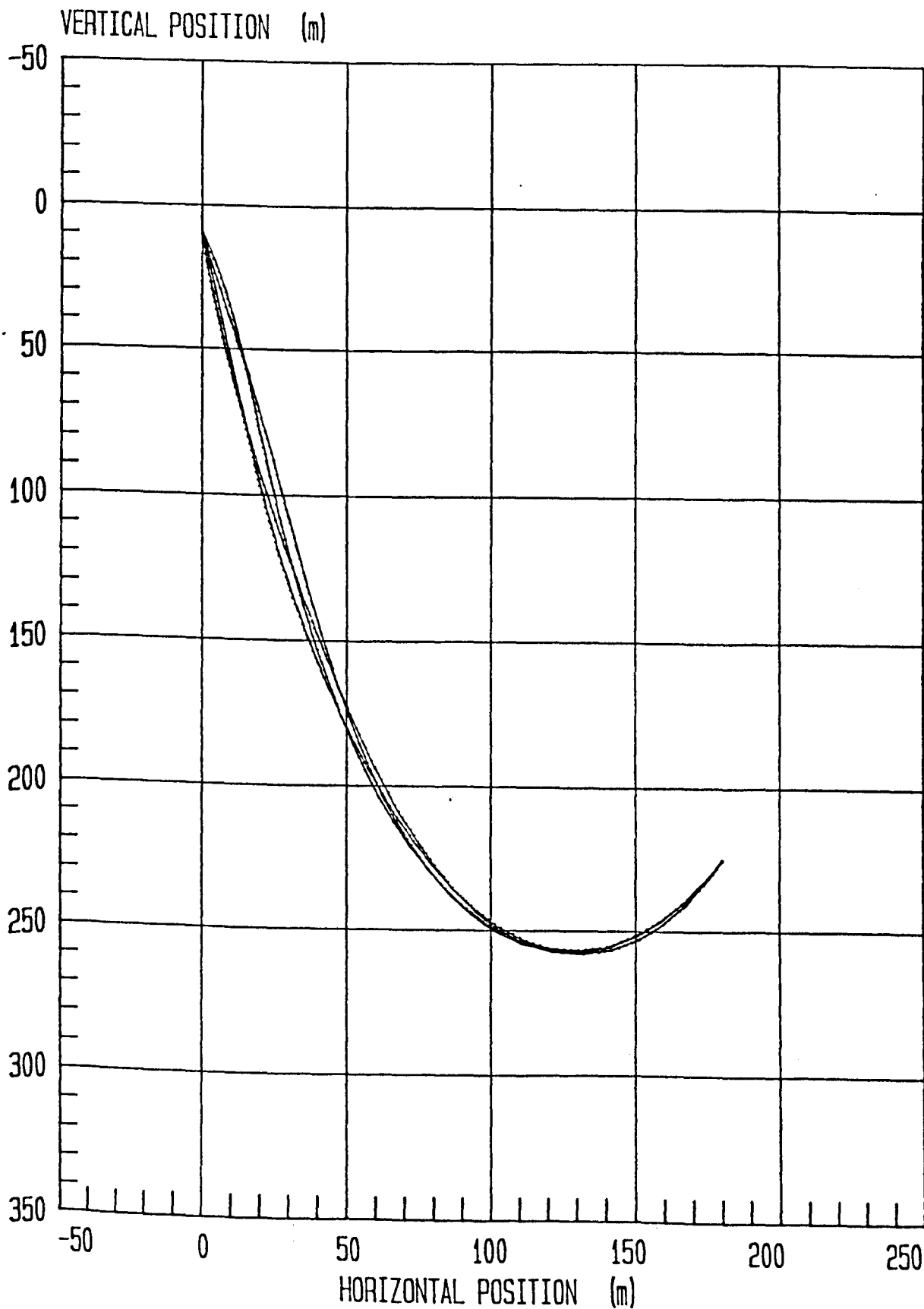
COMPARISON OF SNAP SHOTS FOR DYNAMIC RUN DURING 6TH WAVE CYCLE

DYNAMIC RUN WITH NO PLATFORM MOTION



FIG. 9.9 ZENTECH CONSULTANTS

— FLEXRISER  
..... FLEXDYNAMIC

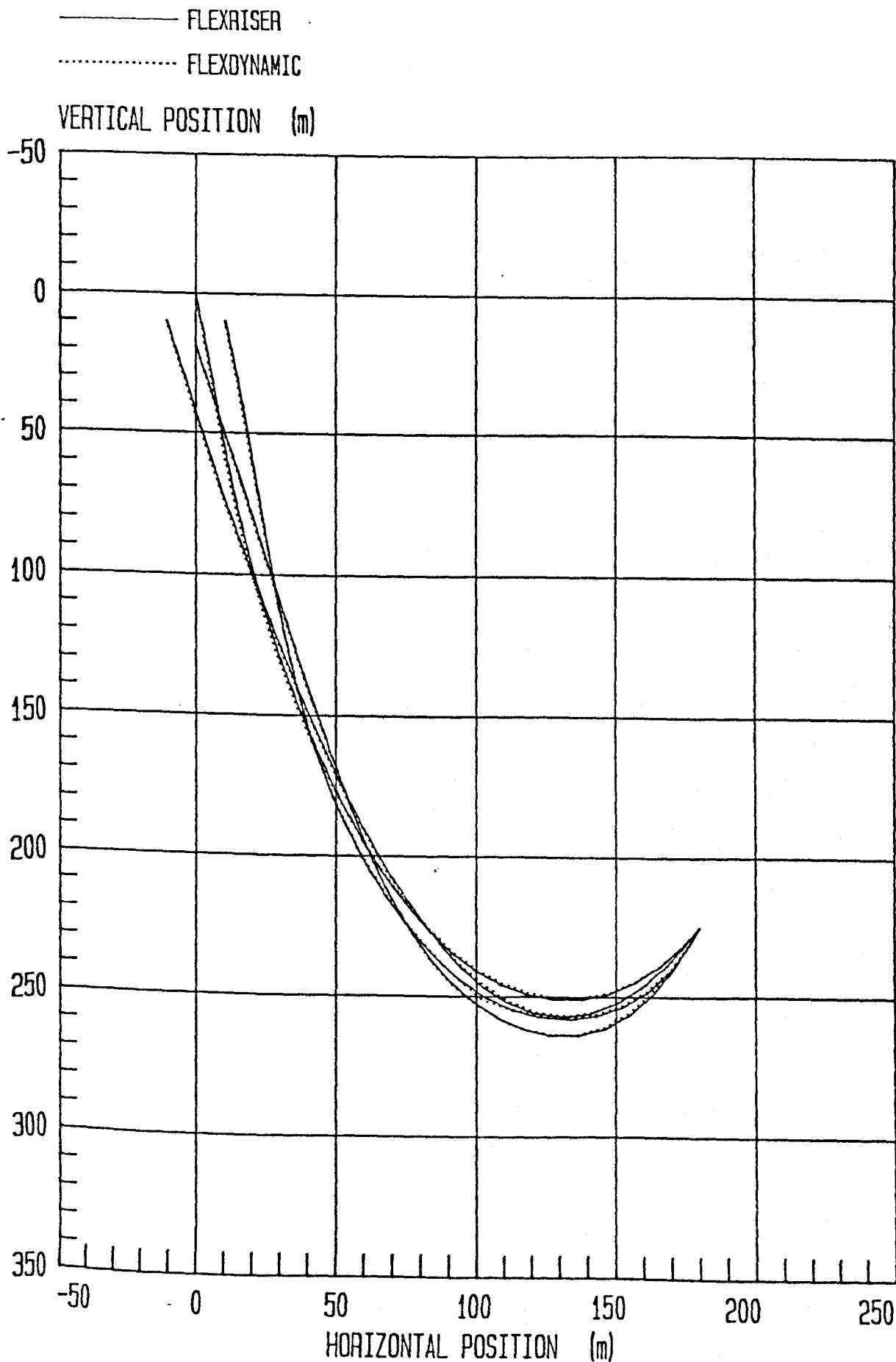


# SIMPLE CATENARY

COMPARISON OF SNAP SHOTS FOR DYNAMIC RUN DURING 6TH WAVE CYCLE  
DYNAMIC RUN WITH PLATFORM MOTION



FIG. 9.10

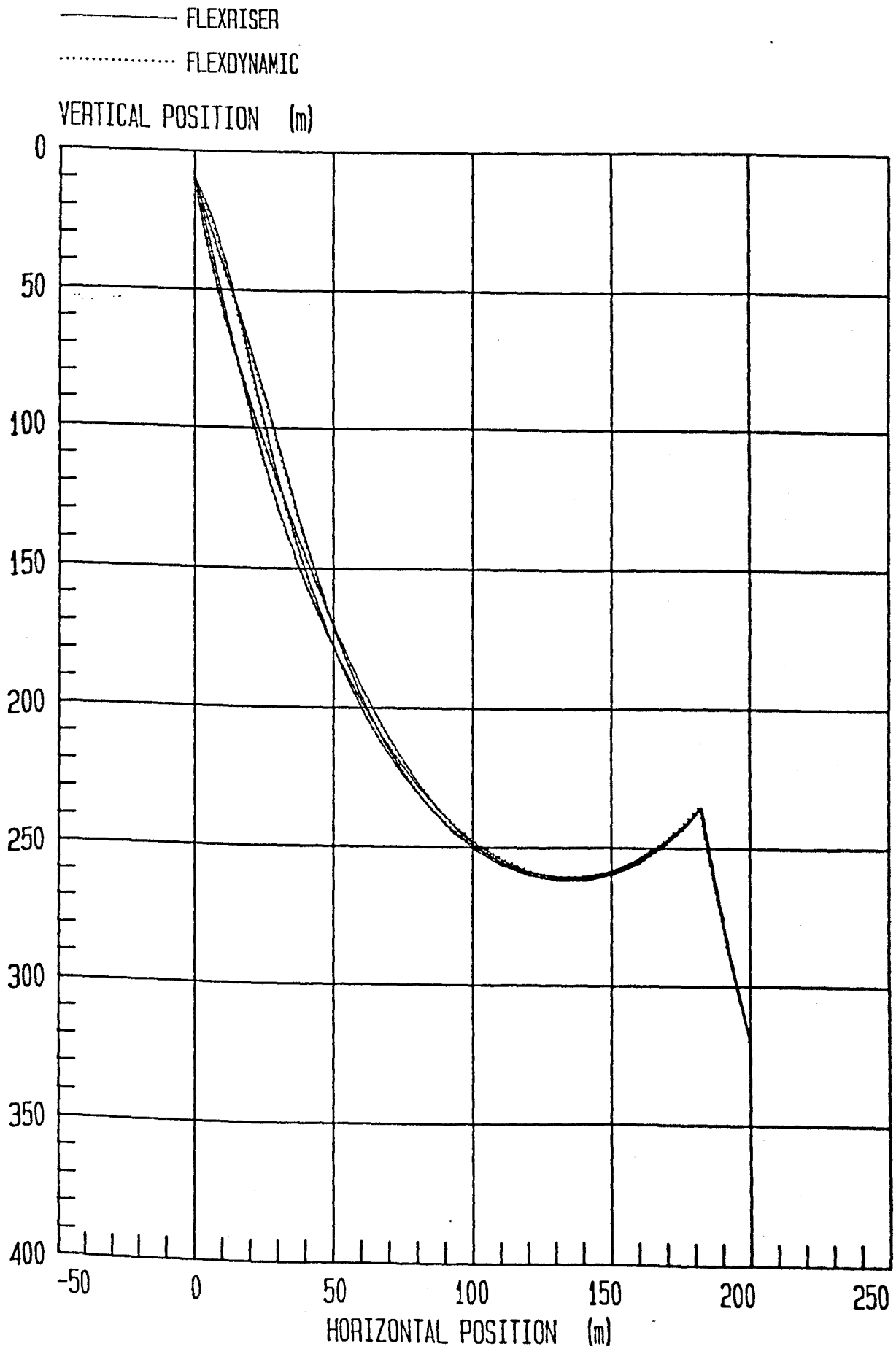


# STEEP S FLEXIBLE RISER

COMPARISON OF SNAP SHOTS FROM DYNAMIC-RUN DURING 6TH WAVE CYCLE  
DYNAMIC RUN WITH NO PLATFORM MOTION



FIG. 9.11

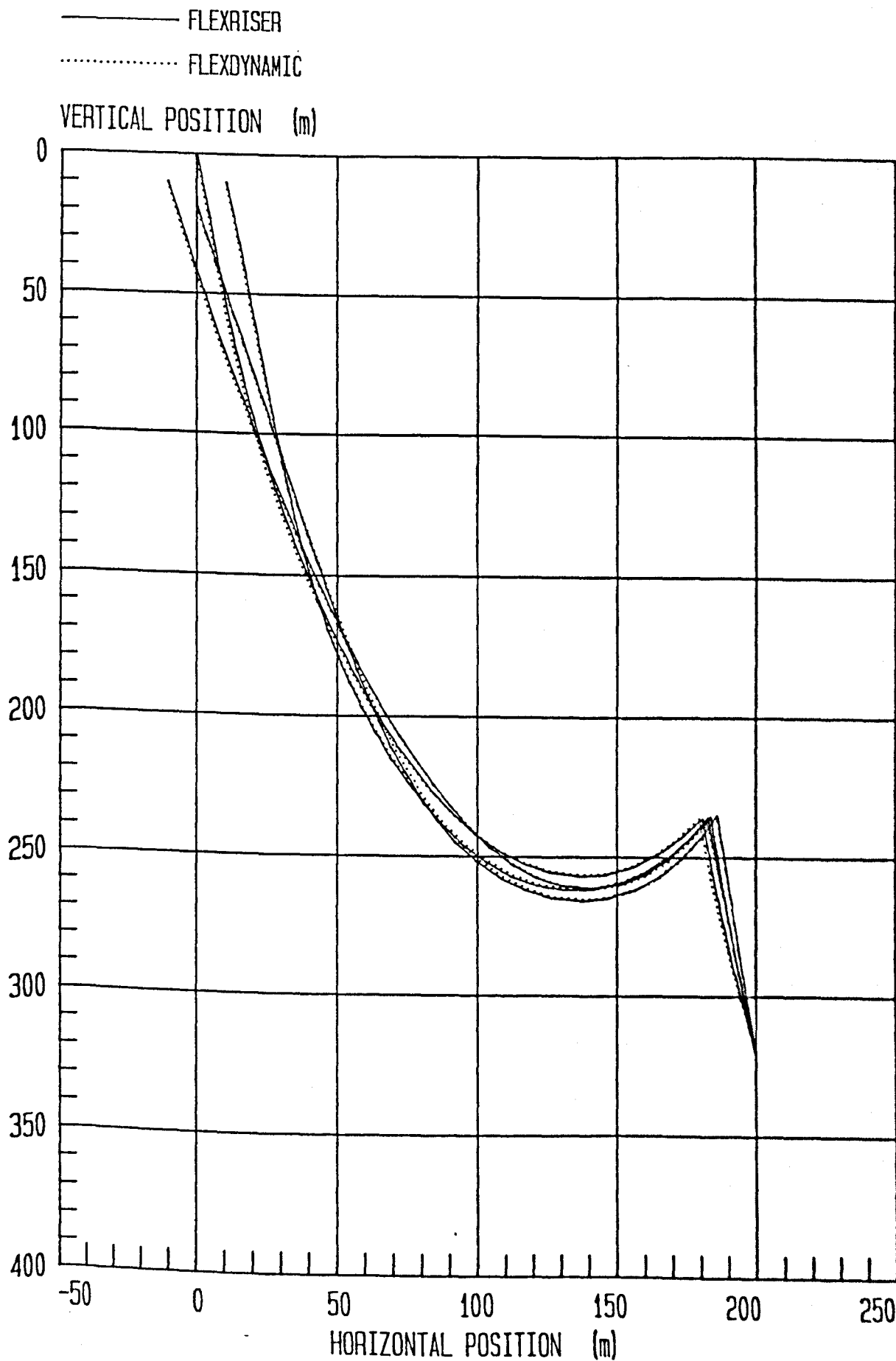


# STEEP S FLEXIBLE RISER

COMPARISON OF SNAP SHOTS FROM DYNAMIC-RUN DURING 6TH WAVE CYCLE  
DYNAMIC RUN WITH PLATFORM MOTION



FIG. 9.12 ZENTECH CONSULTANTS



## CHAPTER 10

### CONCLUSIONS AND RECOMMENDATIONS

#### 10.1 Conclusions

Flexible risers are the simplest and most economical means of linking subsea equipment and floating facilities. From an economic standpoint, the benefits associated with incorporating flexible pipes into production systems are:

- a) Simplicity in system design
- b) Easy and rapid installation
- c) Possibility of retrieval for re-use elsewhere
- d) Built-in flexibility: systems can be easily adapted to changing economic objectives as field development progresses.

Therefore, the flexible riser systems can be regarded as one of the key components for the more advanced future exploitation of oil and gas reserves in deep waters, and a comprehensive knowledge of their behaviour due to any wave and current induced hydrodynamic loading is required.

A number of 3-dimensional non-linear computer programs have been developed in recent years to analyse flexible riser systems but most of them are unusually expensive to run and they do not include the wave and current induced vortex shedding which is essential to simulate the 3-dimensional behaviour of risers. The aim of the present work was to develop an efficient and cost-effective scheme to analyse flexible riser systems.

A numerical method for the analysis of flexible risers by explicit integration of Newton's second law has been presented. The time integration step was calculated automatically using a simple stability criteria. The theory had the advantage of simple formulation and included the effects of material damping and vortex-shedding due to wave and current flows on flexible risers. The theory was implemented in four computer programs, FLEXSTATIC, FLEXDYNAMIC, FLEXCURRENT and STOKWAVE.

Program STOKWAVE calculated the wave parameters for any order (1-5) of Stokes wave theory. The predicted values of the wave parameters for a wave were identical to those published by other authors (Skjelberia and Hendrickson (1960)) who extended Stokes wave theory to fifth order.

Program FLEXSTATIC can be regarded as an efficient 3-dimensional static program which can compute any flexible riser configuration with given boundary-conditions. The CPU computing times on a GOULD 9005 computer system for predicting various riser configurations varied from just 5 to 10 seconds. These computed static configurations compared well with those measured from a hanging snake chain in two different catenary shapes and those predicted by program FLEXRISER.

The results of the parameter studies, which were performed in order to optimize program FLEXSTATIC, indicated the following:

- a) Employing fictitious mass of components together with a reduced axial stiffness for the riser, considerably

reduced the computation effort. The optimized value of the axial stiffness for a riser structure was achieved when the magnitude of the non-dimensional parameter  $EA/(W.L/N)$  was equal to 25.

Where  $EA$  = axial stiffness of a metre of riser  
 $W$  = self weight of riser and contents per metre length  
 $L$  = length of riser  
 $W.L/N$  = average nodal force

- b) The sufficient number of elements required to represent a flexible riser for engineering applications was found to be about 12. However, a total number of 20 to 30 elements are recommended for the final design stage of a flexible riser in order to investigate in detail the local effects such as angles at the top and bottom connectors due to wave and current induced loadings.

Program FLEXCURRENT can be regarded as an efficient 3-dimensional program for computing the static equilibrium state of a flexible riser subjected to current loadings and static platform movements. The CPU computing times on a GOULD 9005 computer system for calculating the static responses of some test cases due to current loadings and platform offsets varied from just 5 to 6 seconds. The accuracy of the results for various test cases predicted by program FLEXCURRENT were verified by the results which were measured from the current channel experiment and those predicted by the industry standard program FLEXRISER. The quick computations for static equilibrium configurations of a flexible

riser by programs FLEXSTATIC and FLEXCURRENT enable a designer to investigate various possible layouts of a riser and to check critical design criteria such as top and bottom angles, bending radius and distance of the sag from the sea-bed.

FLEXDYNAMIC is an efficient 3-dimensional dynamic program which calculates the dynamic behaviour of a flexible riser subjected to wave and current loadings, vessel movements and loadings due to vortex-shedding. The program was optimized successfully by calculating the hydrodynamic loadings only at every  $n$  integration time steps ( $n \cdot \Delta t$ ) which were then assumed to be constant during the following  $n$  time steps. The value of  $n \cdot \Delta t$  was set equal to  $1/2$  of the shortest time which is taken by a transverse wave to travel along any member of the riser. Further optimization was achieved by reducing the EA value of the riser elements by a factor of 10; though this optimization was strictly applicable only when there was no top platform motion.

Numerous runs were performed for various flexible risers subjected primarily to platform movements and subsequently to such movements together with wave induced hydrodynamic forces. The results showed that the response of the sag part (or generally the lower part) of the riser is governed by the platform motion. When a sub-surface sub-buoy is employed, the transformation of the platform movement to the manifold at the sea bed is prevented. Further runs were performed to investigate the effect of bending in the riser dynamic behaviour. The bending had damping effect on the riser dynamic response, but due

to the fact that flexible risers possess very low bending stiffness, the total effect of the bending was insignificant.

The results predicted by program FLEXDYNAMIC compared well with those obtained from extensive experimental work in two wave flumes and also with those predicted by program FLEXRISER. The CPU computing time on a GOULD Computer System to predict the dynamic response of a typical flexible riser for 5 wave cycles was only about 2 minutes. Furthermore, the computed results showed that the periodic response of the riser is achieved after one wave cycle which suggests that only 3 wave cycles can be sufficient for a dynamic solution. Program FLEXDYNAMIC is a general dynamic riser program and is coded so that it can be easily modified to handle any dynamic problem involving a flexible riser. The program has recently been used to predict the dynamic behaviour of a disconnected flexible riser. The riser was arranged in a U shape between a Jack-up fixed platform and a semi-submersible platform. The dynamic behaviours of the riser and semi-submersible platform were to be investigated when the riser was disconnected from the semi-submersible platform during stormy sea conditions. The riser was subjected to wave and current loadings and also to platform motions (surge, heave and pitch).

The comparison of the numerically predicted and measured dynamic responses in the plastic tube model test showed that material damping can be successfully modelled by a single Kelvin system. When the effect of the material damping was ignored the predicted results showed a 6% error in the amplitude of the horizontal top

tension. It is expected that this discrepancy would be higher for an actual flexible riser due to its complex structure which contains thermoplastic sheaths and cross-armoured steel wire layers which are installed in an helicoidal pattern.

The results for the natural frequencies of a free-hanging riser predicted by the scheme used in the present work were in agreement with those given in a published paper (Triantafyllou et. al. (1983)). This scheme is well suited to determine the natural frequencies of any flexible riser.

The computed dynamic responses of the tube model test, taking account of vortex-shedding effects, were in good agreement with those measured from the experiment. The frequency of the lift force was 4 times that of the wave frequency, which is important from the viewpoint of fatigue design of the riser around the top and bottom connectors. The results of the test helped to validate the vortex-shedding model suggested by Rajabi et. al. (1984). This model was extended in the present work to predict the effect of vortex-shedding on a randomly oriented flexible riser. This modification was essential in order to predict the 3-dimensional behaviour of a flexible riser.

One of the undesirable features of laboratory generated waves in wave flumes is the presence of the higher harmonic components. These are usually introduced by the secondary effect of a wedge type wavemaker and reflected waves from the beach. These effects can be minimized by generating various waves and adjusting the beach slope and measuring the higher components of the incident

wave for each individual wave flume. The waves for the present work were chosen so that they had negligible secondary components. The wave generated in the small flume was taken from Ellix's (1984) experimental work, and the waves for the larger flume were proportioned from this wave.

The explicit integration method described in this thesis for the analysis of flexible risers was found to be at least an order of magnitude faster than a widely used matrix based implicit scheme. The main reason for this is that the principal deformation modes of flexible risers are mechanical (rather than "structural").

#### 10.2 - Recommendations

The concept of floating compliant systems has brought promise of efficient petroleum production from deep water gas and oil fields at a wide range of depths. As these explorations move to deeper water, the riser system faces more hostile environmental conditions and the effect of vortex-shedding on the riser system becomes important. If the vortex-shedding frequency coincides with the fundamental structural frequency of the riser, it may endanger the riser integrity which is not desirable. Thus an investigation of the effect of vortex-shedding on flexible risers is recommended. Simple material damping calibration tests such as those carried out in the present work are also recommended for actual flexible risers. Such tests can provide vital information about the actual behaviour of flexible risers which have complex structures containing thermoplastic sheaths and cross-armoured steel wire layers installed in an helicoidal pattern.

Programs FLEXSTATIC and FLEXCURRENT have been modified further by the author at Zentech Consultants to predict the response of several flexible risers sharing a common discrete sub-buoy system. The risers are placed relative to each other in a manner such that there is no bundling effect among them regarding the hydrodynamic loadings. The modification was carried out by considering the sub-buoy as a separate system which is subjected to tension forces from the lower and upper parts of each riser, self weight and hydrodynamic loadings. An experimental work for such riser systems in a large wave tank is recommended for future work.

The fast computation of a flexible riser dynamic response by program FLEXDYNAMIC gives an opportunity to perform the lengthy and costly non-deterministic analysis of flexible risers more quickly and economically. A method such as that described below is recommended for future work to deal with random wave analysis.

A random wave can be assumed to be constructed by  $n$  numbers of incident regular waves with random phase angles. A spectral density graph such as the Jonswap wave spectrum which is suitable for the North Sea environment, or the Pierson-Moskowitz wave spectrum can be used to identify the regular waves. Figure 10.1 shows a typical spectral density graph. In order to specify the regular wave elements, the lower and upper frequencies and the number of regular waves (usually between 10 to 30),  $n$ , are identified and then the x-axis (frequency axis) between the lower and upper frequencies is divided into  $n$  intervals and subsequently the area under the curve is subdivided into  $n$

segments. Each segment represents a regular wave. The area of the segment is the wave height which can be calculated using a trapezoidal rule and the frequency of the wave is the average frequency of the segment. The phase angles for the waves can be chosen from random numbers. Similar spectral density graphs can be used for each degree of freedom of platform movement. The water particle velocities and accelerations induced by the random wave at each node at any time are considered to be the sum of the values induced by each wave and then these total kinematics are used to calculate the nodal hydrodynamic loadings. Similarly the platform motions and the wave profile at any time are considered to be the sum of the individuals.

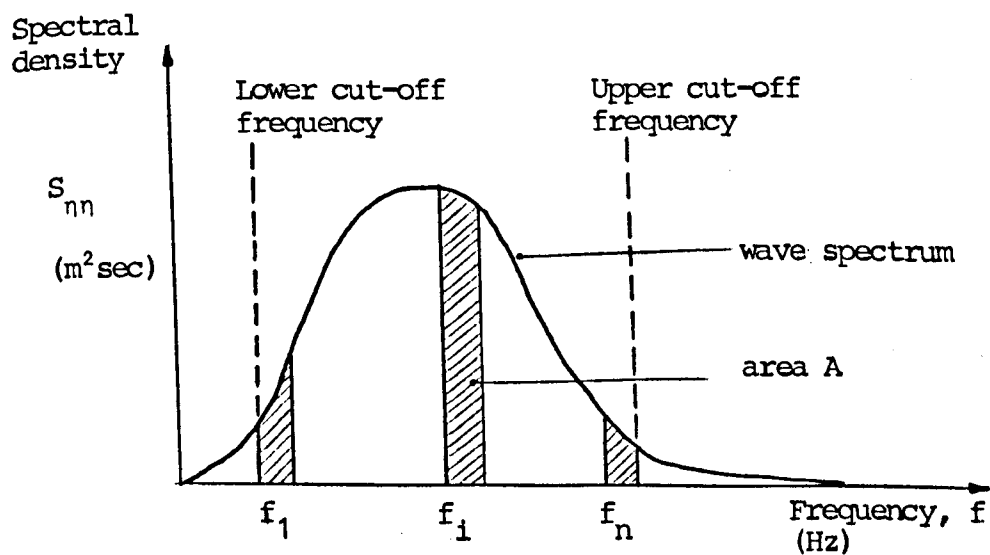


Figure 10.1 - Spectral density graph

Appendix A

Coefficients  $A_{ij}$ ,  $B_{ij}$  and  $C_i$  of Stokes Wave Theory

Let  $m = \sinh Kh$ , and  $n = \cosh Kh$

$$A_{11} = \frac{1}{m}$$

$$A_{13} = \frac{-n^2 (5n^2 + 1)}{8 m^5}$$

$$A_{15} = \frac{- (1184 n^{10} - 1440 n^8 - 1992 n^6 + 2641 n^4 - 249 n^2 + 18)}{1536 m^{11}}$$

$$A_{22} = \frac{3}{8m^4}$$

$$A_{24} = \frac{(192 n^8 - 424 n^6 - 312 n^4 + 480 n^2 - 17)}{748 m^{10}}$$

$$A_{33} = \frac{(13 - 4 n^2)}{64 m^7}$$

$$A_{35} = \frac{(412 n^{12} + 4224 n^{10} - 6800 n^8 - 12808 n^6 + 16704 n^4 - 3154 n^2 + 107)}{4096 m^{13} (6n^2 - 1)}$$

$$A_{44} = \frac{(80 n^6 - 816 n^4 + 1338 n^2 - 197)}{1536 m^{10} (6n^2 - 1)}$$

$$A_{55} = \frac{-(2880 n^{10} - 72480 n^8 + 324000 n^6 - 432000 n^4 + 163470 n^2 - 16245)}{61440 m^{11} (6n^2 - 1) (8n^4 - 11n^2 + 3)}$$

$$B_{22} = \frac{(2n^2 + 1)}{4m^3}$$

$$B_{24} = \frac{n (272 n^8 - 504 n^6 - 192 n^4 + 322 n^2 + 21)}{384 m^9}$$

$$B_{33} = \frac{3 (n^6 + 1)}{64 m^6}$$

$$B_{35} = \frac{(88128n^{14} - 208224n^{12} + 70848n^{10} + 54000n^8 - 21816n^6 + 6264n^4 - 54n^2 - 81)}{12288 m^{12} (6n^2 - 1)}$$

$$B_{44} = \frac{n (768 n^{10} - 448 n^8 - 48 n^6 + 48 n^4 + 106 n^2 - 21)}{384 m^9 (6n^2 - 1)}$$

$$B_{55} = \frac{(192000 n^{16} - 262270 n^{14} + 83680 n^{12} + 20160 n^{10} - 7280 n^8)}{12288 m^{10} (6n^2 - 1) (8n^4 - 11n^2 + 3)}$$
$$+ \frac{(7160 n^6 - 1800 n^4 - 1050 n^2 + 225)}{1288 m^{10} (6n^2 - 1) (8n^4 - 11n^2 + 3)}$$

$$C_1 = \frac{(8n^4 - 8n^2 + 9)}{8 m^4}$$

$$C_2 = \frac{(3840 n^{12} - 4096 n^{10} + 2592 n^8 - 1008 n^6 + 5944 n^4 - 1830 n^2 + 147)}{512 m^{10} (6n^2 - 1)}$$

$$C_3 = \frac{1}{4mn}$$

$$C_4 = \frac{(12 n^8 + 36 n^6 - 162 n^4 + 141 n^2 - 27)}{192 n m^9}$$

APPENDIX B

Derivation of Formulae for Determining the Hydrodynamic Forces on a Riser Element

Consider Simpson's rule

$$I_n = \frac{h_n}{3} (f_0 + 4 f_1 + 2 f_2 + 4 f_3 + \dots + 2 f_{2n-2} + 4 f_{2n-1} + f_{2n})$$

let  $C = f_1 + f_3 + \dots + f_{2n-1}$

$D = f_2 + f_4 + \dots + f_{2n-2}$

thus  $I_n = \frac{h_n}{3} (f_0 + 4 C + 2 D + f_{2n})$  (B.1)

where  $2n$  is the number of subintervals.

For the next step the number of subintervals is doubled, i.e.  $h_{n+1} = \frac{h_n}{2}$ .

thus  $I_{n+1} = \frac{h_{n+1}}{3} (f_0 + 4 C' + 2 D' + f_{2n})$  (B.2)

where  $D' = D + C$ .

The difference between  $I_{n+1}$  and  $I_n$  is:

$$E = I_{n+1} - I_n = \frac{h_{n+1}}{3} (f_0 + 4 C' + 2 (D + C) + f_{2n}) - \frac{h_n}{3} (f_0 + 4 C + 2 D + f_{2n})$$
 (B.3)

Rearranging and simplifying equation (B.3):

$$E = \frac{h_{n+1}}{3} (4 C' - 2 C) - \frac{1}{2} I_n$$
 (B.4)

The following steps are carried out to calculate the area using equation (B.4):

- (1) Set  $n = 1$ ,  $h = \frac{1}{2} (x_0 - x_{2n})$ . Evaluate  $f_0, f_1, f_2$

and set  $I = \frac{1}{3} h (f_0 + 4 f_1 + f_2)$  and  $C' = f_1$

(2) replace  $n$  by  $2n$ ,  $h$  by  $\frac{1}{2} h$ ,  $C$  by  $C'$  and evaluate the new  $C'$ , i.e.

the mid-ordinates,  $f_1, f_3, \dots, f_{2n-1}$  for the new  $h$ .

thus,  $C' = f_1 + f_3 + \dots + f_{2n-1}$

(3) Calculate the correction  $E = \frac{1}{3} h (4 C' - 2 C) - \frac{1}{2} I$  and  
replace  $I$  by  $I + E$ .

(4) The integration is terminated if  $E$  is smaller than a  
specified accuracy parameter, otherwise repeat from step 2.

APPENDIX C

Calculation of Nodal Twisting due to Torsion of Flexible Risers

Consider the orientation of member b with adjacent members a and c in space, figure C.1.

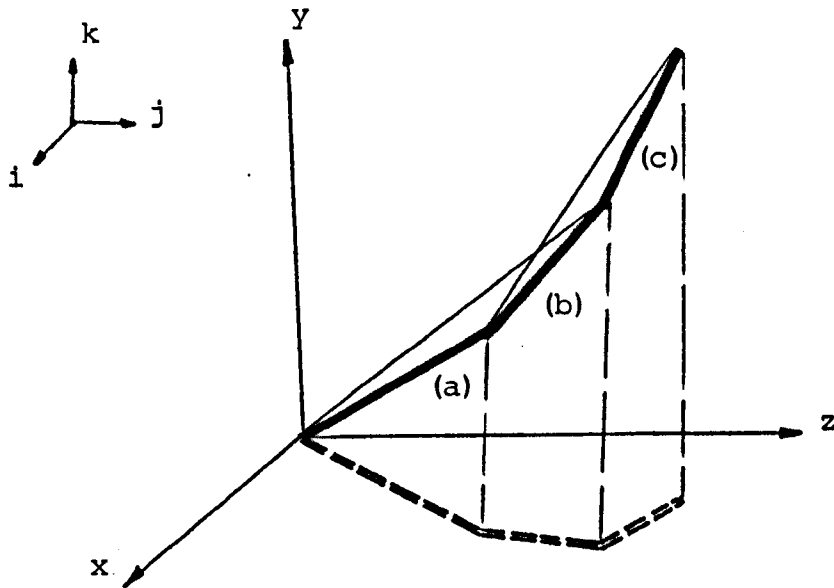


Figure C.1 - Three adjacent members in space

For a lumped idealisation, the twist angle,  $\theta$ , of member b is the angle between the planes defined by members a, b and b, c.

To obtain  $\theta$ , the members are considered to be vectors as follows:

—>

$$a = x_a i + z_a j + y_a k$$

—>

$$b = x_b i + z_b j + y_b k \quad (C.1)$$

—>

$$c = x_c i + z_c j + y_c k$$

where i, j and k are parallel axes to the x, z and y axes respectively. The angle between the planes is the angle between the normals to the planes. The normal line of a plane composed of two vectors is obtained by the cross product of the vectors.

Thus:

$$\begin{aligned} \vec{a} \times \vec{b} &= \det \begin{vmatrix} i & j & k \\ x_a & z_a & y_a \\ x_b & z_b & y_b \end{vmatrix} = (z_a \cdot y_b - y_a \cdot z_b) i + \\ &- (x_a \cdot y_b - y_a \cdot x_b) j + (x_a \cdot z_b - z_a \cdot x_b) k \\ &= m_1 i + m_2 j + m_3 k \end{aligned} \quad (C.2)$$

where  $m_1 = x_a \cdot y_b - y_a \cdot z_b$

$m_2 = -x_a \cdot y_b + y_a \cdot x_b$

$m_3 = x_a \cdot z_b - z_a \cdot x_b$

similarly,

$$\vec{b} \times \vec{c} = n_1 i + n_2 j + n_3 k \quad (C.3)$$

The angle between two vectors can be evaluated from their dot product.

Thus,

$$\cos \theta = (m_1 i + m_2 j + m_3 k) \cdot (n_1 i + n_2 j + n_3 k) = m_1 n_1 + m_2 n_2 + m_3 n_3$$

Thus,

$$\theta = \cos^{-1} (m_1 n_1 + m_2 n_2 + m_3 n_3) \quad (C.4)$$

The corresponding torque can be obtained from the following relation:

$$T_r = JG \frac{\theta}{l} \quad (C.5)$$

where  $T_r = \text{Torque}$

$l = \text{Length of the member}$

$\theta = \text{Twisted angle}$

$JG = \text{Torsion constant}$

The twisting nodal forces of member b in figure C.1 can be obtained as follows:

$$F_{t2} = \frac{T_r}{R_o} \quad , \quad F_{t1} = - \frac{T_r}{R_o} \quad (C.6)$$

Where  $R_o$  is the external diameter of the riser.

However, because of the very small torsional stiffness of risers, the induced twisting forces are practically insignificant and have been ignored in the present work. It is, however, worth noting that torsion in the riser will increase the structural damping, and it can be considered as an extra factor of safety in the design.

Appendix D

Static Solution for the Riser Structure using Dynamic Relaxation with Viscous Damping

The equation of motion of any node  $i$  in the  $x$  direction is, from Newton's second law:

$$M_i \ddot{X}_i = F_{ix} \quad (D.1)$$

where  $M$  = nodal mass

$\ddot{X}$  = nodal structural acceleration in the  $x$  direction

At any time  $t$  the total force acting on the node in this direction,  $F_{ix}$ , comprises two parts, the current residual  $R(t)_{ix}$  of applied and member loads acting on the node, and an imposed viscous damping force acting in the opposite sense to the nodal velocity  $\dot{X}_{ix}$  :

$$M_i \ddot{X}_{ix}^t = R(t)_{ix}^t - C \dot{X}_{ix}^t \quad (D.2)$$

where  $C$  = viscous damping constant.

$\dot{X}$  = nodal structural velocity.

Using the central difference concept for velocity and acceleration:

$$\dot{X}^t = (\dot{X}^{t+\Delta t/2} + \dot{X}^{t-\Delta t/2}) / 2 \quad (D.3)$$

$$\ddot{X}^t = (\dot{X}^{t+\Delta t/2} - \dot{X}^{t-\Delta t/2}) / \Delta t \quad (D.4)$$

Substituting equations (D.3) and (D.4) into equation (D.2) and rearranging for  $\dot{X}^{t+\Delta t/2}$  leads to:

$$\dot{X}_{ix}^{t+\Delta t/2} = \left( \frac{1}{1+C/2} \right) \cdot \frac{\Delta t}{M_i} \cdot R(t)_{ix}^t + \left( \frac{1-C/2}{1+C/2} \right) \dot{X}_{ix}^{t-\Delta t/2}$$

or

$$\dot{X}_{ix}^{t+\Delta t/2} = A R(t)_{ix}^t + B \dot{X}_{ix}^{t-\Delta t/2} \quad (D.5)$$

Where  $A = \left( \frac{1}{1+C/2} \right) \frac{\Delta t}{M}$

$$B = \frac{1-C/2}{1+C/2}$$

Nodal co-ordinates may then be updated for the structure:

$$X_{ix}^{t+\Delta t} = X_{ix}^t + \Delta t \cdot \dot{X}_{ix}^{t+\Delta t/2} \quad (D.6)$$

Current nodal residuals  $R(t)^{t+\Delta t}$  may then be calculated from equilibrium equations and the next stage of the analysis recommenced at equation (D.5).

The optimum efficiency of this scheme is obtained when the damping constant,  $C$ , has a value close to that corresponding to the critically damped state of the structural response, figure D.1:

$$C \cong 4 \pi f_n$$

where  $f_n$  is the fundamental frequency of the structure.

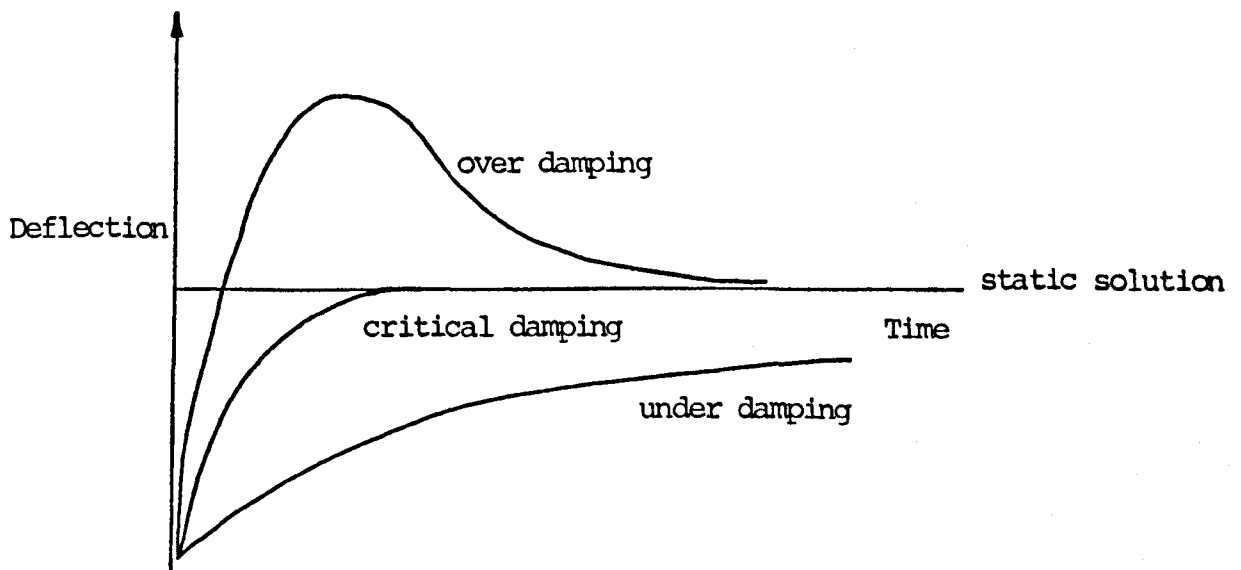


Figure D.1 - Definition of different damping states

APPENDIX E

Input Data of the Test Cases in Chapter 9

Water depth	500	m
Water density	1.025	ton/m <sup>3</sup>
Riser outside diameter	0.2171	m
Riser and its contents weight in air	0.789	KN/m
Axial stiffness, EA	245000	kN
Total length	950	m
Vertical span	480	m
Horizontal span	750	m
Number of elements used for numerical solution	70	

Table E.1 - Input data for the static run of the free hanging riser

Water depth	320	m
Water density	1.025	ton/m <sup>3</sup>
Riser outside diameter	0.295	m
Riser and its contents weight in air	1.857	kN/m
Axial stiffness, EA	72100	kN
Total length	356	m
Vertical distance of riser top from sea bed	310	m
Vertical distance of riser base from sea bed	95	m
Vertical span	215	m
Horizontal span	180	m
Number of elements used for numerical solution	35	

Table E.2 - Input data for the static run of the free hanging riser (simple catenary)

Water depth	320	m
Water density	1.025	ton/m <sup>3</sup>
Riser outside diameter	0.295	m
Riser and its contents weight in air	1.857	kN/m
Axial stiffness, EA	72100	kN
Catenary length	356	m
Taut length	86	m
Vertical span	310	m
Horizontal span	200	m
Buoyancy of sub-buoy	370	m
Number of elements used for numerical solution		
catenary part	35	
taut part	9	

Table E.3 - Input data for the static run  
of the steep-S riser

Water depth	500	m
Water density	1.025	ton/m <sup>3</sup>
Number of riser sections	3	
Data for section 1		
Riser outside diameter	0.2171	m
Riser and its contents weight in air	0.789	kN/m
Axial stiffness, EA	245000	kN
Section length	598.5	m
Number of elements used for numerical solution	49	
Data for section 2		
Riser outside diameter	0.759	m
Riser and its contents weight in air	3.029	kN/m
Axial stiffness, EA	245000	kN
Section length	119.7	m
Number of elements used for numerical solution	15	
Data for section 3		
Riser outside diameter	0.2171	m
Riser and its contents weight in air	0.789	kN/m
Axial stiffness, EA	245000	kN
Section length	68.4	m
Number of elements used for numerical solution	9	
Vertical distance of riser top from sea bed	480	m
Vertical distance of riser base from sea bed	0	m
Vertical span	480	m
Horizontal span	360	m

Table E.4 - Input data for the static run  
of the steep wave riser

Water depth	250	m
Water density	1.025	ton/m <sup>3</sup>
Riser outside diameter	0.243	m
Riser and its contents weight in air	1.089	kN/m
Axial stiffness, EA	1.35E5	kN
Upper catenary length	285	m
Lower catenary length	130	m
Vertical span	232	m
Horizontal span	220	m
Buoyancy of sub-buoy	280	kN
Tethered length	60	m
Horizontal distance of tether base from riser base	102	m
Number of elements used for numerical solution		
Upper catenary	39	
Lower catenary	18	

Table E.5 - Input data for the static run  
of the lazy-S riser

Water depth	500	m
Water density	1.025	ton/m <sup>3</sup>
Number of riser sections	3	
Data for section 1		
Riser outside diameter	0.2171	m
Riser and its contents weight in air	0.789	kN/m
Axial stiffness, EA	245000	kN
Section length	500	m
Number of elements used for numerical solution	49	
Data for section 2		
Riser outside diameter	0.500	m
Riser and its contents weight in air	1.34	kN/m
Axial stiffness, EA	245000	kN
Section length	120	m
Number of elements used for numerical solution	15	
Data for section 3		
Riser outside diameter	0.2171	m
Riser and its contents weight in air	0.789	kN/m
Axial stiffness, EA	245000	kN
Section length	200	m
Number of elements used for numerical solution	29	
Vertical distance of riser top from sea bed	480	m
Vertical distance of riser base from sea bed	0	m
Vertical span	480	m
Horizontal span	400	m

Table E.6 - Input data for the static run  
of the lazy wave riser

Current velocity profile		
at water free surface	1.71	m/sec
at 25 metres below water level	1.42	m/sec
at 50 metres below water level	1.25	m/sec
at 100 metres below water level	0.85	m/sec
at 200 metres below water level	0.7	m/sec
at 3 metres above sea bed	0.5	m/sec
Direction of current flow	from riser top to riser base	
Axial stiffness, EA	72100	kN
Bending stiffness, EI	480	kNm <sup>2</sup>
Drag coefficient for riser, C <sub>d</sub>	0.7	
Data for riser	as in table E.2	

Table E.7 - Data for the simple catenary riser  
subjected to current induced  
hydrodynamic loadings

Current velocity profile		
at water free surface	1.71	m/sec
at 25 metres below water level	1.42	m/sec
at 50 metres below water level	1.25	m/sec
at 100 metres below water level	0.85	m/sec
at 200 metres below water level	0.7	m/sec
at 3 metres above sea bed	0.5	m/sec
Direction of current flow	from riser top to riser base	
Axial stiffness, EA	72100	kN
Bending stiffness, EI	480	kNm <sup>2</sup>
Drag coefficient for riser, C <sub>d</sub>	0.7	
Drag force on sub-buoy due to 1 m/sec fluid velocity	7.4	kN
Sub-buoy mass	13.5	tonnes
Data for riser	as in table E.3	

Table E.8 - Data for the steep-S riser subjected  
to current induced hydrodynamic loadings

Water height	31	m
Wave period	15	sec
Wave direction	from riser top to riser base	
Used wave theory	Linear wave theory	
Current velocity profile	as in table E.7	
Axial stiffness, EA	72100	kN
Bending stiffness, EI	480	kNm <sup>2</sup>
Drag coefficient for riser, $C_d$	0.7	
Inertia coefficient for riser, $C_m$	1.8	
Tangential drag coefficient, $C_{dt}$	0	
No platform motion		
Data for riser	as in table E.2	

Table E.9 - Data for the dynamic run of the simple catenary riser subjected to wave and current induced hydrodynamic loadings with no platform motion

Wave data	as in table E.9
Current data	as in table E.7
Data for riser	as in table E.2
Data for hydrodynamic force coefficient	as in table E.7
Platform motion	
Surge amplitude	10.5 m
Surge phase angle with wave flow	90°
Heave amplitude	9.0
Heave phase angle with wave flow	0°
Riser top is situated at the centre of gravity of the platform	
Wave phase angle at the centre of gravity of the platform	0°

Table E.10 - Data for the dynamic run of the simple catenary riser subjected to wave and current induced hydrodynamic loadings with platform motion

Wave height	31	m
Wave period	15	sec
Wave direction	from riser top to riser base	
Used wave theory	Linear wave theory	
Current velocity profile	as in table E.8	
Axial stiffness, EA	72100	kN
Bending stiffness, EI	480	kNm <sup>2</sup>
Drag coefficient for riser, $C_d$	0.7	
Inertia coefficient for riser, $C_m$	1.8	
Tangential drag coefficient, $C_{dt}$	0	
Drag force on sub-buoy due to 1 m/sec fluid velocity	7.4	kN
Inertia coefficient for sub-buoy	1.8	
Sub-buoy mass	13.5	tonnes
Sub-buoy volume	50	m <sup>3</sup>
No platform motion		
Data for riser	as in table E.3	

Table E.11 - Data for the dynamic run of the steep-S riser  
subjected to wave and current induced  
hydrodynamic loadings with no platform motion

Wave data	as in table E.11
Current data	as in table E.8
Data for riser	as in table E.3
Data for hydrodynamic force coefficient	as in table E.11
Drag force on sub-buoy due to 1 m/sec fluid velocity	7.4 kN
Inertia coefficient for sub-buoy	1.0
Sub-buoy mass	13.5 tonnes
Sub-buoy volume	50 m <sup>3</sup>
Platform motion	
Surge amplitude	10.5 m
Surge phase angle with wave flow	90°
Heave amplitude	9.0 m
Heave phase angle with wave flow	0°
Riser top is situated at the centre of gravity of the platform	
Wave phase angle at the centre of gravity of the platform	0°

Table E.12 - Data for the dynamic run of the steep-S riser subjected to wave and current induced hydrodynamic loadings with platform motion

REFERENCES

- Achenbach, E., (1971), " Influence of surface roughness on the cross-flow around a circular cylinder," J. of Fluid Mech., Vol. 46, Part 2 pp. 321-335 .
- American Petroleum Institute, (1977), " Comparison of marine drilling riser analysis," API Bulletin 2J.
- Angrilli, F., and Cossalter, V., (1982), "Transverse oscillations of a vertical pile in waves," J. of Fluids Engineering, Vol. 104, pp. 46-53.
- Barnes, M. R., (1974), " Dynamic Relaxation analysis of tension network, " Int. Conf. on Tension Structures, London.
- Barnes, M. R., (1975) " Applications of Dynamic Relaxation to the form-finding and analysis of cable, membrane and pneumatic structures, " 2nd Int. Conf. on Space Structures, Guildford.
- Barnes, M. R., (1977), "Form-finding and analysis of tension space structures by dynamic relaxation," Ph.D. Thesis, the City University.
- Barnes, M. R., (1980), " Explicit dynamic analysis of an impulsively loaded pneumatic dome, " Air-Supported Structures Conf., London.
- Barnes, M. R., and Wakefield, D., (1984), "Dynamic Relaxation applied to interactive form finding and analysis of air-supported Structures", Air-Supported Structures Conf., London.

- Bath, K. J., and Wilson, E. L., (1976), " Numerical methods in finite element analysis," Prentice-Hall Inc.
- Beckmann, H., and Merwin, J.E., (1979), " Wave forces on conductor pipe group," Civil Eng. in The Ocean IV, Proceeding of The Specialty Conference held at San Francisco.
- Bergan, P. G., and Clough, R. W., (1972), " Convergence criteria for iterative processes," AIAA Journal, Vol.N8, pp. 1107- 1108.
- Berge, B., and Pen Zien, J., (1974), "Three-dimensional stochastic response of offshore towers to wave forces," Off. Tech. Conf., paper 2050 .
- Beynet, P.A., and Frase, J.R., (1982), " Flexible riser for a floating storage and offloading system," Off. Tech. Conf., paper 4321 .
- Bidde, D.B., (1971), " Laboratory study of lift forces on circular piles," J. of The Waterways, Harbors and Coastal Eng. Div., ASCE, PP. 595-614 .
- Birkhoff, G., and Zarantonells, E.H., (1957), " Jets, wakes and cavities ," Academic Press, New York .
- Bishop, R.E.D., and Hassan, A.Y., (1964), "The lift and drag forces on a circular cylinder in a flowing liquid," Proc. Roy. Soc. A277, pp. 32-51 .

- Borgman, L.E., (1958), "Computation of the ocean-wave forces on inclined cylinders," Trans. Amer. Geophysical Union, Vol. 39, pp. 885-888 .
- British Ship Research Association, (1976), "A critical evaluation of the data on wave force coefficients," British Ship Research Assoc., Wallsend Upon Tyne, Contract Report W-278 .
- Burke, B. G., (1973), "Analysis of marine risers for deep water," Off. Tech. Conf., paper 1771.
- Bushnell, M.J., (1977), "Forces on cylinder arrays in oscillating flow," Off. Tech. Conf., paper 2903.
- Chakrabarti, S.K., (1978), "Wave forces on multiple vertical cylinders." J. Waterways Port. Coast and Ocean Div., ASCE, WW2, pp. 147-161 .
- Chakrabarti, S.K., (1979), " Wave forces on vertical array of tubes," Civil Eng. in The Ocean IV, Proc. of The Specialty Conference held at San Francisco, Vol. I, pp. 241-259 .
- Chakrabarti, S.K., (1980a), "Inline forces on fixed vertical cylinders in waves," J. Waterways Port. Coast. and Ocean Div., ASCE, WW2 .
- Chakrabarti, S.K., (1980b), "Laboratory generated waves and wave theories," J. waterways Port. Coast. and Ocean, DIV., ASCE, WW3 .

- Chakrabarti, S.K., Tam, W.A., and Wolbert, A.L., (1975), "Wave forces on a randomly orientated tube," Off. Tch. Conf., paper 2190 .
- Chakrabarti, S.K., Wolbert, A.L., and Tam, W.A., (1977), "Wave forces on inclined tubes," Coastal Eng., Vol. 1, pp. 149-165 .
- Cokelet, E.D., (1977), "Steep gravity waves in water of arbitrary uniform depth," Phil. Trans. Roy. Soc., Ser. A, Vol. 286, pp. 183-230 .
- Crist, S. A., (1970), "Analysis of the motion of a long wire towed from an orbiting aircraft," "The Shock and Vibration Bulletin", No. 41-Pt.6, Naval Research Lab., Washington, D.C.
- Curdall, P. A., (1976), " Explicit finite-difference methods in geomechanics," Proc. E. F. Conf. Numerical Methods in Geomechanics, Blacksburg Va.
- Day, A. S., (1965), "An introduction to dynamic relaxation," The Engineer.
- Dalton, C., and Helfinstine, R.A., (1971), "Potential flow past a group of circular cylinders," ASME, J. Basic Eng., pp. 636-642 .
- Dalton, C., and Szabo, J.M., (1976), "Drag on a group of cylinders," ASME, paper No. 76-pet-42 .

- Dean, R.G., (1970), "Relative validities of water wave theories," J. Waterways Harbors and Coastal Eng. Div., ASCE, Vol. 96, No. WW1, pp. 105-119 .
- Dean, R.G., and Aagaard, P.M., (1970), " Wave forces : Data analysis and engineering calculation method," J. Pet. Tech.
- Delany, N.K., and Sorensen, N.E., (1953), "Low speed drag of cylinders of various shapes," U.S. National Advisory Committee of Aeronautics, Tech. Note 3038 .
- Dominguez, R. F., (1971), "The static and dynamic analysis of discretely represented moorings and cables by numerical means," Ph.D. Thesis, Oregon State University, Corvallis, Ore.
- Dominguez, R. F. and Smith, D.E., (1972), "Dynamic analysis of cable systems," J. of The Structural Div., ASCE, Vol. 98, No. ST8, Paper9127, pp. 1817-1834.
- Ellix, D. M., (1984), "Second order wave loading on vertical cylinders," Ph.D. Thesis, The City University, London.
- Fage, A., and Warsap, J.H., (1929), "The effect of turbulence and surface roughness on the drag of a circular cylinder," HMSO, London , ARC, R and M 1283 .
- Fenton, J.D., (1979), "A high-order cnoidal wave theory," JFM, Vol. 94, pp. 29-161 .

- Fung, Y.C., (1960), "Fluctuating lift and drag acting on a cylinder in a flow at super critical reynolds number," J. Aerospace Sciences, Vol. 27, No. 11 .
- Fylling, I. J., and Wold, P. T., (1979), "Cable dynamics - Comparison of experimental and analytical results," Report - 8979, The Ship Research Institute of Norway, Trondheim.
- Gardner, T. N., and Kotch, M. A., (1976), "Dynamic analysis of risers and caissons by the finite element method," Off. Tech. Conf., Paper 2651.
- Garrison, C.J., (1980), "A review of drag and inertia forces on circular cylinders," Off. Tech. Conf., paper 3760 .
- Garrison, C., Field, J., and May, M., (1977), "Drag and inertia forces on a cylinder in periodic flow, "J. Water. Port. Coast. and Ocean Div., ASCE, Vol. 103, WW2 .
- Gaston, J.D., and Ohmart, R.D., (1979), "Effects of surface roughness on drag coefficients, "Civil Eng. in the Oceans IV, ASCE, pp. 611-621 .
- Griffin, O.M., (1981), "OTEC cold water pipe design for problems caused by vortex-excited oscillations," Ocean Eng., Vol. 8, pp 119-209 .
- Griffin, O.M., and Ramberg, S.E., (1982), "Some recent studies of vortex shedding with application to marine tubular and risers," ASME, J. of Energy Resources Tech., Vol. 104.

- Hallam, M.G., Heaf, N.J., and Wootton, L.R., (1978), "Dynamics of marine structures," Construction Industry Research and Information Association (CIRIA) Report UR8, London.
- Hansen, N.E.O., and Knudson, M.H., (1980), "Extended production riser model tests," Danish Hydraulics Institute, July.
- Hartlen, R.T., and Currie, I.G., (1970), "Lift-oscillation model for vortex-induced vibration," ASCE, J. of Eng. Mech., Vol. 96, pp. 577-591 .
- Heaf, N.J., (1979), "The effect of marine growth on the performance of fixed offshore platforms in North sea," Off. Tech. Conf., paper 3386.
- Heidement, J.C., and Sarpkaya, T., (1985), "Hydrodynamic forces on dense arrays of cylinders," Off. Tech. Conf., paper 5008.
- Hicks, J. B., and Clark, L. B., (1972), "On the dynamic response of buoy-supported cables and pipes to currents and waves," Off. Tech. Conf., Paper 1556.
- Hoerner, S.F., (1965), "Fluid-dynamic drag," 3rd Ed. Book published by the author, New jersey.
- Hogben, N., Miller, B.L., Searle, J.W., and Ward, G., (1977), "Estimation of fluid loading on offshore structures," Proc. Institution of civil Eng., Vol. 63 Part 2, pp. 551-562.
- Isaacson, M.Q., (1974), "The forces on circular cylinders in waves," Ph.D. Thesis, University of Cambridge.

- Isaacson, M.Q., and Maull, D.J., (1976), "Transverse forces on vertical cylinders in waves," Proc. ASCE, WW1, pp. 49-60.
- Iwan, W.D., and Blevins, R.D., (1974), "A model for vortex induced oscillation of structures," J. of Appl. Mech.
- Keulegan, G.H., and Carpenter, L.H., (1958), "Forces on cylinders and plates in an oscillating fluid," J. of Research of The National Bureau of Standard, Vol. 60, No. 5, pp. 423-440.
- Kim, Y.Y., and Hibbard, H.C., (1975), "Analysis of simultaneous wave force and water particle velocity measurements," Off. Tech. Conf., paper 2192.
- King, R., (1974), "Vortex-excited structural oscillations of a circular cylinder in flowing water," Ph.D. Thesis, Loughbrough University.
- King, R., (1977), "A review of vortex shedding research and its application," Ocean Engineering, Vol. 4, pp. 141-171.
- Kortewege, D.J., and De Vries, G., (1895), "On the change of form of long waves advancing in a rectangular canal, and on a new type of long stationary waves," Phil. Mag., 5th series, Vol. 39, pp.422-443.
- Larsen, C. M., and Fylling, I. J., (1982), "Dynamic behaviour of anchor lines," BOSS 1982, Boston.

- Lawrence, P. L., and Gay, T. A., (1980), "An improved linearization technique for frequency domain riser analysis," Off. Tech. Conf., Paper 3777.
- Laya, E.J., Connor, J.J., and Shyam, S. S., (1984), "Hydrodynamic forces on flexible offshore structures," J. of Engineering Mechanics, Vol. 110, pp. 433-448.
- Le Mehaute, B., (1976), "An introduction to hydrodynamics and water waves," Springer-Verlag, Dusseldorf.
- Leonard, J. W., and Recker, W. W., (1972), "Nonlinear dynamics of cables with low initial tension," J. of The Engineering Mechanics Division, ASCE, Vol. 98, No. EM2, Paper 8805, pp. 293-309.
- Lindahl, J., and Sjoberg, A., (1983), "Dynamic analysis of mooring cables," Second International Symposium on Ocean Engineering and Ship Handling, Gothenburg.
- Liu, C. L., and Drelicharz, J. A., (1969), "Dynamic line force and oscillatory motion of a vessel being winched down in ocean - two computer solutions," TN-1053 (AD697 275), Naval Civil Engineering Lab., Port Hueneme, Calif.
- Løken, A.E., Torset, O.P., Mathiassen, S., and Arnesen, T., (1979), "Aspects of hydrodynamic loading in design of production risers," Off. Tech. Conf., paper 3538.

- MacCamy, R.C., and Fuchs, R.A., (1954), "Wave force on piles : a diffraction theory," U.S. Army Coastal Egnrg. Res. Centre Tech. Memo, No. 69.
- Macnamara, J. F., Joyce, P. J., and Gilroy, P. J., (1981)," Arbitrarily large static and dynamic motions of drilling and production risers," Int. Symposium on Hydrodynamics in Ocean Engineering, Trondheim.
- Mair, W.A., and Maull, D.J., (1971), "Aerodynamic behavior of bodies in the wake of other bodies," Phil. Trans. Soc., London, Vol. 269, pp. 425-437.
- Mathotra, A.K., and Penzien, J., (1970), "Nondeterministic analysis of offshore structures," J. of Eng. Mech. Div., ASCE, Vol. 96, No. EM6, pp. 985-1003.
- Matten, R.B., (1977), "The influence of surface roughness on the drag of circular cylinders in waves," Off. Tech. Conf., paper 2902.
- McGregor, D.M., (1957), "An experimental investigation of the oscillating pressures on a circular cylinder in a fluid stream," Univ. of Toronto, UTIA TN, No. 14.
- Miller, B.L., (1977), "The hydrodynamic drag of roughened circular cylinders," J. Roy. Inst. Naval Architects, RINA, Vol. 119, pp. 55-70.

- Moe, G., and Verley, R.L.P., (1978), "An investigation into the hydrodynamic damping of cylinders oscillated in steady current of various velocities," Rep. of The River and Harbor Lab., Norwegian Ins. of Tech.
- Moe, G., and Verley, R.L.P., (1980), "Hydrodynamic damping of offshore structures in waves and currents," Off. Tech. Conf., paper 3798.
- Morgan, B. J., (1970), "The finite element method and cable dynamics," Paper 3C, Proceedings of The Symposium on Ocean Engineering, Univ. of Pennsylvania, Philadelphia, Pa.
- Morison, J.R., O'Brien, M.P., Johnson, J.W., and Schaaf, S.A., (1950), "The forces exerted by surface waves on piles," Petroleum Trans., AIME, Vol. 189, pp. 149-157.
- Natvig, B. J., and Torset, O. P., (1981), "Design verification of flexible marine risers," Proc. of The 37th ASME Petroleum Mechanical Engineering and Conference, Dallas, Tex., pp. 189-195.
- Nordgren, R. p., (1982), "Dynamic analysis of marine risers with vortex excitation," ASME, J. of Energy Resources Tech., Vol. 102.
- Paquette, R. G., and Henerson, B. E., (1965), "The dynamics of Simple deep-sea buoy moorings," Rept. TR65-79 (AD 623 959), General Motors Defense Research Labs., Santa Barbara, Calif.

- Parkinson, G.V., (1974), "Mathematical models of flow induced vibrations of bluff bodies," Proc. of IUTAM-IAHR Symposium on Flow-Induced Structural Vibrations, Karlsruhe, Berlin, Spring Verlag, pp. 81-127.
- Paul, B., and Soler, A. I., (1972), "Cable dynamics and optimum towing strategies for submersibles," Marine Technology Society Journal, Vol. 6, No. 2, pp. 34-42.
- Pearcey, H.H., and Bishop, J.R., (1979), "Wave loading in the drag and drag inertia regimes; routes to design data," BOSS' 79.
- Peregrine, D.H., (1976), "Interaction of water waves and currents," Advances in Applied Mech., Vol. 16, Academic press, New York, pp. 9-117.
- Rajabi, F., (1979), "Hydroelastic oscillation of smooth and rough cylinders in harmonic flow," Ph.D. Thesis, Naval Postgraduate School, Monterey, Calif.
- Rajabi, F., Zedan, M.F., and Mangiavacchi, A., (1984), "Vortex shedding induced dynamic response of marine risers," J. Energy Resour Technol Trans, ASME, Vol. 106, pp. 214-221.
- Ramberg, S.E., and Griffin, O.M., (1976), "Vortex formation in the wake of a vibrating, flexible cable," ASME, J. of Fluid Eng., Vol. 96, pp. 317-322.
- Rayleigh, Lord, (1896), "Theory of sound," London, Macmillan.

- Roshko, A., (1961), "Experiments on the flow past a circular cylinder at very high Reynold's numbers," J. of Fluid Mech., Vol. 10, No. 3, pp. 345-356.
- Ross, C.W., (1959), "Large-scale tests of wave forces on piling (preliminary report)," U.S. corps of Eng. Beach Erosion Board, Tech. Memo. 111.
- Russell, J.S., (1844), "Report on waves," 14th Meeting Brit. Assoc. Adv. Sci., pp.311-390.
- Sainsbury, R.N., and King, D., (1971), "The flow induced oscillation of marine structure," Proc. Inst. of Civil Eng., Vol. 49, pp. 269-302.
- Sarpkaya, T., (1976a), "In-line and transverse forces on cylinders in oscillatory flow at high Reynolds' number," Off. Tech. Conf., paper 2533.
- Sarpkaya, T., (1976b), "Forces on rough walled circular cylinders," Proc. 15th Conf. Coast. Eng.
- Sarpkaya, T., (1976c), "In-line and transverse forces on smooth and sand roughened cylinders in oscillatory flow at high Reynolds numbers," Tech. Report NPS-96SL 76062, Naval Postgraduate School, Monterey, CA.
- Sarpkaya, T., (1976d), "Vortex shedding and resistance in harmonic flow about smooth and rough cylinders at high Reynolds numbers," Naval Postgraduate School Technical Report No. NPS-59S1 7602.

- Sarpkaya, T., (1979a), "Hydrodynamic forces on various multiple-tube riser configurations," Off. Tech. Conf., paper 3539.
- Sarpkaya, T., (1979b), "Vortex-induced oscillations, A selective review," ASME, J. of Appl. Mech., Vol. 46, pp. 241-258.
- Sarpkaya, T., (1979c), "Effect of surface roughness on the transverse oscillations of a circular cylinder," Naval Postgraduate School Report NRS-69SL 79085-IR.
- Sarpkaya, T., (1981a), "A critical assessment of Morison's equation," Proc. of Hydrodynamic in Ocean Eng., The Norwegian Institute of Technology, Trondheim, Norway, Aug.
- Sarpkaya, T., (1981b), "On hydrodynamic response of risers to waves and currents," Proc. of The 37th ASME Petroleum Mechanical Eng. Workshop and Conf., Dallas, Tex.
- Sarpkaya, T., (1981c), "On hydrodynamic Response of risers to waves and currents," Pro. of The 37th ASME Petroleum Mechanical Engineering Workshop and Conference, Dallas, Tex., pp. 3-5.
- Sarpkaya, T., and Cinar, M., (1980), "Hydrodynamic interference of two cylinders in harmonic flow," Off. Tech. Conf., paper 3775.
- Sarpkaya, T., and Isaacson, M., (1981), "Mechanics of wave forces on offshore structures," Van Nostrand Reinhold.

- Sarpkaya, T., and Rajabi, F., (1979), "Dynamic response of piles to vortex shedding in oscillating flow," Off. Tech. Conf., paper 3647.
- Sarpkaya, T., Rajabi, F., Zedan, M. F., and Fischer, F. J., (1981), "Hydroelastic response of cylinders in harmonic and wave flow," Off. Tech. Conf., Paper 3992.
- Sarpkaya, T., and Tuter, O., (1974), "Periodic flows about bluff bodies. Part 1 : forces on cylinders and spheres in a sinusoidally oscillating fluid," Naval Postgraduate school Report NPSS-59 SL 74091, Monterey, Calif.
- Schwartz, L.W., (1974), "Computer extension and analytic continuation of Stokes' expansion for gravity waves," JFM, Vol. 62, pp. 553-578.
- Skjelbreia, L., (1958), "Gravity waves Stokes' third order approximation tables of functions," Council Wave Research A.S.C.H.
- Skjelbreia, L., and Hendrickson, J.A., (1960), "Fifth order gravity wave theory," Proc. 7th Coastal Eng. Conf., The Hague, pp. 184-196.
- Skop, P.A., and Griffin, O.M., (1973), "A model for the vortex-excited resonant response of bluff cylinder," J. of Sound and Vibration, 27(2), pp. 225-233.

- Skop, R.A., Griffin, O.M., and Ramberg, S.E., (1977), "Strumming predictions for the Seacon II experimental mooring," Off. Tech. Conf., paper 2884.
- Soltanahmadi, A., (1985), "Comparison of step by step solution algorithms for finite element analysis," M.Sc. Thesis, The City University.
- Spring, B.H., and Monkmeyer, P.L., (1974), "Interaction of plane waves with vertical cylinders," Proceedings of The 14th Coastal Engrg. Conf., ASCE, Vol. III, pp. 1828-1847.
- Stokes, G.G., (1847), "On the theory of oscillatory waves," Trans. Camb. Phil. Soc., Vol. 8, pp. 441-455.
- Strandhagen, A. G., and Thomas, C. F., (1963), "Dynamics of towed underwater vehicles," Rept. 219, Navy Mine Defence Lab., Panama City, Fla.
- Strouhal, V., (1878), "About a special type of excitation," Physik und Chemie, 3rd Series, Vol. 5, pp. 216-251.
- Susbielles, G.G., Van Den Bunt, J.R., Deleuil, G., and Michel, D., (1971), " Wave forces on pile section due to irregular and regular waves," Off. Tech. Conf., paper 1379.
- Szechenyi, E., (1975), "Supercritical Reynolds numbers simulation for two-dimensional flow over circular cylinders," J. of Fluid Mech., Vol. 70 part 3, pp. 529-542.

- Toebes, G.H., (1969), "The unsteady flow and wake near an oscillating cylinder," J. of Basic Eng., September, pp. 493-505.
- Triantafyllon, M. S., and Bliet, A., (1983), "The dynamics of taut and slack marine cables," Off. Tech. Conf., Paper 4498.
- Tucker, T. C., and Murtha, J. P., (1973), "Non-deterministic analysis of a marine riser," Off. Tech. Conf., Paper 1770.
- Van den Boom, H. J. J., (1985), "Dynamic behaviour of mooring lines," Behaviour of Offshore Structures, Elsevier Science Publishers B.V., Amsterdam.
- Verley, R.L.P., and Every, M.J., (1977), "Wave induced vibrations of flexible cylinders," Off. Tech. Conf., paper 2899.
- Walton, T. S., and Polachek, H., (1959), "Calculation of nonlinear transient motion of cables," Rept. 1279 (AD 418 603), David Taylor Model Basin, Washington, D.C.
- Walton, T. W., and Polachek, H., (1960), "Calculation of transient motion of submerged cables," Mathematical Tables and Aids to Computation, Vol. 14, pp. 27-60.
- Wang, H. T., (1979), "Technique for efficient time-domain analysis of complete buoy-cable systems," J. Engineering for Industry, ASME, Vol. 101, pp. 416-420.

- Wiegel, R.L., and Delmonte, R.C., (1972), "Wave-induced eddies and lift forces on circular cylinders," Report HEL 9-19, Hydraulic Eng. Laboratory, Univ. of Calif., Berkeley, Calif.
- Wooton, L.R., (1972), "Oscillation of piles in marine structures - a description of the full scale experiments at Immingham," CIRIA Technical Notes 40.
- Yamamoto, T., (1976), "Hydrodynamic forces on multiple circular cylinders," J. Hydraulic Div., ASCE, Vol. 102, No. HY9, pp. 1193-1210.
- Young, R. D., Fowler, J. R., Fisher, E. A., and Luke, R. R., (1977), "Dynamic analysis as an aid to the design of marine risers," Energy Technology Conference and Exhibit, Houston, Texas, ASME, No. 77-pet-82.
- Zdravkovich, M.M., (1977), "Review of flow interference between two circular cylinders in various arrangements," J. of Fluid Eng. Trans., ASME, Vol. 99, Ser. 1, No. 4, pp. 618-633.
- Zedan, M.F., and Rajabi, F., (1981), "Lift forces on cylinders undergoing hydroelastic oscillations in waves and two-dimensional harmonic flow," Proc. of Hydrodynamics in Ocean Eng. The Norwegian Institute of Technology, Trondheim, Norway, Augst.

Zedan, M.F., Young, J., Salane, H., and Fischer, F.J., (1980),  
"Dynamic response of a cantilever pile to vortex  
shedding in regular waves," ASME, J. of Energy  
Resources Tech., Vol. 103, pp. 32-40.

Zentech, (1987), "3-D Flexible-Riser User's Manual", 3-7 Euston  
Centre, London, NW1.